Faculty of Physics and Astronomy

University of Heidelberg

Diploma thesis
in Physics

submitted by
Stefan Schenk
born in Würselen

November 2003

Energy Flow in Hard Diffractive Deep-Inelastic Scattering and Photoproduction with a Leading Proton

This diploma thesis has been carried out by Stefan Schenk at the
Physical Institute
under the supervision of
Prof. Dr. Franz Eisele

Abstract

Energy Flow in Hard Diffractive Deep-Inelastic Scattering and Photoproduction with a Leading Proton

Diffractive events with an elastically scattered proton are identified in the range $x_{I\!P} < 0.17$ using the H1 Forward Proton Spectrometer (FPS). Deep-inelastic scattering (DIS) and photoproduction events are selected from this sample. Energy flow measurements are presented in DIS and photoproduction, focusing on the forward energy flow between the leading proton and the hard scattering process. The measurements are compared to predictions of the resolved Pomeron model, as implemented in a hard diffractive Monte Carlo simulation. The forward energy flow is well described in DIS and photoproduction, if the diffractive parton densities from the H1 QCD analysis of F_2^D are used. Due to the small acceptance of the FPS ($\mathcal{O}(5\ \%)$), diffractive analyses are usually based on a rapidity gap selection. A measurement of the efficiency of the gap selection is presented for the DIS and photoproduction samples. It is consistent with the predictions based on the resolved Pomeron model. A large Reggeon contribution to the DIS event sample is necessary to describe the data, in good agreement with the Reggeon contribution predicted by the resolved Pomeron model when using the results from the H1 QCD Fit of F_2^D.

Zusammenfassung

Energiefluß in harter diffraktiver tief-inelastischer Streuung und Photoproduktion mit vorwärtsgestreutem Proton

Diffraktive Ereignisse mit elastisch gestreutem Proton werden mit dem Vorwärtsprotonenspektrometer (FPS) des H1-Detektors in der Region $x_{I\!P} < 0.17$ identifiziert. Ereignisse der tief-inelastischen Streuung (DIS) und der Photoproduktion werden aus diesem Sample ausgewählt. Energieflußmessungen werden für die DIS und die Photoproduktion vorgestellt, wobei der Schwerpunkt auf dem Vorwärtsenergiefluß zwischen dem führenden Proton und dem harten Streuprozeß liegt. Die Messungen werden mit Vorhersagen des resolved Pomeron-Modells, wie sie in einer harten diffraktiven Monte Carlo Simulation implementiert sind, verglichen. Der Vorwärtsenergiefluß wird sowohl in der DIS als auch in der Photoproduktion gut beschrieben, wenn die diffraktiven Partondichten aus der H1 QCD-Analyse von F_2^D benutzt werden. Wegen der geringen Akzeptanz des FPS ($\mathcal{O}(5\ \%)$) basieren diffraktive Analysen gewöhnlich auf einer Rapidity Gap Auswahl. Eine Messung der Effizienz der Gap Auswahl wird in der DIS und der Photoproduktion vorgestellt. Sie ist konsistent mit der Vorhersage des resolved Pomeron-Modells. Ein großer Reggeonbeitrag zum DIS Datensample wird benötigt, um die Daten zu beschreiben, in guter Übereinstimmung mit dem Reggeonbeitrag, den das resolved Pomeron-Modell vorhersagt, wenn die Ergebnisse des H1 QCD-Fits von F_2^D benutzt werden.

Contents

Contents

Contents

Introduction

The fundamental theory of strong interactions is the theory of Quantum ChromoDynamics (QCD). It describes the interaction between colour-charged particles by the exchange of gluons. In Quantum ElectroDynamics (QED), the carrier of the force – the photon – is electrically neutral. However, not only quarks, but gluons are colour-charged as well. This leads to gluon self-interactions which manifest themselves in the behaviour of the strong coupling constant, α_s. While α_s is small, $\alpha_s \ll 1$, in reactions with large momentum transfer, $Q^2 > 1$ GeV^2, it rises sharply towards small momentum transfers.

Many phenomena of strong interactions can be described successfully using a perturbative expansion in powers of α_s. This perturbative approach can only be applied if $\alpha_s \ll 1$, ie at large momentum transfers, $Q^2 > 1$ GeV^2. Since hadronic interactions are dominated by soft physics, total cross sections cannot be calculated using perturbative methods. In elastic hadron-hadron scattering, only energy and momentum are exchanged. The exchange is colourless, and only carries vacuum quantum numbers. It can thus not be described using perturbative Quantum Chromodynamics.

A pre-QCD approach to these phenomena is Regge theory, in which hadron-hadron scattering is mediated by the exchange of colour-neutral mesons or baryons. Analogous to the partial wave decomposition in Quantum Mechanics, all hadrons with identical quantum numbers, but different spins contribute. They constitute a so-called Regge trajectory (Reggeon). Hadron-hadron scattering is hence described by the exchange of such trajectories. This approach provides a good description of total hadronic cross sections for centre-of-mass energies $\sqrt{s} > 4$ GeV, but – firstly – all known hadron trajectories fail to describe the observed slow rise of the total cross section at large energies. And secondly, since known hadrons do not carry vacuum quantum numbers, their exchange cannot describe elastic scattering processes. To solve these problems, the existence of a new trajectory – the Pomeron trajectory – was postulated. It carries vacuum quantum numbers to mediate elastic scattering, and its parameters were fitted to describe the rise of total hadronic cross sections. Due to the similarities in the behaviour of the elastic hadron-hadron cross section, and the intensity pattern in the diffraction of light, interactions which are mediated by Pomeron exchange are called diffractive. The combination of the Reggeon and Pomeron trajectories describes all total hadronic cross sections, and the elastic proton-proton cross section very well for $\sqrt{s} > 4$ GeV, but no physical particle corresponding to the Pomeron trajectory has yet been observed.

Diffractive events are also observed in electron-proton scattering at the HERA collider, where they contribute about 10 % of all recorded interactions. They can be identified by different methods. The most direct way is the detection of an elastically scattered proton, which is however limited by the small acceptance of the forward proton detectors at the H1 experiment. Since – due to the colourless exchange – no colour string is formed between the final state in the main detector and the outgoing proton, a large rapidity gap evolves. Diffractive events can hence be selected by requiring such a gap between the main event in the central detector and the outgoing proton direction.

One of the most interesting remaining questions of strong interaction theory concerns the description and interpretation of the Pomeron within the theory of Quantum Chromodynamics, which is equivalent to understanding total hadron-hadron interactions at high energies. Many different QCD-based models have been proposed. The most successful is the resolved Pomeron model. In this picture, the proton emits a Pomeron which interacts with a photon, emitted by the incoming electron. Diffractive

scattering is thus interpreted as photon-Pomeron scattering. The Pomeron is described as a partonic object, and the photon scatters of a parton from within the Pomeron, if the scattering possesses a hard scale, ie if the photon is able to resolve the structure within the Pomeron:
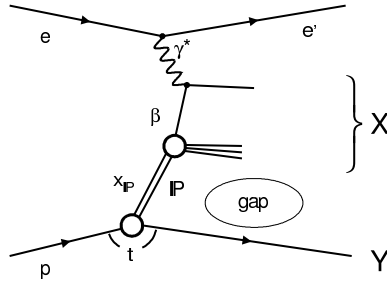
Analogous to the proton remnant in non-diffractive interactions, this results in a coloured Pomeron remnant, which manifests itself in the forward detector region between the hard scattering process and the outgoing proton. Other diffractive models do not predict the existence of a Pomeron remnant. They thus predict different forward particle and energy flows. The investigation of the Pomeron remnant and the forward energy flow hence provides a possibility to examine the validity of the different diffractive models.

Within the resolved Pomeron picture, highly virtual photons in deep-inelastic scattering (DIS) can be used to probe the structure of the Pomeron. Analogous to non-diffractive lepton-nucleon scattering, the diffractive structure function of the proton, and the parton density functions of the Pomeron can be measured in inclusive deep-inelastic scattering. This has been done by the H1-Collaboration.

For the present analysis, an unbiased diffractive event sample is selected from events recorded with the H1 detector at the HERA collider by requiring a scattered leading proton in the H1 Forward Proton Spectrometer (FPS). The FPS selected events are used to measure the energy flow, focusing on the forward energy flow between the final state jets from the hard interaction and the leading proton. Since the forward energy flow in rapidity gap selected diffractive analyses is dominated by non-diffractive background, a leading proton selected event sample is the only possibility to perform these measurements. The data is compared to predictions based on the resolved Pomeron model and the results of the H1 analysis of the diffractive structure function. Three main questions are investigated:

1. How well is the energy flow between the hard scattering process and the leading proton described by the resolved Pomeron model? Does the Pomeron remnant (spectator) reproduce the measured forward energy flow, or do significant discrepancies arise? This measurement allows to check the validity of the resolved Pomeron description.

2. How do the results in photoproduction differ from the ones observed in deep-inelastic scattering? A strong suppression of diffractive events in proton-proton interactions has been observed at the TeVatron collider. It is attributed to interactions between additional spectator partons which fill the observed rapidity gap. Are there any hints for a changed forward energy flow due to additional interactions between the Pomeron and the photon remnant in resolved photon processes?

3. How well is the efficiency of the standard rapidity gap selection of diffractive events described by a resolved Pomeron Monte Carlo simulation? This efficiency is needed in high-statistics diffractive cross section measurements to correct for rejected diffractive events. No check of the predicted corrections has yet been performed.

Additionally, the Reggeon contribution from the combined meson trajectories is well measurable in the inclusive deep-inelastic scattering event sample.

1 The Theoretical Basis

This section briefly introduces the basic concepts and results of Regge theory. Diffractive phenomena at HERA are introduced, and models of diffractive scattering are described. The H1 QCD analysis of the diffractive structure function is summarised. Recent results from the TeVatron collider on diffractive proton-antiproton scattering are presented. Kinematic reconstruction methods used in this analysis are explained, and the Monte Carlo generator is described.

1.1 Hadron-Hadron Interactions and Regge Phenomenology

Early observations in proton-proton scattering experiments showed two important properties of hadronic cross sections ([1], [2]):

1. The elastic cross section differential in the squared four momentum transfer, t, is exponentially peaked for $|t| \rightarrow 0$. This forward scattering peak becomes sharper (ie it *shrinks*) with rising centre-of-mass (cms) energy, $\sqrt{s}$ (cf section 1.1.1, figure 1.1).

2. The total cross section increases with $\sqrt{s}$ at high energies, ie above $\sqrt{s} \approx 10$ GeV (cf section 1.1.2, figure 1.2).

1.1.1 Elastic Hadron-Hadron Scattering and Diffraction

The elastic proton-proton cross section differential in t, $\frac{d\sigma}{dt}$, is shown in figure 1.1 as a function of the squared four momentum transfer, $|t|$. It is displayed for different proton momenta, ie for different centre-of-mass energies. All curves exhibit an exponential increase of the cross section for $|t| \rightarrow 0$. As the proton energy increases, this forward scattering peak becomes sharper, and a secondary maximum appears. The measured cross section can be described by

$$\frac{\frac{d\sigma}{dt}}{\left(\frac{d\sigma}{dt}\right)_{t=0}} = e^{bt} \approx 1 - b\,(p\theta)^2 \qquad [1],$$

(1.1)

where $\sqrt{|t|} = 2p\sin\left(\frac{\theta}{2}\right) \approx p\theta$ for elastic scattering at small angles. p is the momentum of the incident proton, and θ is its scattering angle. b is defined by the above equation as the *slope parameter*. This behaviour is reminiscent of the diffraction of light by a circular disc. The intensity of the scattered light is described by

$$\frac{I}{I_0} \approx 1 - \frac{R^2}{4}\,(k\theta)^2 \qquad [3],$$

(1.2)

where R is the radius of the disc, k the wave number of the photons, and θ their scattering angle. Because of this resemblance, elastic scattering and closely related processes in particle physics are named *diffractive*. A more concise definition of diffraction will be given in section 1.1.3. From the above equations, a relation between the interaction radius, R, and the slope parameter, b, may be devised:

$$b = \frac{R^2}{4} \qquad \Leftrightarrow \qquad R = \sqrt{4b}$$

(1.3)
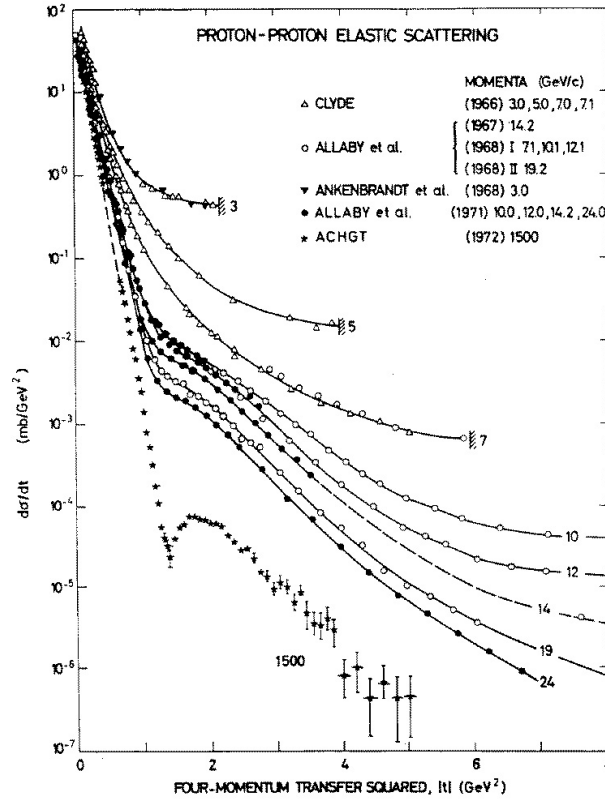
Figure 1.1: The proton-proton elastic scattering cross section differential in the squared four momentum transfer, t. It is shown for different proton momenta, ie for different cms energies. (From [1].)

For a typical strong interaction radius, $R \sim \frac{1}{m_\pi}$, the equation yields $b \sim 12.5$ GeV^{-2}. This is approximately observed at high energies [4].

1.1.2 The Total Hadronic Cross Section

Figure 1.2 displays the total cross section for hadron-proton and photon-proton scattering as a function of the centre-of-mass energy. All cross sections exhibit a sharp decline at small cms energies, and a slow rise with increasing cms energies for $\sqrt{s} > 10$ GeV.

1.1.3 Regge Phenomenology

As explained in the introduction, total hadronic cross sections and elastic scattering processes (cf sections 1.1.1, 1.1.2) cannot be treated within the framework of perturbative QCD. The following sections thus briefly summarise the phenomenological pre-QCD model of Regge theory. A detailed discussion may be found in ([5], [6]).
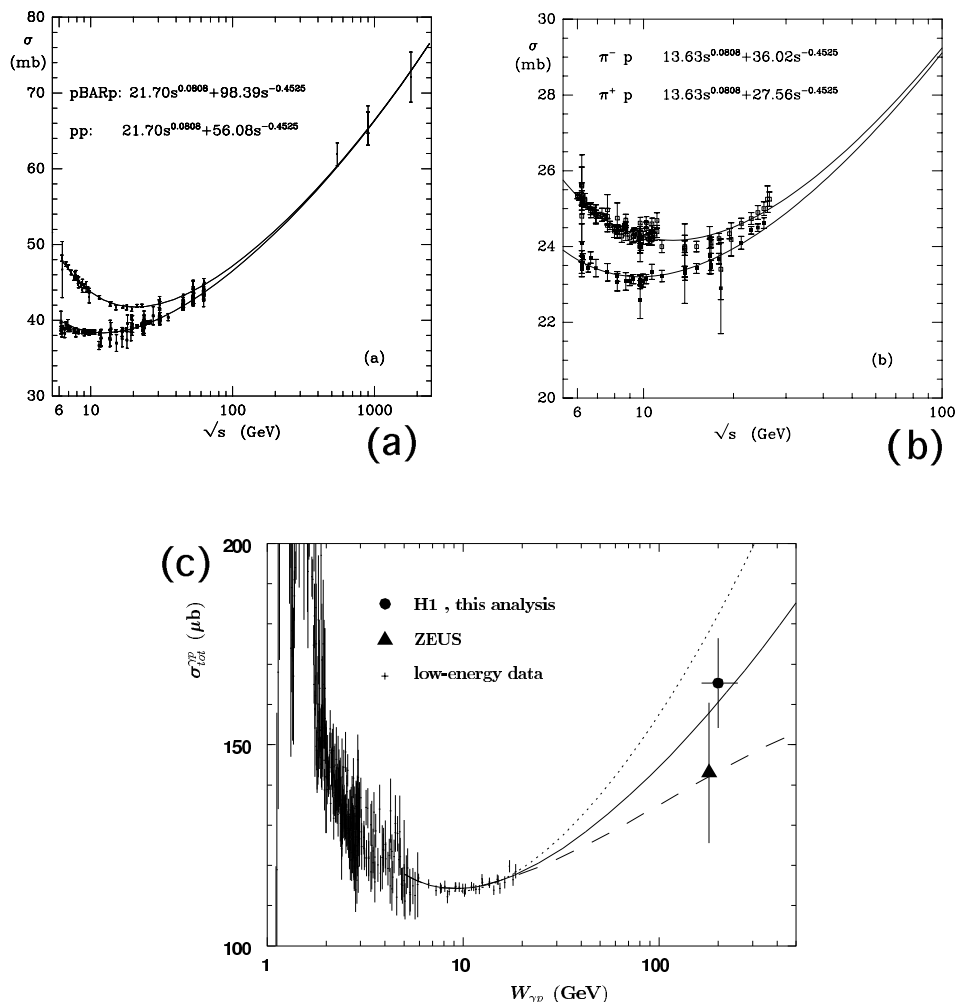
Figure 1.2: The total cross section for **a)** pp and $p\bar{p}$ scattering, **b)** $\pi^{\pm}p$ scattering, and **c)** γp scattering as a function of the centre-of-mass energy. The solid curves indicate the Donnachie-Landshoff Regge theory fits (cf section 1.1.3). (From [2].)

The Regge Model

The Regge model describes hadronic interactions as t-channel exchanges of virtual particles. Within the partial wave picture, all particles with identical quantum numbers but different angular momenta, ie *spins*, have to be included. Experiments show that all hadrons with identical quantum numbers (eg isospin, strangeness), but different spins, J, (ie spin excitations to a common ground state) lie on a straight line – the so-called *trajectory* – in the $(t = M^2, J)$-plane. Within Regge theory, hadronic interactions are thus described by the exchange of *Regge trajectories*. The *Reggeon* ($I\!\!R$) trajectory is illustrated in figure 1.3. It comprises the ρ-, ω-, f_2- and a_2-mesons and their heavier partners. Regge theory considers the angular momentum as a continuous complex variable of the four momentum transfer, $t = M^2$:

$$\alpha = \alpha(t) \in \mathcal{C} \qquad (1.4)$$

For physical resonances in s-channel reactions – ie the exchange of real particles, the real part of α is a half-integer number, $J = \Re e\ \alpha(t) = \frac{n}{2} :\ n \in I\!\!N$. Stable hadrons are characterised by $\Im m\ \alpha(t) = 0$,
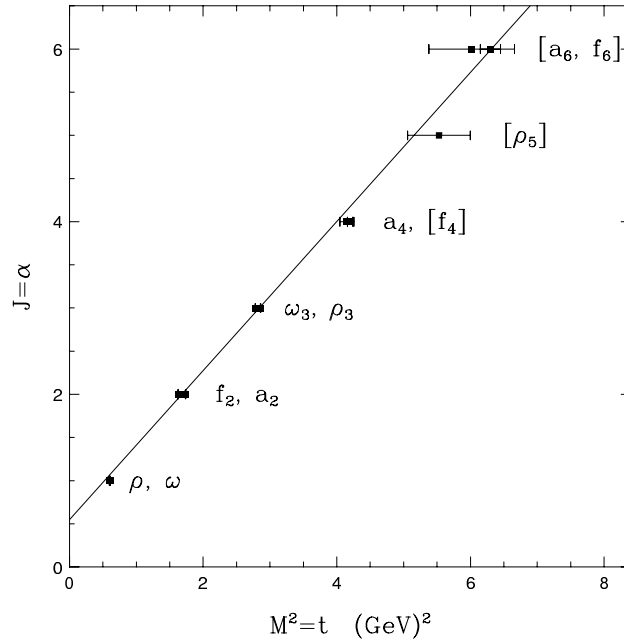
Figure 1.3: The Reggeon trajectory (comprising the ρ, ω, f, and a trajectories) in the $(M^2 = t, J)$-plane. The linear connection between the spin J, and the squared mass $M^2 = t$ of the measured particles is visible. The straight line corresponds to $\alpha(t) = 0.55 + 0.86t$. (From [7].)

unstable ones by $\Im m\ \alpha(t) \neq 0$. The hadron trajectories can be described by

$$\alpha(t) = \alpha(0) + \alpha' t. \tag{1.5}$$

The scattering amplitude for the t-channel exchange of the trajectory $\alpha_i(t)$ can be calculated in the high-energy limit, $s \to \infty$, $\frac{t}{s} \to 0$:

$$T_i(s,t) \sim \beta_i(t) \left(\frac{s}{s_0}\right)^{\alpha_i(t)}, \tag{1.6}$$

where $s_0 = \mathcal{O}(1\ \text{GeV}^2)$. In the general Regge picture, the total scattering amplitude is then given by the summation of all possible trajectories i:

$$T(s,t) = \sum_i T_i(s,t) \sim \sum_i \beta_i(t) \left(\frac{s}{s_0}\right)^{\alpha_i(t)}, \tag{1.7}$$

The success of Regge theory is based on the fact that, at high energies, only the Regge trajectory with the largest value of $\alpha(t)$ survives:

$$\left(\frac{d\sigma}{dt}\right)_{elastic} \sim \frac{1}{s^2} |T(s,t)|^2 \quad \overset{s \to \infty}{\longrightarrow} \quad f(t) \left(\frac{s}{s_0}\right)^{2\alpha(t)-2}, \tag{1.8}$$

where α is the trajectory with the largest value of $\alpha(t)$. The total cross section can be calculated using the optical theorem:

$$\sigma_{total} \sim \Im m\ (T_{elastic})_{t=0} \quad \overset{s \to \infty}{\longrightarrow} \quad s^{\alpha(0)-1}, \tag{1.9}$$

in which α is the trajectory with the largest inercept, $\alpha(0)$.

The Pomeron Trajectory and the Universal Pomeron-Reggeon Model

For all known hadrons, the Regge trajectory with the largest intercept is the Reggeon ($I\!R$) trajectory shown in figure 1.3 with

$$\alpha_{I\!R}(0) \approx 0.55. \tag{1.10}$$

The total cross section should therefore behave as

$$\sigma_{total}(s) \sim \left(\frac{s}{s_0}\right)^{-0.45} \qquad \text{for} \qquad s \to \infty. \tag{1.11}$$

However, this behaviour of declining $\sigma_{total}(s)$ is observed only for cms energies $\sqrt{s} < 10$ GeV (cf figure 1.2). The measured rise of the total cross section for $\sqrt{s} > 10$ GeV would require a Regge trajectory with an intercept $\alpha(0) > 1$, which is not observed for any of the known mesons. Regge phenomenology at high energies therefore postulates such a trajectory,

$$\alpha_{I\!P}(t) = 1.08 + 0.25t, \tag{1.12}$$

which is called *Pomeranchuk* trajectory (Pomeron: $I\!P$). And, indeed, Donnachie and Landshoff have shown that all total hadronic cross sections can be described for $\sqrt{s} > 4$ GeV by a superposition of only two trajectories, the Reggeon ($I\!R$) and the Pomeron ($I\!P$) (Donnachie-Landshoff fit, cf figure 1.2):

$$\sigma_{total}(s) = A_{I\!R} s^{\alpha_{I\!R}(0)-1} + A_{I\!P} s^{\alpha_{I\!P}(0)-1} = A_{I\!R} s^{-0.45} + A_{I\!P} s^{0.08} \qquad [8], \tag{1.13}$$

where the term $s^{-0.45}$ corresponds to the known Regge trajectory. The Pomeron trajectory possesses vacuum quantum numbers, and this model also describes the observed behaviour of the elastic proton-proton cross section. Motivated by the resemblance of the forward elastic scattering peak to the pattern of light diffraction by a circular disc (cf section 1.1.1), processes which are mediated by Pomeron exchange are named *diffractive*.

One of the most interesting questions in today's hadron physics concerns the interpretation of the Pomeron in terms of Quantum Chromodynamics:

- How can the Pomeron be described in terms of QCD, and can it be modelled and calculated in perturbative QCD?

The ideal laboratory for such questions is the HERA storage ring, in which 27.5 GeV electrons probe 920 GeV protons at a centre-of-mass energy of $\sqrt{s} \approx 318$ GeV (cf section 2.1).

1.2 Diffractive Phenomena at HERA

Diffractive processes are not restricted to elastic scattering. They do also exist in inelastic processes, especially in γp scattering as it is observed in ep interactions at HERA [9].

1.2.1 Diffractive Processes in Photon-Proton Scattering

The four principal classes of diffractive scattering processes in γp interactions are illustrated in figure 1.4. They are

a) **Quasi-elastic vector meson production:** $\gamma p \to V p$,
   where the photon fluctuates into a vector meson V.

b) **Proton elastic photon dissociation:** $\gamma p \to X p$,
   where the photon dissociates into a high-mass system X with photon quantum numbers, $J^{PC}(X) = 1^{--}$, since the exchanged Pomeron only carries vacuum quantum numbers.
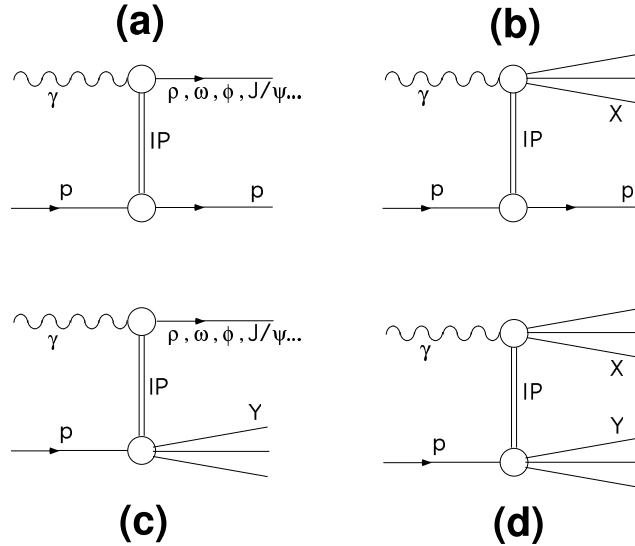
Figure 1.4: The four principal diffractive processes in photon proton interactions. **a)** Quasi-elastic vector meson production, **b)** proton elastic photon dissociation, **c)** proton dissociative vector meson production, and **d)** double dissociation. Double lines denote the colour-neutrality of the Pomeron. (From [9].)

c) **Proton dissociative vector meson production:** $\gamma p \rightarrow VY$,
where the photon fluctuates into a vector meson V, and the proton dissociates into a low-mass system Y with proton quantum numbers, $J^P(Y) = \frac{1}{2}^+$.

d) **Double dissociation:** $\gamma p \rightarrow XY$,
where photon and proton dissociate into systems $X(1^{--})$, and $Y(\frac{1}{2}^+)$.

In all cases, only energy and momentum, an no net colour are exchanged. The characteristic property of diffractive scattering processes is thus a large rapidity gap between the outgoing scattered proton or the colourless proton remnant, and the hadronic final state in the main detector. This rapidity gap is completely void of any particles. In non-diffractive interactions, a colour field develops between the final state particles due to the colour exchange. The energy of the corresponding colour strings increases with the spatial separation of the coloured particles [10]. If the string energy is large enough, fragmentation occurs, ie new quark-antiquark pairs are created from the vacuum [10], until only colour-neutral hadrons remain (hadronisation). This results in a continuous particle flow within the entire detector. In diffractive interactions, no net colour is exchanged, ie no colour string forms, and a large rapidity gap develops between the outgoing proton (or the system Y) and the other final state particles.

Diffractive events can therefore be selected experimentally using two different methods:

1. Identification of the scattered leading proton (cf chapter 3).

2. Identification of a large rapidity gap between the (undetected) outgoing proton and the event in the main detector (cf section 7.1).

1.2.2 HERA Kinematics

This section presents the basic kinematics of ep interactions at HERA. All formula are taken from ([7], [11], [12]). Figure 1.5 displays the Feynman diagram of a deep-inelastic electron-proton interaction
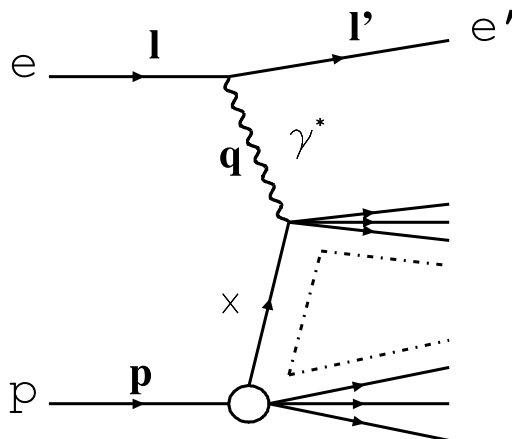
Figure 1.5: HERA kinematics: Feynman diagram of deep-inelastic electron-proton scattering in the Quark Parton Model (QPM). The electron emits a photon which interacts with a quark form the proton. $\mathbf{l}$, $\mathbf{l'}$ are the four momenta of the incoming (e) and scattered (e') electron, $\mathbf{p}$ is the four vector of the incoming proton (p), and $\mathbf{q}$ the one of the (virtual) photon (γ^*). The variable x is explained in the text, and the dotted line symbolises the colour string due to the colour charge of the quark from the proton. (From [7].)

in the basic Quark Parton Model (QPM). The electron interacts with a quark from the proton via the emission of a (virtual) photon. Principally, Z^0 exchange processes are also possible, but their contribution is negligible in the investigated phase space region ([9], [10]).

The centre-of-mass (cms) energy squared of the electron-proton system, s, is

$$s = (\mathbf{p} + \mathbf{l})^2 \approx 4 E_p E_e, \tag{1.14}$$

where $\mathbf{p}$ and $\mathbf{l}$ are the four momenta of the incoming proton and electron. At HERA, $E_e = 27.5$ GeV electrons are collided with $E_p = 920$ GeV protons, resulting in a cms energy of $\sqrt{s} \approx 318$ GeV. The centre-of-mass energy of the photon-proton system, W, is given by

$$W^2 = (\mathbf{p} + \mathbf{q})^2, \tag{1.15}$$

in which $\mathbf{q}$ is the four vector of the (virtual) photon.

Electron Side   The four momentum transfer squared at the electron vertex, ie the squared mass of the (virtual) photon, also called *virtuality*, is defined as

$$Q^2 = -\mathbf{q}^2 = (\mathbf{l} - \mathbf{l'})^2, \tag{1.16}$$

with the four momentum of the scattered electron, $\mathbf{l'}$. Two classes of interactions may be observed at HERA:

i) **Photoproduction** (γp): $Q^2 \approx 0$
   The electron emits a quasi-real photon, and escapes through the beam pipe. It may be detected with a low angle electron detector (cf section 2.2.3).

ii) **Deep-Inelastic Scattering** (DIS): $Q^2 \gg 1$ GeV^2
   The emitted photon is highly virtual, and the scattered electron is detected at large scattering angles in the main detector.

y denotes the fractional energy transfer at the electron vertex in the proton rest frame:

$$y = \frac{\mathbf{pq}}{\mathbf{pl}} \qquad : \qquad 0 \le y \le 1 \tag{1.17}$$

It is sometimes also called *inelasticity*.

Proton Side Within the QPM, the fractional momentum of the emitted quark is given by the Bjørken-x variable,

$$x = -\frac{\mathbf{q}^2}{2\mathbf{pq}} \qquad : \qquad 0 \le x \le 1 \tag{1.18}$$

Resolved Photon Processes The photon can fluctuate into a hadronic system consisting of quarks and gluons (cf figure 1.14, [13]). These processes are called *resolved photon* interactions, and occur most often in the case of quasi-real photons, ie in photoproduction [13]. The parton from the proton then interacts with a parton from the photon. x_γ denotes the momentum fraction of this parton with respect to the photon:

$$x_\gamma = \frac{\mathbf{p}_{i/\gamma}\mathbf{p}}{\mathbf{pq}} \qquad : \qquad 0 \le x_\gamma \le 1, \tag{1.19}$$

where $\mathbf{p_{i/\gamma}}$ is the four momentum of the parton i from the photon.

As products of four vectors, all of these quantities are Lorentz-invariant, but only three of them are independent of each other. It can be shown that the following relations hold:

$$Q^2 = xys \tag{1.20}$$
$$W^2 = ys - Q^2 \tag{1.21}$$

1.2.3 Models of Diffractive Scattering

QCD and Regge factorisation are introduced, and three current models of diffractive scattering processes are presented.

Factorisation and Parton Distributions

QCD Factorisation Analogous to inclusive cross sections (eg [10]), diffractive cross sections are assumed to factorise into the universal partonic cross sections, $\hat{\sigma}^{\gamma^*i}$, for the hard subprocesses between the photon and the parton i from the proton, and the diffractive parton density functions of the proton, p_i^D:

$$\frac{d^2\sigma(x, Q^2, x_{I\!P}, t)^{\gamma^*p \to p'X}}{dx_{I\!P}dt} = \sum_i \int_x^{x_{I\!P}} d\xi \hat{\sigma}^{\gamma^*i}(x, Q^2, \xi) p_i^D(\xi, Q^2, x_{I\!P}, t), \tag{1.22}$$

where t is the squared, and $x_{I\!P}$ the fractional four momentum transfer at the proton vertex. $p_i^D(\xi, Q^2, x_{I\!P}, t)$ describes the probability for a parton i to emerge from the proton for given values of (ξ, Q^2) under the constraint that the proton remains intact with particular values of $(x_{I\!P}, t)$ (diffraction). This is called QCD factorisation. It was proven for diffractive deep-inelastic scattering by Collins et al. in 1998 [14], and it is the basis for the definition of diffractive parton densities.

Regge Factorisation Regge factorisation denotes the additional assumption that the $(x_{I\!P}, t)$-dependence factorises from the hard subprocess [15]. Diffractive scattering can then be interpreted as $\gamma^*I\!P$ scattering, and the hard parton-parton interaction is independent of the emergence of the Pomeron from the proton. This is illustrated in figure 1.6. The diffractive parton density factorises
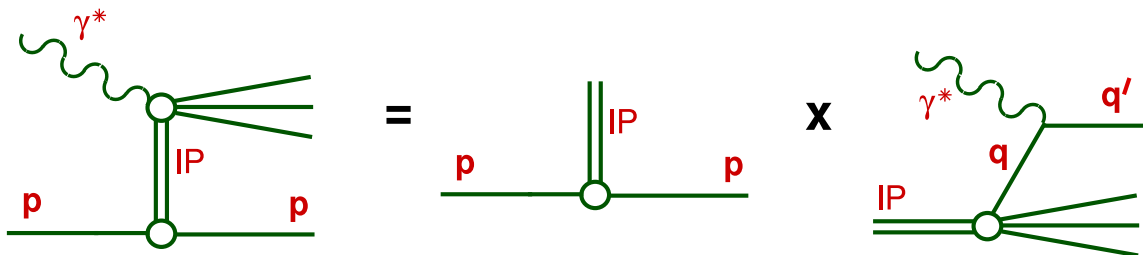
Figure 1.6: Regge factorisation in photon-proton interactions. The Pomeron-proton interaction factorises from the hard scattering process. (From [16].)

into a universal Pomeron flux factor, $f_{I\!P/p}$, and the parton density function of the Pomeron, $p_{i/I\!P}$:

$$p_i^D(x, Q^2, x_{I\!P}, t) = f_{I\!P/p}(x_{I\!P}, t) p_{i/I\!P}(\beta = \frac{x}{x_{I\!P}}, Q^2) \tag{1.23}$$

$f_{I\!P/p}$ describes the probability to find a Pomeron, $I\!P$, with given $(x_{I\!P}, t)$ in the proton. $p_{i/I\!P}$ denotes the probability for a parton i to emerge from the Pomeron with given values of (β, Q^2). It is emphasized that this is an additional assumption which has not been proven so far.

The Resolved Pomeron Model

The Resolved Pomeron model assumes Regge factorisation, and was conceived by Ingelman and Schlein in 1985 [15]. They describe the Pomeron as a hadronic object composed of quarks and gluons. Figure 1.7 shows the corresponding Feynman diagram for leading order inclusive diffractive deep-inelastic scattering $\mathcal{O}(\alpha_{em}\alpha_s^0)$. The virtual photon scatters off a quark in the Pomeron. The
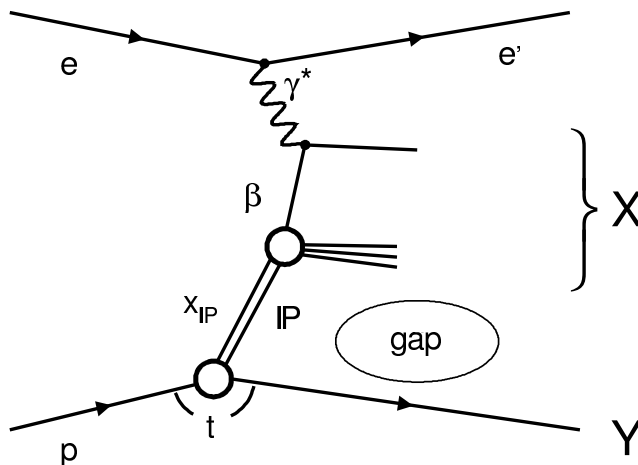
Figure 1.7: Leading order inclusive deep-inelastic scattering in terms of the resolved Pomeron model. The virtual photon scatters off a quark in the Pomeron with a Pomeron momentum fraction β. The Pomeron ($I\!P$) emerges from the proton with a proton momentum fraction $x_{I\!P}$. The double line symbolises the colour-neutrality of the Pomeron, and a gap is observed between the systems X and Y (cf section 1.2.1). (From [11].)

resulting parton, and the coloured *Pomeron remnant* constitute the *photon dissociation system*, X. Within this model, t can be interpreted as the four momentum squared of the Pomeron, and $x_{I\!P}$ is its longitudinal momentum fraction with respect to the proton. Figure 1.8 shows the Feynman diagram

for two jet production in leading order diffractive deep-inelastic scattering ($\mathcal{O}(\alpha_{em}\alpha_s)$). The virtual
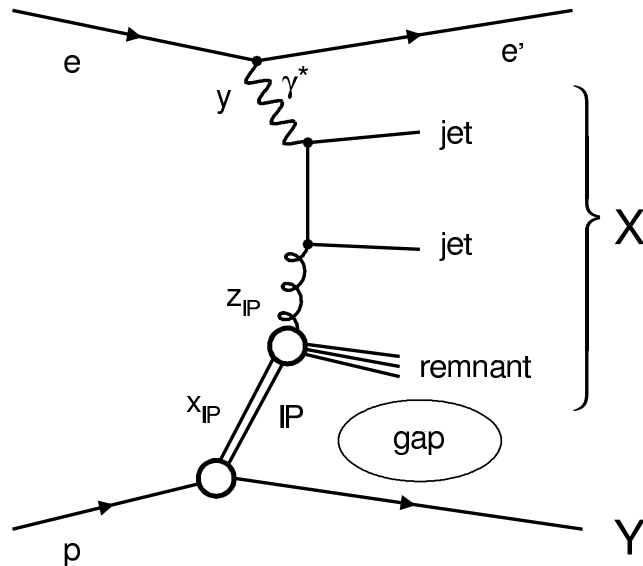
Figure 1.8: Boson-Gluon Fusion: Two jet production in leading order diffractive deep-inelastic scattering in terms of the resolved Pomeron model. The highly virtual photon, γ^*, probes the gluon content of the Pomeron. Two final state quarks are produced by the interaction of the photon with the gluon from the Pomeron. y is the energy fraction of the photon with respect to the incoming electron, and $z_{I\!P}$ the momentum fraction entering the hard scattering process from the Pomeron side. (From [11].)

photon probes the gluon content of the Pomeron. Two final state quarks are produced in the hard scattering process. These quarks can be observed as hadronic final state jets, if they emerge with high transverse momenta (cf section 1.2.7).

This interpretation of diffractive scattering provides the possibility to measure the partonic structure of the Pomeron. Diffractive deep-inelastic scattering can be understood as probing the Pomeron structure with a highly virtual photon. As in inclusive lepton-nucleon scattering, the parton density functions of the Pomeron can thus be extracted from measurements of inclusive diffractive deep-inelastic scattering (cf section 1.2.5, [10]). The resolved Pomeron model is implemented into the Monte Carlo generator RAPGAP [17], which is used within this analysis (cf section 1.4).

The Soft Colour Interaction Model

The soft colour interaction model was presented by Edin, Ingelman, and Schlein in 1995 [18]. According to this model, diffraction occurs through soft colour rearrangements which leave the momentum configuration unchanged. A rapidity gap emerges, if two colour singlet states are obtained in the rearrangement process. Thus, no Pomeron remnant exists within this model. An illustration of the soft colour interaction model is presented in figure 1.9.

Perturbative QCD Models

Photon-proton interactions can be viewed in different reference systems. The picture of the proton infinite momentum frame corresponds to the familiar picture of Feynman diagrams (cf figure 1.7, [19]). In the proton rest frame, the virtual photon fluctuates in lowest order QCD into a $q\bar{q}$ pair (colour dipole) well before the interaction with the proton [20]. This colour dipole then interacts with the
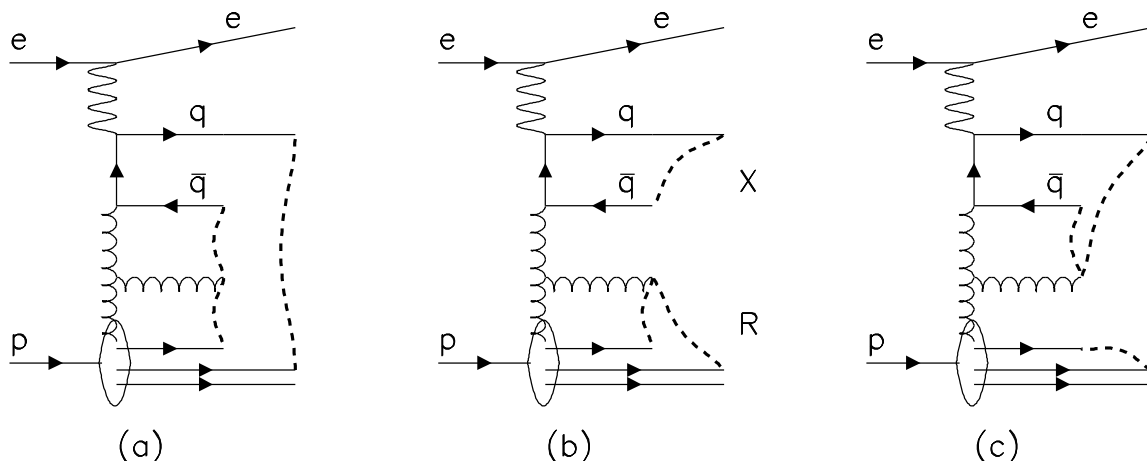
Figure 1.9: The soft colour interaction model for diffractive DIS. **a)** In deep-inelastic scattering, colour strings (dashed lines) are spanned between the final state partons and the proton remnant. **b), c)** Soft colour interactions can lead to rearrangements of the colour string, and hence to colour singlet configurations in the final state. Thus, no Pomeron remnant exists within this model. (From [9].)

proton by the exchange of the colour-neutral Pomeron. The simplest colour-neutral QCD Pomeron is a $2g$-state. Diffraction can thus be approximated in terms of perturbative QCD as exchange of two hard gluons [21]. Figure 1.10 presents an illustration of the dipole picture of diffractive two gluon exchange as seen in the proton rest frame. Since the Pomeron – consisting of two gluons –
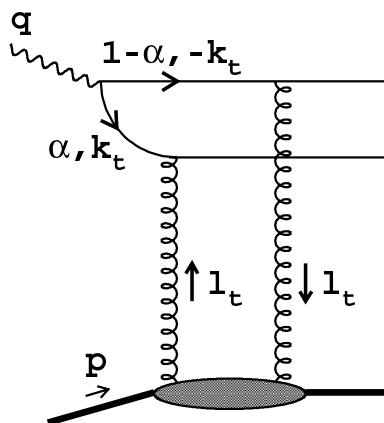
Figure 1.10: Dipole picture of diffractive two gluon exchange in the proton rest frame. The gluons carry transverse momenta $\pm \mathbf{l}_t$. α and $(1 - \alpha)$ are the momentum fractions of the quarks with respect to the photon. Their transverse momenta are $\pm \mathbf{k}_t$. (From [21].)

interacts simultaneously with both quarks from the photon, Regge factorisation is broken by two gluon exchange processes.

1.2.4 Diffractive Kinematics

This section describes the diffractive kinematic quantities as applicable within a factorisable model, such as the resolved Pomeron model. Again, all equations are extracted from ([7], [11], [12]). The

squared four momentum transfer at the proton vertex, ie the four momentum squared of the Pomeron, t, is defined as

$$t = (\mathbf{p} - \mathbf{p}')^2 \qquad : \qquad t \leq 0, \tag{1.24}$$

where $\mathbf{p}'$ is the four vector of the outgoing proton system, Y (cf section 1.2.1). The fractional longitudinal momentum transfer at the proton vertex, ie the momentum fraction of the Pomeron with respect to the proton, $x_{I\!\!P}$ is given by

$$x_{I\!\!P} = \frac{\mathbf{q}\,(\mathbf{p} - \mathbf{p}')}{\mathbf{q}\mathbf{p}} \qquad : \qquad 0 \leq x_{I\!\!P} \leq 1. \tag{1.25}$$

In the resolved Pomeron model, the photon interacts with a parton from the Pomeron. β describes the momentum fraction of this interacting parton with respect to the Pomeron:

$$\beta = -\frac{\mathbf{q}^2}{2\mathbf{q}\,(\mathbf{p} - \mathbf{p}')} \qquad : \qquad 0 \leq \beta \leq 1 \tag{1.26}$$

β and $x_{I\!\!P}$ are related to the Bjørken-x variable via

$$x = \beta x_{I\!\!P} \tag{1.27}$$

The invariant mass of the photon-Pomeron system (photon dissociation system), X, is

$$M_X^2 = (\mathbf{q} + x_{I\!\!P}\mathbf{p})^2 \approx x_{I\!\!P}ys. \tag{1.28}$$

M_Y symbolises the invariant mass of the proton system Y:

$$M_Y^2 = (\mathbf{p}')^2 \tag{1.29}$$

It can be shown [12] that

$$x_{I\!\!P} = \frac{Q^2 + M_X^2 - t}{Q^2 + W^2 - m_p^2} \approx \frac{Q^2 + M_X^2}{Q^2 + W^2} \tag{1.30}$$

for $|t| \ll Q^2 + M_X^2$, and $m_p^2 \ll Q^2 + W^2$. Under the same conditions,

$$\beta \approx \frac{Q^2}{Q^2 + M_X^2}. \tag{1.31}$$

1.2.5 Inclusive Measurements of the Pomeron Structure

The diffractive structure function, F_2^D, and diffractive parton densities are introduced, and the H1 QCD analysis of F_2^D is presented.

The Diffractive Structure Function of the Proton

In principal a fivefold differential cross section can be measured in inclusive diffractive deep-inelastic scattering. Using QCD factorisation (cf section 1.2.3), the diffractive structure function of the proton, $F_2^{D(5)}$ is defined analogous to the inclusive proton structure function, eg in lepton-nucleon scattering [10]:

$$\frac{d^5\sigma_{ep\to eXY}}{dx_{I\!\!P}d\beta dQ^2 dM_Y dt} = \frac{4\pi\alpha_{em}^2}{\beta^4 Q^4}\left(1 - y + \frac{y^2}{2\left(1 + R^{D(5)}\right)}\right)F_2^{D(5)}, \tag{1.32}$$

where α_{em} is the electromagnetic fine structure constant, and $R^{D(5)}$ the ratio of the diffractive cross sections for longitudinal and transverse photons. At HERA, the diffractive cross sections for longitudinal photons are negligible, and hence $R^{D(5)} \approx 0$. In rapidity gap analyses (cf section 7.1), the

outgoing system Y is not measured. This corresponds to an implicit integration over the variables (t, M_Y), which results in a threefold differential cross section:

$$\frac{d^3\sigma_{ep \to eXY}}{d_{x_{I\!\!P}} d\beta dQ^2} = \frac{4\pi\alpha_{em}^2}{\beta^4 Q^4} \left(1 - y + \frac{y^2}{2}\right) F_2^{D(3)} \tag{1.33}$$

Within the resolved Pomeron model, Regge factorisation is assumed (cf section 1.2.3), leading to the factorisation of the proton structure function into a universal Pomeron flux factor, $f_{I\!\!P}$, and the structure function of the Pomeron, $F_2^{I\!\!P}$:

$$F_2^{D(3)}(x_{I\!\!P}, \beta, Q^2) = f_{I\!\!P}(x_{I\!\!P})F_2^{I\!\!P}(\beta, Q^2) \tag{1.34}$$

The Universal Pomeron-Reggeon Model and the Flux Factors

During the analysis of inclusive diffractive deep-inelastic scattering, the breaking of Regge factorisation was observed, if only Pomeron exchange processes were considered [22]. Regge factorisation was found to hold, if the subleading Reggeon trajectory is included. This is called the universal Pomeron-Reggeon model, in which the diffractive structure function is

$$F_2^{D(4)}(x_{I\!\!P}, \beta, Q^2, t) = f_{I\!\!P}(x_{I\!\!P}, t)F_2^{I\!\!P}(\beta, Q^2) + f_{I\!\!R}(x_{I\!\!P}, t)F_2^{I\!\!R}(\beta, Q^2) \tag{1.35}$$

The assumption of Reggeon exchange processes being important in diffractive deep-inelastic scattering is thus based only on an indirect hint due to the otherwise apparent breaking of Regge factorisation. A Regge motivated parametrisation of the flux factors was used in the diffractive DIS analysis mentioned above [22]:

$$f(x_{I\!\!P}, t) = \frac{Ce^{B|t|}}{x_{I\!\!P}^{2\alpha(t)-1}} \tag{1.36}$$

The Pomeron Structure Function

The structure function of the Pomeron can be written as the sum of its parton distributions. The latter describe the probability to find a parton i in the Pomeron with given values of (β, Q^2) [10]. Parton density functions show *scaling violations*, ie they depend on the scale of the interaction, eg Q^2 [10]. This is caused by parton splitting. In first order QCD, the following processes can occur:

$$
\begin{aligned}
&\text{a)} \quad \text{gluon radiation}: \quad q \quad \to \quad qg \\
&\text{b)} \quad \text{pair production}: \quad g \quad \to \quad q\bar{q} \\
&\text{c)} \quad \text{gluon splitting}: \quad g \quad \to \quad gg
\end{aligned}
$$

The probabilites for these processes are given by the splitting functions, $P_{i \to j}(z)$, where $(1 - z)$ is the fractional momentum of the emitted parton. The scale dependence is described in first order QCD by the DGLAP evolution equations (eg [23]), which return eg for the gluon density function, $g(z, Q^2)$:

$$\frac{dg(z, Q^2)}{d \log Q^2} = \frac{\alpha_s(Q^2)}{2\pi} \int_z^1 \frac{dy}{y} \left(\sum_q P_{q \to qg}\left(\frac{z}{y}\right) q(y, Q^2) + P_{g \to gg}\left(\frac{z}{y}\right) g(y, Q^2)\right), \tag{1.37}$$

where z is the momentum fraction of the gluon, α_s the strong coupling constant, and $q(y, Q^2)$ are the quark densities. Since the DGLAP equations only describe the evolution of the parton density functions, the parton densities are parametrised for a starting scale, Q_0^2. The Pomeron structure function is then given by

$$F_2^{I\!\!P}(\beta, Q^2) = \sum_i e_i^2 \beta q_i(\beta, Q^2) + \beta g(\beta, Q^2), \tag{1.38}$$

where e_i is the electric charge of the quark i in units of the proton charge, and q (g) are the quark (gluon) densities. As the Pomeron carries the quantum numbers of the vacuum, all antiquark densities are identical to the corresponding quark densities, $q = \bar{q}$. This is also valid for the densities of u and d quarks, $u = d$ (isoscalar).

The H1 QCD Fit of the Pomeron Parton Density Functions

In 2002, leading and next-to-leading order DGLAP QCD fits were performed to the inclusive diffractive cross section and $F_2^{D(3)}$ measurements at the H1 detector [24]. They replace the older leading order QCD fit from 1997 [22]. The data was recorded in 1994-1997, and diffractive events were selected with the rapidity gap method (cf section 7.1). It covers the virtuality ranges $6.5 < Q^2 < 120$ GeV^2 and $200 < Q^2 < 800$ GeV^2.

QCD and Regge factorisation were assumed to hold, and the cross section was described within the universal Pomeron and Reggeon Model (cf section 1.1.3, equations 1.33, 1.35, 1.36). For the subleading Reggeon trajectory, only the normalisation parameter, $A_{I\!R}$, was included in the fit. The parton density function was used as determined in [25]. Implicit integration over the non-measured four-momentum transfer, t, in equation 1.36 results in

$$f_{I\!P}(x_{I\!P}) = \int dt\, x_{I\!P}^{1-2\alpha_{I\!P}(t)} e^{Bt} \tag{1.39}$$

With this equation, the intercept of the Pomeron trajectory was determined from the data:

$$\alpha_{I\!P}(0) = 1.173 \pm 0.018 \tag{1.40}$$

Since this differs significantly from the value determined in the Donnachie-Landshoff fit of the total hadronic cross sections (cf section 1.1.3), there is no universal Pomeron trajectory describing all diffractive interactions.

A quark singlet distribution, $\sum(z, Q^2) = 6u$, where $u = d = s = \bar{u} = \bar{d} = \bar{s}$, and a gluon distribution, $g(z, Q^2)$, were parametrised as Pomeron parton densities at a starting scale $Q_0^2 = 3$ GeV^2. These parton densities were evolved using the DGLAP equation, and fitted to the data in the region ($x_{I\!P} < 0.05$, $0.01 < \beta < 0.9$, and $M_X > 2$ GeV). The inclusive data is hereby dominated by lowest order quark exchange ($\mathcal{O}(\alpha_{em}\alpha_s^0)$, cf figure 1.7). The gluon distribution is only accessible via scaling violations (cf section 1.2.5), ie higher order processes.

The measured parton densities of the Pomeron are displayed in figure 1.11. It shows the results of a leading and a next-to-leading order QCD fit. The result shows that the Pomeron is dominated by gluons. The fraction of the Pomeron momentum carried by gluons is presented in figure 1.12 as a function of Q^2 for the next-to-leading order fit. It amounts to approximately 75 % in the analysed range $6.5 < Q^2 < 800$ GeV^2.

The Monte Carlo samples used in this analysis (cf sections 4.3.1, 8.4.1) are weighted to the leading order parton density functions from the 2002 fit in the analysis.

Measurement of F_2^D with a Leading Proton

Proton elastic photon dissociation processes, $ep \to e'p'X$ (cf section 1.2.1), can also be identified by the detection of the leading scattered proton, eg in the *Forward Proton Spectrometer* (FPS) of the H1 detector (cf section 2.2.4). A measurement of $F_2^{D(3)}(x_{I\!P}, \beta, Q^2)$ has been performed by the H1 collaboration in the kinematic region ($2 < Q^2 < 50$ GeV^2, $5 \cdot 10^{-3} < \beta < 1$, $x_{I\!P} < 0.09$, $-0.45 < t < -0.08$ GeV^2), using events with a scattered leading proton in the FPS [26]. The data was recorded in 1999 and 2000, and the present analysis is also based on the same FPS preselected data. Figure 1.13 compares the leading proton measurement to preliminary results of the rapidity gap based H1 QCD Fit 2002 (labelled H1 1997, cf section 1.2.5).
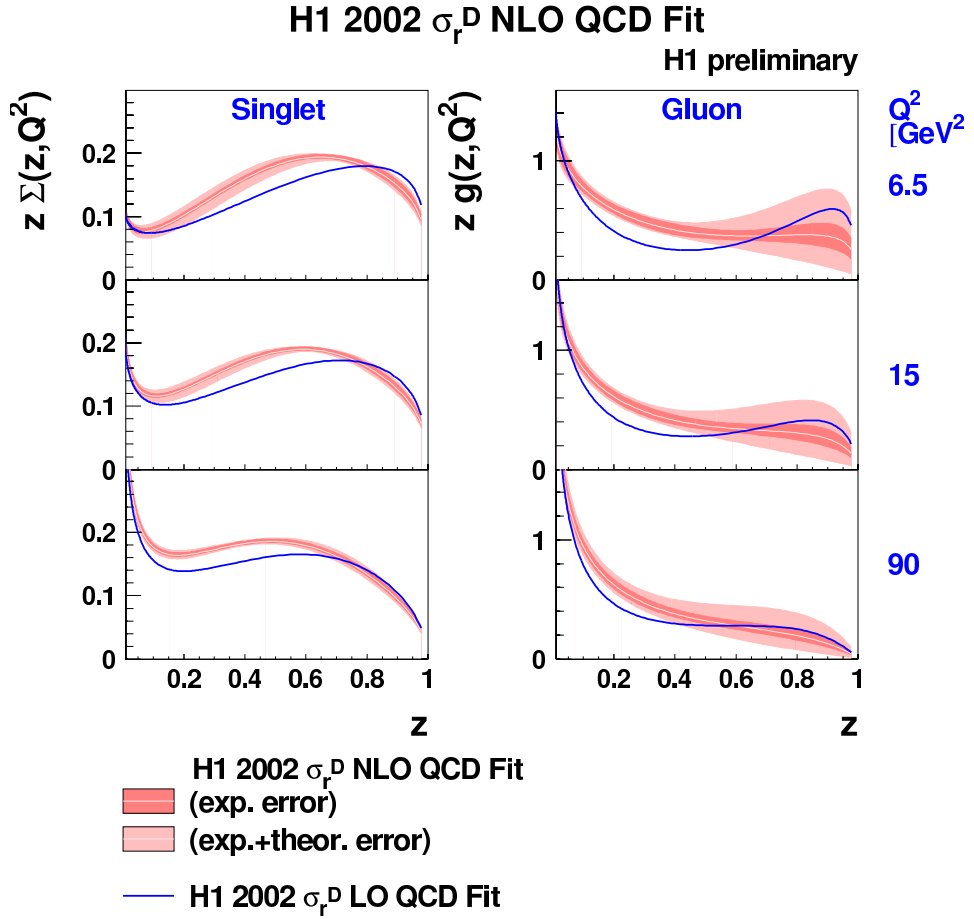
Figure 1.11: The parton densities of the Pomeron: Leading and next-to-leading order QCD fits from 2002. (From [24].)
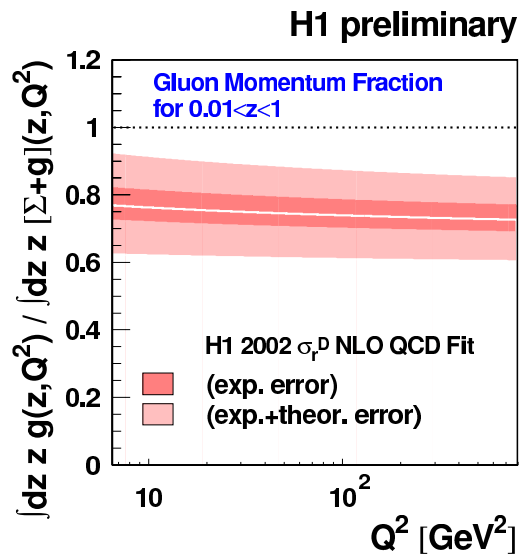
Figure 1.12: The gluon momentum fraction in the Pomeron as determined in the next-to-leading order QCD fit by integration of the parton densities in the measured range $0.01 < z < 1$. (From [24].)
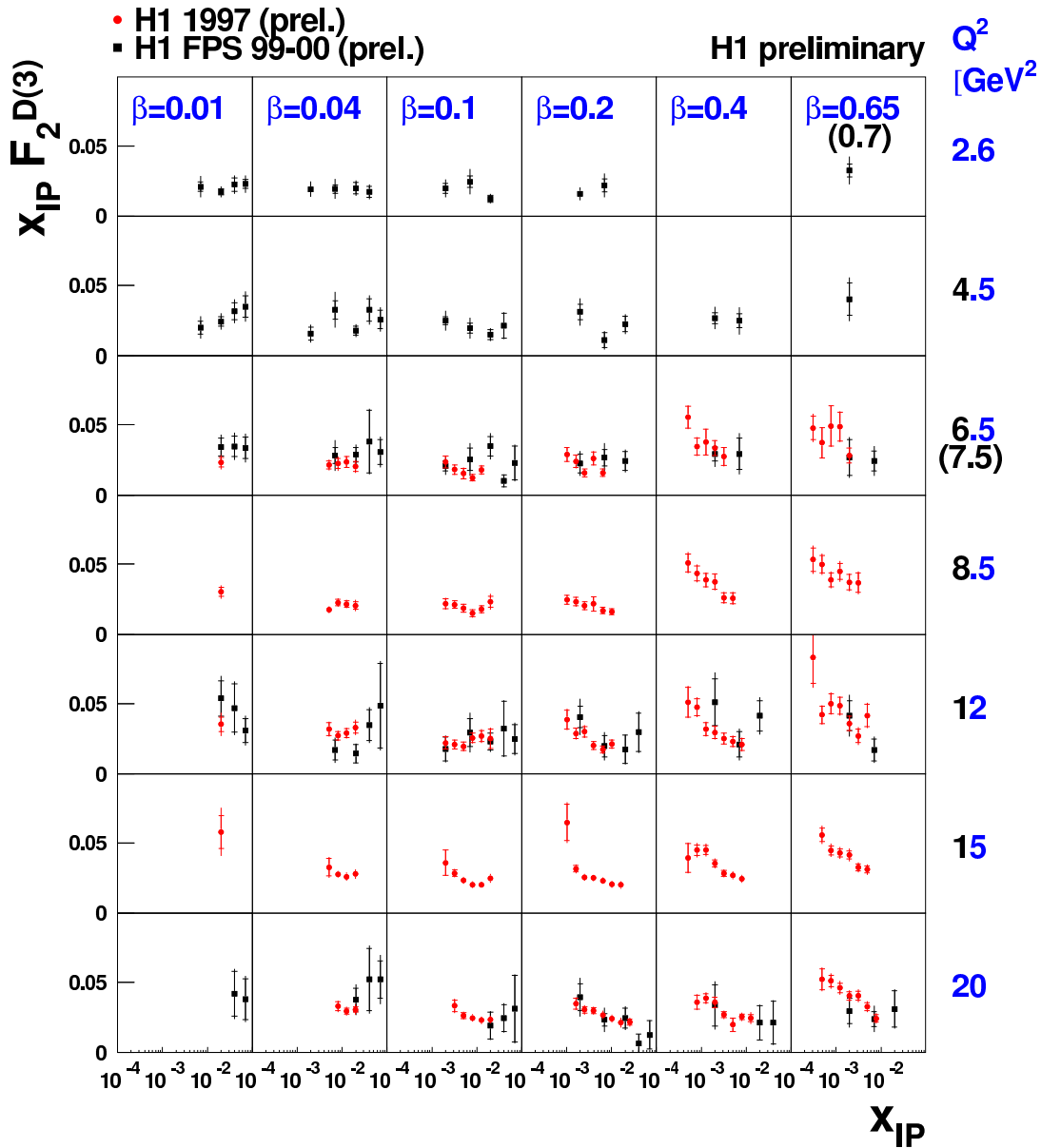
Figure 1.13: Comparison of the leading proton and rapidity gap measurements of F_2^D. $x_{I\!P} F_2^{D(3)}$ is plotted as a function of $x_{I\!P}$ at fixed values of (β, Q^2). The squares represent the data with a leading proton, which has been extrapolated into the range $|t| < 1$ GeV^2. The preliminary results of the H1 QCD Fit 2002 are displayed as circles. The leading proton data at $(\beta = 0.7, Q^2 = 20$ GeV$^2)$ are compared to rapidity gap data at $(\beta = 0.65, Q^2 = 18$ GeV$^2)$. Statistical uncertainties are represented by the inner error bars, the outer error bars display systematic and statistical uncertainties added in quadrature. (From [26].)

An acceptable agreement is observed between the two methods. This confirms the rapidity gap selection method of diffractive events.

1.2.6 Kinematic Reconstruction Methods

Figure 1.14 displays a diffractive dijet process in resolved photon photoproduction in terms of the resolved Pomeron model. x_γ is the longitudinal momentum fraction of the resolved photon which
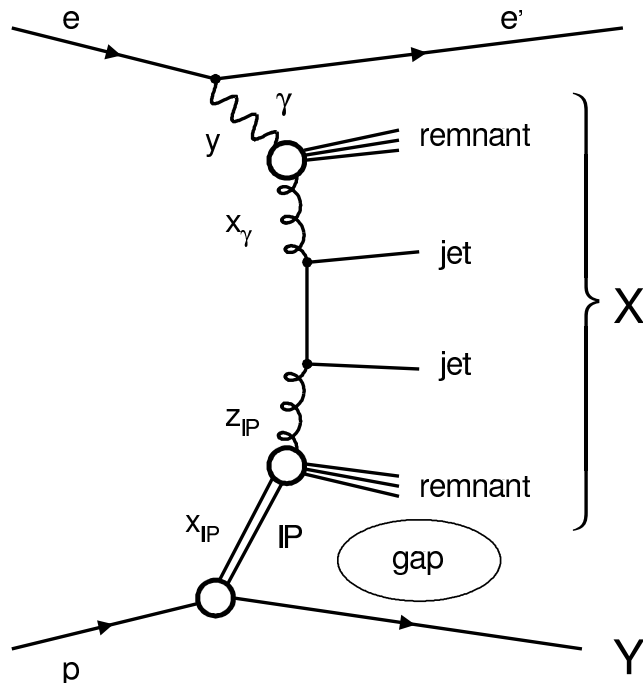
Figure 1.14: Diffractive dijet process in resolved photon photoproduction in terms of the resolved Pomeron model. The scattered proton within the actual analysis corresponds to the system Y in this diagram. (From [11].)

enters into the hard scattering process. The following quantities are directly measurable with the H1 detector (cf section 2.2):

   i) **The scattered electron:**
   The energy, $E_{e'}$, and the scattering angle, $\theta_{e'}$, of the scattered electron are measured with the main detector (DIS), or a special low angle electron detector (photoproduction).

  ii) **The photon dissociation system X:**
   The four vectors of all detected objects belonging to the system X are measured within the H1 main detector. They are used to calculate the four momenta of the selected jets (cf section 1.2.7).

 iii) **The scattered proton:**
   The energy, $E_{p'}$, and the transverse momenta, p_x, p_y of the scattered proton are measured with a special Forward Proton Spectrometer.

M_X is directly calculated from the four momenta of the objects constituting the system X:

$$M_X^2 = \left(\sum_{h \in HFS} E_h \right)^2 - \sum_i \left(\sum_{h \in HFS} p_{h_i} \right)^2 = s_{\gamma I\!P},$$

where h symbolises all particles of the system X, and i represents the coordinate axes $\{x,\ y,\ z\}$.

Rapidity

The polar angle, θ, is often replaced by the *rapidity*, y':

$$y' = \frac{1}{2} \ln \frac{E + p_z}{E - p_z} \tag{1.41}$$

In contrast to θ, and like ϕ, rapidity differences $\Delta y'$ are invariant under Lorentz boosts along the z-axis. For highly relativistic particles, where $E \gg m$, y' can be approximated by the *pseudorapidity*, η, which only depends on the angle θ:

$$y' \approx \eta = \frac{1}{2} \ln \frac{p + p_z}{p - p_z} = -\ln \left(\tan \left(\frac{\theta}{2} \right) \right), \tag{1.42}$$

where p is the magnitude of the conventional three momentum.

The kinematic variables (Q_2, y, W) (cf sections 1.2.2, 1.2.4) can be reconstructed using different ways [12]. Only the methods which are used within this thesis are presented:

Electron Method

Only the scattered electron is used to calculate the kinematic quantities according to the following equations [12]:

$$Q_e^2 \;\; = \;\; 4 E_e E_{e'} \cos^2 \left(\frac{\theta_{e'}}{2} \right) \tag{1.43}$$

$$y_e \;\; = \;\; 1 - \frac{E_{e'}}{E_e} \sin^2 \left(\frac{\theta_{e'}}{2} \right) \tag{1.44}$$

$$W_e \;\; = \;\; y_e s - Q_e^2, \tag{1.45}$$

where s is the centre-of-mass energy squared, $s \approx 4 E_e E_p$, with the incoming electron (E_e), and proton (E_p) energies.

Hadron Method

Within this reconstruction method, only the hadronic final state (HFS) in the main detector, ie the system X, is used to calculate the kinematic variables [12]:

$$y_{had} \;\; = \;\; \frac{E_{had} - p_{had_z}}{2 E_e} \equiv \frac{\sum_{h \in HFS} (E_h - p_{h_z})}{2 E_e} \tag{1.46}$$

$$W_{had} \;\; = \;\; y_{had} s - Q_{had}^2 \approx y_{had} s, \tag{1.47}$$

where *had* symbolises all hadronic final state particles $\{h\}$. $\{E_h\}$ are the energies of those particles, and γ_{had} is defined by $E_{e'} \sin \theta_{e'} = E_{had} \sin \gamma_{had}$. The last equality only holds for photoproduction, where $Q^2 \approx 0$.

Double Angle Method

The kinematic variables are reconstructed only using angle measurements; no energy measurements are considered [12]:

$$y_{da} \;\; = \;\; \frac{\sin \theta_{e'} \left(1 - \cos \gamma_{had} \right)}{\sin \theta_{e'} + \sin \gamma_{had} - \sin \left(\theta_{e'} + \gamma_{had} \right)} \tag{1.48}$$

The fractional four momentum transfer at the proton vertex, $x_{I\!P}$, can be reconstructed using either the scattered leading proton (a), or the hadronic final state, X (b,c) ([11], [12]):

$$
\begin{aligned}
\text{a) Leading proton :} \quad & x_{I\!P} \;=\; 1 - \frac{E_{p'}}{E_p} \\
\text{b) Hadronic final state in DIS :} \quad & x_{I\!P} \;\approx\; \frac{M_X^2 + Q2}{W^2 + Q^2} \\
\text{b) Hadronic final state in } \gamma p : \quad & x_{I\!P} \;\approx\; \frac{\sum_{h \in X}(E_h + p_{h_z})}{2E_p},
\end{aligned}
\tag{1.49}
$$

where the leading proton relation results from equation 1.25, and the fact that $p_x, p_y \ll E_{p'} \approx p_z$ (cf section 2.2). Equation (b) holds for all cases, in which $|t| \ll Q^2 + M_X^2$, and $m_p^2 \ll Q^2 + W^2$. In (c), the sum includes all particles h of the photon dissociation system, X. For dijet events in photoprocution reactions, the momentum fraction entering the hard interaction from the photon side, x_γ (cf equation 1.19) can be calculated as follows [11]:

$$
x_\gamma = \frac{\sum_{h \in jets}(E_h - p_{h_z})}{2yE_e},
\tag{1.50}
$$

where all particles $\{h\}$ of the two hard jets are considered for the summation.

1.2.7 Jet Identification

Different algorithms exist to identify jets within the hadronic final state (HFS). In the present analysis, an inclusive $k_\perp$-algorithm is used [27].

Inclusive $k_\perp$-Algorithms

Inclusive $k_\perp$-algorithms are *clustering algorithms* in which jets are defined by the successive recombination of particles in an iterative procedure. Final state particles are recombined in the order of their relative transverse momenta, $k_\perp$. New objects are defined by their four momenta, $\mathbf{p}'$. These are calculated from the four vectors of the merged particles:

$$
\mathbf{p}' = \mathbf{p_1} + \mathbf{p_2} \qquad \text{(E recombination scheme)}
\tag{1.51}
$$

The resulting combined particles and jets are massive. *Inclusive* refers to the fact that not all final state hadrons are combined into jets. Hadron collisions contain final state particles which do not result from the hard parton-parton interaction (eg beam remnants). These should not be included into the high-$p_\perp$ jets. This is observed by inclusive jet algorithms. They divide the final state into a certain number of jets and any number of particles not included in jets. Inclusive jet definitions are illustrated in figure 1.15 in contrast to exclusive jet algorithms. The latter combine all final state particles into jets.

The procedure of the inclusive $k_\perp$-algorithm used in this analysis can be summarised in the following way [27]:

1. The clustering procedure starts with a list of all final state particles, and an empty list of jets.

2. The distances d_i and d_{ij} are calculated for each particle i, and each pair of particles (i, j):

$$
\begin{aligned}
d_i \;&=\; E_{i_\perp}^2 \\
d_{ij} \;&=\; \min\left(E_{i_\perp}^2, E_{j_\perp}^2 \right) \frac{R_{ij}^2}{R_0^2} \quad \text{with} \quad \mathrm{R}_{ij}^2 = (\Delta\eta_{ij})^2 + (\Delta\phi_{ij})^2,
\end{aligned}
$$

where the parameter R_0 is set to $R_0 = 1$ in this analysis.
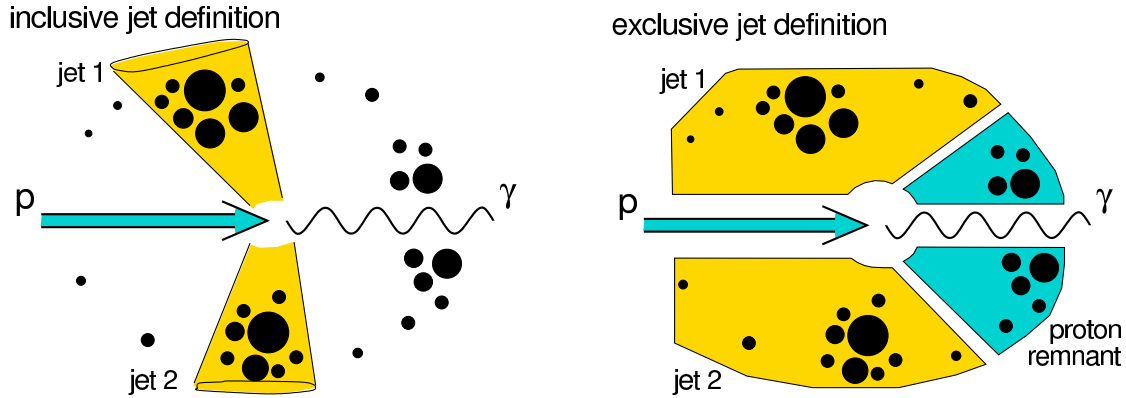
Figure 1.15: Inclusive and exclusive jet definitions. The graphic shows the different ways in which an inclusive (left) and an exclusive (right) jet algorithm group the final state particles of one single deep-inelastic scattering event into jets. (From [27].)

3. The smallest of all values d_i and d_{ij} is labelled

$$d_{min} = \min \left(d_i, d_{ij} \right).$$

4. If d_{min} belongs to the set $\{d_{ij}\}$, the particles i and j are merged into a new particle using the E recombination scheme.

5. If d_{min} belongs to the set $\{d_i\}$, the particle i is removed from the list of particles and added to the list of jets.

6. The procedure is finished when no particles are left, ie when all particles are included in the list of jets.

7. The last jets entered into the list are the ones with the highest transverse momentum, $p_\perp$. All jets with transverse momenta above a minimum $p_\perp^{min}$ are accepted as high-$p_\perp$ jets. The remaining jets are not selected as jets, but their particles are considered individually within the final state.

The jets are specified by their four momenta:

$$\mathbf{p}_{jet} = \sum_{i \in jet} \mathbf{p}_i, \tag{1.52}$$

where the sum includes all particles within the considered jet. The η-difference of the two jets, $\Delta \eta = |\eta_{lab}^{jet\ 1} - \eta_{lab}^{jet\ 2}|$, is related to the scattering angle in the cms system of the hard partons, $\hat{\theta}$ [28]:

$$\left| cos\hat{\theta} \right| = \tanh \left(\frac{\Delta \eta}{2} \right) \tag{1.53}$$

1.3 Diffractive $p\bar{p}$ Scattering at the TeVatron

At the Fermilab TeVatron $p\bar{p}$ collider, diffractive dijet events with an elastically scattered leading proton or antiproton were studied at a centre-of-mass energy of $\sqrt{s} = 1800$ GeV [29]. Figure 1.16 shows the measurement of the diffractive structure function of the antiproton, $\tilde{F}_{JJ}^D$, and a comparison to predictions based on the Pomeron parton densities from the old 1994 H1 Fit of F_2^D (H1 Fit 2,
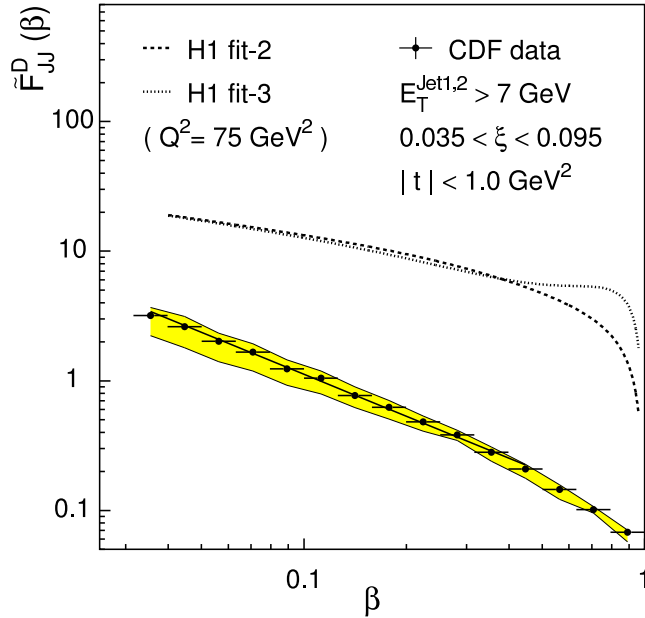
Figure 1.16: The diffractive structure function of the antiproton, $\tilde{F}_{JJ}^{D}$, as measured by the CDF Collaboration [29]. The filled band represents the systematic uncertainties from the evaluation of β. The straight line is a fit of the form $\tilde{F}_{JJ}^{D} \sim \beta^{-n}$. The dashed (dotted) lines represent the predictions from the H1 Fit 2 (3). (From [29].)

and Fit 3). The CDF measurement differs from the prediction, both in shape and in normalisation. The latter discrepancy amounts to one order of magnitude (*TeVatron effect*). One interpretation of this suppression is the occurrence of interactions due to additional partons which fill the observed rapidity gap. A similar effect can occur in diffractive resolved photon interactions at HERA (cf figure 1.14). Additional interactions are possible between the photon and Pomeron remnants. A possible consequence of these remnant-remnant interactions could be the suppression of resolved photon events in diffractive photoproduction. It is investigated within this thesis, if any changes in the forward energy flow due to these additional interactions can be found in the photoproduction compared to the deep-inelastic scattering event samples.

1.4 Monte Carlo Simulation

Monte Carlo simulated event samples are compared to the measured data in order to examine the description of the latter by the underlying diffractive model.

Generation

Within this thesis, the RAPGAP generator, which is based on the resolved Pomeron model (cf section 1.2.3, [17]), is used. It includes the description of the Pomeron remnant, and the related forward particle and energy flow. The diffractive scattering process is described as interaction between the photon and a Pomeron with partonic structure. Pomeron and Reggeon exchange processes are included, and the results from the H1 QCD analysis of the diffractive structure function, F_2^D, are used to describe the partonic structure of the Pomeron, and the relative Pomeron and Reggeon contributions (leading order H1 Fit 2002, cf section 1.2.5).

The hard scattering process is calculated in leading order QCD, ie it contains the lowest order

process of the Quark Parton Model ($\mathcal{O}(\alpha_{em}\alpha_s^0)$, cf figure 1.7), as well as the leading order corrections ($\mathcal{O}(\alpha_{em}\alpha_s)$). These are the diagram of Boson Gluon Fusion (cf figure 1.8), and the crossed process of QCD Compton scattering. Contributions from higher order diagrams are approximated by the emission of further (soft) quarks and gluons in the initial and the final state of the hard scattering process (initial and final state parton showers).

Radiative QED corrections, ie the radiation of real photons in the initial and the final state, and virtual QED loop diagrams, are implemented using the HERACLES program [30]. The hadronisation of the partons into the final state hadrons is performed according to the Lund-String-model [31], as implemented in the JETSET generator [32].

Simulation and Reconstruction of Monte Carlo Events

The calorimetric detector conditions were approximately constant during the 1999 and 2000 data taking periods, whereas the status of the tracking detectors showed substantial variations (eg varying dead regions in the Central Jet Chamber, cf section 2.2, [33]). Since the central part of this analysis – ie the investigation of energy flow in the central and forward detectors – is mainly based on calorimetric information, the detector simulation is only performed for the 1999 e^+ running period. The reconstruction is accomplished using the same modules and programs as for the data.

2 The Experimental Setup

The HERA[1] accelerator at the DESY[2] laboratory in Hamburg, Germany, is the world's only electron[3]-proton collider. Within the present thesis, data events are analysed, which were recorded with the H1 detector – one of the four large scale experiments at HERA – in 1999 and 2000. This chapter briefly introduces the HERA accelerator complex, and the components of the H1 detector most relevant for this analysis.

2.1 The HERA Collider

At the HERA facility, $E_e = 27.5$ GeV electrons are collided with $E_p = 920$ GeV protons, resulting in a centre-of-mass energy, $\sqrt{s} \approx 318$ GeV. A detailed description of HERA may be found in [34]. Only a short summary of the most important characteristics is given in this section. Figure 2.1 shows a schematic view of the HERA collider and its pre-accelerators. The HERA machine consists of
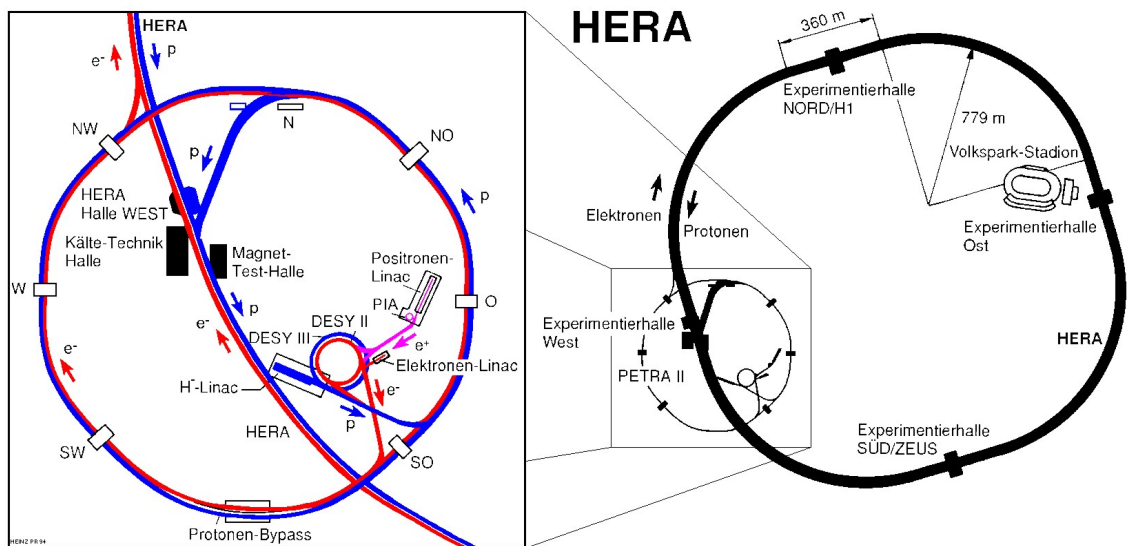
Figure 2.1: The HERA accelerator complex. The figure shows the HERA collider (right), and its system of pre-accelerators (left).

two separate accelerators for electrons and protons, the HERA-e and HERA-p rings, each having a circumference of 6.3 km. While the HERA-e ring is equipped with conventional dipole bending magnets at a magnetic field strength of $B \approx 0.17$ T, the HERA-p accelerator possesses superconducting

---

[1] Hadron-Elektron RingAnlage

[2] Deutsches ElektronenSynchrotron

[3] In the following, the term *electron* is used to refer to both electrons and positrons simultaneously, since there is no difference in the underlying physics relevant for this analysis.

magnets. They are cooled with liquid helium, and provide a field strength of up to $B \approx 5.3$ T. The particles are not distributed continuously around the rings, but they are grouped in *bunches.* Before being filled into the HERA accelerators, electrons and protons undergo several pre-acceleration steps.

Pre-Acceleration

To produce free protons, negatively charged hydrogen atoms, H^-, are accelerated to 50 MeV in the H-LINAC[4]. They are then shot onto a thin foil to strip off the electrons. The resulting proton bunch is accelerated to an energy of 7.5 GeV in DESY-III, and injected into the PETRA-II storage ring. In PETRA-II, up to 70 proton bunches are accumulated, and accelerated to 40 GeV. Four PETRA fillings are then injected into the HERA-p ring, where they are accelerated to the final energy of $E_p = 920$ GeV. Electrons emerge from one of the e-LINACs at an energy of 450 MeV, and are accelerated up to 7.5 GeV in the DESY-II machine. Up to 60 bunches are then stored in the PETRA-II facility, in which they are accelerated up to 12 GeV. Four PETRA-II fillings are injected into the HERA-e ring, and accelerated to their final energy, $E_e = 27.5$ GeV. Since positrons allow longer beam lifetimes, and higher beam currents, they are generally used instead of electrons.

Luminosity

One HERA fill contains approximately $210 - 220$ electron and proton bunches of $10^{10} - 10^{11}$ particles each. This results in the following bunch crossing frequency, ν_{BC}, and time interval, t_{BC}:

$$\nu_{BC} \approx 10.4 \text{ MHz}, \qquad t_{BC} \approx 96 \text{ ns}$$

By the year 2000, peak currents of up to $I_e = 50$ mA, and $I_p = 110$ mA were routinely reached for the electron and proton beams, resulting in a peak luminosity, $\mathcal{L}$, of

$$\mathcal{L} = 1.5 \cdot 10^{31} \text{ cm}^{-2}\text{s}^{-1} = 15 \ \mu\text{b}^{-1}\text{s}^{-1}$$

The integrated luminosity, L, is a measure for the amount of data collected at a collider:

$$L = \int \mathcal{L}(t)dt.$$

Figure 2.2 shows the integrated luminosity delivered by HERA for each year since its start in 1992 (left). The data volume actually recorded by the H1 detector is also displayed (right). Owing to the continuous gain of knowledge about the HERA machine, a better performance was achieved every year. By the end of the year 2000, H1 had collected more than 100 pb^{-1} of data.

The HERA Physics Programme

The HERA accelerator ring contains four points, at which the two circling beams may be collided. Two of these intersection points (north and south) are surrounded by the large H1 and ZEUS multipurpose detectors. They investigate electron-proton collisions since 1992. Some of their main aims are:

- Precision measurements of the proton structure function, $F_2(x, Q^2)$.

- The search for substructures of quarks and leptons.

- The investigation of heavy flavour production mechanisms.

- The investigation of the structure of the photon.

---

[4]LINear ACcelerator.

INTEGRATED   LUMINOSITY (24.08.00)
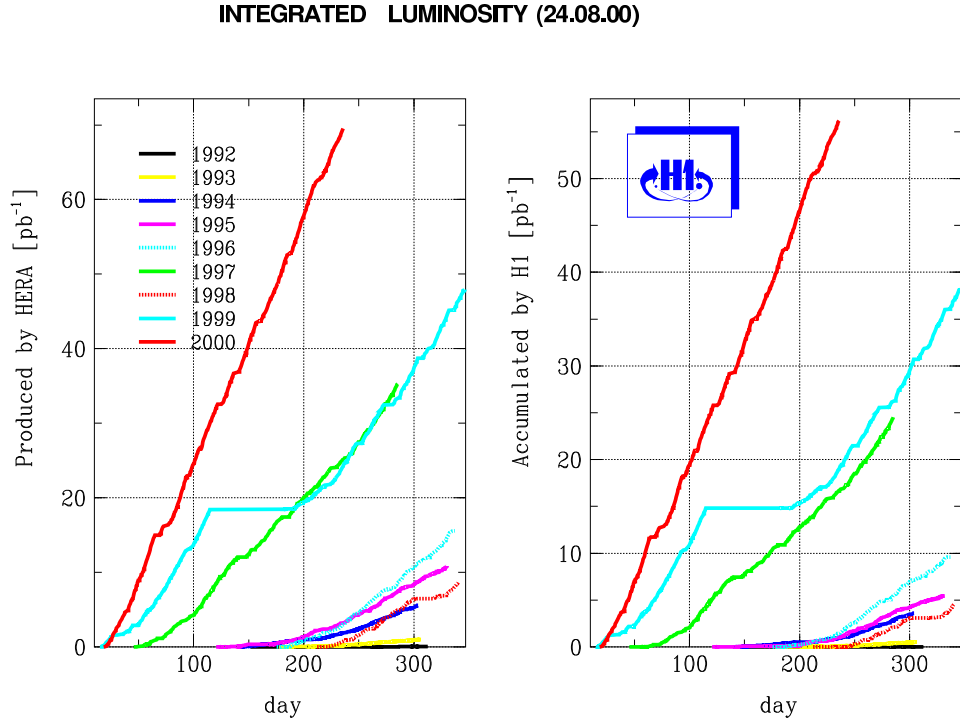
Figure 2.2: The HERA (left) and H1 (right) integrated luminosity shown separately for each year of operation. (From [11].)

- The investigation of diffractive phenomena.

The HERA-B detector was situated in the Hall West until this summer. It used halo protons of the HERA-p beam, which were focused on a fixed target to study CP-violation in B-meson decay. The Hall East contains the HERMES experiment, which measures the spin structure functions of the proton and the neutron by shooting polarised electrons on polarised nuclei in a gaseous target.

2.2 The H1 Detector

Figure 2.3 schematically shows the central part of the H1 detector. It has a mass of 2800 t at a size of $12 \times 10 \times 15$ m^3. Electrons enter form the left side in figure 2.3, protons from the right, and the nominal interaction point is located at the centre of the detector (small mark near $\boxed{2}$). The positive z-axis of the H1 coordinate system is defined by the direction of the outgoing proton beam. The x-axis points into the centre of the HERA ring, and the y-axis is defined by the upward direction. The origin of the H1 coordinate system is located in the centre of the detector. Due to the very different beam energies, the electron-proton centre-of-mass system is boosted in the forward direction. The H1 detector is therefore strongly asymmetric, exhibiting a finer granularity in the forward region. The following sections briefly present the detector parts which are most important for this analysis. A detailed description of the full detector can be found in [35].

2.2.1 The Central Detector Components

A short summary of the central detector components is presented below. The forward and backward detectors will be considered separately in the next sections.

HERA Experiment H1
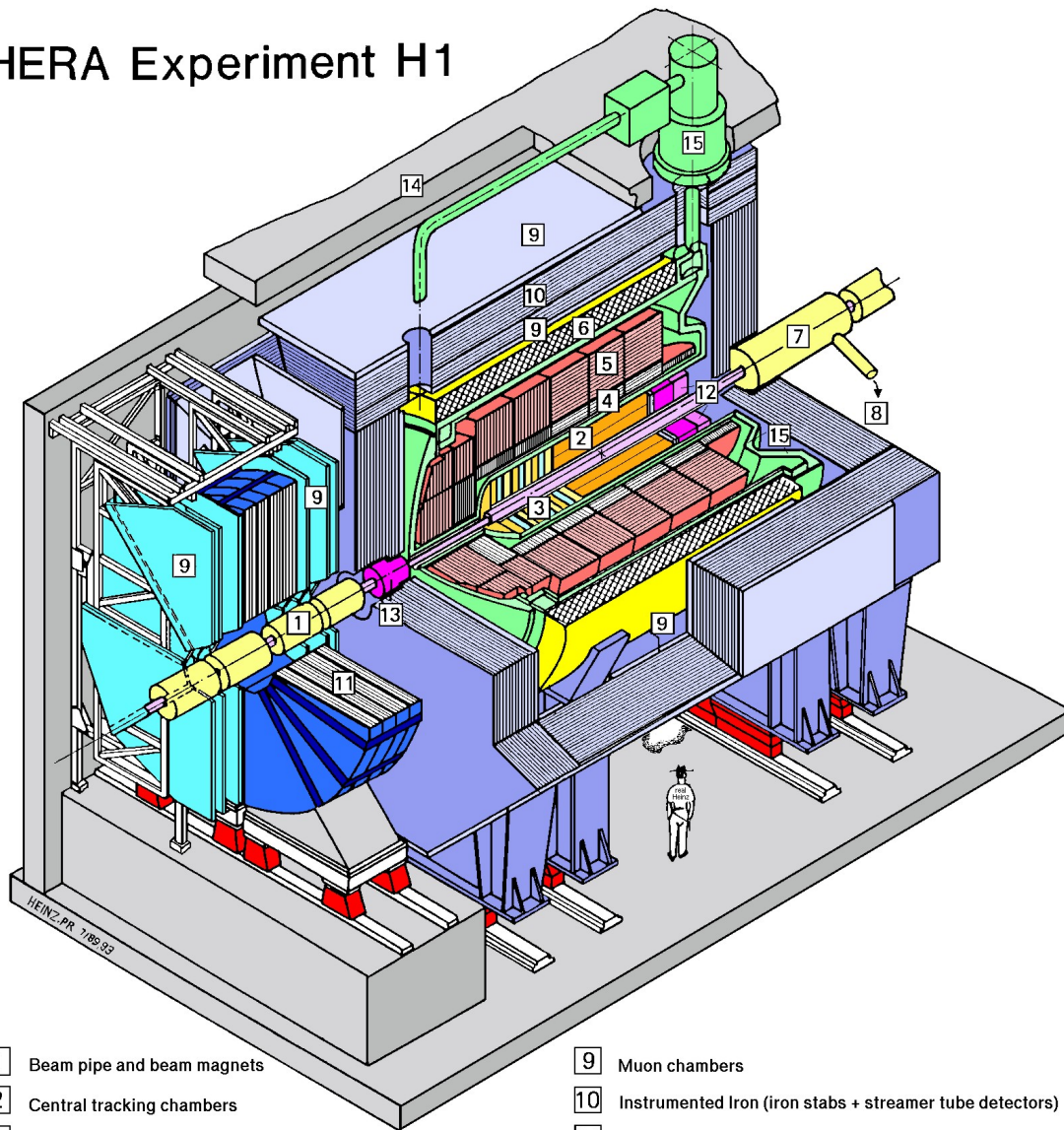
1	Beam pipe and beam magnets	9	Muon chambers
2	Central tracking chambers	10	Instrumented Iron (iron stabs + streamer tube detectors)
3	Forward tracking and Transition radiators	11	Muon toroid magnet
4	Electromagnetic Calorimeter (lead)	12	Warm electromagnetic calorimeter
5	Hadronic Calorimeter (stainless steel)	13	Plug calorimeter (Cu, Si)
6	Superconducting coil (1.2T)	14	Concrete shielding
7	Compensating magnet	15	Liquid Argon cryostat
8	Helium cryogenics		

Liquid Argon

Figure 2.3: The central part of the H1 detector.

The Superconducting Coil

The superconducting coil, $\boxed{6}$, produces a solenoidal magnetic field with a strength of $B \approx 1.16$ T parallel to the beam axis. This allows the momentum measurement of charged particles due to their track curvature in the magnetic field.

The Tracking System

Besides the momentum measurement, the extrapolation of the particle tracks allows the reconstruction of the event vertex. A side view of the H1 tracking system is displayed in figure 2.4. It shows the Central Track Detectors (CTD, $\boxed{2}$), the Forward Track Detector (FTD, $\boxed{3}$), and the backward tracking devices. The resolution of the central track detector (CTD) is approximately
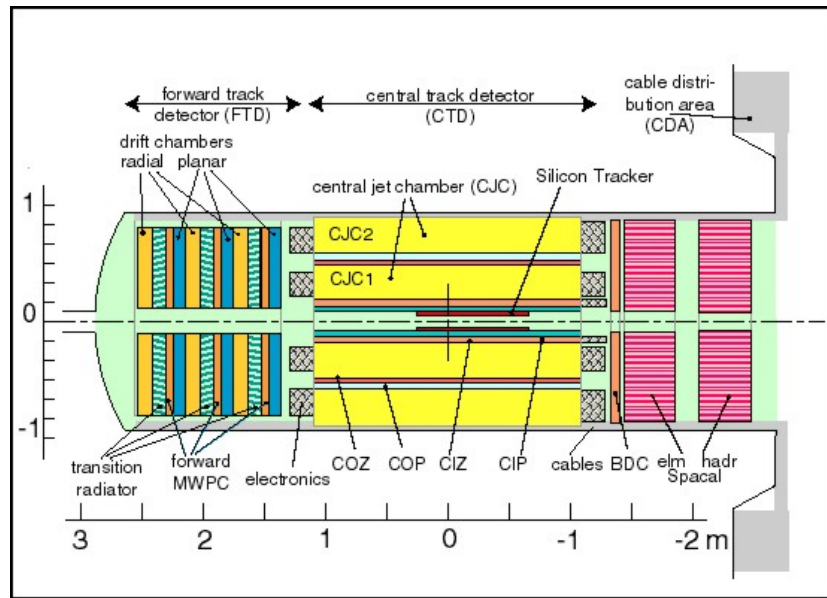
Figure 2.4: Side view of the H1 tracking system.

$$\frac{\sigma_p}{p} \approx 0.007p \text{ [GeV]} \qquad [7],$$

and it covers the angular range $25° < \theta < 155°$. It consists of the central drift chambers (CJC[5] 1/2), the z chambers (CIZ[6], COZ[7]), and two proportional chambers (CIP[8], COP[9]). Within the drift chamber, axial signal wires are used to measure the $(r - \phi)$-coordinates of the track segments from the drift times. The z-coordinate is measured using charge division. Its resolution is ameliorated by the z-chambers. The proportional chambers provide a fast trigger signal for track candidates, and the vertex trigger. The forward track detector (FTD) covers the angular range $5° < \theta < 25°$, and consists of planar and radial drift chambers, as well as additional proportional chambers.

---

[5]Central Jet Chamber.
[6]Central Inner Z chamber.
[7]Central Outer Z chamber.
[8]Central Inner Proportional chamber
[9]Central Outer Proportional chamber

The Liquid Argon Calorimeter

A calorimeter measures the energy deposited by particles. If a particle is completely absorbed, this energy corresponds to its total kinetic energy. A side view of the H1 Liquid Argon calorimeter (LAr) is displayed in figure 2.5. The calorimeter covers the angular range $3° < \theta < 153°$, which corresponds
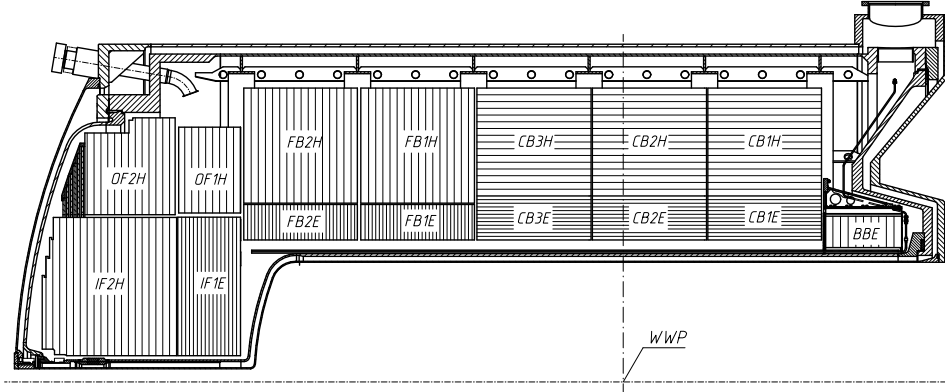
Figure 2.5: Side view of the upper half of the H1 Liquid Argon calorimeter. The nominal interaction point is labelled *WWP*. (From [9].)

to the rapidity range $-1.4 < \eta < 3.6$. It is a sandwich calorimeter, consisting of alternating layers of absorber plates and liquid argon as active detector material. The shower particles which are created in the absorber plates by the incident particle ionise the argon. The number of created ion-electron pairs is proportional to the incident particle's energy. The electrons are collected producing a signal which is proportional to the collected charge, and thus to the initial energy deposit. Since the ionisation process is of statistical nature, the absolute energy resolution is $\sigma_E \sim \sqrt{E}$.

The LAr calorimeter consists of an inner electromagnetic part, $\boxed{4}$, and an outer hadronic part, $\boxed{5}$. The electromagnetic part contains lead absorber plates, and amounts to a thickness of $20 - 30$ radiation lenghts, X_0 [10]. Its resolution for electrons and photons is

$$\frac{\sigma_E}{E} \approx \frac{11 \ \%}{\sqrt{E \ [\text{GeV}]}} \qquad [9].$$

The hadronic part is built with steel absorber plates, corresponding to $4.5 - 7$ hadronic interaction lengths, λ [10]. Its resolution is

$$\frac{\sigma_E}{E} \approx \frac{50 \ \%}{\sqrt{E \ [\text{GeV}]}} \qquad [9].$$

The absolute energy calibration exhibits an uncertainty of 5 %, which has to be added in both cases.

The Backward Detectors

The backward detectors, $\boxed{12}$, consist of the SpaCal (Spaghetti Calorimeter), and the Backward Drift Chamber (BDC). The SpaCal is a lead scintillating fibre calorimeter with fibres parallel to the beam axis. It covers the rapidity range $-3.82 < \eta < -1.42$, and its resolution for electrons and photons is

$$\frac{\sigma_E}{E} \approx \frac{7 \ \%}{\sqrt{E \ [\text{GeV}]}} \qquad [9].$$

As the LAr calorimeter, the SpaCal also consists of an electromagnetic and a hadronic part, the former being in front of the latter when viewed from the interaction point. The BDC provides track segments from passing charged particles with a resolution of $\sigma_r \approx 0.4$ mm, and $\sigma_\phi \approx 0.8$ mm. It is used for a better identification and separation of electrons and hadrons.

2.2.2 The Forward Detectors

This section presents the forward detectors, which are crucial to the forward energy flow measurements, and the standard rapidity gap selection of diffractive events (cf chapters 5, 7).

The Forward Muon Detection System

The Forward Muon Detection System (FMD) is located outside the massive iron return yoke. Its main purpose is the identification of muons, but it can also be reached by particles which scatter off the collimators around the beam pipe. It consists of a toroidal magnet, $\boxed{11}$, and six double layers of drift chambers, $\boxed{9}$ – three in front of, and three behind the magnet when viewed from the interaction point. The direct coverage of the FMD is $1.4 < \eta < 2.9$, but it can detect particles from the range $1.9 < \eta < 3.7$ via secondary scattering. Within the present analysis, only the three pre-toroid double layers are used (cf section 5.2).

The Plug Calorimeter

Figure 2.6 shows a cut through the Plug calorimeter, $\boxed{13}$. The Plug calorimeter is a copper-silicon
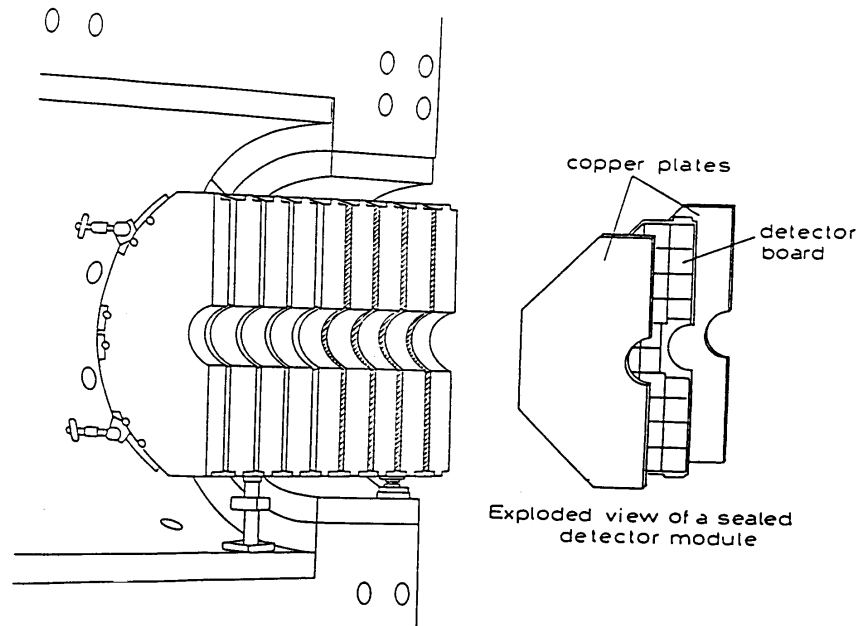
Figure 2.6: Cut through the Plug calorimeter. The diagram shows the (thick) copper absorber plates, and the thinner detector boards. The detector boards contain silicon detection planes.

calorimeter with copper absorber plates and silicon detectors. It is used for the detection of extremely forward scattered hadrons in the region of $3.6 < \eta < 5.1$, but its energy resolution is rather poor:

$$\frac{\sigma_E}{E} \approx \frac{150 \ \%}{\sqrt{E \ [\text{GeV}]}} \qquad [7]$$

The Forward Tagging System

A schematic view of the Forward Tagging System (FTS) is displayed in figure 2.7. The FTS consists of five scintillator planes at 9 m, 16 m, 24 m, 53 m, and 92 m from the interaction point. The stations
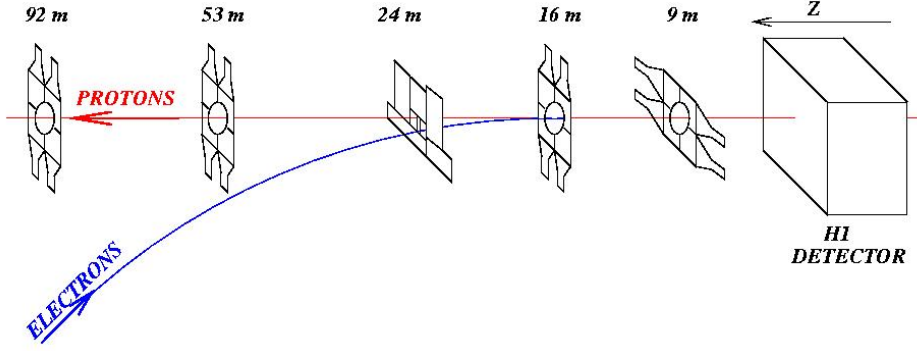
Figure 2.7: Schematic view of the Forward Tagging System.

at 9 m, 16 m, 53 m, and 92 m each contain four lead shielded scintillation counters. Their geometry is schematically shown in figure 2.8. The station at 24 m is formed by the old Proton Remnant
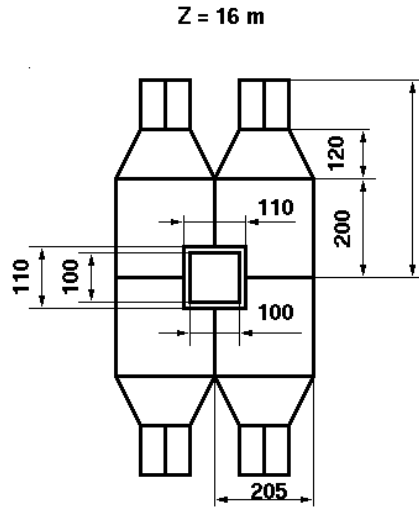
Figure 2.8: Geometry of the FTS station at 16 m from the interaction point. All distances are specified in mm.

Tagger (PRT), and consists of seven scintillation counters [9]. The FTS is used for the measurement of proton fragmentation, and covers the rapidity range $4.5 < \eta < 8.0$. Due to problems in the Monte Carlo description, only the first two stations at 9 m and 16 m are considered within this analysis (cf section 5.3). Their detection range is limited to $4.5 < \eta < 6.2$.

2.2.3 The Low Angle Electron Detector

Figure 2.9 shows a schematic view of the HERA beam line at the backward end of the H1 detector. The Low Angle Electron Detector (Electron Tagger, ET) is located at $z = -33$ m from the interaction point. It is a Čerenkov calorimeter for the detection of electrons with a scattering angle of $\theta'_{e'} = 180° - \theta_{e'} < 5$ mrad, and an energy of $5.5 < E_{e'} < 22$ GeV. This translates into an upper limit of $Q^2 < 0.01$ GeV^2, and the inelasticity range $0.2 \leq y \leq 0.8$. Figure 2.10 shows the acceptance curves
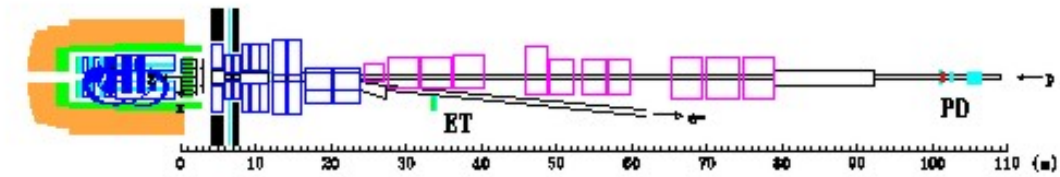
Figure 2.9: Schematic view of the HERA beam line at the backward end of the H1 detector. The plot
shows the HERA magnets, the Low Angle Electron Detector (Electron Tagger, ET), and
the Photon Detector (PD). (From [36].)

for the H1 low angle electron detectors[10] as a function of y for the year 2000. The Photon Detector
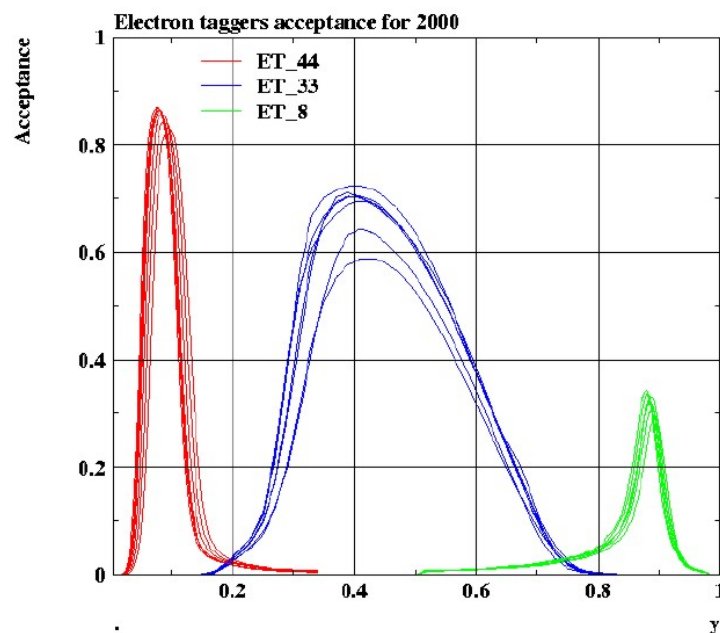
Figure 2.10: Acceptance curves of the electron taggers for 2000. (From [37].)

(PD) is situated at $z = -103$ m from the interaction point, and consists of a Čerenkov calorimeter
with photomultiplier read-out. It is used to measure the luminosity in conjunction with the electron
tagger, and to veto Bethe-Heitler bremsstrahlungs processes in tagged photoproduction analyses (cf
chapter 8).

---

[10] Two more low angle electron detectors exist at $z = -8$ m, and $z = -44$ m from the interaction point, but they are
not used within the present analysis.

2.2.4 The Forward Proton Spectrometer

The Forward Proton Spectrometer (FPS) is used to detect elastically scattered protons in the angular range $\theta \leq 1$ mrad. This section briefly presents the FTS, and sketches the principal mechanisms of the proton track reconstruction. A more detailed explanation may be found in [38].

Due to their reduced energy, $E_{p'} < E_p = 920$ GeV, and their scattering angle at the event vertex, scattered protons are separated from the proton beam by the HERA bending and focusing magnets. They can thus be detected by forward proton detectors in well defined places along the proton beam line. These places are defined by the construction and the properties of the HERA magnetic fields. The forward proton detectors can then be used together with the HERA magnets as a magnetic spectrometer for the measurement of proton trajectories and four momenta. The proton trajectory is hereby approximated by a straight line between the event vertex, and the intersection point of the proton with a plane at the mean distance of the FPS stations from the vertex. The intersection point is calculated from the measured track segments in the forward proton detectors. From this intersection point, and the proton scattering angle at the event vertex, the scattered proton energy, and its momenta can be calculated using the known beam optics, ie the magnetic fields along the beam line.

The H1 Forward Proton Spectrometer consists of four detection stations at 64 m, 80 m, 81 m, and 90 m from the interaction point. During data taking, these detectors are inserted into the proton beam pipe using a hydraulic system. The two stations at 81 m and 90 m are inserted vertically, thus constituting the *vertical* FPS, those at 64 m and 80 m are approached horizontally (*horizontal FPS*). The schematic structure of a vertical detection station is illustrated in figure 2.11. The vertical
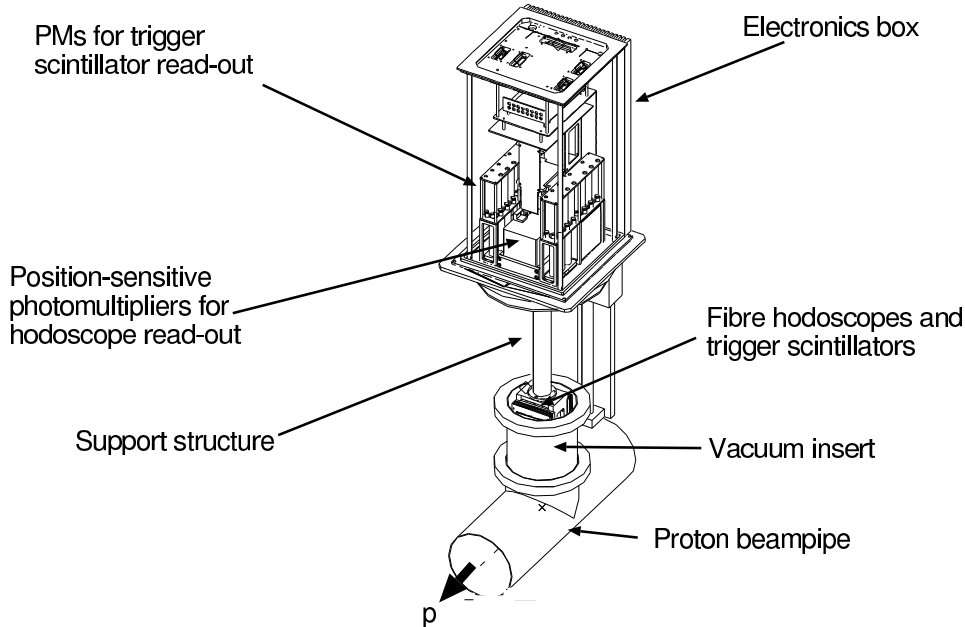
Figure 2.11: Schematic structure of a vertical FPS station, including the vacuum insert into the proton beam pipe, the support structure, and the read-out electronics.

stations cover the energy range $550 < E_{p'} < 830$ GeV, in which elastic proton processes are dominated by Reggeon and pion exchange [38]. Within this thesis, only the two horizontal stations are used. They are sensitive to scattered protons with $740 < E_{p'} < 920$ GeV [38], including the diffractive region at small $x_{I\!\!P}$, ie large scattered proton energies, which is dominated by Pomeron exchange

processes. The geometric acceptance of the two stations translates into an acceptance for scattered protons with transverse momenta $-0.4 < p_x < -0.2$ GeV, and $|p_y| < 0.7$ GeV.

The setup of the horizontal stations is shown in figure 2.12. Each station contains two subdetectors,
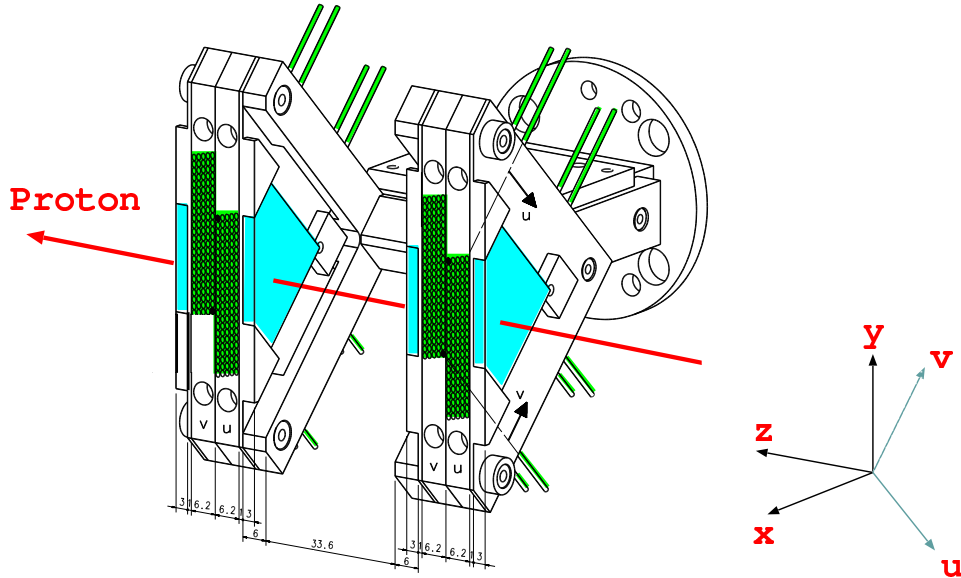
Figure 2.12: Setup of the horizontal FPS stations. The digram shows the two subdetectors, each containing two fibre hodoscopes which in turn consist of five layers of scintillating fibres. Fibres in neighbouring hodoscopes are rotated by 45°, and those in neighbouring layers are shifted by one fifth of a fibre diameter. Each station also contains four scintillator tiles for trigger purposes.

each consisting of two fibre hodoscopes. Each fibre hodoscope consists of five layers of parallel scintillation fibres, and the orientation of the fibres in two neighbouring hodoscopes is rotated by 45° to allow the measurement of two independent coordinates. Neighbouring fibre layers are shifted by one fifth of a fibre diameter to resolve ambiguities, and to increase the precision of the position measurement. Each stations also contains four scintillator tiles which are used for trigger purposes.

Reconstruction of the Proton Trajectory

All hits in the horizontal FPS stations are combined into local clusters. A cluster consists of all hits in two neighbouring fibre layers[11] in one of the four hodoscopes. If enough clusters exist in a FPS station, a *local track*[12] is reconstructed under the assumption that the proton trajectory can be approximated by a parallel to the proton beam within one station. This local track defines the intersection point of the proton track with the midplane of the station[13]. From the two intersection points of the two stations, the intersection point with the midplane of the two horizontal FPS stations at the mean distance of 72 m from the event vertex is reconstructed. The global proton trajectory is approximated by a straight line between this intersection point and the event vertex.

---

[11] In this context, a fibre layer is composed of all fibres in a plane defined by the orientation of the fibres and the proton beam direction (cf figure 2.12).

[12] A *local track* is a track segment in one of the two stations of the horizontal FPS.

[13] The midplane of a station is defined as the plane in the middle of the two subdetectors, and perpendicular to the proton beam.

2.2.5 The H1 Trigger System

The probability for an interaction per bunch crossing is approximately 10^{-3}, resulting in a collision frequency of the order of 10 kHz. These collisions are dominated by background processes. Physically relevant events are selected by a hard ware trigger system. In DIS, they are eg expected at a rate of $\mathcal{O}(Hz)$.

The trigger system is divided into four levels $L1 - L5$ (L3 is not yet operating). L1 is based on trigger elements which provide fast information from the different detector parts. From these trigger elements, 128 subtriggers $s0 - s127$ are constructed via logical conjunctions. The L1 system provides a fast decision within 2 μs. It is fully pipelined, and therefore dead-time free. If at least one of these subtriggers is activated, the event is passed to L2. This happens typically at a rate of 50 Hz. Frequent subtriggers can be downscaled, such that only every n^{th} event activating this subtrigger is kept, to allow for the recording of events from rare subtriggers. These *prescales* have to be included as event weights into any analysis. For L2, the event information is read out, and a decision is made within 20 μs on the basis of correlations between the subtriggers. If an event is accepted by L2, the event information is read out completely, resulting in a dead time of 1.5 ms. Otherwise, the read-out is stopped immediately, and data taking continues. From L2, the events are passed to L4, where the subtriggers are verified using a parallel processor farm which examines the full event information. If at least one of the subtriggers is verified, the data is stored on tape. The event is then fully reconstructed offline by L5. This includes the classification according to the different types of underlying physics, eg leading baryon events are put in *class* 14.

3 Selection of Events with a Leading Proton

In this chapter, the basic selection of *ep* events with a reconstructed leading proton in the *Forward Proton Spectrometer* (FPS) is explained.

3.1 Preselection

The data used in this analysis was recorded with the H1 detector in the years 1999 and 2000. In this period, HERA collided $E_p = 920$ GeV protons with $E_e = 27.5$ GeV electrons and positrons, resulting in a centre-of-mass energy of $\sqrt{s} \approx 318$ GeV. The event sample is based on a FPS-orientated preselection by Mikhail Kapishin [26]. In addition, a general preselection with respect to the detector status and the data quality is performed. The position of the event vertex is used for background rejection.

3.1.1 Detector Status and Data Quality

Events are only selected if all components of the detector which are relevant for this analysis were fully operational. This is achieved by applying the following requirements.

Run Selection

According to the operational status of the detector, the individual runs are classified as *good*, *medium*, or *poor* by the shift crew. The accepted run ranges are required to have medium or good data quality.

Monitoring of the Detector Status

Additionally, an event-by-event selection based on the operational status of the most important detector components used in this analysis is performed. These are the CJC, the LAr and the SpaCal calorimeters, the BDC, the Plug Calorimeter, the FMD and the FTS, and the FPS (cf section 2.2). The corresponding high voltage (HV) power supplies and the readout systems are required to have worked properly for these detector parts.

FPS Position and Calibration

The Forward Proton Spectrometer took its data taking position (cf section 2.2.4) close to the proton beam for only a small part of the data taking period. Luminosity fills of the HERA collider are used for this analysis, if the Roman pots of the horizontal FPS stations were in such a position close to the proton beam. It is also required that the FPS position had been calibrated relative to the proton beam.

Background Rejection

A standard background finder [11] is used to reject events with known readout problems in the calorimeters. These readout problems are commonly referred to as *coherent noise*.

3.1.2 Event Vertex Requirements

To reduce background events due to beam-gas and beam-wall interactions, only events with a reconstructed interaction vertex are selected. It is reconstructed from tracks originating in the H1 interaction region (cf section 2.2). The event vertices of ep-collisions are approximately Gaussian distributed along the beam line around the nominal event vertex at $z_{vertex} \approx 0$ cm. The standard deviation of the vertex distribution is $\sigma_{z_{vertex}} \approx 12$ cm. This is illustrated by figure 3.1. It shows the z_{vertex}-distribution of the preselected data, including a Gaussian fit. Beam-gas and beam-wall
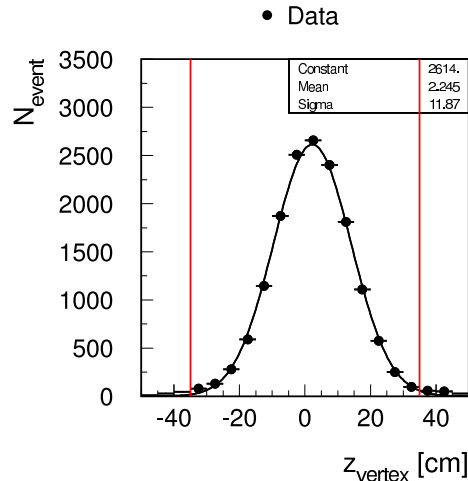
Figure 3.1: The z_{vertex}-distribution of the preselected data (cf section 3.1.1), including a Gaussian fit to determine the parameters of the distribution. The applied cuts are shown as vertical lines.

interactions may happen anywhere along the beam pipe. They are partially suppressed by applying a cut on the z-coordinate of the reconstructed vertex position:

$$|z_{vertex}| < 35 \text{ cm} \approx 3\sigma_{z_{vertex}}$$

Thus, virtually all ep events are selected.

3.1.3 Activity in the Horizontal FPS Stations

Figure 3.2 shows an event display of the two horizontal FPS stations for a data event with a reconstructed leading proton. The scintillating hodoscope fibres, and all hits on these fibres are shown together with the reconstructed local tracks[1] (top). All trigger scintillator tiles are displayed, indicating those which gave a trigger signal. The intersection of the scattered proton trajectory with the FPS stations, and the nominal proton orbit are shown (bottom). An ellipse indicates the divergence of the proton beam. The larger divergence of the proton beam at 64 m can be seen compared to the one at 80 m [38].

All hits in the horizontal FPS stations are combined into local clusters (cf section 2.2.4). A cluster consists of all hits in two neighbouring fibre layers[2] in one of the four subdetectors of the FPS (cf figures 2.12, 3.2). Events are assumed to have a proton candidate, if enough groups are found for the

---

[1]A *local track* is a reconstructed track segment in any of the two FPS stations at 64 m and 80 m from the interaction point (cf section 2.2.4).

[2]A *fibre layer* is composed of all fibres in a vertical plane, ie a plane perpendicular to the top cut in figure 3.2, and parallel to the proton beam (cf section 2.2.4).
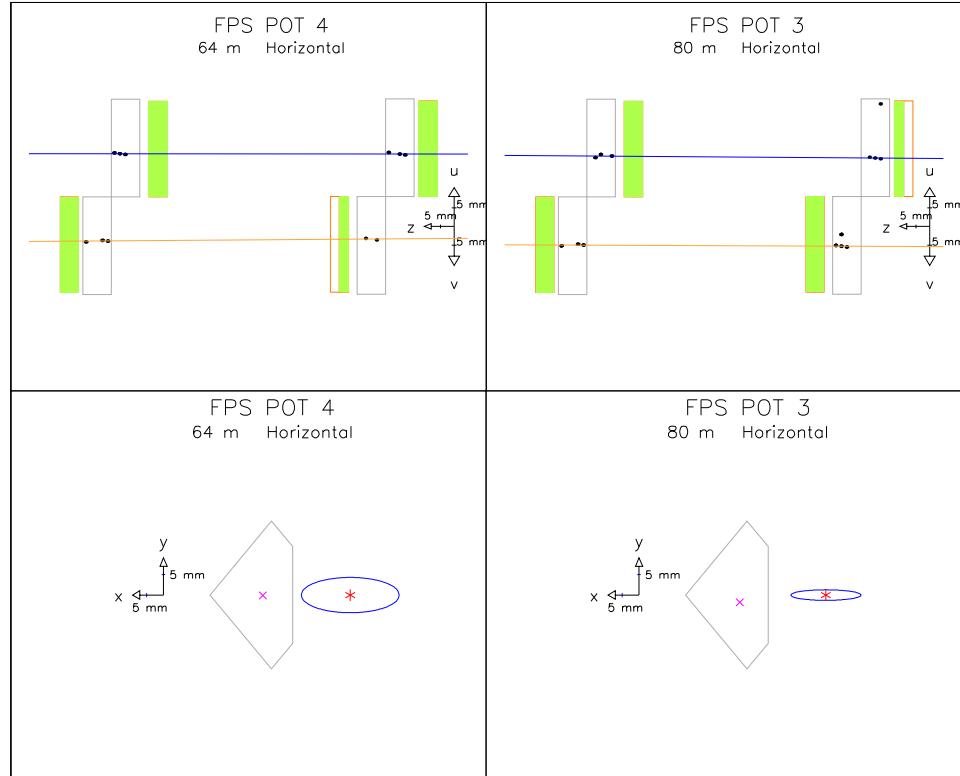
Figure 3.2: An event display of the horizontal Forward Proton Spectrometer for a data event with a reconstructed leading proton. Top row: A cut perpendicular to the scintillating fibres. All fibre hits are shown as black points. The trigger scintillator tiles are displayed, and those which gave a signal are indicated by filled rectangles. Projections of the reconstructed local tracks are illustrated by straight lines. Bottom row: The FPS stations as seen along the beam pipe. While the intersection of the scattered proton trajectory is specified by a cross, the proton orbit is marked by a star. An ellipse indicates the divergence of the proton beam.

reconstruction of a local proton trajectory within one FPS station. Only events having a candidate for a leading proton are accepted. This corresponds to requiring event class 14 (leading baryons, cf section 2.2.5). At least one reconstructed track segment – called local track – is required in each of the horizontal Roman pots at 64 m and 80 m. These track requirements define the trigger elements 164 and 165 for activity in the FPS (section 2.2.5).

No other requirements on subtriggers or other characteristics of the event topology in the H1 main detector are made at this preselection stage. Thus, an analysis of both deep-inelastic scattering (DIS), as well as photoproduction (γp) is possible with the selected data sample.

3.2 Leading Proton Selection with the FPS

A leading proton in the horizontal Forward Proton Spectrometer is selected by requiring a track in the two Roman pots (64 m and 80 m). Acceptance cuts are applied to suppress badly measured proton trajectories.

3.2.1 Proton Track Selection

At least one reconstructed global track[3] is required in addition to the local track segments required in the preselection procedure (section 3.1.3). Such a global track is necessary for the proper measurement of the leading proton trajectory, the proton momentum, and its energy (cf section 2.2.4). The latter is assigned a positive value only if a reconstructed proton is found. To select events with a leading proton, a minimum energy of this reconstructed proton, $E_{p'}$, is thus required:

$$E_{p'} > 1.0 \text{ GeV}$$

These cuts are summarised in table 3.1 at the end of this chapter.

3.2.2 Kinematic Acceptance of the Horizontal FPS Stations

The acceptance range of the horizontal FPS stations depends on the size and the position of the scintillating fibre hodoscopes in the Roman pots. It is also influenced by the HERA beam optics between the interaction point in the centre of the H1 detector and the FPS stations [38]. The scattered proton momenta at the interaction vertex, p_x (horizontal) and p_y (vertical), are directly connected to the position of the proton trajectory via the deflection in the magnetic fields along the beam pipe (cf section 2.2.4). They can be used to restrict protons to the limited acceptance range covered by the FPS ([26], [39]):

$$
\begin{aligned}
-0.38 \quad < \quad p_x \quad &< \quad -0.23 \text{ GeV} \\
|p_y| \quad &< \quad 0.7 \text{ GeV}
\end{aligned}
$$

Additionally, cuts on the fractional ($x_{I\!P}$) and the squared (t) four momentum transfer at the proton vertex are performed ([26], [39]):

$$
\begin{aligned}
x_{I\!P}^{FPS} \quad &< \quad 0.17 \\
0.07 \quad < \quad |t| \quad &< \quad 0.7 \text{ GeV}^2
\end{aligned}
$$

These acceptance cuts are also summarised in table 3.1, and the relevant quantities are displayed in figure 3.3. They are shown for the preselected data (cf section 3.1) with additional cuts on the track selection (cf section 3.2.1). The cut values are marked by vertical lines.

3.3 Summary of the Leading Proton Selection

The basic selection of *ep*-events with a leading proton in the FPS is summarised in table 3.1. The resulting data sample consists of

$$N_{event} = 4799$$

events. They are the basis for the analysis of diffractive deep-inelastic scattering (chapters 4, 6, 7), as well as diffractive photoproduction (chapters 8, 9, 10). It remains to be proven that this data sample only contains events with a *scattered* leading proton. This will be discussed in section 4.7.

---

[3]A *global track* is a linear trajectory connecting the event vertex with the intersection point of the scattered proton through the $(r - \phi)$-plane at 72 m from the interaction point (cf section 2.2.4).
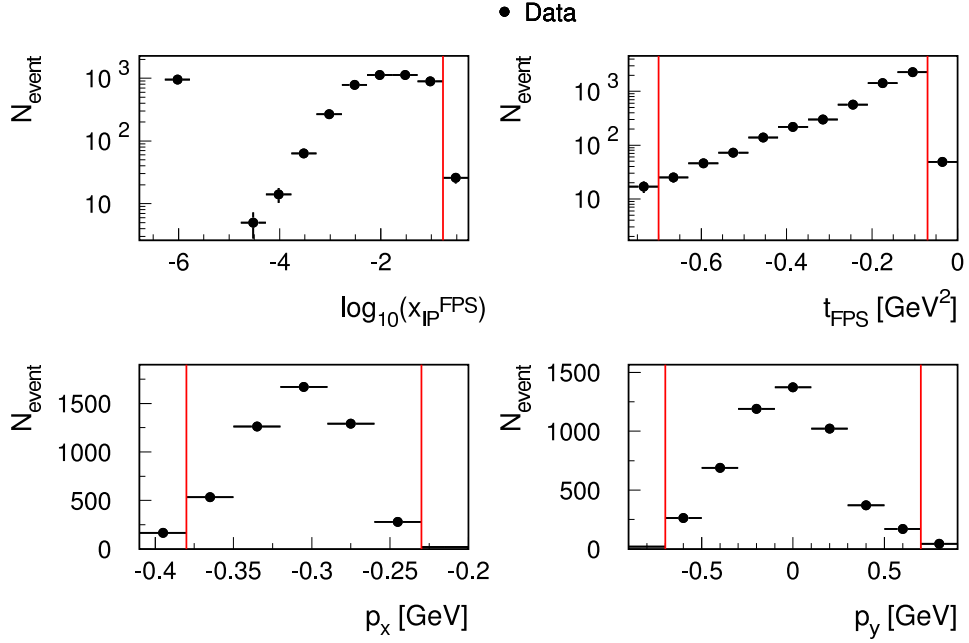
Figure 3.3: The FPS quantities relevant for the acceptance cuts. They are shown for the preselected data (cf section 3.1) with additional cuts on the track selection (cf section 3.2.1). The applied cuts are illustrated by the vertical lines.

Table 3.1: The selection cuts for ep-events with a leading proton in the FPS.

Description		Cut		
ep-preselection				
Vertex requirement		$\lvert z_{vertex} \rvert$	$<$	35 cm
FPS preselection				
Proton candidate		$n_{class}(event)$	$=$	14
Local track at 64 m		$N_{track}^{local}(64\ \mathrm{m})$	$\geq$	1
Local track at 80 m		$N_{track}^{local}(80\ \mathrm{m})$	$\geq$	1
FPS track selection				
Global track in FPS		N_{track}^{global}	$\geq$	1
Reconstructed proton energy		$E_{p'}$	$>$	1.0 GeV
FPS acceptance				
Horizontal proton momentum	$-0.38 <$	p_x	$<$	-0.23 GeV
Vertical proton momentum		$\lvert p_y \rvert$	$<$	0.7 GeV
Fractional four momentum transfer		$x_{I\!P}^{FPS}$	$<$	0.17 GeV
Squared four momentum transfer	$0.07 <$	$\lvert t \rvert$	$<$	0.7 GeV^2

4 Analysis of Deep-Inelastic Scattering

This chapter explains the analysis of deep-inelastic scattering (DIS) events. It includes the final event selection, and the comparison of Monte Carlo simulated event samples with the data. A direct proof for the existence of Reggeon exchange reactions in the DIS data is presented, and the Pomeron and Reggeon fractions are estimated for the data samples. The accuracy of the Monte Carlo prediction based on the measurement of the inclusive diffractive structure function, F_2^D, is examined.

4.1 Selection of DIS Events

In this section, the selection performed to obtain a clean sample of deep-inelastic scattering events is presented. It follows procedures well-established within the H1 collaboration, and is only briefly summarised here. A more detailed discussion may be found in [9]. The DIS selection is based on:

1. A high energetic cluster in the SpaCal calorimeter as electron candidate.

2. The electron identification and reconstruction on the basis of shower shapes and track requirements.

3. The reduction of non-e photoproduction background by kinematic cuts and further selection criteria.

4.1.1 Trigger Selection

In this analysis, the subtriggers $s35$ and $s61$ are considered to preselect DIS events. They impose the following requirements on signatures in the H1 detector. All requirements are combined by logical ANDs, ie they all need to be fulfilled for an event to be selected. A general description of the H1 trigger system may be found in section 2.2.5.

- s35

  - **Electron candidate:** A minimum energy deposit in any of the predefined regions of the outer electromagnetic part of the SpaCal calorimeter: $E_{min}^{em} > 6.5$ GeV

- s61

  - **Electron candidate:** A minimum energy deposit in any of the predefined regions of the outer OR the central electromagnetic part of the SpaCal calorimeter: $E_{min}^{em} > 6.5$ GeV
  - **Jet seeds:** At least one high-$p_\perp$ track in the CJC: $p_\perp > 800$ MeV
  - **Event vertex:** A significant peak in the z_{vertex}-histogram.

The two subtriggers differ in their requirements on the electron candidate, and in the additional track and vertex requirements in $s61$. They are imposed due to the lower requirements on the electron candidate which – in the case of s61 – may also be detected in the inner SpaCal region. This region suffers from high beam-induced background rates [9]. Additional selection criteria are imposed to

keep the trigger rates below the hardware capacities, and to avoid large dead times. In this thesis, only runs are accepted in which the prescales of both subtriggers, $s35$ and $s61$, are equal to one. This avoids any complications resulting from events which have different prescale factors for the two triggers.

4.1.2 Identification and Reconstruction of the Scattered Electron

In low-Q^2 DIS ($Q^2 < 100$ GeV^2, [40]), the scattered electron is identified in the SpaCal calorimeter with the help of the Backward Drift Chamber by a series of selection cuts.

The electromagnetic SpaCal cluster[1] with the highest energy deposits in the entire event is considered to be the electron candidate. The following selection cuts are applied to this calorimeter cluster.

Fiducial Region for the Electron Candidate

To achieve a high-quality selection with high efficiency, the electron candidate has to be well contained within the SpaCal calorimeter. The distance between the electromagnetic cluster and the beam pipe, d_{cl-bp}, is therefore required to fulfil

$$10.0 < d_{cl-bp} < 67.0 \text{ cm.}$$

This cut also rejects beam-induced background at the inner edge of the SpaCal calorimeter.

A cut on the energy deposited in the veto layer directly adjacent to the beam pipe, E_{veto}, is applied to avoid energy leakage into the beam pipe:

$$E_{veto} < 1.0 \text{ GeV}$$

Electron Identification

Hadrons in photoproduction events may fake electron candidates in the SpaCal calorimeter. In this case, the scattered electron escapes undetected through the beam pipe. Such background is suppressed using cuts on the shape of the electromagnetic shower produced by the electron candidate in the SpaCal calorimeter [10], and by applying track requirements in the BDC.

Since electromagnetic showers have a smaller transverse size in the calorimeter than hadronic showers [10], a cut on the cluster radius of the electron candidates, r_{cl}^e, is used. Only events which fulfil

$$r_{cl}^e < 4.0 \text{ cm}$$

are selected.

Whereas hadrons often reach the hadronic part of the SpaCal calorimeter, electrons should be well contained within the electromagnetic section [10]. The energy deposited in the hadronic calorimeter part in a cone around the extrapolated trajectory of the electron candidate, E_{had}, is hence required to be

$$E_{had} < 0.5 \text{ GeV.}$$

Because of the strong increase of hadronic background towards lower energies of the electron candidate [9], a minimum electron energy is requested:

$$E_{e'} > 8.0 \text{ GeV}$$

Neutral hadrons (eg π^0) which could produce high-energy SpaCal clusters do not produce any tracks. They are rejected by demanding a BDC track connected to the SpaCal cluster. The distance

---

[1]A *cluster* is an association of neighbouring calorimeter cells.

between the centre-of-gravity [10] of the calorimeter cluster and the closest BDC track, Δ_{BDC}, is restricted to

$$\Delta_{BDC} < 3.5 \text{ cm}$$

for all selected events.

4.1.3 Kinematic Reconstruction and Selection

The kinematics of deep-inelastic scattering events are described in terms of the four momentum of the virtual photon (*virtuality*), Q^2, and the fractional energy transfer at the electron vertex, y, also called *inelasticity*. They are reconstructed using only the scattered electron (cf section 1.2.6):

$$
\begin{aligned}
Q_e^2 &= 4E_e E_{e'} \cos^2\left(\frac{\theta_{e'}}{2}\right) \\
y_e &= 1 - \frac{E_{e'}}{E_e} \sin^2\left(\frac{\theta_{e'}}{2}\right),
\end{aligned}
$$

where E_e and $E_{e'}$ are the energies of the incoming and the scattered electron. $\theta_{e'}$ is the scattering angle of the electron with respect to the outgoing proton direction (cf section 2.2).

The following cuts are applied to select well measured events in the deep-inelastic scattering regime:

$$
\begin{aligned}
3.0 &< Q_e^2 < 80.0 \text{ GeV}^2 \\
0.1 &< y_e < 0.7
\end{aligned}
$$

The lower boundary on Q^2 rejects events with a reconstructed electron in the inner part of the SpaCal calorimeter. This detector region suffers from high beam-induced background [9]. The cut is also motivated by the desire to stay in the DIS regime. In DIS events, the virtual photon is required to introduce a hard interaction scale [10]. The upper boundary on Q^2 achieves the detection of the electron shower within the SpaCal calorimeter. Very low y are excluded since the major aim of this thesis is the investigation of hard interaction processes. Another reason is the degrading resolution of the electron method for low $y_e < 0.1$ due to the difficult measurement of small scattering angles, $\theta_{e'}$. The upper restriction on y suppresses photoproduction events in which a hadron fakes a scattered electron in the SpaCal calorimeter [9].

4.1.4 Reconstruction of the Hadronic Final State

The hadronic final state (HFS) comprises all particles which emerge from the interaction of the virtual photon with the proton. In the case of a leading proton, the latter leaves no trace in the central detector. The HFS is then defined as the particle system resulting from the interaction of the photon with the colourless exchange particle ($\mathrm{I\!P}$, or $\mathrm{I\!R}$, cf figure 1.7), and corresponds to the photon dissociation system, X.

The reconstruction of the hadronic final state is based on a combination of calorimetric and tracking information. Calorimetric cluster energies have to be calibrated taking into account material and energy losses in front of the calorimeters, and the energy measurement itself is based on statistical processes (cf section 2.2.1). This results in a degrading resolution towards low energies [10]:

$$\frac{\Delta E}{E} \sim \frac{1}{\sqrt{E}}$$

Track momenta are measured via the track curvature in a magnetic field. The resolution degrades towards higher momenta [10]:

$$\frac{\Delta p}{p} \sim p$$

Combination of Clusters and Tracks

Combined objects contain the energy measurements of both, the calorimetric and the tracking method. They achieve the best resolution when considering low-energy tracks and high-energy calorimeter clusters. It is crucial to avoid any double counting of measured energies. A detailed combination algorithm is given in [41], but the general principle can be summarised as follows.

Only CJC-tracks up to a transverse momentum of $p_\perp < 2.0$ GeV are considered. The combination procedure starts from a list of all tracks and calorimeter clusters. It consists of five steps:

1. The selected tracks are extrapolated into the calorimeter.

2. The calorimeter clusters around each extrapolated track are sorted with respect to their distance from the track axis.

3. The cluster energies around each extrapolated track are summed in the order of the track-cluster distances.

4. The summation is stopped when the sum of the cluster energies fulfils the following relation:

$$\left| E_{track} - \sum_i E_{cluster_i} \right| < \sigma_E$$

   in which σ_E is the resolution of the energy sum.

5. The clusters which are included in the above sums are removed from the list of input objects.

The remaining clusters and tracks are the combined objects. Their final resolution is [9]

$$\frac{\sigma_E}{E} \approx \left(\begin{array}{ll} 0.007E \text{ [GeV]} & : \quad E_\perp < 2.0 \text{GeV} \\ \frac{50\%}{\sqrt{E \text{ [GeV]}}} \oplus 0.02 & : \quad E_\perp > 2.0 \text{GeV} \end{array} \right)$$

for hadrons in the central tracking system and the LAr calorimeter.

4.1.5 Background Rejection

The selected event sample still contains background from non-DIS – especially photoproduction – ep-interactions, and from non-ep events ([9], [26]). It can be further reduced by requiring energy and momentum conservation, and by considering the different reconstruction methods for the DIS variables.

Energy and Momentum Conservation

The conservation of energy and longitudinal momentum can be re-expressed as

$$\sum_j \left(E_j - p_{j_z} \right),$$

in which j denotes all particles of the considered state. The initial state is defined by $j \equiv i = e$, p, and for relativistic particles in a head-on collision,

$$\sum_i \left(E_i - p_{i_z} \right) \approx 2E_e \approx 55 \text{ GeV}.$$

Since $E_p \approx p_{p_z}$, only the energy from the electron side contributes to the sum over the initial state. A perfectly measured DIS final state would comply with $\sum_f \left(E_f - p_{f_z} \right) \approx 55$ GeV. The real data
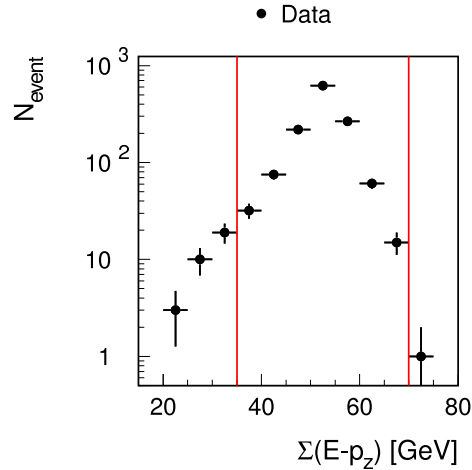
Figure 4.1: The quantity $\sum_f \left(E_f - p_{f_z} \right)$. It is displayed after the FPS and the electron selections, as well as the kinematic DIS cuts (cf sections 3, 4.1.1, 4.1.2, 4.1.3). The cut boundaries are indicated by the vertical lines.

distribution is smeared around the nominal value due to finite detector acceptance and resolution. It is shown for the data in figure 4.1. All selection cuts discussed so far have been applied (cf table 3.1, sections 4.1.1, 4.1.2, 4.1.3). Cuts on the final state sum are applied to reject non-DIS background and badly measured events. A lower boundary discards events with escaping high-$p_\perp$ particles. It also reduces the photoproduction background, since photoproduction electrons escape through the beam pipe, resulting in

$$\left(\sum_f \left(E_f - p_{f_z} \right) \right)_{\gamma p} \ll 55 \text{ GeV.}$$

An upper cut boundary rejects events in which additional particles, not resulting from the actual *ep*-interaction, are detected in coincidence with the real event. These additional particles may be initial state radiation (ISR) photons from non-interacting electrons, beam electrons deviated due to ISR, or cosmic muons. The cut also discards events with high measured energies due to calorimeter problems. The following cut boundaries are applied [9]:

$$35.0 < \sum_f \left(E_f - p_{f_z} \right) < 70.0 \text{ GeV}$$

Reconstruction Methods

Another efficient way to suppress background is the consideration of the different reconstruction methods for the kinematic DIS variables. The latter can be determined using the scattered electron, the hadronic final state, or a combination of both (cf sections 1.2.6, 4.1.3):

a) Electron method:
$$y_e = 1 - \frac{E_{e'}}{E_e} \sin^2 \left(\frac{\theta_{e'}}{2} \right)$$

b) Hadron method:
$$y_{had} = \frac{E_{had} - p_{had_z}}{2 E_e} \equiv \frac{\sum_{h \in HFS} \left(E_h - p_{h_z} \right)}{2 E_e}$$

c) Double angle method:

$$y_{da} = \frac{\sin\theta_{e'}\,(1 - \cos\gamma_{had})}{\sin\theta_{e'} + \sin\gamma_{had} - \sin\left(\theta_{e'} + \gamma_{had}\right)},$$

where E_e is the initial, $E_{e'}$ the scattered electron energy. $\theta_{e'}$ is the scattering angle of the electron, and had symbolises all hadronic final state particles $\{h\}$. $\{E_h\}$ are the energies of those particles. γ_{had} is defined by $E_{e'}\sin\theta_{e'} = E_{had}\sin\gamma_{had}$ [12].

This is used to suppress background due to photoproduction, beam-gas interactions, or bremsstrahlung. If a photoproduction event is considered, the scattered electron escapes through the beam pipe. A hadron fakes an electron in the SpaCal calorimeter, and all electron quantities are measured wrongly. Only y_{had} is determined correctly. In the case of initial state bremsstrahlung, the initial electron energy, E_e, is smaller than the standard value of $E_e = 27.5$ GeV. While y_e and y_{had} are reconstructed to small, y_{da} returns the real value of y. For well-measured DIS events, all three methods should provide similar results, $y_e \approx y_{had} \approx y_{da} \approx y$. The following cuts are thus applied to reject such background, and to select well-measured DIS events [26]:

$$
\begin{aligned}
|y_e - y_{had}| &< 0.3 \\
|y_e - y_{da}| &< 0.3
\end{aligned}
$$

4.1.6 Summary of the DIS Selection Cuts

The complete list of cuts for the selection of deep-inelastic scattering events is given in table 4.1. The

Table 4.1: The complete list of cuts for the selection of DIS events (cf sections 4.1.1, 4.1.2, 4.1.3, 4.1.5).

Description	Cut				
Trigger selection					
Subtriggers	$(s35$	or	$s61)$	$=$	1
Prescales	$(s35_{presc}$	and	$s61_{presc})$	$=$	1
Electron reconstruction					
Distance (cluster - beam pipe)	10.0	$<$	d_{cl-bp}	$<$	67.0 cm
Energy in veto layer			E_{veto}	$<$	1.0 GeV
Cluster radius			r^e_{cl}	$<$	4.0 cm
Energy in hadronic SpaCal			E_{had}	$<$	0.5 GeV
Electron energy	8.0 GeV	$<$	$E_{e'}$		
Distance (track - cluster)			Δ_{BDC}	$<$	3.5 cm
Kinematic selection					
Four momentum transfer	3.0	$<$	Q^2_e	$<$	80.0 GeV^2
Inelasticity	0.1	$<$	y_e	$<$	0.7
Background rejection					
Energy and momentum	35.0	$<$	$\sum_f\left(E_f - p_{f_z}\right)$	$<$	70.0 GeV
Hadron method			$|y_e - y_{had}|$	$<$	0.3
Double angle method			$|y_e - y_{da}|$	$<$	0.3

selected DIS sample contains

$$N_{event} = 1253$$

events.

4.2 Jet Selection and Hard Interaction Scales

Deep-inelastic scattering offers one intrinsic hard interaction scale, the four momentum transfer at the electron vertex, Q^2. But this does not guarantee a hard scale in the underlying parton-parton interaction. The most convenient way to achieve such a scale are high-$p_\perp$ *jets* in the hadronic final state (cf section 1.2.7).

4.2.1 Jet Selection

Jets are defined as collimated sprays of hadrons. Their identification within the hadronic final state is performed by a *jet algorithm*. In this thesis, an *inclusive $k_\perp$-algorithm* (cf section 1.2.7, [27]) is used.

The input objects for the jet selection used in this thesis are the *combined objects* introduced in section 4.1.4. They are fed to the $k_\perp$-algorithm in the $\gamma^* p$ centre-of-mass (cms) frame. The latter is defined by

$$\mathbf{q}^* + \mathbf{p}^* = \mathbf{l}^* - \mathbf{l'}^* + \mathbf{p}^* = \mathbf{0},$$

where $\mathbf{l}^{*2}$, $\mathbf{l'}^*$ are the four vectors of the incoming and the scattered lepton. $\mathbf{p}^*$ is the four momentum of the incoming proton, and $\mathbf{q}^*$ denotes the four momentum transfer at the electron vertex. The $\gamma^* p$ frame is used since the relevant scale for QCD dynamics is the transverse momentum relative to the photon-proton collision.

The following parameters are utilised for the $k_\perp$-algorithm within this analysis. An asymmetric cut is applied to the transverse momenta of the first and all further jets:

$$
\begin{aligned}
p_\perp^*(jet\ 1) &> 4 \text{ GeV} \\
p_\perp^*(jet\ n) &> 2.5 \text{ GeV} \qquad \text{with} \quad n \geq 2
\end{aligned}
$$

These $p_\perp$-requirements on the hard interaction scales are rather low in comparison with other jet analyses (eg [9], [11]). They are chosen due to the very low event numbers (cf below). The cut on the first jet is sharper in order to obtain a minimum hard scale in all jet events.

To achieve a precise measurement of the relevant momenta and energies, all jets are required to be contained in the LAr calorimeter:

$$-1.5 < \eta_{jet} < 2.5,$$

where η_{jet} is the pseudorapidity of any jet. This corresponds to the angular range $9.4 < \theta_{jet} < 154.8°$ (cf section 1.2.6).

Figure 4.2 shows the number of jets in the inclusive[3] data sample after the basic FPS and the complete DIS selection (cf sections 3, 4.1). The particularly high fraction of events with two jets – compared to events with only one jet – results from the lower $p_\perp$-threshold for all subleading jets. $\mathcal{O}(\alpha_s)$-processes always lead to two hard partons which produce two final state jets. Their transverse momenta are always balanced in the parton-parton centre-of-mass system. But $p_\perp^*$ is not balanced in the $\gamma^* p$ cms frame due to initial state radiation (ISR), and intrinsic $p_\perp$ of the parton-parton cms system. The interacting partons thus have different transverse momenta in the $\gamma^* p$ cms frame.

---

[2] Quantities given in the $\gamma^* p$ centre-of-mass frame are denoted by a *. Bare symbols generally refer to the laboratory system, unless stated otherwise.

[3] Unless stated otherwise, *inclusive* in this thesis refers to diffractive event samples with a scattered leading proton in the FPS, but without any requirements on hadronic final state jets.
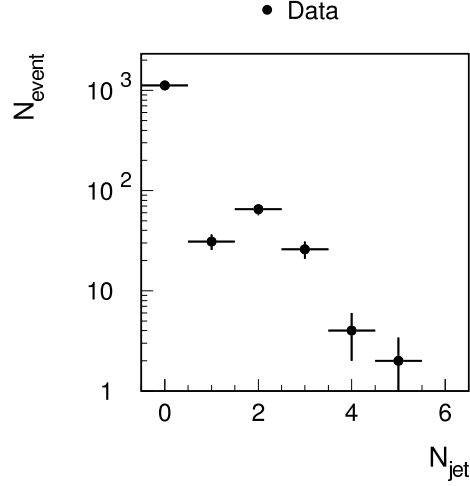
Figure 4.2: The number of jets for the inclusive DIS data sample. It is shown after the FPS (cf chapter 3) and the complete DIS selection (cf section 4.1).

Sometimes, only the leading jet is selected, but the asymmetric $p_\perp$-cut allows the selection of the second jet in the majority of all events.

In the following analysis, two jet samples[4] are investigated:

$$
\begin{array}{llllllll}
\text{a) Singlejet sample} & N_{jet} & \geq & 1 & : & N_{event} & = & 128 \\
\text{b) Dijet sample} & N_{jet} & \geq & 2 & : & N_{event} & = & 97
\end{array}
$$

4.2.2 Hard Scales in Inclusive DIS Events

Due to the very low event numbers (cf section 4.2.1), the inclusive data sample without any jet requirements is also investigated.

In the case of deep-inelastic scattering, a hard scale is provided by the four momentum transfer at the electron vertex: $Q^2 > 3$ GeV^2 (cf section 4.1.3). The invariant mass of the photon dissociation system, X (cf figure 1.7), provides a measure for the energy scale of the parton-parton interaction:

$$
M_X^2 = \left(\sum_{h \in HFS} E_h \right)^2 - \sum_i \left(\sum_{h \in HFS} p_{h_i} \right)^2 = s_{\gamma\!I\!P},
$$

where h symbolises all particles of the hadronic final state (HFS), and i represents the coordinate axes $\{x, y, z\}$. The following cut is applied:

$$
M_X > 4 \text{ GeV}
$$

It guarantees a minimum final state energy, and strongly suppresses soft physics like vector meson production (eg exclusive ρ production with $M_X \equiv m_\rho \approx 770$ MeV [38]). The M_X-distributions are shown for the inclusive, the singlejet, and the dijet data samples in figure 4.3. The cut on M_X has no effect on the jet samples. Soft physics are already discarded by the cuts on the hard jet scales.

---

[4]Within this thesis, *singlejet* refers to events with $N_{jet} \geq 1$, while *dijet* symbolises events with $N_{jet} \geq 2$.
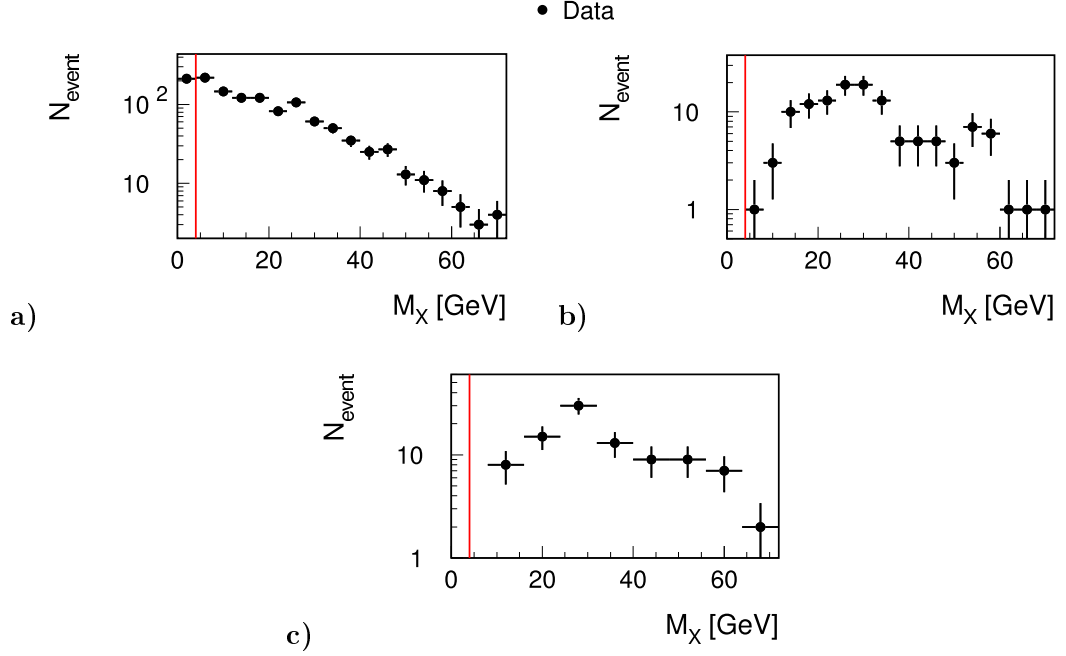
Figure 4.3: The invariant mass of the photon dissociation system for **a)** the inclusive, **b)** the singlejet ($N_{jet} \geq 1$), and **c)** the dijet event sample ($N_{jet} \geq 2$). It is shown after the FPS and the complete DIS selection, as well as the relevant jet cuts (cf sections 3, 4.1, 4.2.1). The applied cuts are indicated by the vertical lines.

4.2.3 Summary

The jet cuts, and the cut on the invariant mass of the hadronic final state are summarised in table 4.2. It also provides the event numbers for each data sample. The jet samples remain unchanged by the M_X-cut, and the inclusive sample contains

$$N_{event} = 1041$$

events.

4.3 Comparison to the Monte Carlo Simulation and Rejection of Non-Diffractive Background

In this section, the selected data sample is compared with a Monte Carlo simulated event sample. The application of the data selection cuts to the Monte Carlo events is discussed. Remaining non-diffractive background is estimated using simulated event distributions. Appropriate rejection cuts against this background are deduced.

4.3.1 The Monte Carlo Sample Used in this Analysis

A leading order Monte Carlo simulation of diffractive events with a scattered leading proton is used in this analysis. It was produced by Sebastian Schätzel on the basis of the RAPGAP generator, version 2.08/13 [17].

Table 4.2: The jet selection cuts, and the cut on the invariant mass of the hadronic final state. Event numbers are specified for the three data samples.

Description	Cut				Events		
Inclusive sample					N_{event}	$=$	1041
Invariant HFS mass		M_X	$>$	4.0 GeV			
Singlejet sample					N_{event}	$=$	128
Jet number		N_{jet}	$\geq$	1			
Transverse momentum		$p_\perp^*(jet\ 1)$	$>$	4.0 GeV			
Jet containment	-1.5 $<$	$\eta(jet\ 1)$	$<$	2.5			
Dijet sample					N_{event}	$=$	97
Jet number		N_{jet}	$\geq$	2			
Transverse momentum jet 1		$p_\perp^*(jet\ 1)$	$>$	4.0 GeV			
Transverse momentum jet 2		$p_\perp^*(jet\ 2)$	$>$	2.5 GeV			
Jet containment	-1.5 $<$	$\eta(jet\ 1/2)$	$<$	2.5			

Generation of Monte Carlo Events

The RAPGAP generator is based on the resolved Pomeron model (spectator model). It describes the colourless exchange as a pseudo-particle – the Pomeron or the Reggeon – with a given parton density function (pdf). This is explained in more detail in sections 1.2.3, 1.4. In the original generation, the diffractive parton densities from [22] (called H1 Fit 2 (1994)) were applied for the Pomeron, but the Monte Carlo sample is reweighted to the more precise parton densities from [24] (H1 Fit 2002) during the actual analysis. The photon structure function from [42] (SAS) was used for resolved photon processes (cf figure 1.14).

Since the major aim of this thesis is the investigation of hard interaction processes (cf section 1.2.7), a hard diffractive Monte Carlo event sample was generated. Its kinematic parameters are given in table 4.3. Events with a scattered proton in the acceptance range of the horizontal FPS stations (cf section 3.2.2) were preselected before subjecting the generated events to the time-consuming full detector simulation (cf section 1.4). The preselection cuts are also summarised in table 4.3, where $\hat{p}_\perp$ symbolises the transverse momentum of the hard interaction. $x_{I\!P}$ is the fractional longitudinal momentum transfer at the proton vertex (cf figure 1.7). All other variables are explained in sections 3 and 4.1.

To cover all important subprocesses occurring within the resolved Pomeron model, four different subsamples were generated (cf chapter 1):

1. Pomeron ($I\!P$) exchange with light quarks (u, d, s)

2. Pomeron ($I\!P$) exchange with a charm quark (c)

3. Pomeron ($I\!P$) exchange with resolved photon processes

4. Reggeon ($I\!R$) exchange with all four quark flavours (u, d, s, c)

Reggeon exchange with resolved photon processes was not considered due to its negligible contribution in the investigated phase space region [9]. The luminosities and event numbers of the generated and simulated Monte Carlo samples are specified in table 4.4. Because there is no difference between

Table 4.3: The kinematic range of the generated DIS Monte Carlo samples, and the preselection cuts on the acceptance range of the horizontal FPS stations for scattered protons (cf section 3.2.2).

Description	Range				
DIS kinematics					
Four momentum transfer	3.0	$<$	Q^2	$<$	100.0 GeV^2
Inelasticity	0.005	$<$	y	$<$	0.95
Hard interaction scale			$\hat{p}_\perp$	$>$	3.0 GeV
Scattered proton preselection					
Horizontal momentum	-0.4	$<$	p_x	$<$	-0.2 GeV
Vertical momentum			$|p_y|$	$<$	0.7 GeV
Fractional momentum transfer			$x_{I\!P}$	$<$	0.2
Four momentum transfer	0.05	$<$	$|t|$	$<$	0.8 GeV^2

Table 4.4: The generated and simulated DIS Monte Carlo samples.

Process	$\mathcal{L}$ [pb^{-1}]	Generated Events	Simulated Events
Pomeron ($I\!P$) u, d, s	50.0	$1,456,850$	$221,337$
Pomeron ($I\!P$) c	50.0	$348,936$	$57,604$
Pomeron ($I\!P$) resolved γ	55.0	$38,146$	$5,432$
Reggeon ($I\!R$) u, d, s, c	23.44	$2,040,750$	$301,190$

electrons and positrons as far as the underlying physics relevant for this thesis is concerned, only events with incoming positrons were generated.

Selection and Combination of the Monte Carlo Event Samples

Inclusive, singlejet, and dijet DIS Monte Carlo samples are defined by applying the data event selection devised above. The four Monte Carlo sets are added to the complete Monte Carlo sample. All events are weighted with the inverse luminosity to obtain a correct mixture of the different subprocesses without loosing any statistics. In the following diagrams, the data is plotted as full points. An open histogram represents the complete Monte Carlo sample. The Reggeon (light) and the sum of the Pomeron (dark) subprocesses are illustrated by hatched histograms. Since no cross sections are calculated in this analysis, only shape comparisons are considered. A Monte Carlo normalisation factor is calculated by normalising the complete Monte Carlo sample to the area of the data set in each diagram. This normalisation factor is applied to the Pomeron and Reggeon subsamples to obtain their correct contributions to the total Monte Carlo sample. Only the dominant statistical uncertainties are displayed (cf section 4.4). The cuts are specified in tables 3.2, 4.1, and 4.2. Two topics need further investigation:

Trigger Selection   Within the statistical accuracy of this thesis (cf section 4.4), the efficiency of the used subtriggers, $s35$ and $s61$, are sufficiently well described by the Monte Carlo simulation [9]. All Monte Carlo events are assigned trigger prescales of one for both subtriggers, since there are no hardware restrictions on event rates in the Monte Carlo simulation.

Migration Problems   Migrations always occur when data is binned, or a cut is applied. Since the resolution of any detector is finite, there are finite differences between the true and the reconstructed values of a certain quantity X. If a cut is performed on X_{rec}, some events are not accepted although they should be selected according to their true value, X_{true}. Their reconstructed value, X_{rec}, is migrated over the cut boundary (outward migrations). On the other hand, some events which do not fulfil the cut when considering X_{true} are selected (inward migrations). In Monte Carlo simulated events, the true value of X is the generated quantity: $X_{true} \equiv X_{gen}$. Migrations can thus be automatically considered in Monte Carlo simulated events, if the generated values, X_{gen}, cover a sensible range on both sides of the cut boundary.

This is not the case for the vertical proton momentum, p_y, and the lower boundary on the virtuality, Q^2. The cut on p_y will be discussed in section 4.5.2. Q^2 is examined in the next paragraphs.

Migration in the Four Momentum Transfer Q^2

The migration over the cut boundary at $Q^2_{rec} = Q^2_e = 3.0 \text{ GeV}^2$ is estimated using two simulated Monte Carlo samples:

$$
\begin{aligned}
&\text{a) Inward migration :} &Q^2_{rec} &> 4.0 \text{ GeV}^2, &\text{no cut on } Q^2_{gen} \\
&\text{b) Outward migration :} &Q^2_{gen} &> 3.0 \text{ GeV}^2, &\text{no cut on } Q^2_{rec}
\end{aligned}
$$

All other FPS and DIS cuts are applied as defined in sections 3 and 4.1. Figure 4.4 displays Q^2_{gen} for the event sample a) (left), and Q^2_{rec} for b) (right). The histograms are normalised to unit area, and the cuts are indicated by vertical lines. The following conclusions can be drawn from these diagrams:

a) Inward migration: (left)

- All events with $Q^2_{gen} < 4.0 \text{ GeV}^2$ are migrated over the cut boundary.
- The level of inward migration is approximately 2 %.

b) Outward migration: (right)

- All events with $Q^2_{rec} < 3.0 \text{ GeV}^2$ are migrated over the cut boundary.
- The level of outward migration is approximately 1.5 %.

Both, inward and outward migrations can be neglected considering the statistical uncertainties in this analysis (cf section 4.4).

4.3.2 The Fractional Longitudinal Momentum Transfer $x_{I\!P}$

The fractional longitudinal momentum transfer at the proton vertex, $x_{I\!P}$, can be measured in two different ways:
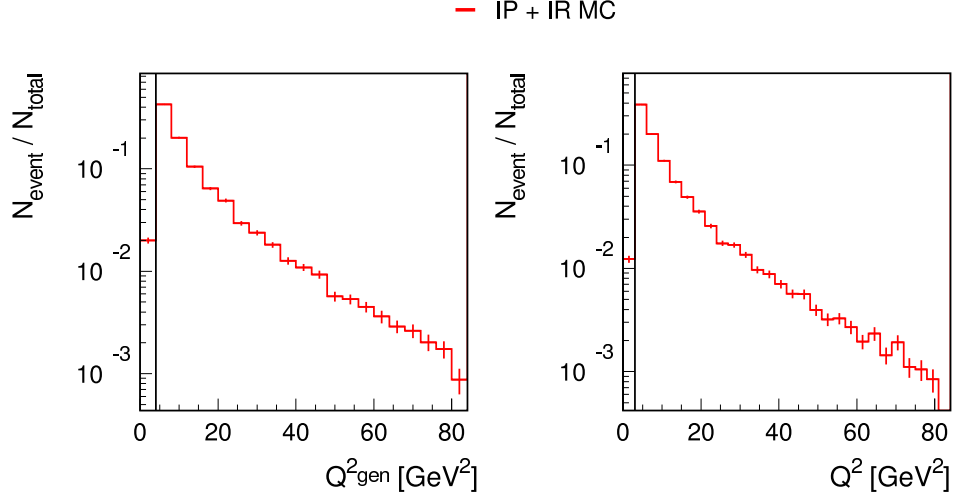
Figure 4.4: The investigation of inward (left) and outward (right) migration over the lower boundary of the cut on Q^2. The Monte Carlo samples are shown after the FPS and the DIS selection, including the cut on M_X (sections 3, 4.1, 4.2.2). Only the lower cuts on Q^2 are changed to $Q^2_{rec} > 4.0$ GeV^2 (left), and $Q^2_{gen} > 3.0$ GeV^2 (right). Both histograms are normalised to unit area, and the cuts are marked by the vertical lines. The migration level is given by the event fraction lying to the left of the cut boundaries.

The FPS Method   Firstly, $x_{I\!\!P}$ is determined using the scattered leading proton, ie by measuring the energy difference between the incoming and the outgoing proton:

$$x_{I\!\!P}^{FPS} \approx \frac{E_p - E_{p'}}{E_p} = 1 - \frac{E_{p'}}{E_p}.$$

Due to the finite resolution of the Forward Proton Spectrometer [38], migrations over the true maximal value for the proton energy, $E_p^{max} = E_p = 920$ GeV, are possible. They result in reconstructed energies of $E_{p'} > 920$ GeV. Because values of $x_{I\!\!P} < 0$ are not sensible, the variable is in this case set to a default value, $x_{I\!\!P} = 10^{-6}$. This value is beyond the acceptance range of the FPS [38], and thus allows a simple recognition of such events.

The Main Detector Method   Secondly, the longitudinal momentum transfer is reconstructed using the main detector, ie by measuring the energy which enters the photon dissociation system, X, from the proton side (cf figure 1.7). It is given by

$$x_{I\!\!P}^{main} = \frac{Q^2 + M_X^2 - t}{Q^2 + W^2 - m_p^2} \approx \frac{Q^2 + M_X^2}{Q^2 + W^2},$$

since $|t|$, $m_p^2 \ll Q^2$, W^2 (cf sections 3.2, 4.1).

   Both reconstruction methods, $x_{I\!\!P}^{FPS}$ (left), and $x_{I\!\!P}^{main}$ (right), are displayed in figure 4.5 against the generated quantity, $x_{I\!\!P}^{gen}$, for the complete Monte Carlo sample. The histograms show that the resolution of the FPS method is better down to values of $x_{I\!\!P} \approx 10^{-2}$, whereas the measurement with the main detector is more precise in the region of smaller $x_{I\!\!P} < 10^{-2}$. This is comprehensible, if the two reconstruction methods are considered in more detail.

Resolution of the FPS Method   Given the FPS resolution to be

$$\sigma_{E_{p'}} = \mathcal{O}(10\ \text{GeV}) \qquad [38],$$
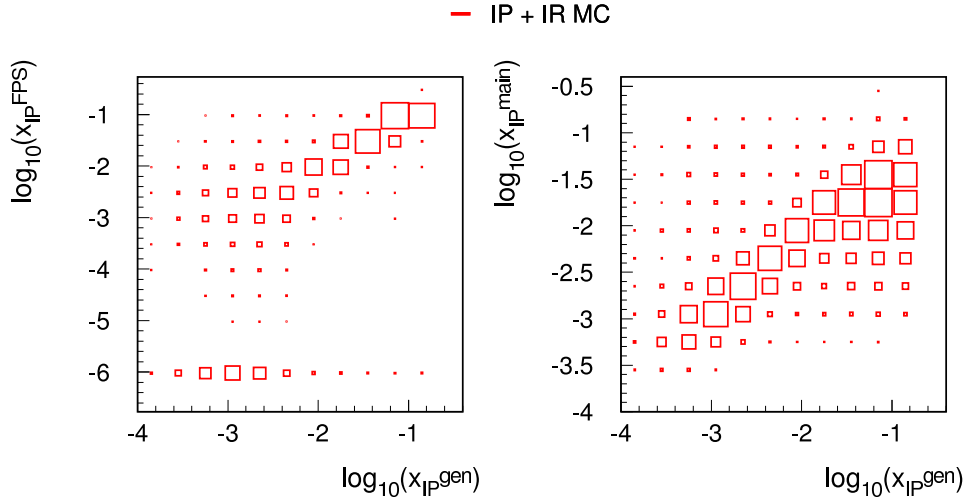
Figure 4.5: The resolution of the FPS and the main detector reconstruction methods for $x_{I\!P}$. The Monte Carlo sample is shown after the FPS and the DIS selection, including the cut on M_X (cf sections 3, 4.1, 4.2.2). Events for which $x_{I\!P}^{FPS}$ is set to the default value are visible as a line at $\log_{10}(x_{I\!P}^{FPS}) = -6$. The plots display the degrading resolution of the FPS method towards lower, and of the main detector method towards higher values of $x_{I\!P}$.

the resolution of $x_{I\!P}^{FPS}$ is approximately

$$\sigma_{x_{I\!P}^{FPS}} \sim \frac{\sigma_{E_{p'}}}{E_p} \sim 10^{-2}.$$

Hence, the accuracy of the FPS method is expected to degrade quickly below $x_{I\!P} \approx 10^{-2}$. This is observed in figure 4.5. The histogram shows an increasing spread in $x_{I\!P}^{FPS}$ towards lower values of $x_{I\!P}^{gen}$. It also exhibits a growing number of events with the default value of $x_{I\!P}^{FPS}$.

Resolution of the Main Detector Method A large momentum transfer from the incoming proton to the hadronic final state results in a greater forward boost of the latter. More and more final state particles escape undetected through the beam pipe in outgoing proton direction. Thus, the measured final state energies are generally too low, causing $x_{I\!P}^{main}$ to be reconstructed at lower values. This systematic shift of $x_{I\!P}^{main}$ towards higher values of $x_{I\!P}^{gen}$ is visible in figure 4.5.

The fractional longitudinal momentum transfer is therefore reconstructed in this analysis as

$$x_{I\!P} = \left\{ \begin{array}{llll} x_{I\!P}^{FPS} & : & x_{I\!P}^{FPS} & \geq & 10^{-2} \\ x_{I\!P}^{main} & : & x_{I\!P}^{FPS} & < & 10^{-2} \end{array} \right\}$$

4.3.3 Background Studies in the FPS Sample

An early comparison of the FPS hit pattern (cf figure 3.2) in data and Monte Carlo events showed that the data events generally display much more hits in the FPS stations than Monte Carlo simulated events. This effect is particularly strong in the first two planes of the horizontal detector at 64 m from the interaction point. The phenomenon has been thoroughly examined, and is now well understood and no longer problematic. It is only briefly reported here. Background hits are caused by synchrotron

radiation which is emitted by the nearby electron beam, and δ-rays[5] in the scintillator fibres. The reconstruction software is able to discard those hits and measure the true proton track [38].

A comparison of the two reconstruction methods for the fractional longitudinal momentum transfer, $x_{I\!P}^{FPS}$ and $x_{I\!P}^{main}$, revealed some events which have very small $x_{I\!P}^{FPS}$ but rather large $x_{I\!P}^{main}$. If the FPS measurement were correct, the measurement with the main detector should also return a small value of $x_{I\!P}^{main}$, since the main detector method is more precise for small $x_{I\!P}$. On the other hand, if the result of the main detector were true, the FPS ought to return an even larger value of $x_{I\!P}^{FPS}$. The reasons are the underestimation of the true value by the main detector method, and the higher precision of the FPS measurement for large $x_{I\!P}$ (cf section 4.3.2). After a detailed investigation, these events were found to be overlays. An overlay event is in this context an event in which a normal *ep*-collision in the main detector is recorded in coincidence with a *halo proton*[6] in the FPS stations.

Rejection of Overlay Events

In the case of an overlay, a normal event topology is observed in the main detector, while the FPS measures an essentially unscattered proton. The measured proton energy is

$$E_{p'} = E_p \approx 920 \text{ GeV}, \qquad \text{and therefore} \qquad x_{I\!P}^{FPS} \sim 10^{-6},$$

whereas $x_{I\!P}^{main}$ can assume any value. The reconstructed proton and the detected event are completely uncorrelated, and an energy excess is generally observed in the complete detector system compared to the assumed initial state $e(27.5 \text{ GeV})p(920 \text{ GeV})$.

Those events can therefore be recognised by considering the total longitudinal energy and momentum,

$$\sum_j \left(E_j + p_{j_z} \right),$$

in which the sum includes all particles of the considered state. The initial electron cancels in the above sum, since it fulfils the relation $E_e \approx -p_{e_z}$. Only the energy related to the initial proton is retained. For the initial state, ep, the total longitudinal energy and momentum is

$$\sum_i \left(E_i + p_{i_z} \right) \approx 2E_p \approx 1840 \text{ GeV},$$

where the sum comprises all initial state particles, ie $i = e, p$. If a scattered proton connected to the observed main event is detected, the final state will satisfy

$$\sum_f \left(E_f + p_{f_z} \right) = \sum_i \left(E_i + p_{i_z} \right) \approx 1840 \text{ GeV},$$

where i denotes all initial, and f all final state particles. In contrast, initial and final state of an overlay reaction are not correlated, resulting in

$$\left(\sum_f \left(E_f + p_{f_z} \right) \right)_{overlay} > 1840 \text{ GeV}.$$

Figure 4.6 shows the distribution of $\sum_f \left(E_f + p_{f_z} \right)$. An excess of events with $\sum_f \left(E_f + p_{f_z} \right) > 1840$ GeV is visible in the data compared to the Monte Carlo sample. This cannot be due to the resolution of the FPS which can be estimated from the Monte Carlo simulation [38]:

$$\sigma_{E_{p'}} \approx 5.5 \text{ GeV}$$

---

[5] δ-*rays* or *knock-on* electrons are high-energy recoil electrons which are produced by ionisation processes within the scintillator material [44].

[6] A *halo proton* is an unscattered beam proton at the edge of the circling beam.
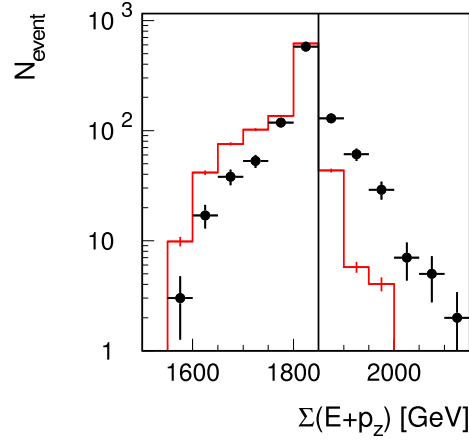
Figure 4.6: The total longitudinal energy and momentum, $\sum_f \left(E_f + p_{f_z} \right)$. It is displayed for the data and the Monte Carlo sample after the FPS and the DIS selections, including the cut on M_X (cf sections 3, 4.1, 4.2.2). The cut boundary is indicated by the vertical line.

The excess is interpreted as overlay events which have not been rejected by the other selection cuts. Most of the discrepancies at low values of $\sum_f \left(E_f + p_{f_z} \right)$ are due to this data excess at high values, and to the area normalisation of the Monte Carlo sample to the data set (cf section 4.3.1). Any remaining discrepancies will be discussed in section 4.5.2.

Considering the above energy resolution of the FPS measurement, a cut on the total longitudinal energy and momentum,

$$\sum_f \left(E_f + p_{f_z} \right) < 1850 \text{ GeV},$$

is applied to reject these overlay events.

4.4 Summary of the Event Selection

Tables 4.5, 4.6 summarise the complete list of cuts for the selection of deep-inelastic scattering events with a scattered leading proton. The applied jet selection cuts for the singlejet ($N_{jet} \geq 1$), and the dijet ($N_{jet} \geq 2$) event samples were specified in table 4.2. Three data samples are considered in the further analysis:

a) Inclusive sample			:	N_{event}	=	806	:	$\frac{\Delta N}{N}$	$\sim$ 3.5 %
b) Singlejet sample	N_{jet}	$\geq$ 1	:	N_{event}	=	86	:	$\frac{\Delta N}{N}$	$\sim$ 10.8 %
c) Dijet sample	N_{jet}	$\geq$ 2	:	N_{event}	=	59	:	$\frac{\Delta N}{N}$	$\sim$ 13.0 %

These event samples are rather limited. Their overall uncertainties are dominated by statistical fluctuations. Solely statistical uncertainties are therefore displayed in all following plots. Since no cross sections are calculated in this analysis, only shape comparisons are considered. A Monte Carlo normalisation factor is determined for each of the three considered event samples by normalising the complete Monte Carlo sample to the area of the data set in each diagram. This normalisation factor is applied to the Pomeron and Reggeon subsamples to obtain their correct contributions to the complete Monte Carlo sample. Unless stated otherwise, the inclusive event selection is applied for all further event samples.

Table 4.5: The complete selection cuts for *ep*-events with a leading proton in the FPS.

Description	Cut			
ep-preselection				
Vertex requirement		$\|z_{vertex}\|$	$<$	35 cm
FPS preselection				
Proton candidate		$n_{class}(event)$	$=$	14
Local track at 64 m		$N_{track}^{local}(64 \text{ m})$	$\geq$	1
Local track at 80 m		$N_{track}^{local}(80 \text{ m})$	$\geq$	1
FPS track selection				
Global track in FPS		N_{track}^{global}	$\geq$	1
Reconstructed proton energy		$E_{p'}$	$>$	1.0 GeV
FPS acceptance				
Horizontal proton momentum	$-0.38 <$	p_x	$<$	-0.23 GeV
Vertical proton momentum		$\|p_y\|$	$<$	0.7 GeV
Fractional four momentum transfer		$x_{I\!P}^{FPS}$	$<$	0.17 GeV
Squared four momentum transfer	$0.07 <$	$\|t\|$	$<$	0.7 GeV^2
FPS overlay rejection				
Energy and momentum		$\sum_f (E_f + p_{f_z})$	$<$	1850 GeV

4.4.1 Event Display

Figure 4.7 shows an event display of the main detector for a data event with a reconstructed leading proton and exactly two jets. The scattered electron is detected in the SpaCal calorimeter. Both jets are well measured in the central tracking system and the LAr calorimeter. Their back-to-back topology with respect to ϕ is visible. The scattered proton is measured in the FPS, and leaves no trace in the main detector. Due to the colourless exchange between scattered proton and hadronic final state, the forward region of the main detector is completely void of any energy deposit. A large *rapidity gap* (cf section 1.2) is observed between the most forward high-energy cluster ($E_{cluster} > 400$ MeV) in the LAr calorimeter and the outgoing proton direction.

4.5 Kinematic Ranges and Acceptances in the Data and the Monte Carlo Simulation

Similar kinematic ranges and detector acceptances in data and Monte Carlo simulation are crucial to any analysis. Measures to adjust the conditions in the Monte Carlo simulation to the data are discussed in this section.

4.5.1 Reweighting of the Vertex Distribution

The vertex position strongly influences the event kinematics, eg Q^2, x. Similar vertex distributions in data and Monte Carlo samples are hence important for any analysis. Since the vertex distributions in data and Monte Carlo generally slightly differ in mean and width due to varying data taking

Table 4.6: The complete selection cuts for deep-inelastic scattering events.

Description	Cut				
Trigger selection					
Subtriggers	$(s35$	or	$s61)$	$=$	1
Prescales	$(s35_{presc}$	and	$s61_{presc})$	$=$	1
Electron reconstruction					
Distance (cluster - beam pipe)	10.0	$<$	d_{cl-bp}	$<$	67.0 cm
Energy in veto layer			E_{veto}	$<$	1.0 GeV
Cluster radius			r_{cl}^{e}	$<$	4.0 cm
Energy in hadronic SpaCal			E_{had}	$<$	0.5 GeV
Electron energy	8.0 GeV	$<$	$E_{e'}$		
Distance (track - cluster)			Δ_{BDC}	$<$	3.5 cm
Kinematic selection					
Four momentum transfer	3.0	$<$	Q_e^2	$<$	80.0 GeV^2
Inelasticity	0.1	$<$	y_e	$<$	0.7
Background rejection					
Energy and momentum	35.0	$<$	$\sum_f (E_f - p_{f_z})$	$<$	70.0 GeV
Hadron method			$\|y_e - y_{had}\|$	$<$	0.3
Double angle method			$\|y_e - y_{da}\|$	$<$	0.3
Minimum HFS energy scale					
Invariant HFS mass			M_X	$>$	4.0 GeV

conditions, the reconstructed z_{vertex}-distribution of the simulated events is reweighted to the one of the data.

A Gaussian function is fitted to the z_{vertex}-distributions of the data and of the complete Monte Carlo sample. The ratio of the two functions,

$$g_{MC}(z_{vertex}) = \frac{G_{data}(z_{vertex})}{G_{MC}(z_{vertex})},$$

is applied as an event weight to each simulated Monte Carlo event. Figure 4.8 displays the effect of the reweighting procedure. It shows the data and the Monte Carlo samples including the fitted Gaussian functions before (a), and after (b) the reweighting. A better agreement of data and Monte Carlo distributions after the reweighting is visible. The latter is applied to the Monte Carlo distributions in all further plots.

4.5.2 Correction for the Varying FPS Acceptance

Proton rates in the Forward Proton Spectrometer are limited by hardware capacities [38]. To comply with those requirements, the Roman pots are kept at different positions relative to the proton beam during data taking. They vary according to beam conditions and stability. Monte Carlo events, on the other hand, are simulated with just one position of the Roman pots. Hence, the acceptance distributions differ between the data and the simulated Monte Carlo sample. This can be seen in
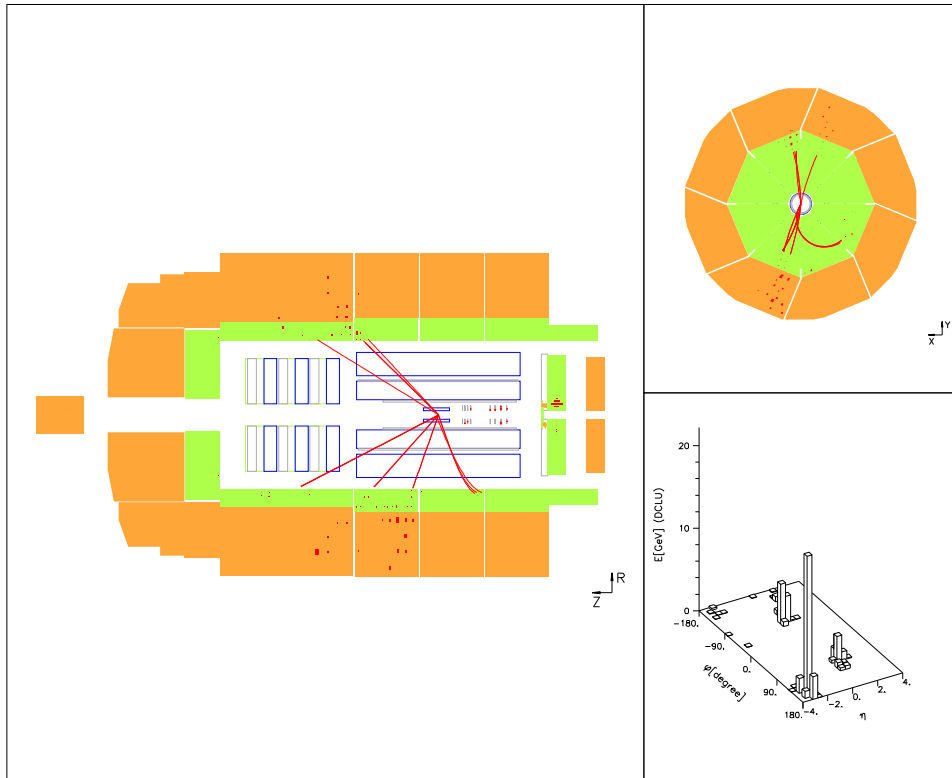
Figure 4.7: An event display of the main detector for a data event with a reconstructed leading proton and exactly two jets. Left: Cut along the beam direction. The scattered electron is detected in the SpaCal calorimeter. Both jets are well visible in the central tracking system and the LAr calorimeter. No energy deposit is observed in the forward part of the main detector (rapidity gap). Top right: $(x - y)$-view. The back-to-back topology of the jets with respect to ϕ is obvious. Bottom right: Energy deposit in the $(\eta - \phi)$-plane. The highest peak is the scattered electron, the two other peaks are the well collimated jets.

figure 4.9. It displays the scattered proton quantities, ie the horizontal and the vertical momentum, p_x, p_y, the energy, $E_{p'}$, and the fractional longitudinal momentum transfer measured with the FPS, $x_{I\!P}^{FPS}$. Especially the distribution of the horizontal momentum, p_x, shows a prominent shift of the Monte Carlo relative to the data distribution. This is due to the fact that the positions of the horizontal stations of the FPS vary in the *horizontal* plane (cf section 2.2.4). These acceptance differences are also partly responsible for the observed differences in the $\sum_f (E_f + p_{f_z})$-distribution at low values of $\sum_f (E_f + p_{f_z})$ in section 4.3.3 (cf figure 4.6).

The physics aim of this analysis is the investigation of energy flow in the main and forward detectors of the H1 apparatus in events with a leading proton. Scattered protons in the FPS are detected in the energy range

$$E_{p'} \sim 740 - 920 \text{ GeV} \qquad \text{(cf section 3.2.2)}.$$

Their transverse momentum, $p_\perp = \sqrt{p_x^2 + p_y^2}$, is restricted to

$$0.23 < p_\perp < 0.8 \text{ GeV} \ll E_{p'} \approx p_z \qquad \text{(cf section 3.2.2)}.$$

The event kinematic in the main detector is thus in leading order independent of the transverse momentum of the scattered proton, $p_\perp$, ie of the distributions of p_x and p_y. It only depends on the
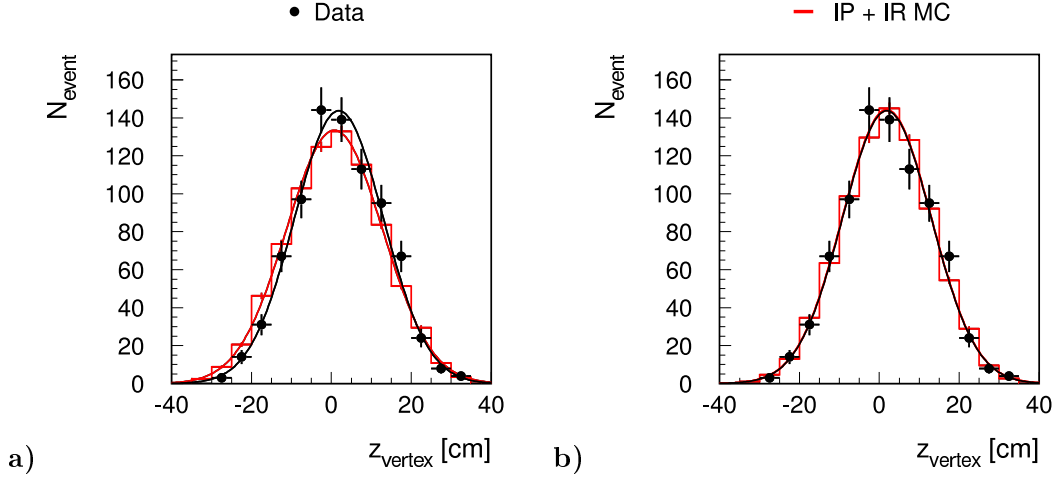
Figure 4.8: The effect of the z_{vertex}-reweighting procedure. The data and Monte Carlo distributions are displayed **a)** before, and **b)** after the reweighting. All selection cuts (tables 4.5, 4.6) are applied.

energy transferred from the proton to the main event, ie on the fractional longitudinal momentum transfer at the proton vertex,

$$x_{I\!P}^{FPS} \approx 1 - \frac{E_{p'}}{E_p}.$$

In consequence, the energy flow in the main and the forward detectors also solely depends on $x_{I\!P}$.

Reweighting of the $x_{I\!P}$-Distribution

It is therefore sufficient to reweight the Monte Carlo distribution of $x_{I\!P}^{FPS}$ to the one of the data. No cross section measurements are possible after this reweighting, but the energy flow can still be determined correctly. A more uniform distribution in which statistical fluctuations are smoothed is achieved by using the variable $\log_{10}\left(x_{I\!P}^{FPS}\right)$ for the reweighting instead of $x_{I\!P}^{FPS}$ itself. The weighting factor is determined for each bin of the $\log_{10}\left(x_{I\!P}^{FPS}\right)$-histogram by division of the data and the corresponding Monte Carlo histogram:

$$g(bin\ i) = \frac{N_{data}(bin\ i)}{N_{MC}(bin\ i)}$$

It is applied to each Monte Carlo event according to its value of $\log_{10}\left(x_{I\!P}^{FPS}\right)$. The effect of this reweighting procedure is shown in figure 4.10. It displays the fractional longitudinal momentum transfer at the proton vertex, $\log_{10}\left(x_{I\!P}^{FPS}\right)$, and the energy of the scattered proton, $E_{p'}$, after the reweighting. They agree almost perfectly. Any remaining differences in the $E_{p'}$-distributions are due to the smoothing effect and to binning differences between $x_{I\!P}^{FPS}$ and $\log_{10}(x_{I\!P}^{FPS})$. The distributions of the horizontal and vertical momentum of the scattered proton, p_x and p_y, are not considered any further, since they are not relevant for the topic of this thesis.

Reweighting in $x_{I\!P}$ for Inclusive and Jet Samples

The hardness of the interaction in the main detector crucially depends on the amount of energy transferred from the incoming proton to the hadronic final state, ie on $x_{I\!P}$. The more energy is
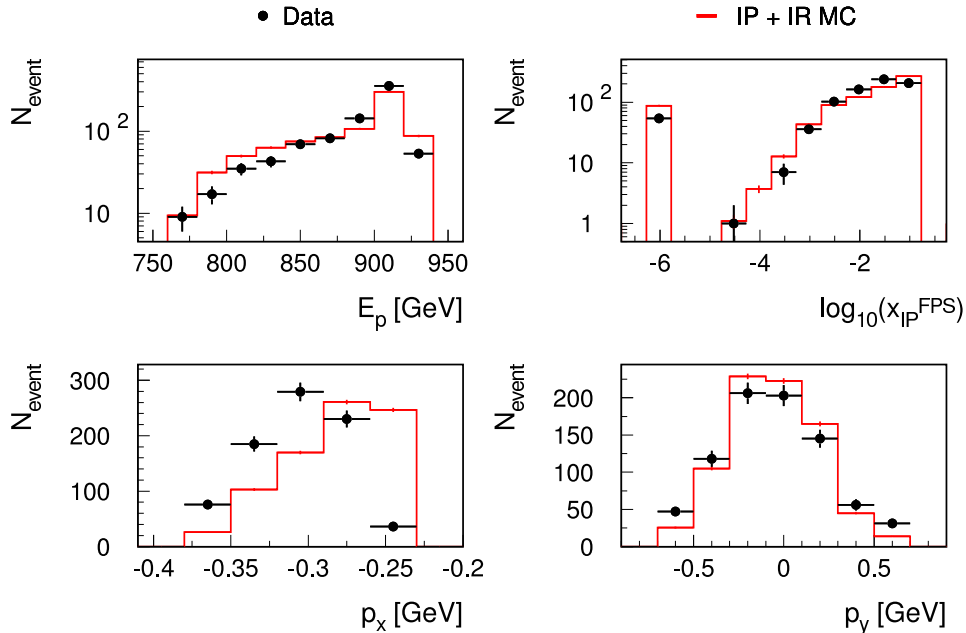
Figure 4.9: The leading proton quantities mostly affected by different FPS pot positions in the data and the Monte Carlo simulation. Both samples are shown after the full event selection (cf tables 4.5, 4.6), and the vertex reweighting is applied.

transferred from the proton, ie the larger $x_{I\!P}$ is, the more likely is the occurrence of a hard parton-parton interaction, ie of high-$p_\perp$ jets in the hadronic final state. The distributions of $x_{I\!P}$ are hence genuinely different for the inclusive and the jet event samples. This is visible in figures 4.10, 4.11. They display the reweighted distributions of $\log_{10}\left(x_{I\!P}^{FPS}\right)$ and $E_{p'}$ for the inclusive (figure 4.10), and the jet event samples (figure 4.11: a) singlejets, b) dijets). The reweighting of the $x_{I\!P}$-distribution of the simulated to the data events is therefore performed separately for the inclusive, the singlejet, and the dijet event samples. The resulting event weights in z_{vertex} and $x_{I\!P}^{FPS}$ are used for all following data-Monte Carlo comparisons. Both distributions of $E_{p'}$ in figure 4.11 show the smoothing effect of applying the reweighting in $\log_{10}(x_{I\!P}^{FPS})$ instead of $x_{I\!P}^{FPS}$. The data show strong statistical fluctuations in $E_{p'}$ which are not transferred to the Monte Carlo simulation.

Migration in the Leading Proton Variables

Due to the reweighting procedure, the leading proton quantities of the Monte Carlo events are no longer free variables, but adjusted to reflect the data taking conditions. Migration of events over the defined cut boundaries (cf table 3.2) are thus not important. The data selection cuts – especially the one on p_x (cf tables 3.2, 4.3) – can also be applied to the reconstructed Monte Carlo events.

The complete event selection, and the adjustment of data taking conditions in the simulated events to the data now being finished, the next sections are concerned with the estimation of Pomeron and Reggeon contributions to the data, and the description of the most important data quantities by the Monte Carlo simulation.

Unless stated otherwise, all distributions in the remaining parts of this chapter thus display the data and the Monte Carlo samples after the complete event selection (cf tables 4.5, 4.6). Data distributions are plotted as full points, the complete Monte Carlo sample is indicated by an open histogram. Hatched histograms represent the distributions of the Pomeron ($I\!P$: dark) and the Reggeon ($I\!R$: light) Monte Carlo subsamples. Except for the distributions in figures 4.12 a), and 4.13 a), the
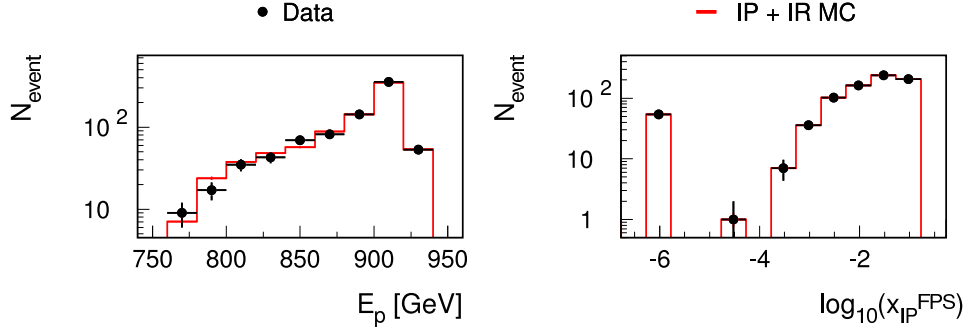
Figure 4.10: The leading proton quantities after the $x_{I\!P}$-reweighting of the Monte Carlo simulation. All samples are shown after the full event selection (cf tables 4.5, 4.6), but without any jet requirements, and the vertex reweighting is applied.

Monte Carlo distributions are reweighted to the data in z_{vertex} and $x_{I\!P}$. All Monte Carlo samples are normalised to the data as explained in section 4.4. Only the dominant statistical uncertainties are displayed. The jet selection criteria applied are specified for each event sample.

4.6 Estimation of Pomeron and Reggeon Contributions to the Data

The Monte Carlo simulation predicts a large fraction of Reggeon exchange events for the selected inclusive data sample (cf table 4.7). It can therefore be used to measure this fraction, and to verify the prediction based on the analysis of the inclusive diffractive structure function, F_2^D (cf section 1.2.5, 1.4). In this section, a direct proof is provided for the existence of Reggeon exchange reactions in the DIS data. The Reggeon and Pomeron contributions are displayed as predicted by the Monte Carlo event samples, and they are measured for the data. A correction factor is estimated to calculate the ratio of Reggeon to Pomeron exchanges in the data from the one predicted by the Monte Carlo simulation. Due to the reweighting in $x_{I\!P}^{FPS}$, which does not correct in a detailed way for the geometric acceptance differences between data and Monte Carlo simulation (cf section 4.5.2), these calculations can only be understood as rough estimates of the Pomeron and Reggeon contributions.

4.6.1 The Inclusive Data Sample

Figure 4.12 displays the distributions of $x_{I\!P}$ in the inclusive DIS sample before (a), and after (b) the reweighting in $x_{I\!P}^{FPS}$. Although significant differences are observed between data and Monte Carlo simulation before the reweighting (cf section 4.5.2), both plots show that a large Reggeon contribution is needed to describe the data. In contrast to the indirect hint for Reggeon exchange processes by the breaking of Regge factorisation in the analysis of the diffractive structure function, F_2^D (cf section 1.2.5), this is a direct proof of the existence of Reggeon exchange reactions in diffractive event samples. The fractional contributions of Pomeron and Reggeon exchange processes are presented in table 4.7 as predicted by the Monte Carlo simulation. They are displayed for the inclusive event sample both, before and after the reweighting in $x_{I\!P}^{FPS}$. Despite the considerable differences in the shape of the $x_{I\!P}$-distribution in the Monte Carlo simulation before and after the reweighting, the overall change of the fractional contributions is only 2 %.

Generally, the Pomeron and Reggeon contributions in the data can differ from those predicted by the Monte Carlo simulation, but the reweighting tunes the Pomeron and Reggeon contributions to perfectly describe the data. The Pomeron and Reggeon contributions in the data are thus equal to those predicted by the Monte Carlo simulation. The systematic uncertainties of the fractional
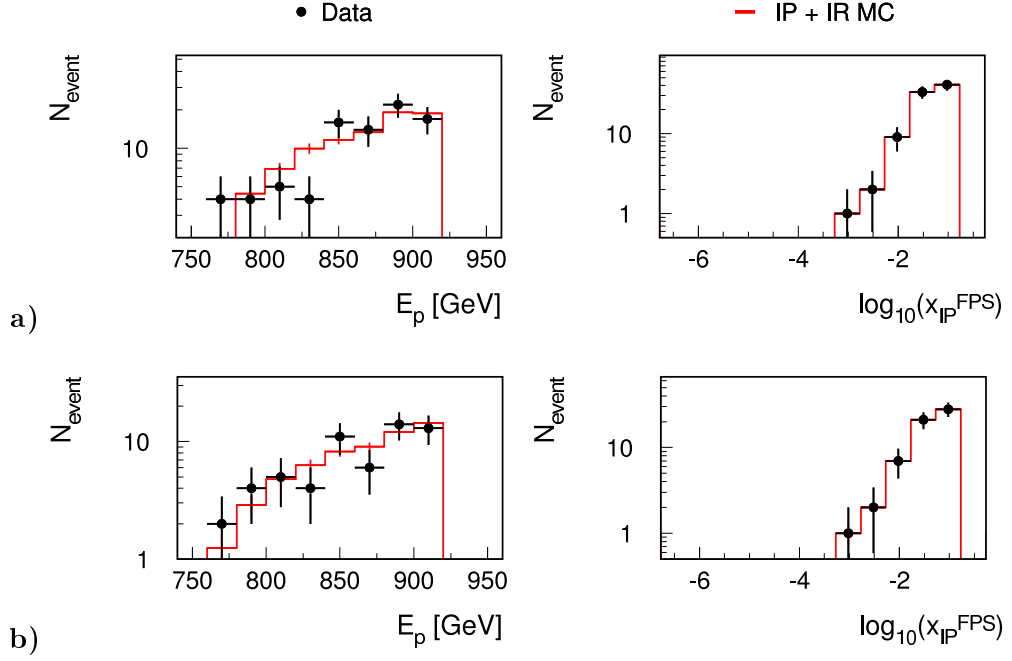
Figure 4.11: The leading proton quantities after the $x_{I\!P}$-reweighting of the Monte Carlo simulation. All samples are shown after the full event selection (cf tables 4.5, 4.6), displaying **a)** the singlejet distributions ($N_{jet} \geq 1$), and **b)** the dijet ones ($N_{jet} \geq 2$). The vertex reweighting is applied.

Table 4.7: The fractional contributions of the Pomeron ($I\!P$) and the Reggeon ($I\!R$) exchange processes to the inclusive DIS Monte Carlo sample: $f_X = \frac{N_{event}(X)}{N_{event}}$

	$f_{I\!P}$ [%]	$f_{I\!R}$ [%]
Before reweighting in $x_{I\!P}^{FPS}$	55	45
After reweighting in $x_{I\!P}^{FPS}$	57	43

contributions can be estimated from their variations due to the reweighting procedure:

$$f_{I\!P} = 0.57 \pm 0.02_{syst} \pm 0.03_{stat} = 0.57 \pm 0.04$$
$$f_{I\!R} = 0.43 \pm 0.02_{syst} \pm 0.03_{stat} = 0.43 \pm 0.04,$$

where systematic and statistical uncertainties have been added quadratically. The correction factor to calculate the ratio of Reggeon to Pomeron contributions in the data from the one predicted by the Monte Carlo simulation, f_{corr}, is defined by

$$\left(\frac{f_{I\!R}}{f_{I\!P}}\right)_{data} = f_{corr} \left(\frac{f_{I\!R}}{f_{I\!P}}\right)_{MC}.$$

Due to the reweighting in $x_{I\!P}^{FPS}$, the correction factor is equal to one, and its systematic uncertainties can also be estimated from the variation of the fractional contributions due to the reweighting procedure:

$$f_{corr} = 1.00 \pm 0.07_{syst} \pm 0.07_{stat} = 1.00 \pm 0.10$$
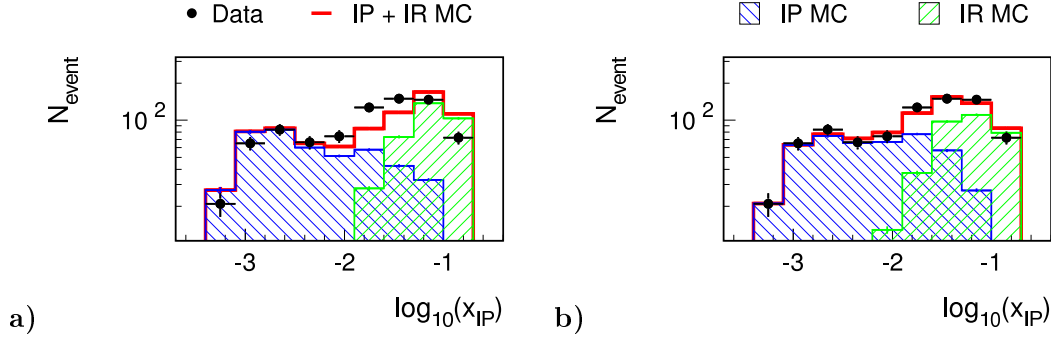
Figure 4.12: The longitudinal momentum transfer, $x_{I\!\!P}$, **a)** before, and **b)** after the reweighting in $x_{I\!\!P}^{FPS}$. All diagrams show the inclusive event samples after the full event selection (cf tables 4.5, 4.6). The vertex reweighting is applied.

An exact simulation of the FPS acceptance (ie the positions of the Roman pots) would be needed for a more accurate measurement.

The comparison of data and Monte Carlo simulation shows that a large Reggeon contribution is needed to describe the measured inclusive distributions. This contribution is quantitatively well described by the diffractive structure function as obtained from the QCD analysis of F_2^D (cf section 1.2.5). The prediction based on this QCD analysis is verified with an accuracy of 10 %.

4.6.2 The Singlejet Data Sample

The distributions of $x_{I\!\!P}$ are displayed in figure 4.13 for the singlejet ($N_{jet} \geq 1$) DIS event samples before (a), and after (b) the reweighting in $x_{I\!\!P}^{FPS}$. Despite the increased statistical uncertainties, they
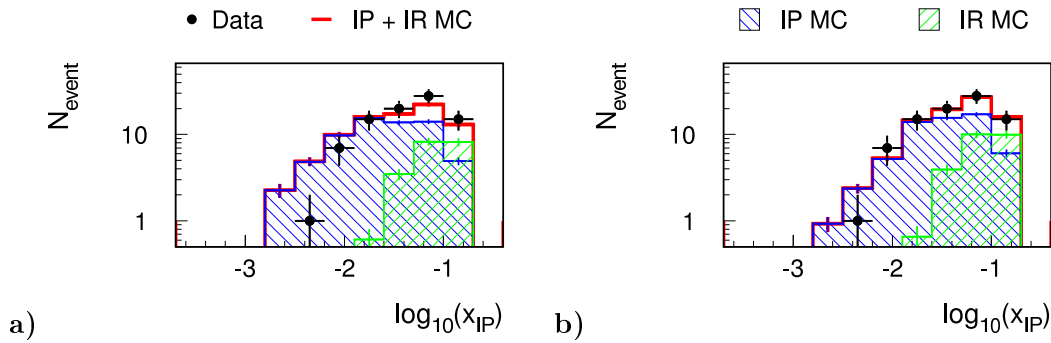
Figure 4.13: The longitudinal momentum transfer, $x_{I\!\!P}$, **a)** before, and **b)** after the reweighting in $x_{I\!\!P}^{FPS}$. All diagrams show the singlejet ($N_{jet} \geq 1$) event samples after the full event selection (cf tables 4.5, 4.6). The vertex reweighting is applied.

still show that the Reggeon contribution is needed to describe the data. Both plots display a strong enrichment of Pomeron exchange processes compared to the inclusive Monte Carlo sample. Table 4.8 presents the fractional contributions of Pomeron and Reggeon exchange as predicted by the Monte Carlo simulation. They are displayed for the singlejet ($N_{jet} \geq 1$) event sample both, before and after the reweighting in $x_{I\!\!P}^{FPS}$. The table shows that the singlejet event sample is more sensitive to the reweighting procedure in $x_{I\!\!P}^{FPS}$ than the inclusive sample. Pomeron and Reggeon contributions are changed by about 5 % in favour of the Reggeon exchange. Only a slight enhancement of the Pomeron contribution (cf table 4.7) is displayed in the inclusive event sample.

Table 4.8: The fractional contributions of the Pomeron ($I\!P$) and the Reggeon ($I\!R$) exchange processes to the singlejet ($N_{jet} \geq 1$) DIS Monte Carlo sample: $f_X = \frac{N_{event}(X)}{N_{event}}$

	$f_{I\!P}$ [%]	$f_{I\!R}$ [%]
Before reweighting in $x_{I\!P}^{FPS}$	76	24
After reweighting in $x_{I\!P}^{FPS}$	71	29

The contributions of Reggeon and Pomeron exchange processes in the singlejet DIS data sample are measured as for the inclusive event sample:

$$f_{I\!P} = 0.71 \pm 0.05_{syst} \pm 0.12_{stat} = 0.71 \pm 0.13$$
$$f_{I\!R} = 0.29 \pm 0.05_{syst} \pm 0.07_{stat} = 0.29 \pm 0.09$$

The correction factor to calculate the fraction of Reggeon to Pomeron events in the data from the one predicted by the Monte Carlo simulation, f_{corr} (cf section 4.6.1), is

$$f_{corr} = 1.00 \pm 0.21_{syst} \pm 0.24_{stat} = 1.00 \pm 0.32.$$

As for the inclusive event sample, a good agreement is observed between the data and the Monte Carlo prediction based on the inclusive F_2^D measurement. But due to the large relative uncertainties, the agreement can only be tested to a level of 32 %. Since, within these uncertainties, no significant differences are observed between the Reggeon and Pomeron contributions to the singejet and dijet data samples, the dijet event sample is not examined separately.

4.7 Description of the Data by the Monte Carlo Simulation

This section compares the data and the Monte Carlo simulated distributions of the selected DIS samples with a scattered leading proton. Pomeron and Reggeon contributions to the complete Monte Carlo event sample are also investigated.

4.7.1 The Inclusive Event Sample

Figure 4.14 shows the standard event variables for the inclusive DIS event samples. The overall agreement between data and Monte Carlo distributions is good. Since the Monte Carlo samples are reweighted to the data in $x_{I\!P}^{FPS}$ (cf section 4.5.2), the scattered proton quantities, $E_{p'}$ and $x_{I\!P}$, are described almost perfectly. Any remaining discrepancies in $E_{p'}$ are caused by the smoothing effect of reweighting in $\log_{10}\left(x_{I\!P}^{FPS}\right)$ (cf section 4.5.2). The differences in the distribution of $x_{I\!P}$ are caused by the combination of two reconstruction methods (FPS and main detector, cf section 4.3.2). Good agreement is observed for the scattered electron energy, $E_{e'}$, within the given uncertainties, although the data show strong statistical fluctuations. The description of the electron scattering angle, $\theta_{e'}$, is also reasonable, but a slight lack of data events at medium values of $\theta_{e'}$ is observed. This effect is mirrored in the Q_e^2-distribution (cf section 4.1.3). The general description of Q_e^2 is good. Data and Monte Carlo simulation agree almost perfectly in y_e. As for $E_{e'}$, the data distribution of the centre-of-mass energy of the photon-proton system, W_e (cf section 1.2.6), shows strong statistical fluctuations, but the overall agreement is reasonable within the given uncertainties.
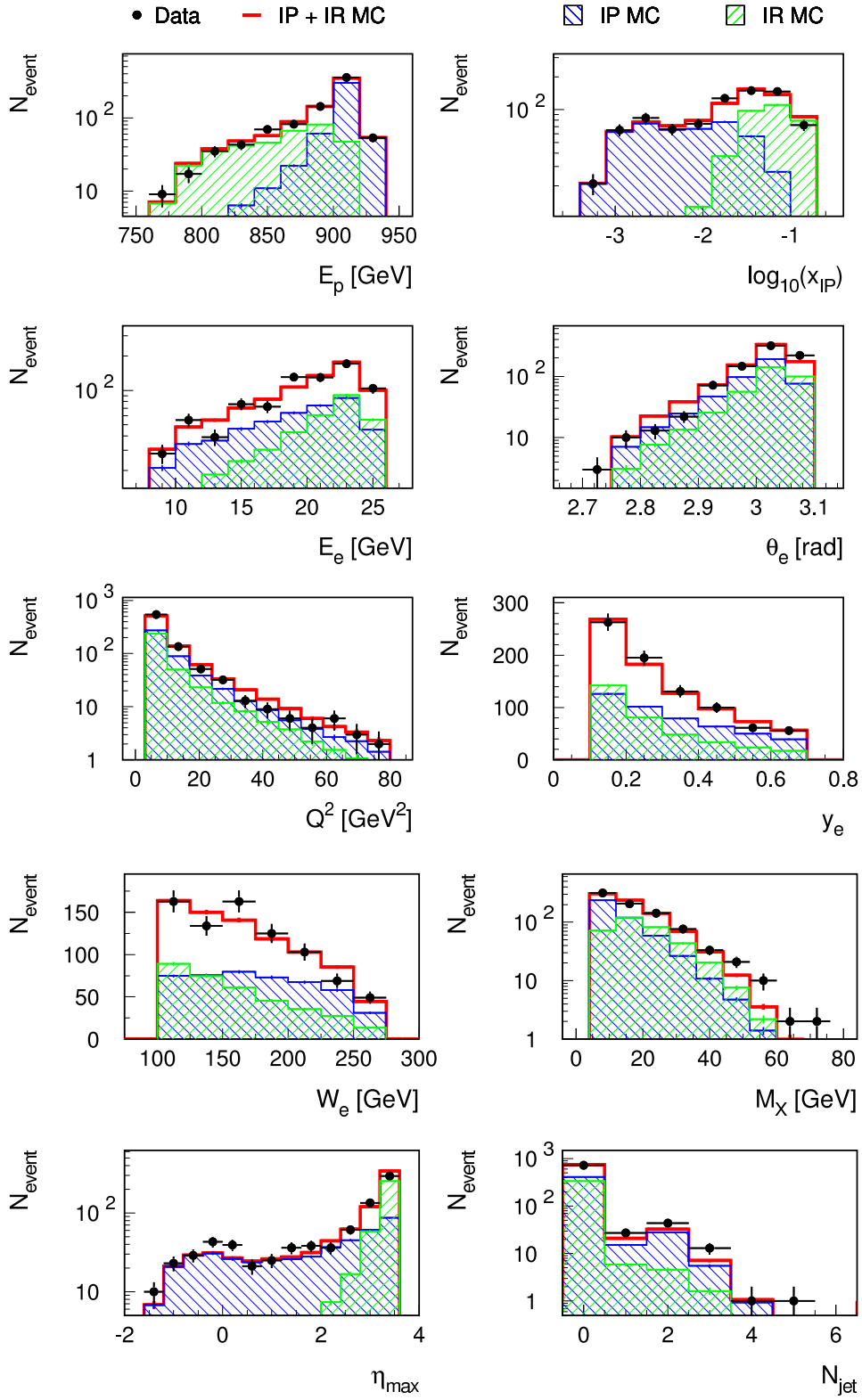
Figure 4.14: The description of the standard event variables in the DIS data by the Monte Carlo simulation. All histograms show the inclusive event samples.

In contrast, the M_X-distributions display a considerable excess of data events at large values. This is not caused by using a hard Monte Carlo simulation which could only produce the opposite effect. It might result form next-to-leading order QCD effects, or inaccurate structure functions. All Monte Carlo samples are only based on leading order QCD calculations (cf section 1.4). η_{max} symbolises the pseudorapidity of the most forward high-energy cluster ($E_{cluster} > 400$ MeV) in the LAr calorimeter. Its description by the Monte Carlo simulation is acceptable, although a slight lack of data events is observed in the most forward η-bin, and a slight excess around $\eta \sim 0$. The number of high-$p_\perp$ jets agrees astonishingly well for a leading order Monte Carlo simulation. The slight excess of multijet events in the data is caused by higher order QCD effects.

The distributions of $\log_{10}(x_{I\!P})$ and η_{max} show a high separation power for the Pomeron (dark hatched) and the Reggeon (light hatched) contributions to the complete Monte Carlo sample. Both histograms prove the need for both, the Pomeron and the Reggeon exchange processes to describe the data (cf section 4.6.1). They also show that the relative contributions are well modelled by the Monte Carlo simulation, and that – in agreement with the M_X-distribution – Reggeon exchange processes are on average harder and more forward, ie at larger η, than Pomeron interactions. In contrast, N_{jet} suggests that jet events are dominated by Pomeron exchange processes.

4.7.2 The Singlejet Event Sample

The standard event variables are displayed for the singlejet ($N_{jet} \geq 1$) DIS event samples in figure 4.15. The singlejet distributions of the data are – within the statistical uncertainties – well described by the Monte Carlo simulation. They exhibit the same behaviour as those of the inclusive event samples. Statistical uncertainties and fluctuations in the data are much larger than for the inclusive sample. This is especially visible in the distributions of $E_{p'}$, $E_{e'}$, and W_e. The $\theta_{e'}$- and Q_e^2-histograms show the same lack of data events at medium values as described above. A slight excess of data events is observed for high M_X, and medium values of η_{max}. But due to the large statistical uncertainties, none of these effects is statistically significant. N_{jet} displays a perfect description of the relative contributions of events with different jet numbers. This is a remarkable observation considering that the Monte Carlo events are calculated only in leading order QCD (cf section 1.4).

All plots display an enrichment of Pomeron exchange processes compared to the inclusive Monte Carlo sample. The diagrams of $\log_{10}(x_{I\!P})$, M_X, and η_{max} confirm the expectation that jet events are on average harder and more forward than inclusive ep-events.

Figure 4.16 presents the jet variables of the first jet in the singlejet event samples. The $p_\perp^{jet\ 1}$-distribution of the data is well described by the Monte Carlo sample. In contrast, the $\eta_{lab}^{jet\ 1}$-histograms display differences between data and Monte Carlo distributions. An excess of data events is observed around $\eta \sim 0$ and at very small values. The region of $\eta \sim 1$ exhibits a considerable lack of data events. Both effects result in a shift of the data distribution towards lower values of η, but data and Monte Carlo distributions are compatible within the (large) statistical uncertainties. A similar effect has been observed in diffractive rapidity gap analyses with large event numbers [43].

4.7.3 The Dijet Event Sample

The distributions of the dijet event sample have also been investigated. Due to the large fraction of dijet events within the singlejet sample (cf section 4.2.1), all distributions exhibit the same effects as described for the singlejet sample above. They are thus not displayed here. Only the jet variables of the first and the second jet in the dijet events are presented in figure 4.17.
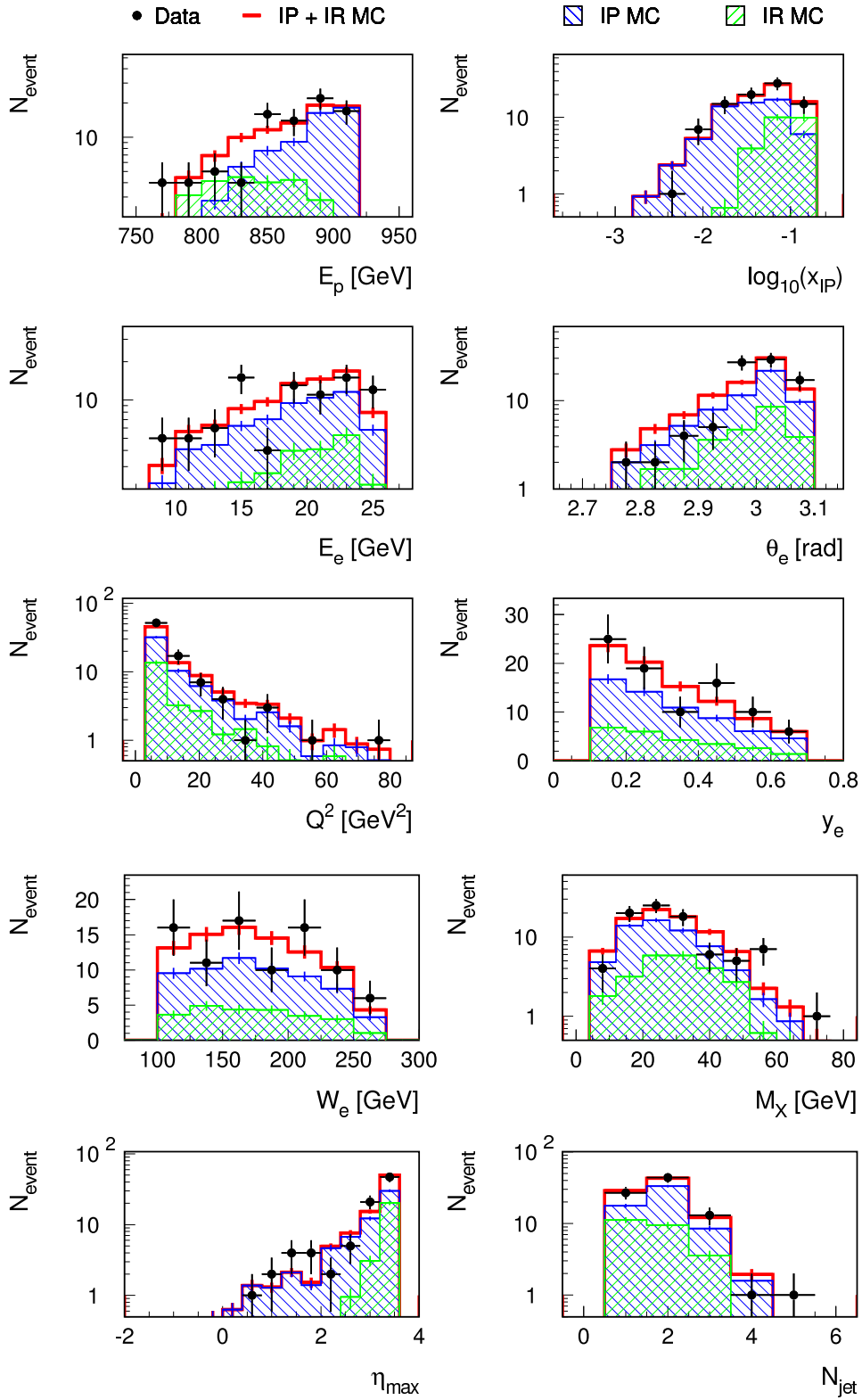
Figure 4.15: The description of the standard event variables in the DIS data by the Monte Carlo simulation. The histograms show the singlejet ($N_{jet} \geq 1$) event samples.
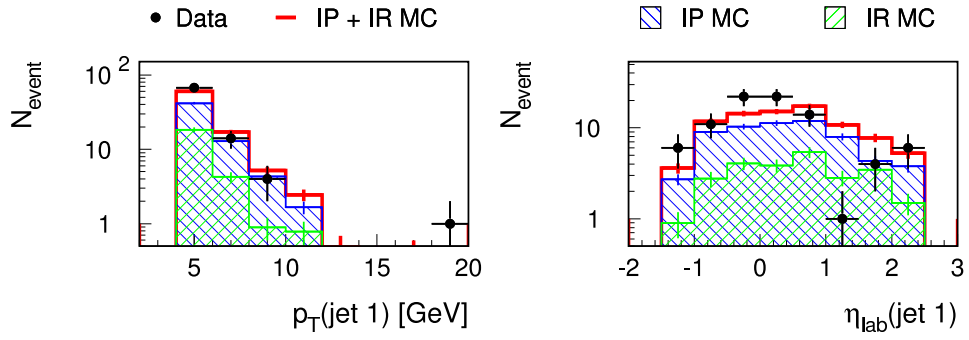
Figure 4.16: The jet variables of the first jet in the singlejet ($N_{jet} \geq 1$) DIS event samples.
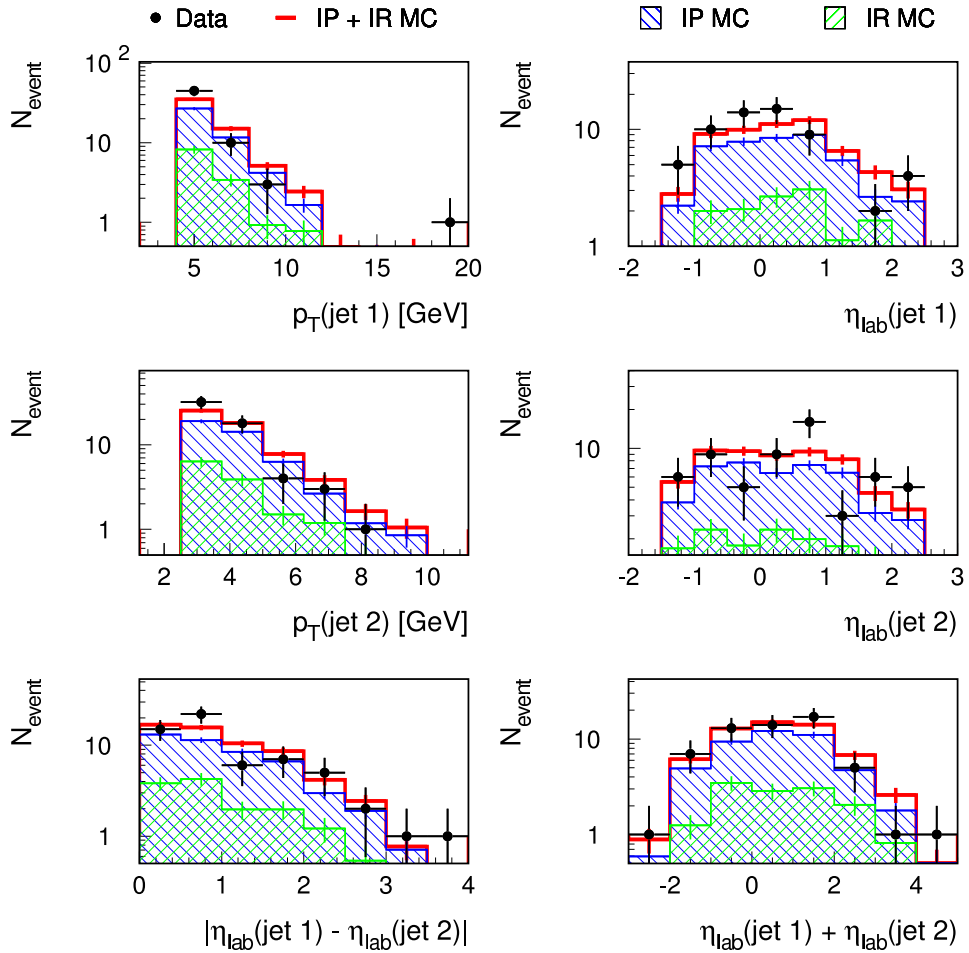
Figure 4.17: The jet variables of the first and the second jet in the dijet ($N_{jet} \geq 2$) DIS event samples.

Both $p_\perp$-distributions of the data are well described by the Monte Carlo simulation within the statistical uncertainties. The η-distribution of the first jet still exhibits an excess of data events in the backward region (ie at low values of η), and a strong lack around $\eta \sim 1.1$ (cf section 4.7.2). The resulting backward shift of the data compared to the Monte Carlo simulation is still visible, but no significant deviations are observed within the large statistical uncertainties. $\eta_{lab}^{jet\ 2}$ shows a better agreement between data and Monte Carlo simulation. More importantly, the kinematically crucial quantities, $|\eta_{lab}^{jet\ 1} - \eta_{lab}^{jet\ 2}|$, and $\eta_{lab}^{jet\ 1} + \eta_{lab}^{jet\ 2}$ agree well between the data and the Monte Carlo simulation. $|\eta_{lab}^{jet\ 1} - \eta_{lab}^{jet\ 2}|$ is related to the scattering angle of the hard partons in the parton-parton cms frame (cf section 1.2.7, [28]). The observed agreement thus shows that the hard scattering process is properly described in the Monte Carlo event sample.

4.8 Summary of the DIS Analysis

In this chapter, a sample of DIS events with a scattered leading proton has been selected. The DIS selection (section 4.1) is based on selection criteria well-established within the H1 collaboration [9]. After a basic FPS selection in chapter 3, further background rejection (eg against overlays of halo protons) has been performed (section 4.3.3). High-$p_\perp$ jets were defined in the hadronic final state (section 4.2.1). Due to the low event numbers (section 4.4), the inclusive event sample without any jets has also been considered. A cut on the hadronic final state mass has been applied to reject soft physics (section 4.2.2). Monte Carlo events were generated using a leading order resolved Pomeron model (RAPGAP 2.08/13 [17], section 4.3.1). The following data event samples have been investigated:

$$
\begin{array}{lllllll}
\text{a) Inclusive sample} & & & : & N_{event} & = & 806 \\
\text{b) Singlejet sample} & N_{jet} & \geq\ 1 & : & N_{event} & = & 86 \\
\text{c) Dijet sample} & N_{jet} & \geq\ 2 & : & N_{event} & = & 59
\end{array}
$$

A direct proof has been provided for the existence of Reggeon exchange processes in the inclusive and singlejet data samples. The relative contributions of Reggeon and Pomeron exchange processes have been investigated. They are well described by the prediction based on the inclusive measurement of the diffractive structure function, F_2^D (cf section 1.2.5). A correction factor, f_{corr}, has been estimated to calculate the ratio of Reggeon to Pomeron mediated interactions in the data from the one predicted by the Monte Carlo simulation:

$$
\begin{array}{llll}
f_{corr}^{inclusive} & = & 1.00 & \pm\ \ 0.10 \\
f_{corr}^{singlejet} & = & 1.00 & \pm\ \ 0.32,
\end{array}
$$

$$
\text{where} \qquad \left(\frac{f_{\mathbb{R}}}{f_{\mathbb{P}}} \right)_{data} = f_{corr} \left(\frac{f_{\mathbb{R}}}{f_{\mathbb{P}}} \right)_{MC}
$$

The prediction based on the F_2^D-analysis has thus been verified by a direct measurement with an accuracy of approximately 10 % for the inclusive event sample, and 32 % for the hard jet sample.

All considered event variables – except the η-distribution of the first jet – show good agreement between data and Monte Carlo distributions (cf section 4.7). The $\eta_{lab}^{jet\ 1}$-distribution exhibits a slight backward shift of the data with respect to the Monte Carlo simulation. But within the large statistical uncertainties, no significant deviations have been observed. Only slight differences were found. Some of these could be due to next-to-leading order effects.

In consequence, it is noted that the simple leading order Monte Carlo simulation, which is based on the resolved Pomeron model, and includes the parton density functions from the inclusive measurement of the diffractive structure function, F_2^D, describes the measured data rather well.

5 Investigations on Energy Flow Measurements with the Forward Detectors

The principal aim of this thesis are energy flow measurements with the main and the forward detectors. Forward detectors to be considered are the Plug calorimeter, the Forward Muon Detection System (FMD), and the Forward Tagging System (FTS) (cf section 2.2). The latter is available since 1999, and incorporates the Proton Remnant Tagger (PRT). A good measurement quality is crucial in order to obtain sensible energy flow data with these detectors. This especially includes the estimation of noise levels in these detectors, as well as an energy calibration of the Plug calorimeter. These topics are discussed in this chapter.

5.1 The Plug Calorimeter

In 1999 and 2000, the old copper-silicon sandwich Plug calorimeter (cf section 2.2.2, [46]) was used. It covers the spatial range $3.55 < \eta < 4.95$. Due to its coarse granularity and the relatively low number of calorimeter cells, the Plug energy cells are not combined into clusters. All energy deposits in the Plug calorimeter considered in this section are thus cell energies. The Plug calorimeter is positioned behind much dead material, which is partially poorly known (eg the forward tracking system, cf figure 2.4). The impact of the material on passing particle trajectories and shower evolution is not well known, and its simulation is complicated. In this section, the energy calibration of the Plug calorimeter is checked. The noise level in the Plug calorimeter is also investigated. Measures for noise reduction are devised.

5.1.1 Calibration of the Plug Calorimeter

According to the coarse granularity of the Plug calorimeter (cf figure 2.6), its calibration is performed in three bins of η ([47], [48], [49]). The η-ranges, and the calibration factors on cell level are given in table 5.1. A correction for the material in front of the Plug calorimeter, and a calibration of the

Table 5.1: The η-bins, and the correction factors, f, on cell level of the energy calibration of the Plug calorimeter ([47], [48]).

η-bin						f
Outer bin	3.55	<	η	<	3.95	1.3
Middle bin	3.95	<	η	<	4.45	1.0
Inner bin	4.45	<	η	<	4.95	1.5

measured energies are thus performed. In consequence, the Plug calorimeter is generally usable for energy flow measurements. Unfortunately, its resolution is rather poor:

$$\frac{\sigma_E}{E} \approx \frac{150 \ \%}{\sqrt{E \ [\text{GeV}]}} \qquad [7]$$

5.1.2 Noise Level in the Plug Calorimeter

The noise level in the Plug calorimeter is investigated using inclusive diffractive and non-diffractive deep-inelastic scattering events[1]. This is the only event sample in which fragmentation processes are sufficiently well modelled [9]. The Monte Carlo simulation contains no noise in the Plug calorimeter. Its level can thus be estimated by comparing the Plug energy deposits in the data and the simulated events.

The Data and the Monte Carlo Samples

DIS events recorded in 1999 and 2000 ($E_e = 27.5$ GeV, $E_p = 920$ GeV, $\sqrt{s} \approx 318$ GeV) are selected with similar selection criteria as for the DIS sample described in section 4.1. The analysis code is based on the one used by Matthias Mozer who investigates diffractive interactions in this very data sample [50]. Table 5.2 summarises the DIS selection cuts. Thanks to the much larger event numbers,

Table 5.2: The selection cuts for inlcusive diffractive and non-diffractive DIS events.

Description	Cut				
Electron reconstruction					
Distance (cluster - beam pipe)	10.0	<	d_{cl-bp}	<	67.0 cm
Energy in veto layer			E_{veto}	<	1.0 GeV
Cluster radius			r^e_{cl}	<	3.5 cm
Energy in hadronic SpaCal			E_{had}	<	0.5 GeV
Electron energy	8.0 GeV	<	$E_{e'}$		
Distance (track - cluster)			Δ_{BDC}	<	3.0 cm
Kinematic selection					
Four momentum transfer	4.0	<	Q^2_e	<	80.0 GeV^2
Inelasticity	0.1	<	y_e	<	0.7
Background rejection					
Energy and momentum	35.0	<	$\sum_f (E_f - p_{f_z})$	<	70.0 GeV

some selection cuts (r^e_{cl}, Δ_{BDC}, Q^2) are slightly harder than those of section 4.1. This suppresses non-DIS background still more effectively. Since the energy flow is not well described in the Monte Carlo simulation for low Bjørken-x [9], the following cut is performed:

$$x_e > 0.001 \equiv 10^{-3}$$

The selected event sample contains

$$N_{event} = 797$$

events. It corresponds to a luminosity of $\mathcal{L} = 1.1$ pb^{-1}.

The Monte Carlo sample used for this comparison was produced by Kamil Sedlak [51] with the RAPGAP generator, version 2.08/13 [17]. It is based on leading order QCD processes, and uses the proton structure function from [52] (MRS-G 2/95). The events were generated and simulated for the 1999 and 2000 e^+ data taking periods. Some generation parameters are specified in table 5.3, more detailed information may be found in [51]. Due to the small contribution of diffractive events to the

---

[1]In this section, *inclusive* refers to diffractive and non-diffractive events. It is connected to the diffractive event sample without any jet requirements on the hadronic final state in all other sections of this thesis.

Table 5.3: The kinematic range of the generated DIS Monte Carlo sample.

Description	Range			
Four momentum transfer	1.4 GeV	$<$	Q^2	
Hard interaction scale			$\hat{p}_\perp$	$>$ 3.0 GeV

energy flow in the forward region compared to the non-diffractive contribution [9], only non-diffractive interaction processes were considered. Separate samples were generated and simulated for direct and resolved photon interactions (cf section 1.2.2). Their luminosities and generated event numbers are given in table 5.4. All events are weighted with the inverse of the corresponding luminosities to get

Table 5.4: The generated and simulated DIS Monte Carlo samples.

Process	$\mathcal{L}$ [pb^{-1}]	Generated Events
Direct γ	13.97	39,988
Resolved γ	12.46	28,579

the correct contributions from each subprocess while still keeping all events (cf section 4.3.1).

Estimation of the Noise Level in the Plug Calorimeter

The noise level in the Plug calorimeter is investigated separately for the three calibration ranges (cf section 5.1.1). Figure 5.1 shows the cell energy per event as a function of η. It displays the data and the complete Monte Carlo sample. The first plot (top left) covers the most forward part of the LAr calorimeter and the outer calibration bin of the Plug calorimeter. All LAr energies presented are cluster energies ($\eta < 3.55$), only the Plug energies ($\eta > 3.55$) are displayed on cell level. The following plots show the energies in the three different Plug calibration bins. They exhibit a general excess of Plug energy in the data compared to the simulated events. This excess is especially large in the outer η-bin ($3.55 < \eta < 3.95$). On contrary, the energy deposits in the LAr calorimeter are well described by the Monte Carlo simulation. Hence, the huge energy excess in the first η-bin is not caused by shower leakage from the LAr calorimeter. A far better description of the data is observed in the middle and the outer η-bins (bottom). This can be understood from the geometry of the H1 detector (figure 2.3). The larger the η-values, the closer the considered region is to the beam pipe (cf table 5.1, figure 2.6). And the closer a region is to the beam pipe, the less it is covered by inactive material when viewed from the interaction point (cf figure 2.3). The middle and the inner η-bins are thus covered by less material than the outer bin. Since the effects of the inactive material on passing particles are not precisely known, and difficult to simulate, the noise level and the discrepancies between data and Monte Carlo simulation are expected to increase with the amount of covering material. The structure within the η-distributions of the energy deposits results from the the coarse granularity and the design of the Plug calorimeter - ie the assembly of its detection planes and panels (cf figure 2.6).

The number of cells per event is shown as a function of the cell energy in figure 5.2. All three plots display a huge excess of cells with low energies ($E_{cell} < 5$ GeV) in the data compared to the Monte Carlo simulation. This is due to low-energy noise which is not simulated in the Monte Carlo events. The highest noise level is observed in the outer calibration bin ($3.55 < \eta < 3.95$). Cell numbers at higher energies are well described by the Monte Carlo simulation for the middle and inner
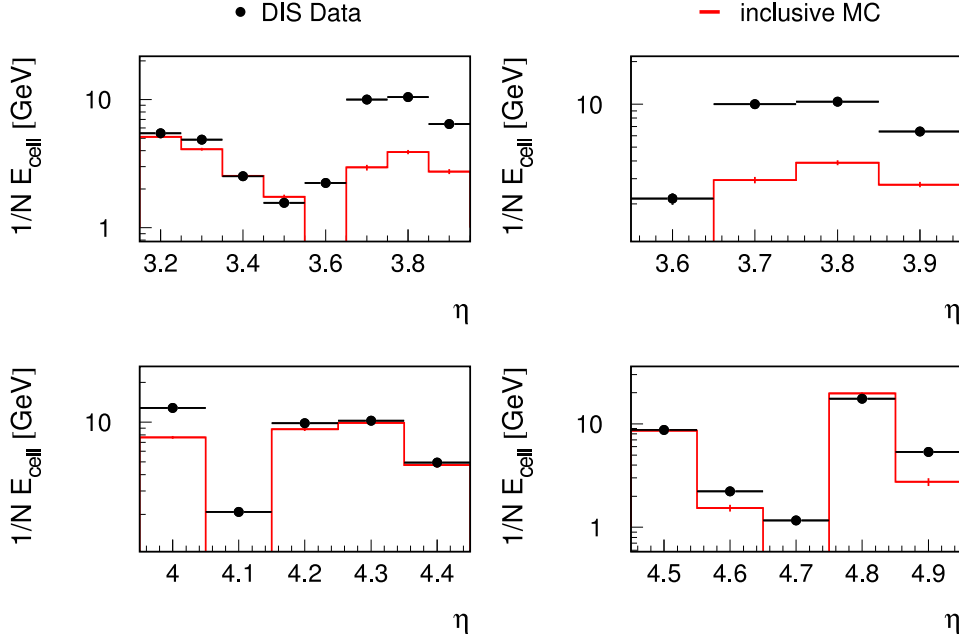
Figure 5.1: The cell energies in the Plug, and the cluster energies in the LAr calorimeter. Top left: Combination of LAr cluster energies ($\eta < 3.55$), and Plug cell energies ($\eta > 3.55$). The three other plots show the Plug cell energies in the three calibration bins (cf section 5.1.1). All plots display the inclusive (diffractive and non-diffractive) event sample (cf table 5.2).

bin, whereas the outer bin also exhibits more high-energy cells in the data than in the Monte Carlo simulation. The reason of this effect is not known.

Figure 5.3 presents the fraction of events with a certain total energy in each of the three η-bins as a function of this total energy. The Monte Carlo sample shows much more events with no or almost no energy deposit in the Plug calorimeter than the data. The latter, however, contains more events with low Plug energies ($E_{\Sigma(bin)} < 20$ GeV). This is due to noise in the data which is not simulated in the Monte Carlo events. Concerned data events contain mostly low-energy noise cells, and no energy deposit resulting from the ep-interaction. The sum of these noise cells is measured in the data. The largest discrepancies are found in the outer calibration bin ($3.55 < \eta < 3.95$). A lack of data events is observed at high energies in the middle bin, but statistical uncertainties are rather large. In conclusion, the description of the data by the Monte Carlo simulation is best for the inner η-bin. This is consistent with the interpretation of noise and unknown effects on shower evolution being caused by the material in front of the Plug calorimeter (cf above).

Noise Reduction in the Plug Calorimeter

Two possibilities exist to reduce noise effects in the Plug calorimeter:

1. Reject all low-energy Plug cells. Only consider cells with $E_{cell} > E_{min}$.

2. Reject all events with low total energies in the different calibration bins. Only consider events with $E_{\Sigma(bin\ i)}(i = 1, 2, 3) > E_{\Sigma(bin)}^{min}$.

The first measure does not only reject low-energy noise cells, it also removes low-energy deposits resulting from the ep-interaction. It introduces a bias into the energy deposit of events with low-energy cells, and distorts their total energy flow distributions. A cut on the cell energy is thus

Figure 5.2: The cell energies in the three calibration bins of the Plug Calorimeter (cf section 5.1.1). They are shown for the inclusive (diffractive and non-diffractive) event samples (cf table 5.2).

not applied. The second possibility strongly reduces the available event numbers, but it does not distort the energy spectra of the investigated events. Only events in which the noise level is negligible compared to the total energy deposit are considered for the energy flow in the Plug calorimeter. In consequence, a cut on the total energy in each η-bin is performed:

$$E_{\Sigma(bin\ i)}(i = 1, 2, 3) > 20 \text{ GeV}$$

It is indicated in figure 5.3 by vertical lines.

The above considerations suggest that the Plug calorimeter is only usable as a rough indication of the forward energy flow in the region of $3.55 < \eta < 4.95$. Due to its coarse granularity, its low energy resolution (cf section 5.1.1, [46]), and the complicated effects of the material in front of the Plug calorimeter, it is not suited for a high-precision measurement. Its behaviour is not well simulated in Monte Carlo events. All energy flow considerations based on the Plug calorimeter are therefore rather qualitative than quantitative.

5.2 The Forward Muon Detection System

The Forward Muon Detector (FMD) directly covers the pseudorapidity range $1.4 < \eta < 2.9$ (cf section 2.2.2, [11]), but due to secondary scattering with the beam pipe, beam collimators, and shielding, it is sensitive to particle production at larger values of η ($1.9 < \eta < 3.7$, [9]). The detection system consists of six double layers of drift chambers, three in front of, and three behind the toroid magnet when viewed from the interaction point (cf section 2.2.2). Since the post-toroid layers suffer from high background rates due to synchrotron radiation [9], only the three pre-toroid layers are used

Figure 5.3: The total η-bin energies in the three calibration bins of the Plug Calorimeter (cf section 5.1.1). They are shown for the inclusive (diffractive and non-diffractive) event samples (cf table 5.2). The applied cuts are marked by the vertical lines.

within this analysis. The energy flow measurements with these FMD layers are per se limited. They only allow to count the hits of passing particles. No calibrated energy measurements are possible. In this section, the electronic noise rate is estimated for the used FMD layers. As no noise is simulated in the Monte Carlo events, it has to be added to the Monte Carlo events when comparing them to the data [9].

Noise in the Forward Muon Detector

The noise level in the Forward Muon Detector is estimated using random trigger events. In random trigger runs, the response of the H1 detector is recorded at random. Most of the resulting events do not contain an ep-interaction. They provide a measure for the noise level in the different detector parts. Random trigger data from 1999 and 2000 is used to get an accurate estimate of the detector conditions.

Figure 5.4 shows the total number of hit pairs per random trigger event in the first two (left) and the third (right) double layers of the FMD. This combination is presented, since it is considered for the rapidity gap selection of diffractive events (cf section 7.1, [53]). Randomly triggered ep-interactions are vetoed by applying a cut against reconstructed event vertices. The registered hits are due to
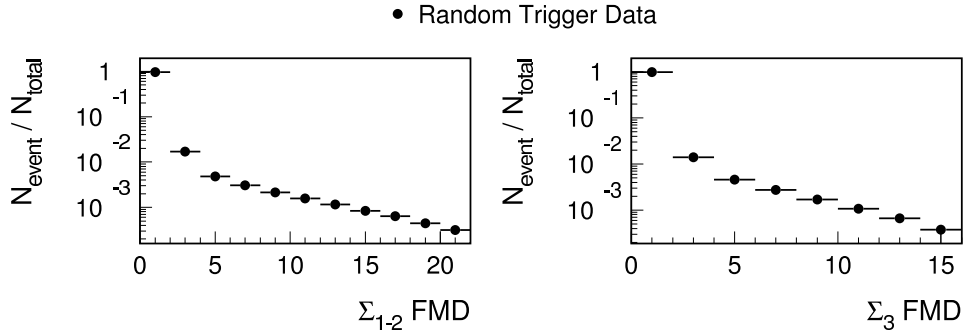
Figure 5.4: The number of FMD hit pairs per event in the 1999 and 2000 random trigger files. *ep*-interactions are vetoed by an anti-vertex cut.

detector noise. They are added to the Monte Carlo events when comparing them to the data. Each of the two combinations of FMD layers displays a total noise level of about 2 %.

5.3 The Forward Tagging System

The Forward Tagging System (FTS) is an upgrade of the Proton Remnant Tagger (PRT), and was installed in 1999. It consists of five planes of scintillation counters at 9 m, 16 m, 24 m, 53 m, and 92 m from the interaction point (cf section 2.2.2, figure 2.7). They cover the rapidity range $4.5 < \eta < 8.0$ [54]. Due to problems with the Monte Carlo simulation of the detectors at 24 m, 53 m, and 92 m [55], only the first two counters at 9 m and 16 m ($4.5 < \eta < 6.2$, [54]) are used for this analysis. As for the FMD, no calibrated energy measurements are possible. Solely the number of hits in each of the scintillation planes is accessible.

Noise in the Forward Tagging System

Noise in the FTS stations at 9 m and 16 m is estimated in the same way as for the Forward Muon System (cf section 5.2). The total number of hits per random trigger event is displayed in figure 5.5 for the two detection planes used. *ep*-interactions are vetoed by an anti-vertex cut. Each of the two
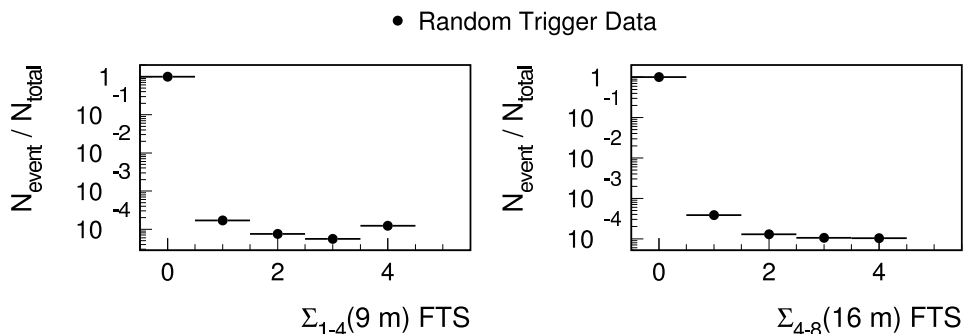
Figure 5.5: The FTS hit numbers per event in the 1999 and 2000 random trigger files. An anti-vertex cut is applied to veto *ep*-intercations.

FTS stations exhibits a total noise level below 10^{-3} hits per event. This is completely negligible within the statistical uncertainties of this thesis (cf section 4.4). Noise hits in the FTS are therefore not considered any further within the following analysis.

6 Energy Flow in Deep-Inelastic Scattering

In this chapter, the energy flow in the main and forward detectors is presented for the selected DIS event samples. The forward energy flow in Monte Carlo simulated diffractive events which are based on the resolved Pomeron model is mainly described by the Pomeron and Reggeon remnant jets. The present measurement therefore allows to check the validity of this Monte Carlo description. An FPS selected leading proton event sample is the only way to perform this investigation, since the rapidity gap selection rejects all events with significant forward energy flow. The energy flow in the forward detectors is measured using the Plug calorimeter, the Forward Muon Detector, and the Forward Tagging System (cf section 2.2.2). Noise and calibration of these detectors were discussed in chapter 5.

Energy Flow Measurements in the Main Detector

Energy flow in the main detector can be measured using calorimetric and tracking methods. The tracking system mainly consists of the Central Jet Chambers (CJC 1/2), and the Forward Tracking Detector (FTD) (cf section 2.2.1). Due to much inactive material in front of the FTD, it exhibits high background rates, and its response is not well understood [9]. The FTD is thus not used within this analysis. CJC 1 and CJC 2 were affected by large and varying broken detector parts in 1999 and 2000 [33]. Some segments were dead in both, CJC 1 and CJC 2, resulting in complete inactive detector regions. Unphysical structures caused by these varying detector conditions were observed in energy flow distributions which included tracking information. Only calorimetric energy flow is therefore considered in this thesis. Since the instrumented iron (cf figure 2.3) is not relevant at the investigated energies, it is not included in the measurement to remove any unnecessary uncertainties. Because of its high noise rates and special noise reduction cuts (cf section 5.1.2), the Plug energy flow measurements are displayed in separate plots. The energy flow in the main detector is thus measured using the LAr and the SpaCal calorimeter clusters (cf section 2.2.1). Noise levels in these detectors are well known, and included into the Monte Carlo simulation [9].

Reference Systems and Jet Profiles

All calorimetric energy flow histograms – except the jet profiles – are displayed as functions of η_{lab} in the laboratory system. The jet profiles are shown in the $\gamma^* p$ centre-of-mass system. They are presented as functions of the distances in η^* and ϕ^* from the leading jet:

$$
\begin{aligned}
\Delta\eta^* &= \eta^*_{cluster} - \eta^*_{jet\ 1} \\
\Delta\phi^* &= \phi^*_{cluster} - \phi^*_{jet\ 1}
\end{aligned}
$$

Only clusters in the neighbourhood of the considered jet are included into the measurement, ie

$$
\begin{aligned}
|\Delta\phi^*| &< 1 \quad \text{for energy flow in } \Delta\eta^* \\
|\Delta\eta^*| &< 1 \quad \text{for energy flow in } \Delta\phi^*
\end{aligned}
$$

This excludes the energy flow resulting from the non-leading jets.

The absolute energy flow in the main detector (LAr and SpaCal) is presented for the total (E), and the transverse energy ($E_\perp = E \sin\theta$). Jet profiles only show the transverse energy flow, while Plug histograms display the total energy. All energy flow plots are normalised by the number of events displayed.

Energy Flow Measurements in the Forward Detectors

Energy flow in the forward detectors (FMD and FTS) is presented as the number of hits per event in the considered subdetectors – ie the sum of the first and the second layer, and separately the third layer for the FMD, and the two stations at 9 m and 16 m for the FTS. Noise is included into the Monte Carlo simulation as described in the previous chapter (cf sections 5.2, 5.3).

6.1 The Inclusive DIS Sample

Figures 6.1 and 6.2 show the complete set of energy flow plots for the inclusive event sample (ie without any jet requirements). All of them display a good agreement between data and simulated
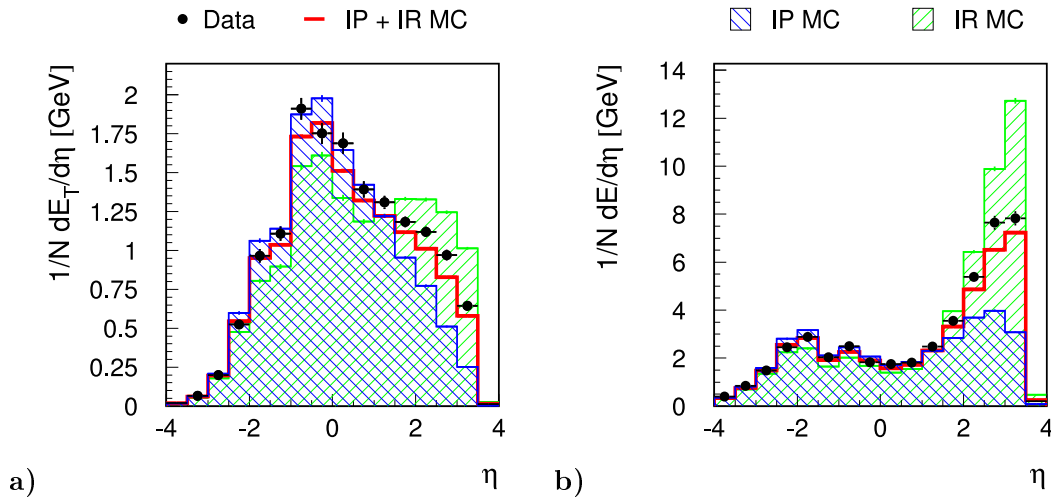
Figure 6.1: The central energy flow in the inclusive DIS data and Monte Carlo events. **a)** Transverse, and **b)** total energy flow in the main detector (LAr and SpaCal).

Monte Carlo distributions. The transverse (figure 6.1a), and the total (figure 6.1b) energy flow in the main detector (LAr and SpaCAl) are described reasonably well by the simulated events. The data show a slight excess of transverse energy in the forward half of the detector, $\eta > -1$, and of total energy at large values of η. A similar effect has been observed previously in non-diffractive deep-inelastic scattering if compared to events which were produced by the same leading order Monte Carlo generator (RAPGAP) [56]. RAPGAP generally underestimates the forward energy flow, while other Monte Carlo generators, eg DJANGO [57], provide a good description of the data [56]. The effect is thus a specific feature of RAPGAP generated Monte Carlo samples which is probably not connected to diffractive physics, and its origin is believed to be an effect of higher order QCD corrections. The shapes of both, transverse and total energy flow distributions are reproduced by the Monte Carlo simulation. The hit pairs in the Forward Muon Detector (figure 6.2a) – mainly due to the Pomeron spectator – display a very good description of the data by the Monte Carlo distribution. Any events with extremely high hit numbers could be remaining background events, eg from overlays of halo protons (cf section 4.3.3).
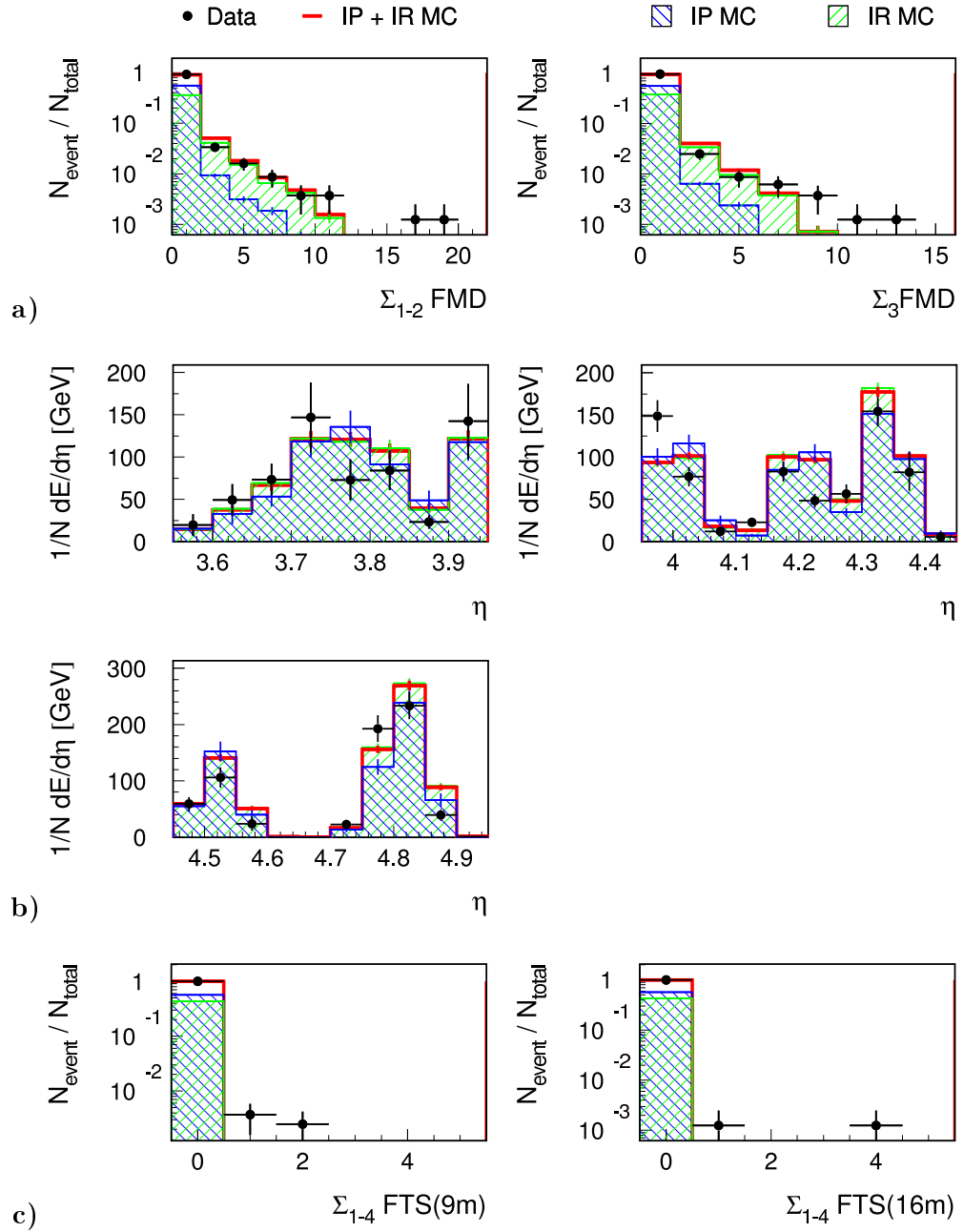
Figure 6.2: The forward energy flow in the inclusive DIS data and Monte Carlo events. **a)** Number of hit pairs per event in the FMD. **b)** Total energy flow in the three Plug calibration bins after the noise reduction cuts (cf section 5.1). **c)** Number of hits per event in the FTS.

All four histograms prove that both, Pomeron (dark hatched) and Reggeon (light hatched) exchange processes are needed to describe the data, and that their relative contributions are described well by the Monte Carlo simulation (cf section 4.6). They show that Reggeon exchange events are generally more forward, and more energetic than Pomeron exchange reactions.

The histograms of the energy flow in the Plug calorimeter (figure 6.2b) display a reasonable agreement between data and Monte Carlo simulation. Due to the rejection of events with Plug energies below $E_{\Sigma(bin)} < 20$ GeV in the considered calibration bin (cf section 5.1.2), event numbers are strongly reduced, leading to large statistical uncertainties. They are especially large for the outer η-bin (top left) which exhibits the highest background rates (cf figure 5.1). Precision measurements are not possible because of those uncertainties. Within their limits, no significant discrepancies between data and Monte Carlo distributions are observed.

Since only events with high forward energies are accepted in the Plug calorimeter, Pomeron and Reggeon energy flow distributions exhibit only minor differences. But considering the statistical uncertainties, and the fact that the distributions of the total Monte Carlo sample are almost indistinguishable from those of the Reggeon sample, it can be deduced that most events with high energy deposits in the Plug calorimeter are mediated by Reggeon exchange.

The number of hits in the FTS stations at 9 m and 16 m (figure 6.2c) allows no conclusion on the description of the data energy flow by the Monte Carlo simulation. No Monte Carlo event, and only very few data events, $\frac{N_{event}}{N_{total}} < 0.01 \,\hat{=}\, 1$ %, display any hits. The data events could be non-diffractive background, eg from overlays of halo protons (cf section 4.3.3). Due to this lack of information, the energy flow in the FTS is not considered any further in this chapter.

6.2 The Singlejet DIS Sample

The complete set of energy flow plots for the singlejet ($N_{jet} \geq 1$) event sample is shown in figures 6.3 and 6.4. They display a similar behaviour as for the inclusive event sample, and exhibit much
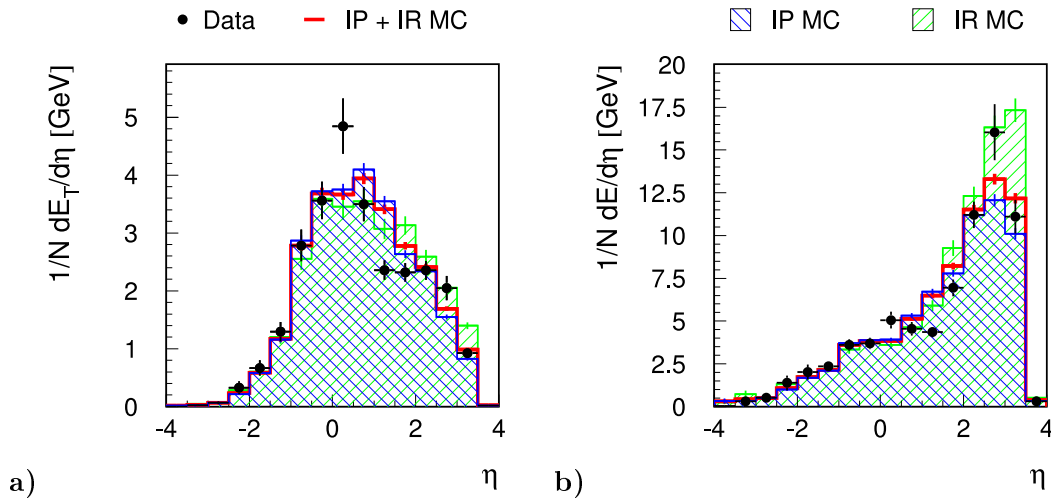
Figure 6.3: The central energy flow in the singlejet ($N_{jet} \geq 1$) DIS data and Monte Carlo events. **a)** Transverse, and **b)** total energy flow in the main detector (LAr and SpaCal).

increased statistical uncertainties. An excess of data energy flow is observed around $\eta \sim 0$ (transverse energy, figure 6.3a), and in the very forward region (total energy, figure 6.3b). This supports the evidence that the forward energy flow is generally too small in RAPGAP generated Monte Carlo events (cf section 6.1, [56]).
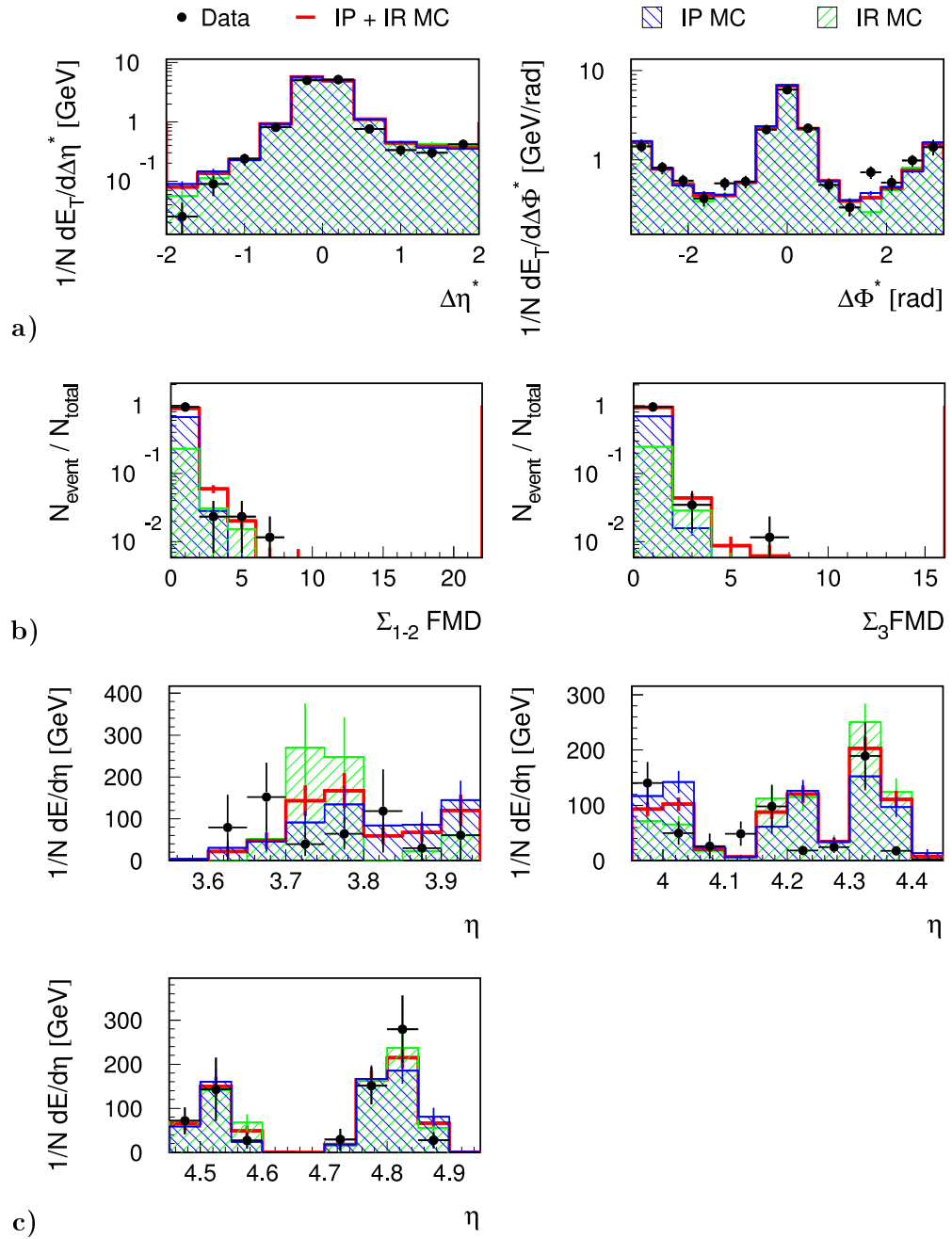
Figure 6.4: The forward energy flow in the singlejet ($N_{jet} \geq 1$) DIS data and Monte Carlo events. **a)** Transverse energy flow relative to the leading jet (jet profile). **b)** Number of hit pairs per event in the FMD. **c)** Total energy flow in the three Plug calibration bins after the noise reduction cuts (cf section 5.1).

Both jet profiles, in $\Delta\eta^*$ and $\Delta\phi^*$ (figure 6.4a), are described well by the Monte Carlo simulation. A slight lack of energy flow behind the jet is observed in the data. Any differences in the jet profile with respect to $\Delta\phi^*$ might be due to the FPS selection which introduces a bias in any aziumthal angle distribution by its $p_\perp$-acceptance range. Since these acceptance distributions differ between data and Monte Carlo simulation (cf section 4.5.2, figure 4.9), different biases are introduced into the jet profile. The FMD hit numbers in data and Monte Carlo events (figure 6.4b) show almost perfect agreement.

The absolute energy flow plots (figure 6.3), and the FMD diagrams (figure 6.4b) exhibit a strong enrichment of Pomeron exchange events in the singlejet sample compared to the inclusive event sample (cf tables 4.7, 4.8). Reggeon events are more forward than Pomeron events, but no difference is observed between the jet profiles of the two contributions. Any differences in the energy flow of Pomeron and Reggeon exchange events hence results from subleading jets, or the Pomeron/Reggeon and photon remnants which are not included in the high-$p_\perp$ jets.

All plots of energy flow in the Plug calorimeter (figure 6.4c) show much increased statistical uncertainties. Within these statistical uncertainties, all diagrams display a reasonable agreement between data and Monte Carlo distributions. The best description of the data is observed for the inner calibration bin (bottom). This is expected from the consideration of noise in the Plug calorimeter (cf section 5.1.2).

6.3 The Dijet DIS Sample

Figures 6.5 and 6.6 show the complete set of energy flow plots for the dijet ($N_{jet} \geq 2$) event sample. Due to the high fraction of dijet events in the singlejet sample (cf section 4.2.1), few differences are
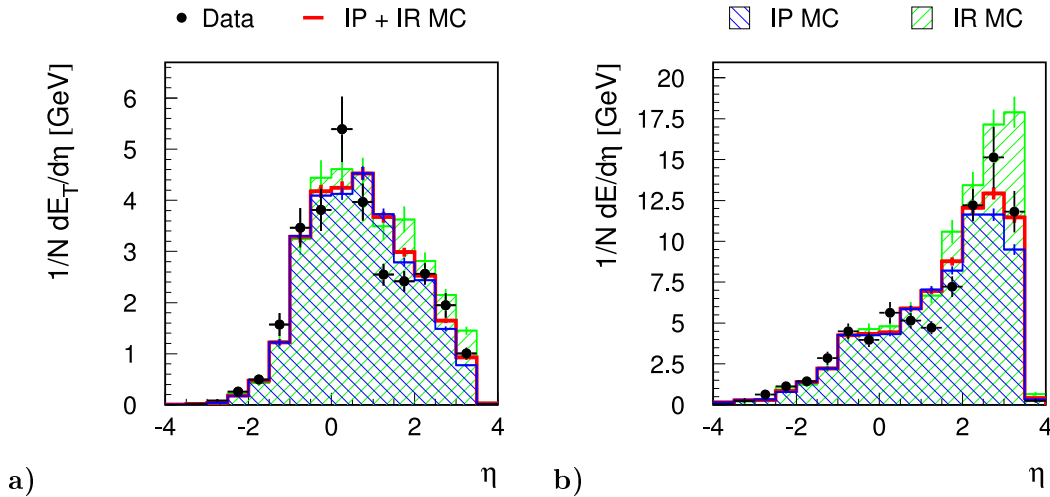
Figure 6.5: The central energy flow in the dijet ($N_{jet} \geq 2$) DIS data and Monte Carlo events. **a)** Transverse, and **b)** total energy flow in the main detector (LAr and SpaCal).

observed between the dijet and singlejet energy flow distributions. Almost no events with FMD hits (figure 6.6b) are left in the event sample. All other plots show no significant changes compared to the singlejet event sample.
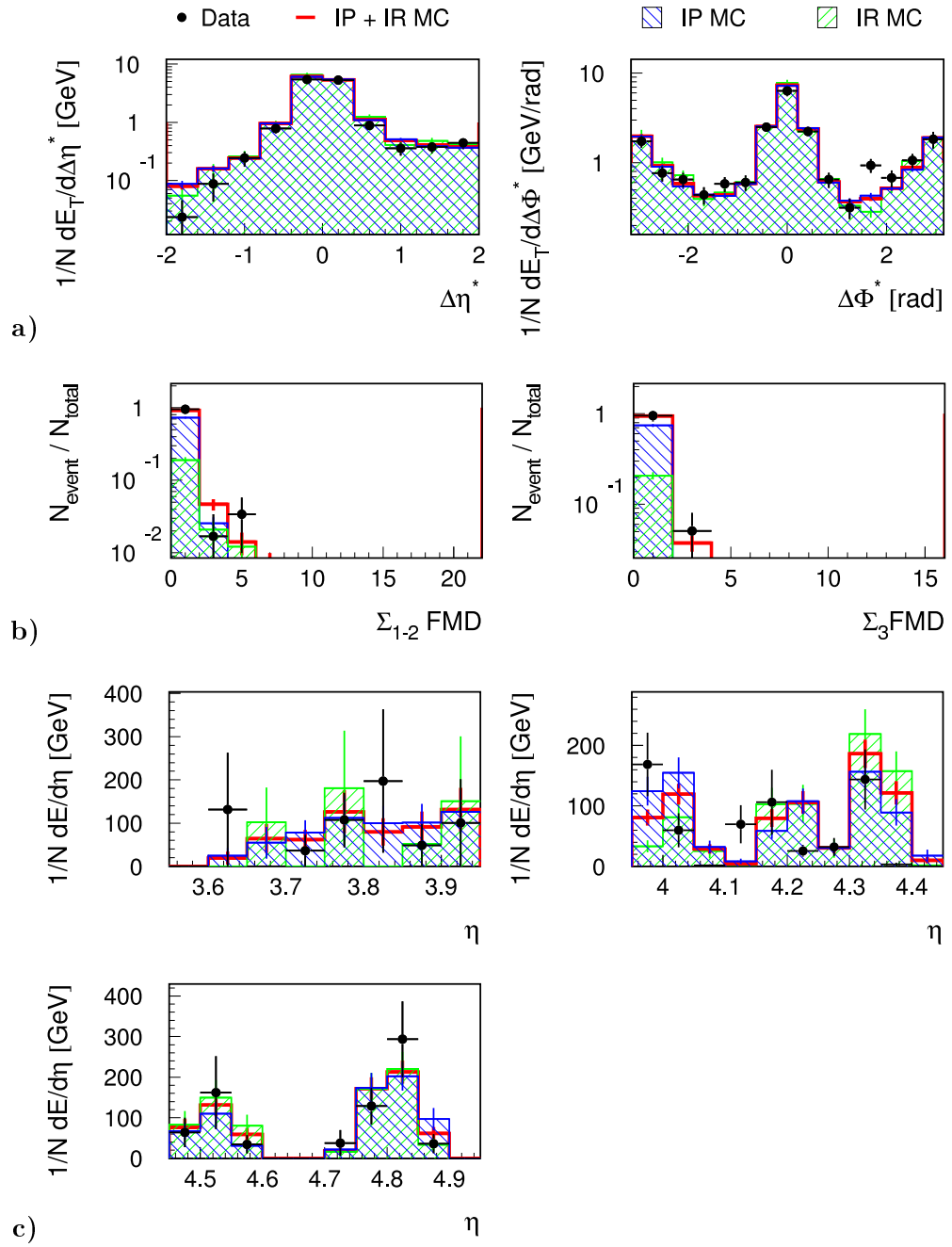
Figure 6.6: The forward energy flow in the dijet ($N_{jet} \geq 2$) DIS data and Monte Carlo events. **a)** Transverse energy flow relative to the leading jet (jet profile). **b)** Number of hit pairs per event in the FMD. **c)** Total energy flow in the three Plug calibration bins after the noise reduction cuts (cf section 5.1).

6.4 Summary of the Energy Flow in DIS Events with a Leading Proton

The energy flow in deep-inelastic scattering events with a leading proton is well described by the Monte Carlo simulation. A slight excess of energy flow in the data is observed in the forward region of the main detector. This effect is most prominent in the inclusive event sample, and has also been observed in non-diffractive deep-inelastic scattering. It is thus a general property of RAPGAP generated event samples, which is probably not connected to the description of diffractive physics within the resolved Pomeron model. Due to the much increased statistical fluctuations and uncertainties, the excess is less significant for the jet samples. All other distributions agree well between data and Monte Carlo simulation. They all prove the need for both, Pomeron and Reggeon exchange processes, and they show that the relative contributions are well modelled by the Monte Carlo simulation.

In the resolved Pomeron model, the energy flow and the hits in the forward detectors are mainly due to the Pomeron and Reggeon remnants. The investigation of the (forward) energy flow distributions hence shows that the concept of the Pomeron and Reggeon remnants describes the data well. This provides further support for the resolved Pomeron model – in contrast to other models, eg the soft colour interaction model, which do not predict the existence of such remnants (cf section 1.2.3).

7 Effects of the Rapidity Gap Selection of Diffractive Events

This chapter investigates the effects of the standard rapidity gap selection of diffractive events [9] on the description of the DIS data samples. The rapidity gap selection reduces the efficiency for diffractive events, which has to be corrected for in a measurement of diffractive cross sections. A FPS selected leading proton event sample is the only way to verify the validity of the gap corrections predicted by the Monte Carlo simulation. The rapidity gap selection is explained, and the description of the efficiency of the selection cuts, and of the standard event variables is examined. Energy flow measurements are presented.

7.1 Rapidity Gap Selection of Diffractive Events

In the standard diffractive selection at the H1 detector, diffractive events are selected by requiring a large rapidity gap between the outgoing proton and the hadronic final state (HFS) in the main detector (cf figure 1.7). In this section, a brief review of this selection method is presented. A more detailed description may be found in [9].

Events with a large rapidity gap are selected using the forward detectors FMD and FTS, and the most forward part of the LAr calorimeter.

7.1.1 Energy Flow in the Forward LAr Calorimeter

Due to the rapidity gap, no energy flow should be present in the forward part of the LAr calorimeter. This is accounted for by applying a cut to the pseudorapidity of the most forward LAr cluster with $E_{cluster} > 400$ MeV, η_{max} (cf section 4.7.1):

$$\eta_{max} < 3.2$$

The energy threshold is introduced to reduce the sensitivity to low-energy noise in the calorimeter. This noise is monitored regularly, and incorporated into the Monte Carlo simulation [9].

7.1.2 Activity in the Forward Muon Detector

Only the three pre-toroid layers of the Forward Muon Detector are considered due to high noise levels in the other layers (cf sections 2.2.2, 5.2). To reject events with particle production in the detector region covered by the FMD, a cut is applied to the numbers of reconstructed hit pairs in the pre-toroid FMD layers. Since the random noise level in the third FMD layer is higher than the one in the first two layers, the sum of the hit pairs in the first two layers, $N_{FMD(1,2)}$, and the number of hit pairs in the third layer, $N_{FMD(3)}$, are considered separately ([58], [59]). The noise level is determined from random trigger files, and added to the Monte Carlo simulation before applying the selection criteria (cf section 5.2). Because of this random noise, the hit numbers are not required to be exactly zero. Otherwise, too many diffractive events would be rejected:

$$
\begin{aligned}
N_{FMD(1,2)} &\leq 1 \\
N_{FMD(3)} &\leq 1
\end{aligned}
$$

7.1.3 Activity in the Forward Tagging System

Since the beginning of the 1999 data taking period, the Proton Remnant Tagger has been extended to the Forward Tagging System (FTS) (cf sections 2.2.2, 5.3, [58]). The FTS is now used for the rapidity gap selection instead of the old PRT [58]. Only the FTS stations at 9 m and 16 m are considered in this analysis due to problems with the Monte Carlo simulation of all other FTS detectors (cf section 5.3, [55]). The noise level in these two stations is estimated from random trigger files. It is found to be negligible (cf section 5.3). Thus, events with a large rapidity gap are selected by requiring no hits in the two FTS stations:

$$N_{FTS(9,16)} = 0$$

7.1.4 The Fractional Longitudinal Momentum Transfer $x_{I\!\!P}$

Diffractive events with a scattered leading proton can be observed in the range $x_{I\!\!P} < 0.2$ (cf section 3.2.2). In order to select events in the region of $x_{I\!\!P}$ in which the cross section is dominated by Pomeron exchange, and the contribution from Reggeon exchange is small (cf figure 4.14), an additional cut is applied in standard diffractive analyses at H1 [9]:

$$x_{I\!\!P} < 0.05$$

Since this cut is not related to the rapidity gap selection, but enhances Pomeron exchange processes, it is not applied in the rapidity gap analysis discussed within this thesis.

7.1.5 Summary of the Rapidity Gap Selection

The rapidity gap selection cuts are summarised in table 7.1. They are illustrated in figure 7.1 which

Table 7.1: The selection cuts for the standard H1 rapidity gap selection of diffractive events [9].

Description	Cut		
Energy flow in forward LAr	η_{max}	$<$	3.2
Activity in FMD(1,2)	$N_{FMD(1,2)}$	$\leq$	1
Activity in FMD(3)	$N_{FMD(3)}$	$\leq$	1
Activity in FTS(9,16)	$N_{FTS(9,16)}$	$=$	0

shows the relevant quantities for the inclusive event samples. In these, and in all following plots after the rapidity gap selection, the complete Monte Carlo sample is no longer normalised to the area of the data distribution in each diagram. The Monte Carlo distributions are normalised with the universal normalisation factor as it has been determined for the FPS event samples without rapidity gap selection (cf section 4.4). This allows the investigation of the effects of the rapidity gap selection, and of the losses of diffractive events separately for the data and the Monte Carlo distributions. Each variable in figure 7.1 is displayed after the cut on the previously presented variable. The full FPS and DIS selections (cf tables 4.5, 4.6) have been applied to all distributions. In this way, the effect of each cut can be investigated.
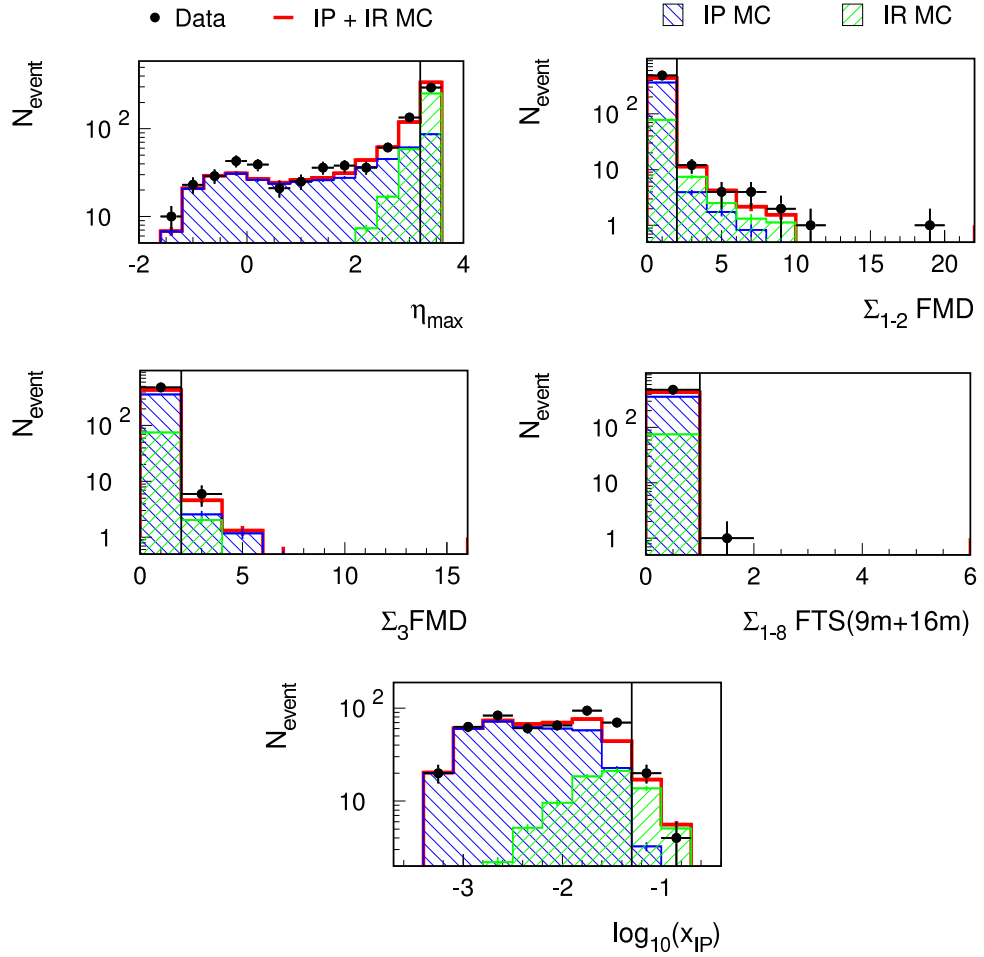
Figure 7.1: The description of the rapidity gap selection variables in the data by the Monte Carlo simulation. Each variable is displayed after the cut on the previously presented quantity. The full FPS and DIS selections (cf tables 4.5, 4.6) have been applied to all displayed event samples. All Monte Carlo distributions have been normalised using the Monte Carlo normalisation factor of the FPS selected event samples without rapidity gap cuts (cf section 4.4). The rapidity gap cuts, and the cut on $x_{I\!P}$, which is not applied within this thesis, are indicated by the vertical lines.

The η_{max}-distribution displays a slight excess of Monte Carlo simulated events in the very forward region (large η, cf section 4.7). This leads to a slight overestimation of the number of rejected events in the Monte Carlo simulation (cf table 7.2), which persists through the further rapidity gap selection cuts. It is particularly obvious in the distribution of $\log_{10}(x_{I\!P})$, and will be further discussed in the following sections. Apart from this difference, all distributions are described well by the Monte Carlo simulation (cf section 4.7). The suppression of Reggeon exchange events by the rapidity gap selection – especially by the cut on η_{max} (cf section 4.7.1) – is visible. Three rapidity gap selected event samples are investigated in the following sections:

a) Inclusive sample $\qquad\qquad\qquad$: $\; N_{event} \;=\; 480 \;$: $\; \frac{\Delta N}{N} \;\sim\; 4.6\,\%$

b) Singlejet sample $\; N_{jet} \;\geq\; 1 \;$: $\; N_{event} \;=\; 37 \;$: $\; \frac{\Delta N}{N} \;\sim\; 16.4\,\%$

c) Dijet sample $\qquad N_{jet} \;\geq\; 2 \;$: $\; N_{event} \;=\; 27 \;$: $\; \frac{\Delta N}{N} \;\sim\; 19.2\,\%$

Unless stated otherwise, all following plots in this chapter show the data and the Monte Carlo event samples after the full FPS and DIS selection (cf section 4.4), including the rapidity gap selection cuts. All Monte Carlo event samples with identical jet requirements are normalised using the universal normalisation factor determined from the complete data and Monte Carlo event samples without gap cuts (cf sections 4.4). Applied jet cuts are specified for each plot individually.

7.2 Description of the Efficiency of the Rapidity Gap Cuts

This section examines the description of the efficiency of the rapidity gap selection. It is needed in diffractive cross section measurements, based on rapidity gap selected event samples, to correct for the diffractive event losses due to the selection cuts. A FPS based event sample is the only way to verify the prediction by the diffractive Monte Carlo simulation, which is used as correction factor in the rapidity gap analyses ([9], [11]).

For the FPS selected DIS event samples – ie without rapidity gap cuts, a reasonable agreement between data and Monte Carlo simulation has been observed for all event variables (cf section 4.7). Pomeron and Reggeon contributions were tuned to describe the data (cf sections 4.5.2, 4.6). All energy flow distributions displayed a slight underestimation of the forward energy flow in the main detector by the Monte Carlo simulation. This effect is known for RAPGAP generated event samples, and has also been observed in non-diffractive analyses [56]. It is thus not connected to diffractive properties, eg the description of Pomeron and Reggeon subprocesses, or of the Pomeron and Reggeon remnants (cf section 6.1).

7.2.1 The Inclusive DIS Event Samples

Table 7.2 presents the event numbers of the inclusive data and Monte Carlo event samples. It also displays the efficiency of the rapididty gap selection. A strong suppression of Reggeon mediated interactions is visible, and an underestimation of the selection efficiency is observed for the Monte Carlo simulation. The rapidity gap selection is based on the forward energy flow in the LAr calorimeter, and the forward detectors. The energy flow in the forward detectors is mainly due to the Pomeron and Reggeon remnants, and is well described by the Monte Carlo simulation (cf section 6.1). But due to the deficiencies of the RAPGAP generator, the forward energy flow in the main detector – ie the LAr calorimeter – is not well described (cf section 6.1). The efficiency of the rapidity gap cuts can thus not be described very well by the Monte Carlo simulation. Since Reggeon exchange events are generally harder and more forward than Pomeron mediated interactions (cf section 4.7.1), the former are mainly affected by the rapidity gap cuts, and the deficiencies in the description of the forward energy flow. This interpretation is supported by the fact that the missing events in the Monte Carlo samples are mainly observed in the Reggeon dominated region of large $x_{I\!P}$ (cf figures 7.2, 7.3).

Table 7.2: The efficiency of the rapidity gap selection for the inclusive DIS event sample. The table shows the inclusive DIS event numbers before and after the rapidity gap selection of diffractive events. It also displays the number of events after the cuts on the forward detectors (FMD, FTS), but before the cut on η_{max}, $N_{event}^{forward}$, and the efficiency of the rapidity gap cuts, $\varepsilon = \frac{N_{after}}{N_{before}}$, including its statistical uncertainties.

	N_{event}^{before}	$N_{event}^{forward}$	N_{event}^{after}	ε [%]
Data	806	724	480	60 ± 4
MC	806	709	437	54 ± 3
$I\!P$	460	428	361	79 ± 6
$I\!R$	346	281	76	22 ± 3

The main reason for the underestimation of the efficiency by the Monte Carlo simulation is thus not a bad description of the Reggeon exchange processes themselves, or a failure of the Pomeron remnant description, but the general bad description of the forward energy flow in the main detector within RAPGAP generated events [56].

A correction factor, f_ε, is calculated to correct the efficiency predicted by the Monte Carlo simulation to the one measured in the data. The main systematic uncertainty is due to the above explained deficiencies in the description of the forward energy flow in the main detector. Since the energy flow in the forward detectors (FMD, FTS) is described well, this uncertainty is estimated by the full difference of the efficiency of the η_{max}-cut in the data and the Monte Carlo simulation, after the application of the cuts on the forward detectors:

$$f_\varepsilon = \frac{\varepsilon_{data}}{\varepsilon_{MC}} = 1.11 \pm 0.04_{syst} \pm 0.10_{stat} = 1.11 \pm 0.11$$

The predicted efficiency agrees reasonably well with the value measured for the data. The correction factor has been measured for the first time with an accuracy of 11 %.

7.2.2 The Singlejet DIS Event Samples

The event numbers of the singlejet ($N_{jet} \geq 1$) data and Monte Carlo event samples are shown in table 7.3. It also presents the efficiency of the gap selection. A stronger suppression of diffractive, FPS selected events is observed for the singlejet sample compared to the inclusive events. This is caused by the fact that jet events are generally harder and thus more forward than inclusive events (cf section 4.7.2). As for the inclusive event sample, a strong suppression of Reggeon mediated interactions is visible, and a slight underestimation of the selection efficiency is observed in the Monte Carlo simulation. Within the large statistical uncertainties, however, all event numbers agree reasonably well between data and Monte Carlo simulation.

Estimating the systematic uncertainties as for the inclusive event sample, and adding them quadratically to the statistical uncertainties, the correction factor from the Monte Carlo predicted to the measured data efficiency, f_ε, is

$$f_\varepsilon = \frac{\varepsilon_{data}}{\varepsilon_{MC}} = 1.13 \pm 0.34.$$

This measurement is the first verification of the gap selection efficiency for a hard diffractive event sample, and it confirms the prediction of the Monte Carlo simulation with an accuracy of approximately 34 %. The above ratio is a crucial quantity for hard rapidity gap selected diffractive analyses,

Table 7.3: The efficiency of the rapidity gap selection for the singlejet DIS event sample. The table shows the singlejet DIS event numbers before and after the rapidity gap selection of diffractive events. It also displays the number of events after the cuts on the forward detectors (FMD, FTS), but before the cut on η_{max}, $N_{event}^{forward}$, and the efficiency of the rapidity gap cuts, $\varepsilon = \frac{N_{after}}{N_{before}}$, including its statistical uncertainties.

	N_{event}^{before}	$N_{event}^{forward}$	N_{event}^{after}	ε [%]
Data	86	80	37	43 ± 9
MC	86	76	33	38 ± 8
$I\!\!P$	61	57	30	48 ± 11
$I\!\!R$	25	19	3	13 ± 8

since the Monte Carlo prediction of the selection efficiency is used to correct for event losses in the data. Due to the virtually complete rejection of Reggeon exchange events, the measurement can be considered as a verification of the prediction of the gap selection efficiency for Pomeron exchange events.

7.3 Main Effects of the Rapidity Gap Selection

This section investigates the main effects of the rapidity gap selection on the description of the data by the Monte Carlo simulation. The distributions of $x_{I\!\!P}$, and the transverse energy flow in the main detector are directly compared before and after the rapidity gap selection. A more detailed discussion of the standard event variables after the rapidity gap selection of diffractive events will be presented in section 7.4.

7.3.1 The Inclusive DIS Sample

Figure 7.2 presents the distributions of the data and the complete Monte Carlo event sample before (data: black points, Monte Carlo simulation: open histogram), and after (data: black triangles, Monte Carlo simulation: hatched) the rapidity gap selection. The Pomeron and Reggeon contributions are shown in figure 7.3. They are also displayed before ($I\!\!P$: dark open histogram, $I\!\!R$: light open histogram), and after ($I\!\!P$: dark hatched, $I\!\!R$: light hatched) the rapidity gap selection. While the distribution of $x_{I\!\!P}$ is almost perfectly described by the Monte Carlo simulation before the rapidity gap cuts (due to the reweighting in $x_{I\!\!P}^{FPS}$, cf section 4.5.2), a lack of Monte Carlo simulated events is observed at large values after the gap selection (cf section 7.2.1).

Considering the Pomeron and Reggeon distributions before and after the gap selection cuts (cf figure 7.3), Reggeon exchange events are mostly affected by the rapidity gap cuts, and the deficiencies in the description of the forward energy flow (cf section 7.2.1, table 7.2).

Whereas the transverse energy flow is underestimated in the forward region by the Monte Carlo simulation before the rapidity gap selection, it is almost perfectly described afterwards.
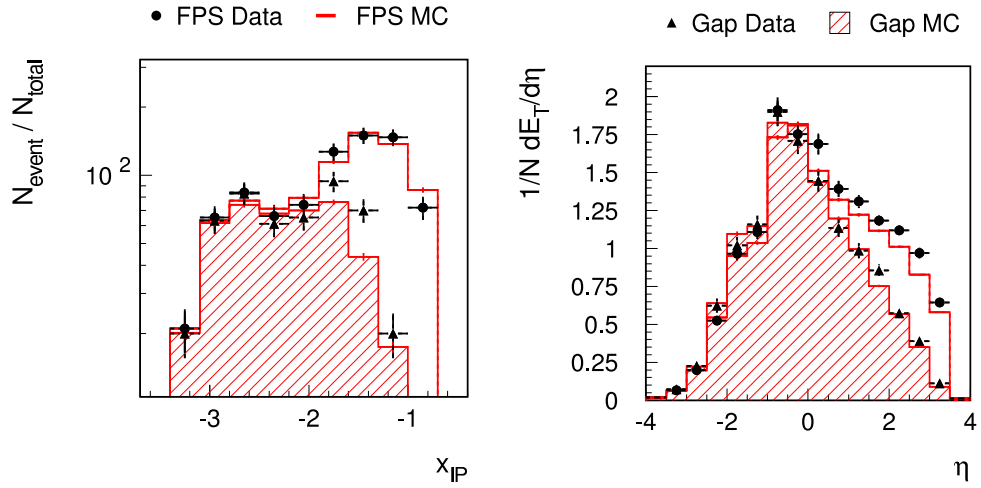
Figure 7.2: The main effects of the rapidity gap selection in the inclusive DIS event sample. Both plots show the data and the complete Monte Carlo samples before (data: black points, Monte Carlo simulation: open histogram), and after (data: black triangles, Monte Carlo simulation: hatched) the rapidity gap selection of diffractive events (cf table 7.1).
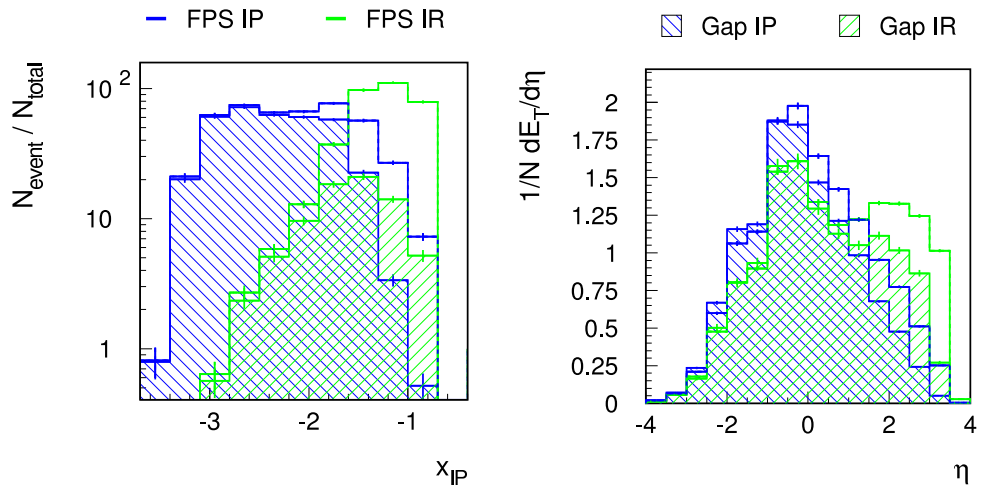
Figure 7.3: The main effects of the rapidity gap selection in the inclusive DIS event sample. Both plots show the Pomeron ($I\!P$) and the Reggeon ($I\!R$) contributions to the Monte Carlo sample before ($I\!P$: dark open histogram, $I\!R$: light open histogram), and after ($I\!P$: dark hatched, $I\!R$: light hatched) the rapidity gap selection of diffractive events (cf table 7.1).

7.3.2 The Singlejet DIS Sample

The distributions of the data and the complete Monte Carlo simulation are shown before and after the rapidity gap selection in figure 7.4. Figure 7.5 presents the Pomeron and Reggeon contributions.
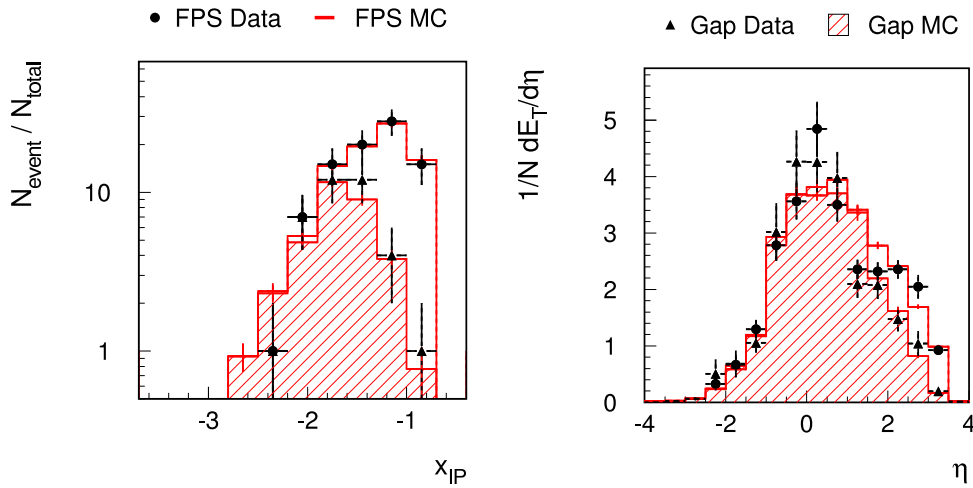
Figure 7.4: The main effects of the rapidity gap selection in the singlejet ($N_{jet} \geq 1$) DIS event sample. Both plots show the data and the complete Monte Carlo samples before (data: black points, Monte Carlo simulation: open histogram), and after (data: black triangles, Monte Carlo simulation: hatched) the rapidity gap selection of diffractive events (cf table 7.1).

Within the statistical uncertainties, the $x_{I\!P}$-distribution, both before and after the rapidity gap cuts, is well described by the Monte Carlo simulation. A slight, statistically not significant overestimation of the event losses by the Monte simulation is still visible (cf table 7.3). The Pomeron and Reggeon distributions exhibit a significant suppression of the harder and more forward Reggeon contribution by the gap cuts (cf figure 7.5). A slight excess of energy flow is observed in the data around $\eta \sim 0$, both before and after the rapidity gap selection, and a slight lack is displayed around $\eta \sim 1$ (cf section 4.7.2). But due to the large statistical uncertainties, the description of the data is reasonable for both event samples, and no significant deviations are observed.

The dijet samples have also been investigated. All plots show a similar behaviour, and similar differences as observed for the singlejet event sample. They are thus not shown separately.

7.4 Description of the Data by the Monte Carlo Simulation

This section investigates the description of the standard DIS event variables (cf section 4.7) in the data by the Monte Carlo simulation in more detail. In the rest of this chapter, as in section 4.7, the data is symbolised by black points, and the complete Monte Carlo sample by an open histogram. The Pomeron (dark hatched), and Reggeon (light hatched) distributions are also displayed.

7.4.1 The Inclusive DIS Event Sample

Figure 7.6 shows the standard event variables for the inclusive event sample. The proton energy, $E_{p'}$, and the fractional longitudinal momentum transfer at the proton vertex, $x_{I\!P}$, exhibit a slight excess of data events at medium to high $x_{I\!P}$, ie at medium values of $E_{p'}$. An excess of data events is also observed at larger electron energies, $E_{e'}$, and scattering angles, $\theta_{e'}$, and correspondingly at low values of y_e, and W_e. A better description of the data could be achieved by increasing the Reggeon
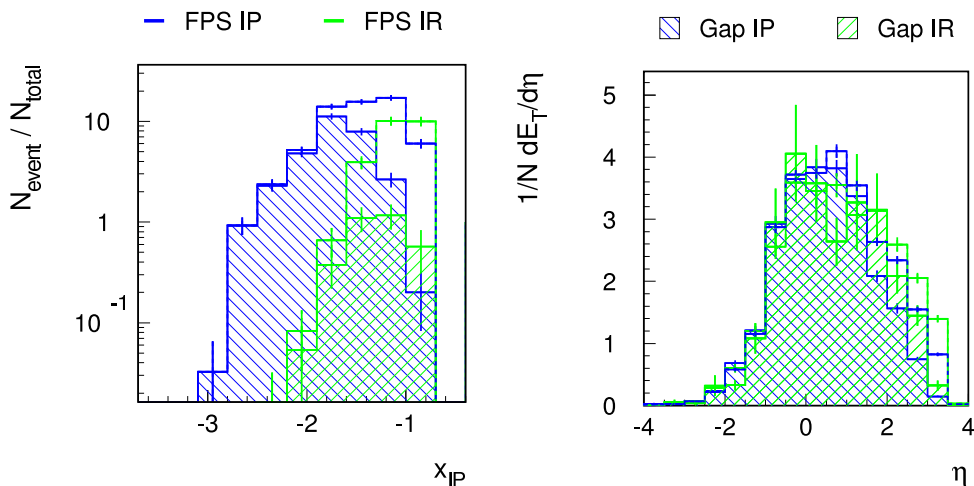
Figure 7.5: The main effects of the rapidity gap selection in the singlejet ($N_{jet} \geq 1$) DIS event sample. Both plots show the Pomeron ($I\!\!P$) and the Reggeon ($I\!\!R$) contributions to the Monte Carlo sample before ($I\!\!P$: dark open histogram, $I\!\!R$: light open histogram), and after ($I\!\!P$: dark hatched, $I\!\!R$: light hatched) the rapidity gap selection of diffractive events (cf table 7.1).

contribution (light hatched) to the Monte Carlo event sample. This is caused by the deficiencies in the description of the forward energy flow in the main detector within RAPGAP (cf section 7.2.2).

All other plots are well described within the statistical uncertainties. The η_{max}-histograms still show a slight excess of data events around $\eta_{max} \sim 0$ (cf section 4.7). According to the M_X-plots, the data events are slightly harder than the Monte Carlo ones, and the data sample contains more multijet events than the simulated event sample. This could result from next-to-leading order effects which are not incorporated in the leading order Monte Carlo simulation (cf section 4.7).

7.4.2 The Singlejet DIS Event Sample

The standard event variables are shown in figure 7.7 for the singlejet event sample. Figure 7.8 presents the jet variables for the first jet. All distributions are reasonably well described within the given statistical uncertainties. A slight excess of data events (cf table 7.3) is observed in most of the diagrams, eg $E_{e'}$, y_e, W_e. The η-distribution of the jets still exhibits a lack of data events around $\eta_{lab}^{jet1} \sim 1.25$ (cf section 4.7). But the statistical uncertainties are rather large, and statistical fluctuations are dominant – eg in the distributions of $E_{e'}$, $\theta_{e'}$, y_e, W_e, and η_{max}. No significant differences between the data and the Monte Carlo simulation are observed.

7.4.3 The Dijet DIS Event Sample

As for the FPS selected event sample (cf section 4.7.3), only the jet variables for the first and the second jet of the dijet ($N_{jet} \geq 2$) event sample are displayed in figure 7.9. All distributions are well described within the statistical uncertainties.
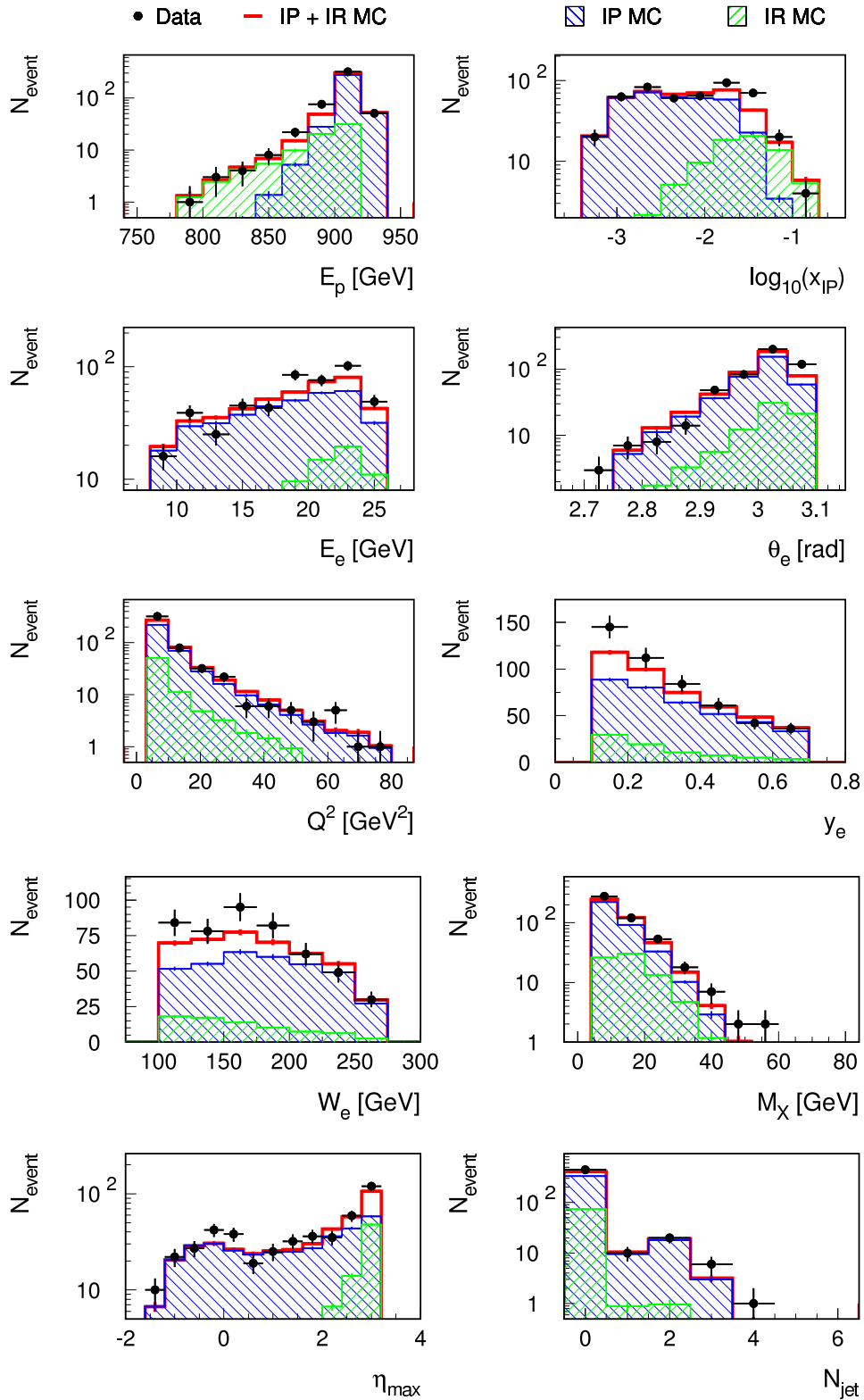
Figure 7.6: The description of the standard event variables in the DIS data by the Monte Carlo simulation after the complete DIS, FPS, and rapidity gap selections (cf tables 4.5, 4.6, 7.1). All histograms show the inclusive event samples.
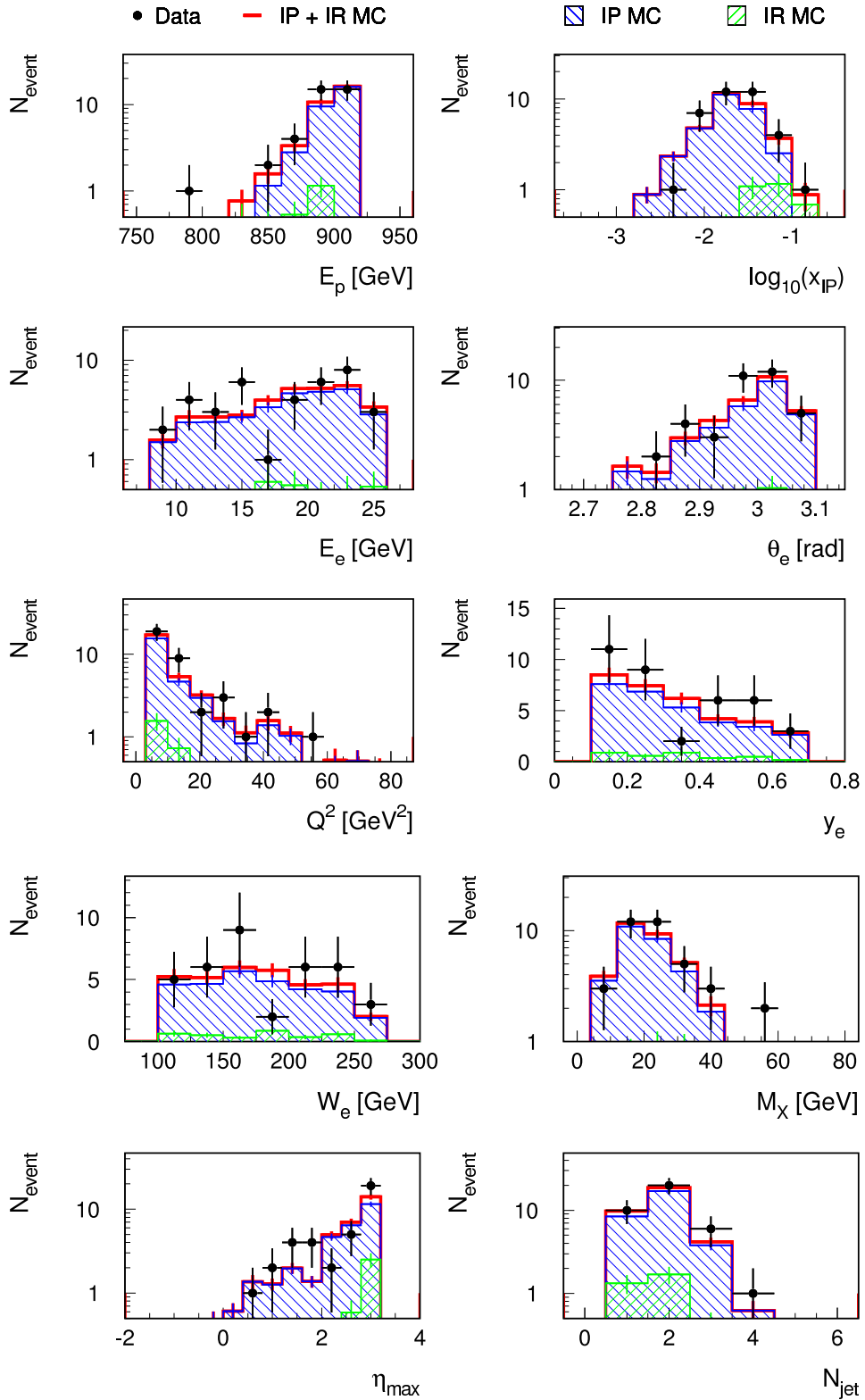
Figure 7.7: The description of the standard event variables in the DIS data by the Monte Carlo simulation after the complete DIS, FPS, and rapidity gap selections (cf tables 4.5, 4.6, 7.1). All histograms show the singlejet ($N_{jet} \geq 1$) event samples.
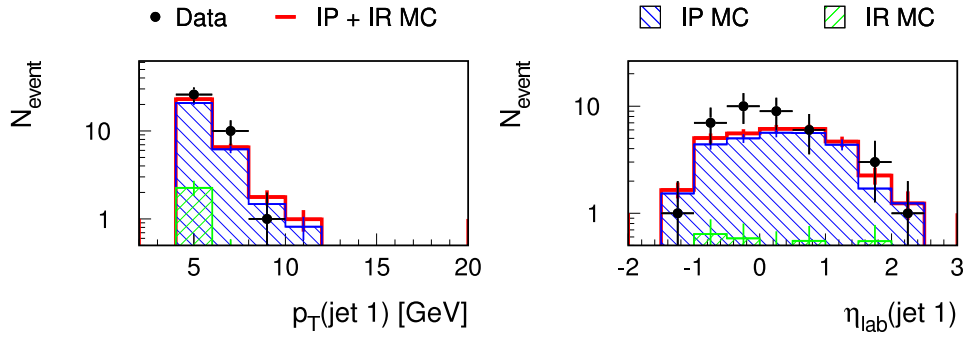
Figure 7.8: The jet variables for the first jet in the singlejet ($N_{jet} \geq 1$) DIS event samples after the rapidity gap selection.
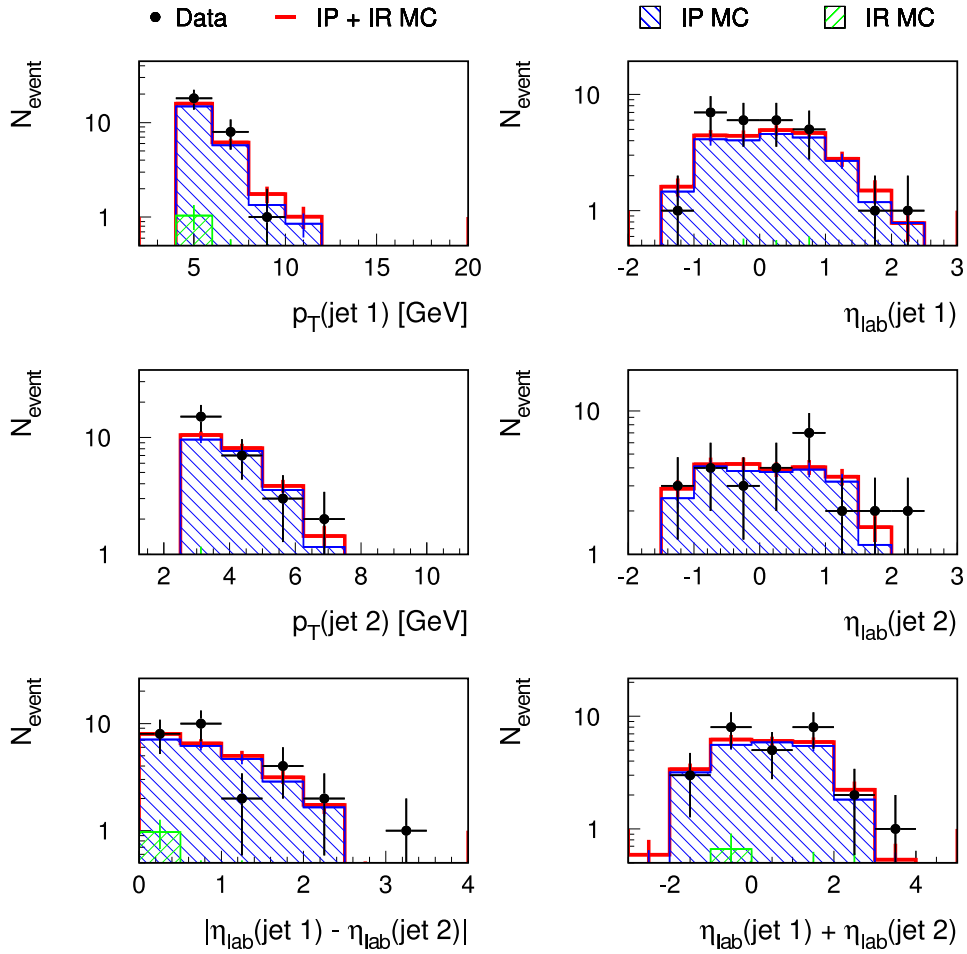
Figure 7.9: The jet variables for the first and the second jet in the dijet ($N_{jet} \geq 2$) DIS event samples after the rapidity gap selection.

7.5 Energy Flow in Rapidity Gap Selected Diffractive DIS Events

The energy flow is discussed after the standard rapidity gap selection of diffractive events. Since there is – per defintion – no energy flow in the forward detectors (FMD, FTS, and Plug calorimeter, cf section 7.1), only the energy flow in the main detector (LAr and SpaCal calorimeters) is presented. As for the event sample without rapidity gap cuts (cf section 6), absolute energy flows are measured in the laboratory system, while jet profiles are displayed in the $\gamma^* p$ centre-of-mass frame.

7.5.1 The Inclusive Data Sample

The transverse (a), and total (b) energy flow are shown in figure 7.10 for the inclusive event samples. A good description of the data by the Monte Carlo simulation is observed. In contrast to the inclusive
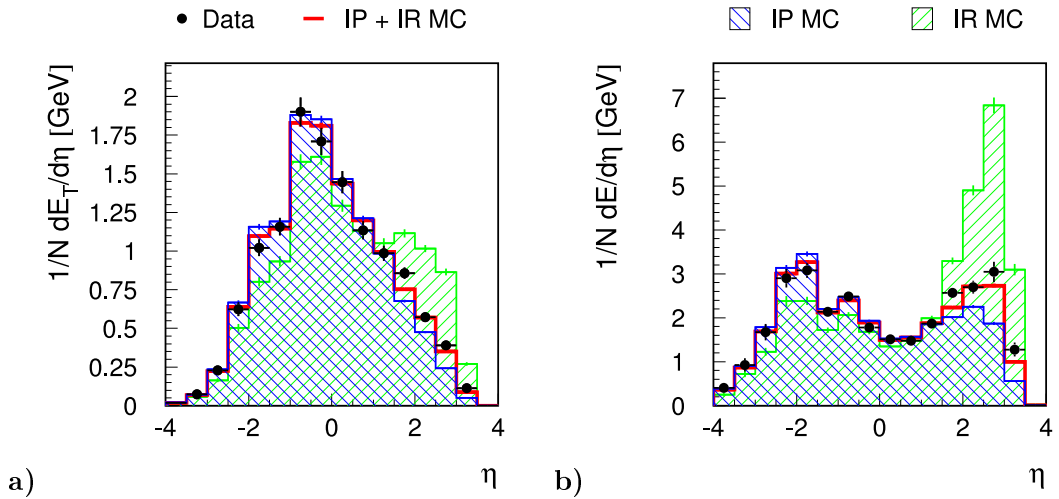
Figure 7.10: The energy flow in the inclusive DIS data and Monte Carlo events. **a)** Transverse, and **b)** total energy flow in the main detector (LAr and SpaCal).

event sample without rapidity gap cuts, only a very slight – and statistically not significant – excess of forward total energy flow is observed in the data. Both plots show that the rapidity gap selected event sample mainly consists of Pomeron exchange reactions (cf section 7.4.1).

7.5.2 The Singlejet Data Sample

Figure 7.11 displays the transverse (a) left), and total (a) right) energy flow, and the jet profiles of the leading jet (b) for the singlejet ($N_{jet} \geq 1$) event sample. All Monte Carlo histograms agree well with the corresponding data distributions. A slight lack of energy flow is observed in the data around $\eta \sim 1.5$. Both jet profiles (bottom) are reasonably well described by the Monte Carlo simulation. A slight lack of energy flow in the data is observed behind the leading jet (ie at small $\Delta\eta^*$). Any differences in the jet profile with respect to $\Delta\phi^*$ might be caused by the different FPS acceptances in data and Monte Carlo simulation (cf section 6.2).

7.5.3 The Dijet Data Sample

The transverse (a) left), and the total (a) right) energy flow are presented in figure 7.12 for the dijet ($N_{jet} \geq 2$) event samples. It also shows the jet profiles of the leading jet (b). All plots generally exhibit a similar behaviour as for the singlejet event sample. Statistical uncertainties have further increased, and thus no significant differences are observed in the transverse and total energy flow (a).
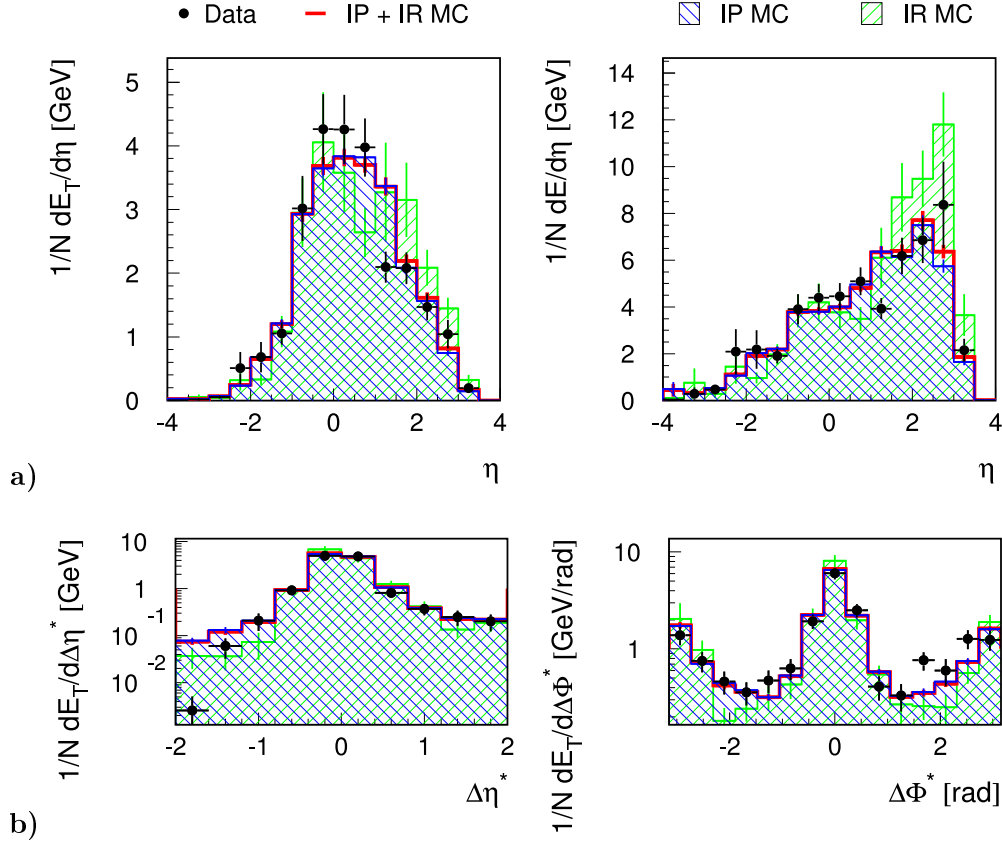
Figure 7.11: The energy flow in the singlejet ($N_{jet} \geq 1$) DIS data and Monte Carlo events. **a)** Transverse (left) and total (right) energy flow in the main detector (LAr and SpaCal). **b)** Transverse energy flow relative to the leading jet (jet profile).

The jet profile in $\Delta\eta^*$ displays a slight lack of energy in the data behind the leading jets. Otherwise, both jet profiles are well described by the Monte Carlo simulation.

7.6 Summary of the Effects of the Rapidity Gap Selection

In this chapter, a rapidity gap selection of diffractive events has been applied to the diffractive DIS event samples with a leading proton (cf chapters 3, 4, 6). The selection is based on the forward energy flow in the main and the forward detectors. It follows a standard procedure used to select diffractive interactions at the H1 detector (eg [9], cf [58]). The description of the following data event samples has been investigated after the gap selection cuts (cf tables 4.5, 4.6, 4.2):

$$
\begin{aligned}
&\text{a) Inclusive sample} && : \; N_{event} \;=\; 480 \\
&\text{b) Singlejet sample} \quad N_{jet} \;\geq\; 1 \; : \; N_{event} \;=\; 37 \\
&\text{c) Dijet sample} \qquad\;\; N_{jet} \;\geq\; 2 \; : \; N_{event} \;=\; 27
\end{aligned}
$$

For the first time, the predicted efficiencies of the rapidity gap selection have been compared to the one measured in the data. They agree within an accuracy of 11 % for the inclusive, and 34 % for the hard jet event sample, limited mainly by data statistics. The latter one is used in the standard rapidity gap analyses of hard diffractive scattering to correct for the diffractive event losses due to the selection cuts.
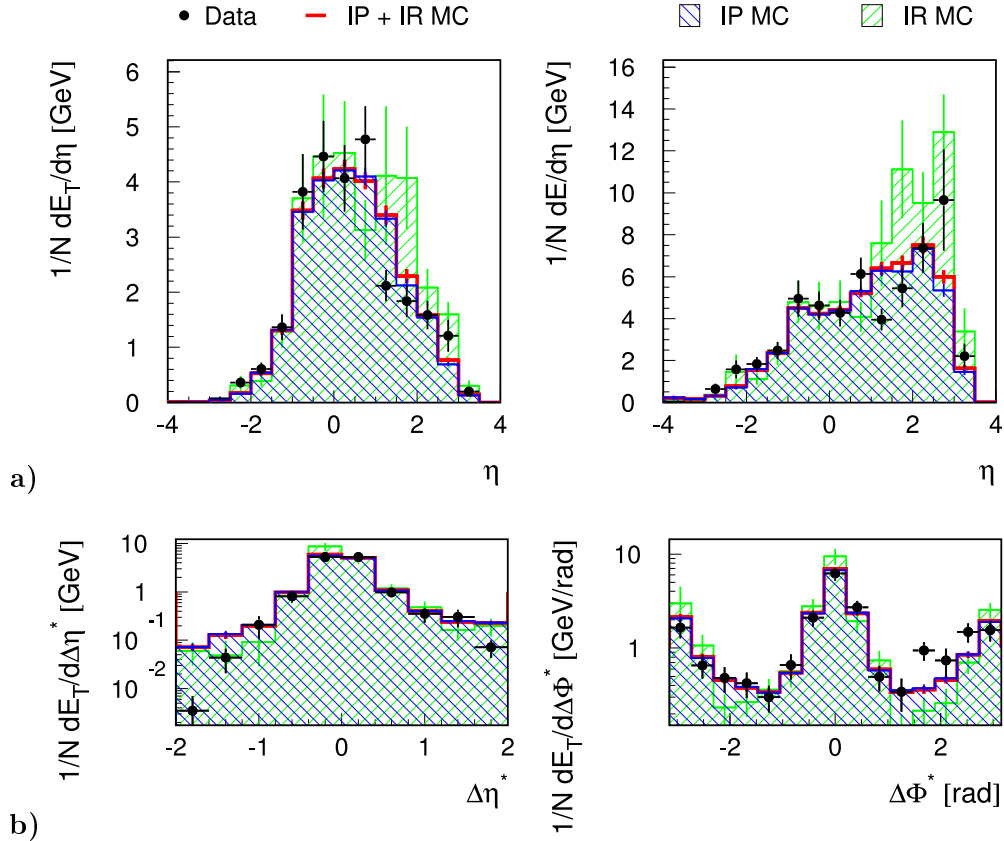
Figure 7.12: The energy flow in the dijet ($N_{jet} \geq 2$) DIS data and Monte Carlo events. **a)** Transverse (left) and total (right) energy flow in the main detector (LAr and SpaCal). **b)** Transverse energy flow relative to the leading jet (jet profile).

The main effect is a strong suppression of Reggeon exchange processes. This is due to the fact that Reggeon exchange events are generally more forward than Pomeron mediated interactions. The selection efficiency decreases for the jet samples, since jet events are on average harder, and thus more forward than inclusive events. Within the statistical uncertainties, no differences are observed between the two jet samples.

All Monte Carlo event samples exhibit a slight underestimation of the efficiency of the gap selection compared to the data. This may be caused by deficiencies in the description of the forward energy flow in the main detector within RAPGAP generated events, which is observed in the transverse energy flow before the rapidity gap cuts, and has also been observed previously [56]. These deficiencies might be due to the leading order description of the hard scattering process, and are thus probably not connected to the diffractive physics.

Significant effects are observed mainly for the inclusive event sample. They affect the Reggeon contribution much stronger than the Pomeron fraction, since Reggeon events are more forward than Pomeron mediated interactions.

Recapitulating, it is noted that – apart from the slight underestimation of the efficiency of the gap selection – the simple leading order Monte Carlo simulation, which is based on the resolved Pomeron model, describes the measured data, both before and after the rapidity gap selection.

8 Analysis of Photoproduction

In this chapter, the analysis of photoproduction (γp) events is described. It presents the event selection, and the comparison of the Monte Carlo simulated event samples with the data.

The same preselection has been applied as for the DIS event selection (cf section 3.1). Events with leading protons are identified, selected, and measured with the procedure described for the DIS events in sections 3.2 and 4.3.3. Table 4.5 summarises the applied FPS selection cuts.

8.1 Selection of Photoproduction Events

Photoproduction events (cf section 1.2.2) are selected within this analysis by requiring the scattered electron to be measured in the low angle electron detector (e-tagger) at $z = -33$ m from the interaction point (cf section 2.2.3). The acceptance of the low angle electron detector restricts the four momentum transfer at the electron vertex, Q^2, to

$$Q^2 < 0.01 \text{ GeV}^2 \qquad ([11], [37]).$$

8.1.1 Trigger Selection

In this thesis, the subtrigger $s106$ is used to preselect photoproduction events with a leading proton. It consists of the following requirements which are combined by logical ANDs, ie they all need to be fulfilled for an event to be selected. The H1 trigger system is outlined in section 2.2.5.

- **Proton candidate:** At least one track segment (local track) in the horizontal (64 m and 80 m) OR the vertical (81 m and 90 m) FPS stations.

- **Electron candidate:** A minimum energy deposit in the low angle electron detectors at $z = -33$ m OR $z = -44$ m: $E_{min}^{ET} > 4.0$ GeV

- **Jet seeds:** At least one track candidate in the CJC.

- **Event vertex:** A significant peak in the z_{vertex}-histogram.

All runs with prescales of one or two are accepted for this analysis (cf section 2.2.5).

8.1.2 The Low Angle Electron Detector

Only events with a reconstructed electron in the low angle electron detector (e-tagger) at $z = -33$ m from the nominal interaction point (cf section 2.2.3) are accepted within this analysis. To guarantee the full containment of the electron shower [10], a cut on the distance between the centre of the shower and the centre of the electron detector is applied ([11], [37]):

$$X_{el} < 6.5 \text{ cm}$$

The measurement of the scattered electron allows the calculation of the inelasticity, $y_{etagger}$ (cf section 1.2.6). Due to the acceptance of the e-tagger (cf figure 2.10, [37]), an efficient electron detection is possible in the range

$$0.3 < y_{etagger} < 0.65.$$

Only events which fulfil this condition are hence selected for this analysis.

Electrons in the e-tagger can also result from Bethe-Heitler bremsstrahlung processes. In this case, the radiated photon is detected in the photon detector at $z = -103$ m from the interaction point (cf section 2.2.3, [36]). To reject these events, an upper limit is imposed on the energy deposited in the photon detector [11]:

$$E_{pd} < 2.0 \text{ GeV}$$

8.1.3 Summary of the Photoproduction Selection Cuts

All cuts for the selection of photoproduction events are summarised in table 8.1. The selected photo-

Table 8.1: The complete list of cuts for the selection of photoproduction events.

Description	Cut				
Trigger selection					
Subtrigger			$s106$	$=$	1
Prescales			$s106_{presc}$	$\leq$	2
E-tagger selection					
E-tagger at $z = -33$ m					
Distance (shower centre)			X_{el}	$<$	6.5 cm
Acceptance	0.3	$<$	$y_{etagger}$	$<$	0.65
Background rejection					
Photon detector			E_{pd}	$<$	2.0 GeV

production sample contains

$$N_{event} = 2078$$

events.

8.2 Jet Selection and Hard Interaction Scales

In contrast to deep-inelastic scattering, no intrinsic hard interaction scale is present in photoproduction ($Q^2 < 0.01 \text{ GeV}^2$, cf section 8.1). High-$p_\perp$ jets in the hadronic final state are the most convenient way to achieve such hard interaction scales (cf section 1.2.7).

8.2.1 Jet Selection

As for DIS jet events, jets are identified using an inclusive $k_\perp$-algorithm (cf section 1.2.7, [27]). The input objects to the jet algorithm are the combined objects defined in section 4.1.4. For scattered electrons detected in the e-tagger (*low* angle electron detector), the virtual photon is emitted almost parallel to the incoming beams. The $\gamma^* p$ cms frame hence differs from the laboratory frame only by a longitudinal boost. Transverse momenta are thus identical in both systems, and the jet algorithm can be performed in the laboratory system (cf section 4.2.1) without the need to apply an additional boost to the measured four vectors. Photoproduction jets are therefore calculated in the laboratory system within this analysis. The requirements on the transverse momenta of the jets are identical to

those in the DIS analysis (cf section 4.2.1), but they are applied to the transverse momenta in the laboratory system:

$$p_\perp(jet\ 1) > 4\text{ GeV}$$
$$p_\perp(jet\ n) > 2.5\text{ GeV} \quad \text{with} \quad n \geq 2$$

To achieve precise measurements of the jet quantities within the LAr calorimeter, identical acceptance cuts are applied as in the case of deep-inelastic scattering (cf section 4.2.1):

$$-1.5 < \eta_{jet} < 2.5,$$

where η_{jet} is the pseudorapidity of any jet. All cuts are summarised in table 4.2 (Quantities in the $\gamma^* p$ cms frame are replaced by the identical quantities in the laboratory system.).

In the following analysis, two jet samples are investigated:

$$\text{a) Singlejet sample} \quad N_{jet} \geq 1 \quad : \quad N_{event} = 141$$
$$\text{b) Dijet sample} \quad N_{jet} \geq 2 \quad : \quad N_{event} = 98$$

8.2.2 Hard Interaction Scales in Photoproduction

Due to the very low event numbers (cf section 8.2.1), the inclusive data sample without any jet requirements is also investigated. As in the case of the inclusive DIS event sample (cf section 4.2.2), a minimum energy scale is required for the hadronic final state:

$$M_X > 4\text{ GeV}$$

Figure 8.1 displays the M_X-distributions for the inclusive, the singlejet, and the dijet event samples. Some of the soft physics are discarded by this cut on the hadronic final state mass. It has no effect on the jet samples, since, in this case, the soft interactions are already rejected by the cuts on the transverse momentum of the jets (cf section 8.2.1). The remaining inclusive event sample contains

$$N_{event} = 1969$$

events. Since there is no intrinsic hard interaction scale present in photoproduction reactions ($Q^2 < 0.01\text{ GeV}^2$, cf section 8.1), the cut on M_X is not sufficient to suppress all soft physics, and to achieve a minimum hard interaction scale. Another variable which provides some measure of the interaction scale is the total transverse energy in the hadronic final state:

$$E_\perp^{total} = \sum_{h \in HFS} E_\perp^h,$$

where h symbolises all particles of the hadronic final state (HFS). Only combined objects from the LAr and the SpaCal calorimeters, and the CJC are incorporated into this transverse energy. They are restricted to the acceptance region of final state jets:

$$-1.5 < \eta_h < 2.5 \quad \forall h$$

Figure 8.2 shows the distributions of $E_\perp^{total}$ for the inclusive, the singlejet, and the dijet event samples. The dominance of soft, low-$E_\perp$ physics – even after the cut on M_X – is visible for the inclusive event sample. In the case of the jet samples, a high $E_\perp$ scale is already provided by the jet selection cuts (cf section 8.2.1). The following cut is applied to further reject the remaining soft physics, and to require a minimum hard scale in all selected events:

$$E_\perp^{total} > 8\text{ GeV}$$
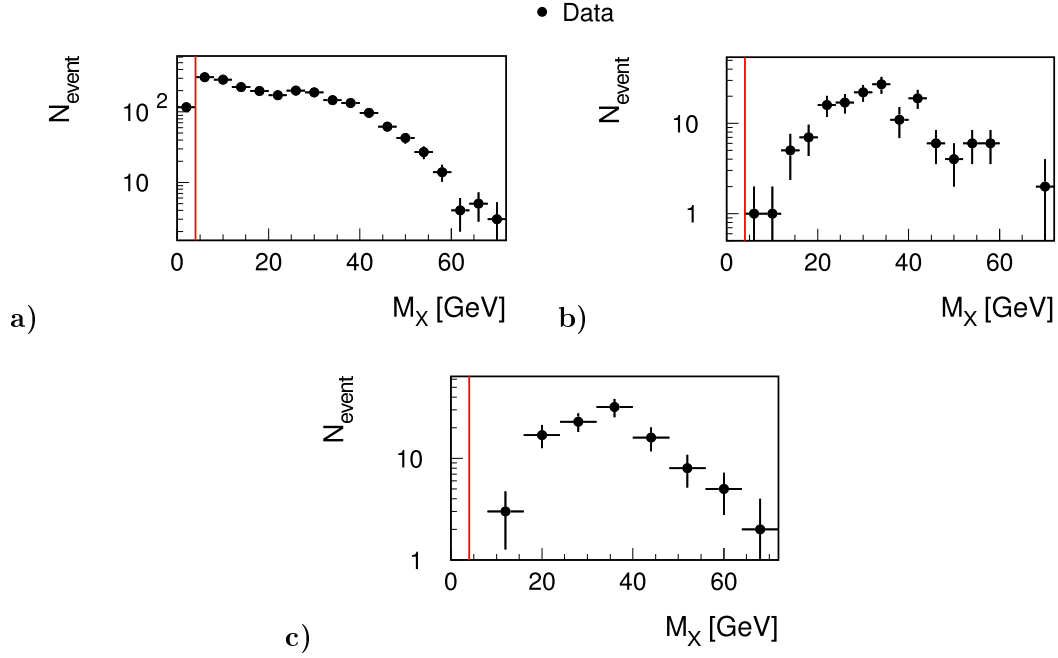
Figure 8.1: The invariant mass of the photon dissociation system for **a)** the inclusive, **b)** the singlejet ($N_{jet} \geq 1$), and **c)** the dijet event samples ($N_{jet} \geq 2$). It is shown after the complete FPS and photoproduction selections, as well as the relevant jet cuts (cf tables 4.5, 8.1). The applied cut is indicated by the vertical lines.

8.3 Summary of the Selection of Photoproduction Events

The complete leading proton selection cuts are specified in table 4.5, table 8.1 summarises the photoproduction selection cuts. A list of the jet selection cuts is provided in table 4.2. Two cuts are applied to require a minimum hard interaction scale in all photoproduction events. They are summarised in table 8.2. Three data samples are considered in the further analysis:

Table 8.2: The cuts on interaction scales in photoproduction events. They are applied to require a minimum hard interaction scale in all photoproduction reactions (cf section 8.2.2).

Description	Cut		
Hard interaction scales			
Invariant HFS mass	M_X	>	4.0 GeV
Total transverse energy	$E_\perp^{total}$	>	8.0 GeV

a) Inclusive sample $\quad\quad\quad\quad\quad\quad :\ N_{event}\ =\ 551\ :\ \frac{\Delta N}{N}\ \sim\ 4.3\ \%$

b) Singlejet sample $\quad N_{jet}\ \geq\ 1\ :\ N_{event}\ =\ 146\ :\ \frac{\Delta N}{N}\ \sim\ 8.3\ \%$

c) Dijet sample $\quad\quad\quad N_{jet}\ \geq\ 2\ :\ N_{event}\ =\ 107\ :\ \frac{\Delta N}{N}\ \sim\ 9.7\ \%$

As in the case of the DIS selection, these event samples are rather limited. Their overall uncertainties are dominated by statistical fluctuations, and typically larger than the systematic uncertainties ([9],
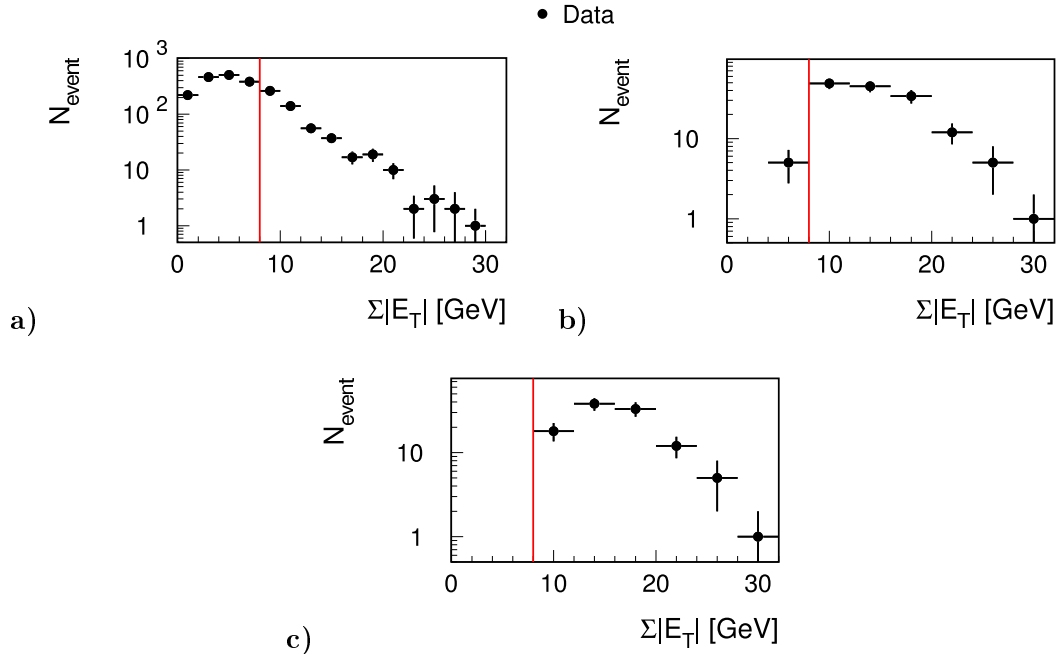
Figure 8.2: The total transverse energy for **a)** the inclusive, **b)** the singlejet ($N_{jet} \geq 1$), and **c)** the dijet event samples ($N_{jet} \geq 2$). It is shown after the complete FPS and photoproduction selections, as well as the cut on M_X, and the relevant jet cuts (cf tables 4.5, 8.1). The applied cut is indicated by the vertical lines.

[38]). Solely statistical uncertainties are therefore displayed in all following plots. Since no cross sections are calculated in this analysis, only shape comparisons are investigated. The complete Monte Carlo distribution is normalised to the area of the data distribution in each diagram, and the resulting normalisation factor is applied to the Pomeron and Reggeon subsamples (cf section 4.4). Unless stated otherwise, the complete inclusive event selection, including the cut on $E_\perp^{total} > 8$ GeV, is applied for all further event samples.

8.3.1 Event Display

Figure 8.3 shows an event display of the main detector for a data event with a reconstructed leading proton and exactly two jets. Both jets are well measured in the central tracking system and the LAr calorimeter. Their back-to-back topology with respect to ϕ is visible. The scattered proton is measured in the FPS, and the scattered electron is detected in the low angle electron detector. Both leave no trace in the main detector. Due to the colourless exchange between the scattered proton and the hadronic final state, the forward region of the main detector is completely void of any energy deposit. A large *rapidity gap* is observed between the most forward high-energy ($E_{cluster} > 400$ MeV) cluster in the LAr and the outgoing proton direction.

8.4 Photoproduction Selection of Monte Carlo Simulated Events

In this section, the Monte Carlo sample used in this analysis is introduced. The application of the data selection cuts to the Monte Carlo events is discussed.
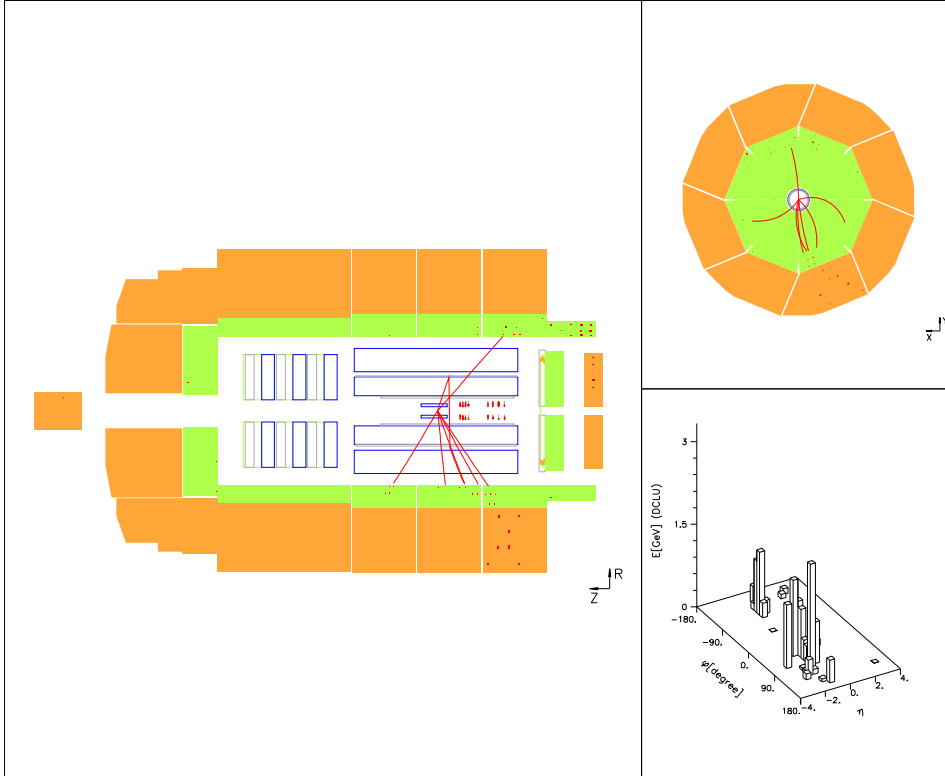
Figure 8.3: An event display of the main detector for a data event with a reconstructed leading proton and exactly two jets. Left: Cut along the beam direction. Both jets are well visible in the central tracking system and the LAr calorimeter. No energy deposit is observed in the forward part of the main detector (rapidity gap). Top right: $(x-y)$-view. The back-to-back topology of the jets with respect to ϕ is obvious. Bottom right: Energy deposit in the $(\eta-\phi)$-plane. The two visible peaks are the well collimated jets.

8.4.1 The Monte Carlo Sample Used in this Analysis

A leading order Monte Carlo simulation of diffractive events with a scattered leading proton is used in this analysis. It was produced by Sebastian Schätzel on the basis of the RAPGAP generator, version 2.08/18 (cf section 4.3.1, [17]).

Generation of Monte Carlo Events

In the original generation, the diffractive parton densities from [22] (called H1 Fit 2 (1994)) were applied for the Pomeron, but the Monte Carlo sample is reweighted to the more accurate parton densities from [24] (H1 Fit 2002) during the actual analysis. The structure function from [60] (GRV) was used for the photon (cf figure 1.14).

Since the major aim of this thesis is the investigation of hard interaction processes (cf section 1.2.7), a hard diffractive Monte Carlo event sample was generated. Its kinematic parameters are given in table 8.3. A preselection on the leading proton quantities was performed before the time-consuming detector simulation (cf section 1.4). Only protons in the acceptance range of the horizontal FPS stations (cf section 3.2.2) were selected. These acceptance cuts are also summarised in table 8.3. All variables have been explained in sections 3 and 4.1.

Table 8.3: The kinematic range of the generated photoproduction Monte Carlo samples, and the FPS acceptance cuts on the leading proton variables (cf section 3.2.2).

Description	Range			
Electron kinematics				
Four momentum transfer			Q^2	$<$	0.01 GeV^2
Inelasticity	0.25	$<$	y	$<$	0.7
Hard interaction scale			$\hat{p}_\perp$	$>$	2.0 GeV
Scattered proton preselection				
Horizontal momentum	-0.4	$<$	p_x	$<$	-0.2 GeV
Vertical momentum			$|p_y|$	$<$	0.7 GeV
Fractional momentum transfer			$x_{I\!P}$	$<$	0.2
Four momentum transfer	0.05	$<$	$|t|$	$<$	0.8 GeV^2

To cover all important subprocesses occurring within the resolved Pomeron model, eight different subsamples were generated:

1. Pomeron ($I\!P$) exchange with resolved photon processes

2. Pomeron ($I\!P$) exchange with boson gluon fusion (BGF): light quarks (u, d, s)

3. Pomeron ($I\!P$) exchange with boson gluon fusion (BGF): charm quark (c)

4. Pomeron ($I\!P$) exchange with QCD Compton effect (QCDC)

5. Reggeon ($I\!R$) exchange with resolved photon processes

6. Reggeon ($I\!R$) exchange with boson gluon fusion (BGF): light quarks (u, d, s)

7. Reggeon ($I\!R$) exchange with boson gluon fusion (BGF): charm quark (c)

8. Reggeon ($I\!R$) exchange with QCD Compton effect (QCDC)

The luminosities and event numbers of the generated and simulated Monte Carlo samples are specified in table 8.4. Because there is no difference between electrons and positrons as far as the underlying physics relevant for this thesis is concerned, only events with incoming positrons were generated.

8.4.2 Photoproduction Selection in the Monte Carlo Sample

The application of the leading proton selection cuts (cf table 4.5) to the Monte Carlo events has already been discussed in section 4.5. Since the Monte Carlo samples are reweighted to the data distributions in z_{vertex} (cf section 4.5.1) and $x_{I\!P}$ (cf section 4.5.2), the FPS cuts for data events can also be applied to the Monte Carlo simulation.

Trigger Selection

The trigger response (cf sections 2.2.5, 8.1.1) of the FPS and the e-tagger are not simulated in the Monte Carlo event samples. They can thus not be considered for the event selection. During the FPS selection, all events are required to have local and global reconstructed tracks in the horizontal FPS

Table 8.4: The generated and simulated photoproduction Monte Carlo samples.

Process	$\mathcal{L}$ [pb^{-1}]	Generated Events	Simulated Events
Pomeron ($I\!\!P$) resolved γ	24.4	4, 190, 485	234, 930
Pomeron ($I\!\!P$) BGF u, d, s	25.0	322, 878	22, 570
Pomeron ($I\!\!P$) BGF c	26.2	597, 234	38, 164
Pomeron ($I\!\!P$) QCD Compton	27.8	30, 067	2, 373
Reggeon ($I\!\!R$) resolved γ	25.8	3, 652, 557	206, 344
Reggeon ($I\!\!R$) BGF u, d, s	25.0	142, 571	11, 770
Reggeon ($I\!\!R$) BGF c	23.4	205, 398	15, 831
Reggeon ($I\!\!R$) QCD Compton	25.7	76, 613	6, 343

(cf sections 3.1.3, 3.2.1). Events with tracks in the vertical FPS stations (cf section 2.2.4) are not investigated within this analysis. The FPS trigger requirements (cf section 8.1.1) are hence redundant, and need not be considered in the Monte Carlo simulation. The treatment of the e-tagger trigger requirements in the Monte Carlo simulation is discussed in the next section.

In consequence, only the trigger requirements concerning the main detector (CJC-track, and event vertex, cf section 8.1.1) are applied to the Monte Carlo simulation. They are well simulated within the statistical uncertainties of this analysis [11], and they are required to be fulfilled in all selected Monte Carlo events.

The Low Angle Electron Detector

Due to its long distance from the main detector, the low angle electron detector is not simulated. Its acceptance is incorporated into the Monte Carlo simulation by applying a y-dependant event weight to all Monte Carlo events. The event weight is calculated using a H1 standard analysis algorithm [37]. Only the acceptance range is defined by applying the acceptance cuts to the generated inelasticity, y_{gen} (cf section 8.1.2). To account for migration effects (cf section 4.3.1), it is smeared with the resolution of $y_{etagger}$ as determined from the data [11]. Bethe-Heitler background processes are not included in the Monte Carlo simulation. No cut is hence applied to the energy deposit in the photon detector (cf section 8.1.2).

Combination of the Monte Carlo Event Samples

The eight Monte Carlo sets are added to the complete Monte Carlo sample. All events are weighted with the inverse luminosity to obtain a correct mixture of the different subprocesses without loosing any statistics.

The complete event selection now being finished for both, data and Monte Carlo simulation, the next sections are concerned with the description of the most important data quantities by the Monte Carlo simulation.

Unless stated otherwise, all distributions in the remaining parts of this chapter thus display the data and the Monte Carlo samples after the complete event selection (cf tables 4.5, 8.1, 8.2). Data distributions are plotted as full points, the complete Monte Carlo sample is indicated by an open histogram. Hatched histograms represent the distributions of the Pomeron ($I\!\!P$: dark) and the Reggeon ($I\!\!R$: light) Monte Carlo subsamples. Except for the distributions in figure 8.4 a), the Monte Carlo distributions are reweighted to the data in z_{vertex} and $x_{I\!\!P}$. All Monte Carlo samples are normalised

to the data as explained in section 8.3. Only the dominant statistical uncertainties are displayed. The jet selection criteria applied are specified for each event sample.

8.5 Pomeron and Reggeon Contributions to the γp Data

Figure 8.4 displays the distributions of $x_{I\!P}$ in the inclusive photoproduction sample before (a), and after (b) the reweighting in $x_{I\!P}^{FPS}$. The fractional Reggeon and Pomeron contributions are displayed
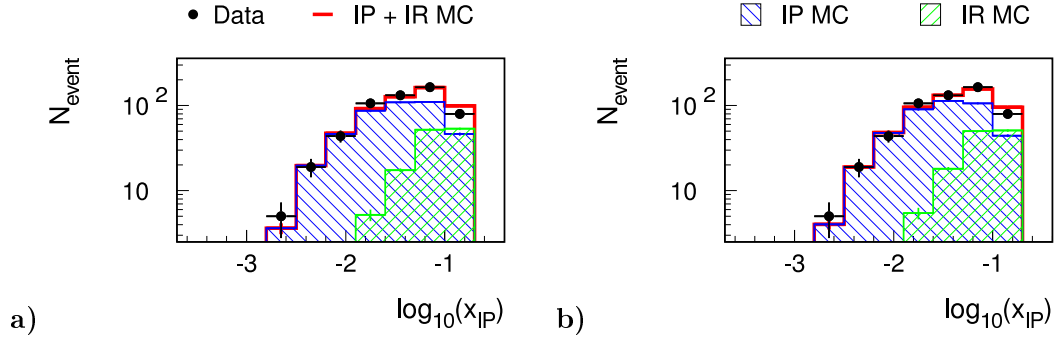
Figure 8.4: The longitudinal momentum transfer, $x_{I\!P}$, **a)** before, and **b)** after the reweighting in $x_{I\!P}^{FPS}$. All diagrams show the inclusive event samples after the full event selection (cf tables 4.5, 8.1, 8.2). The vertex reweighting is applied.

in table 8.5 as predicted by the Monte Carlo simulation both, before and after the reweighting in $x_{I\!P}^{FPS}$. No significant change is observed. A low Reggeon contribution is predicted already for the

Table 8.5: The fractional contributions of the Pomeron ($I\!P$) and the Reggeon ($I\!R$) exchange processes to the inclusive photoproduction Monte Carlo sample: $f_X = \frac{N_{event}(X)}{N_{event}}$

	$f_{I\!P}$ [%]	$f_{I\!R}$ [%]
Before reweighting in $x_{I\!P}^{FPS}$	77	23
After reweighting in $x_{I\!P}^{FPS}$	77	23

inclusive event sample. This is caused by the hard cut on the total transverse energy $E_{\perp}^{total}$, which has not been applied during the DIS event selection (cf sections 4.2.2, 8.2.2). Due to this low Reggeon contribution, and the resulting large uncertainties, no measurement of the Reggeon contribution is presented for the data sample in the case of photoproduction.

8.6 Description of the Data by the Monte Carlo Simulation

This section compares the data and the Monte Carlo simulated distributions of the selected photoproduction samples with a scattered leading proton. Pomeron and Reggeon contributions to the complete Monte Carlo sample are also examined.

8.6.1 The Inclusive Event Sample

Figure 8.5 shows the standard event variables for the inclusive event samples.
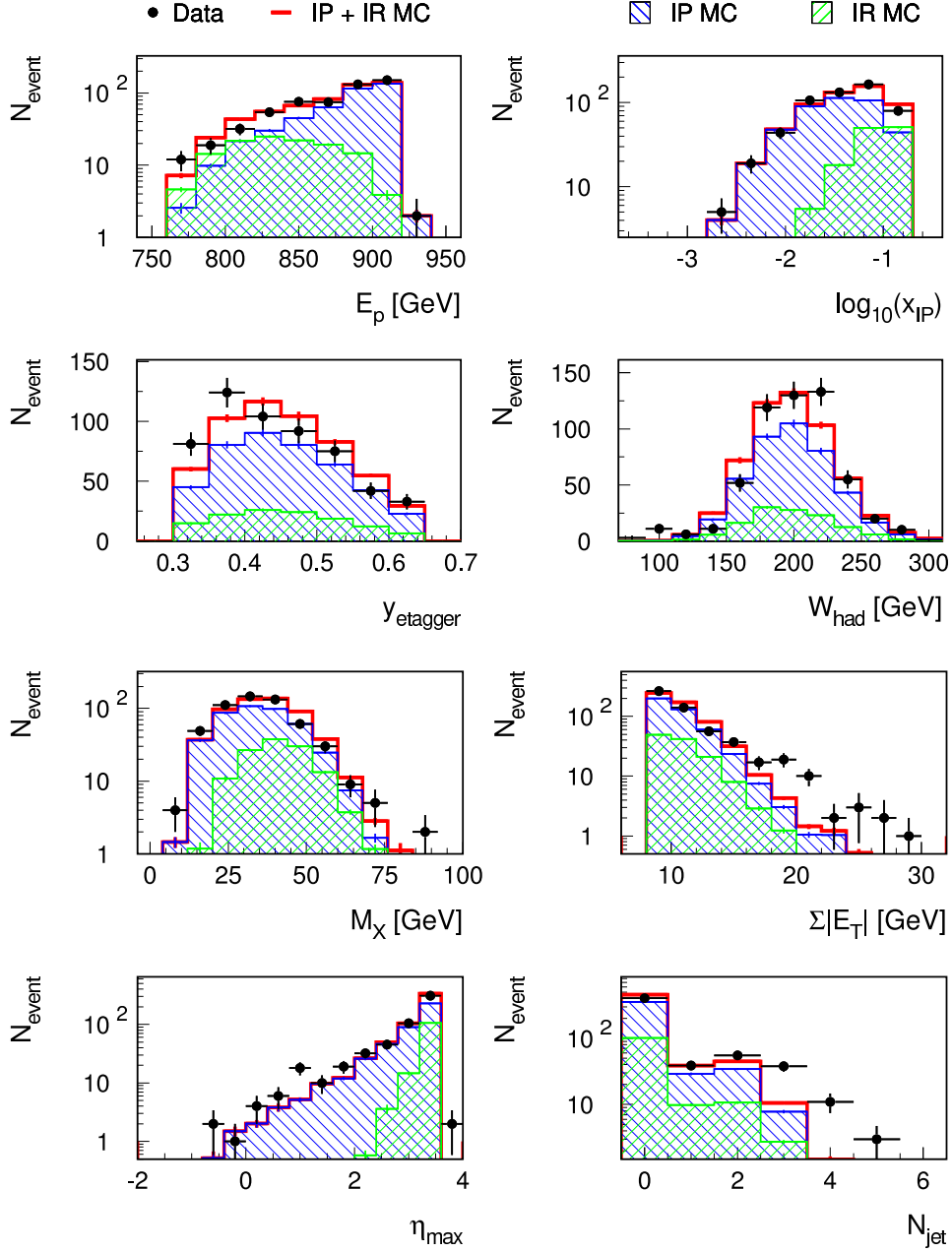
Figure 8.5: The description of the standard event variables in the photoproduction data by the Monte Carlo simulation. All histograms show the inclusive event samples with $E_\perp^{total} > 8.0$ GeV.

The overall agreement between data and Monte Carlo distributions is reasonable, but it is distinctly worse than for the DIS event samples (cf section 4.7). Due to the reweighting in $x_{I\!P}$, the description of $E_{p'}$ and $x_{I\!P}$ is almost perfect. Any remaining discrepancies are caused by smoothing effects, and binning variations (cf section 4.7.1). The inelasticity as derived from the scattered electron in the e-tagger, $y_{etagger}$, is shifted to lower values in the data compared to the Monte Carlo simulation. But this effect is not statistically significant, and the low angle electron detector is not correctly simulated (cf section 8.4.2). Most of the quantities derived from the hadronic final state are not well described by the Monte Carlo simulation. The γp cms energy, W_{had}, displays a slight shift of the data towards higher energies. M_X is reasonably well described within the statistical uncertainties, but the total transverse energy, $E_{\perp}^{total}$ (cf section 8.2.2), exhibits a significant excess of data events at large values. A large surplus of multijet events in the data compared to the Monte Carlo simulation is also observed. η_{max} agrees well between data and Monte Carlo distributions. Only a slight excess of data events is displayed at rather small values. The discrepancies concerning the hadronic final state are correlated, and they have also been observed in diffractive rapidity gap selected event samples with two hard jets and large event numbers [61]. They are thus no artefact of the FPS selection, but a deficit in the Monte Carlo simulation with the RAPGAP generator, which is used in both analyses. Possibly due to the missing hard scale in Q^2, the QCD scattering process is probably not well described by the hard Monte Carlo simulation – even for hard jet events in rapidity gap selected samples. The discrepancies are thus possibly caused by a problem in the description of the QCD scattering process, which is probably not related to the description of the diffractive physics within the resolved Pomeron model.

The distributions of $\log_{10}(x_{I\!P})$, M_X, and η_{max} show that Reggeon exchange events are generally harder and more forward than Pomeron mediated interactions (cf section 4.7). They indicate that both processes are needed to describe the data. A variation of their contributions cannot explain the discrepancies between data and Monte Carlo simulation in $E_{\perp}^{total}$, since Pomeron and Reggeon mediated interactions exhibit only slight differences. No differences between the two exchange processes are observed in the distribution of the jet numbers.

8.6.2 The Singlejet Event Sample

The standard event variables are displayed for the singlejet ($N_{jet} \geq 1$) event samples in figure 8.6. Their description in the data by the Monte Carlo simulation shows a similar behaviour as for the inclusive event samples. Statistical uncertainties have further increased, and hence no significant shifts are observed in the distributions of $y_{etagger}$ and W_{had}. The distortion of the $E_{\perp}^{total}$-spectrum is worse than for the inclusive event sample. As opposed to deep-inelastic scattering, the fractional contributions of events with different jet numbers to the singlejet sample are not well described by the Monte Carlo simulation. A large excess of events with high jet numbers ($N_{jet} \geq 3$) is observed. This is partly due to higher order QCD effects. But a comparison to the case of deep-inelastic scattering, which was well described by the hard RAPGAP Monte Carlo simulation, even for the inclusive event sample, shows that a general problem with the description of the hard scattering process is observed in photoproduction. The distributions of $E_{p'}$, $\log_{10}(x_{I\!P})$, M_X, and η_{max} in figure 8.6 still indicate that Reggeon and Pomeron contributions are needed to describe the data.
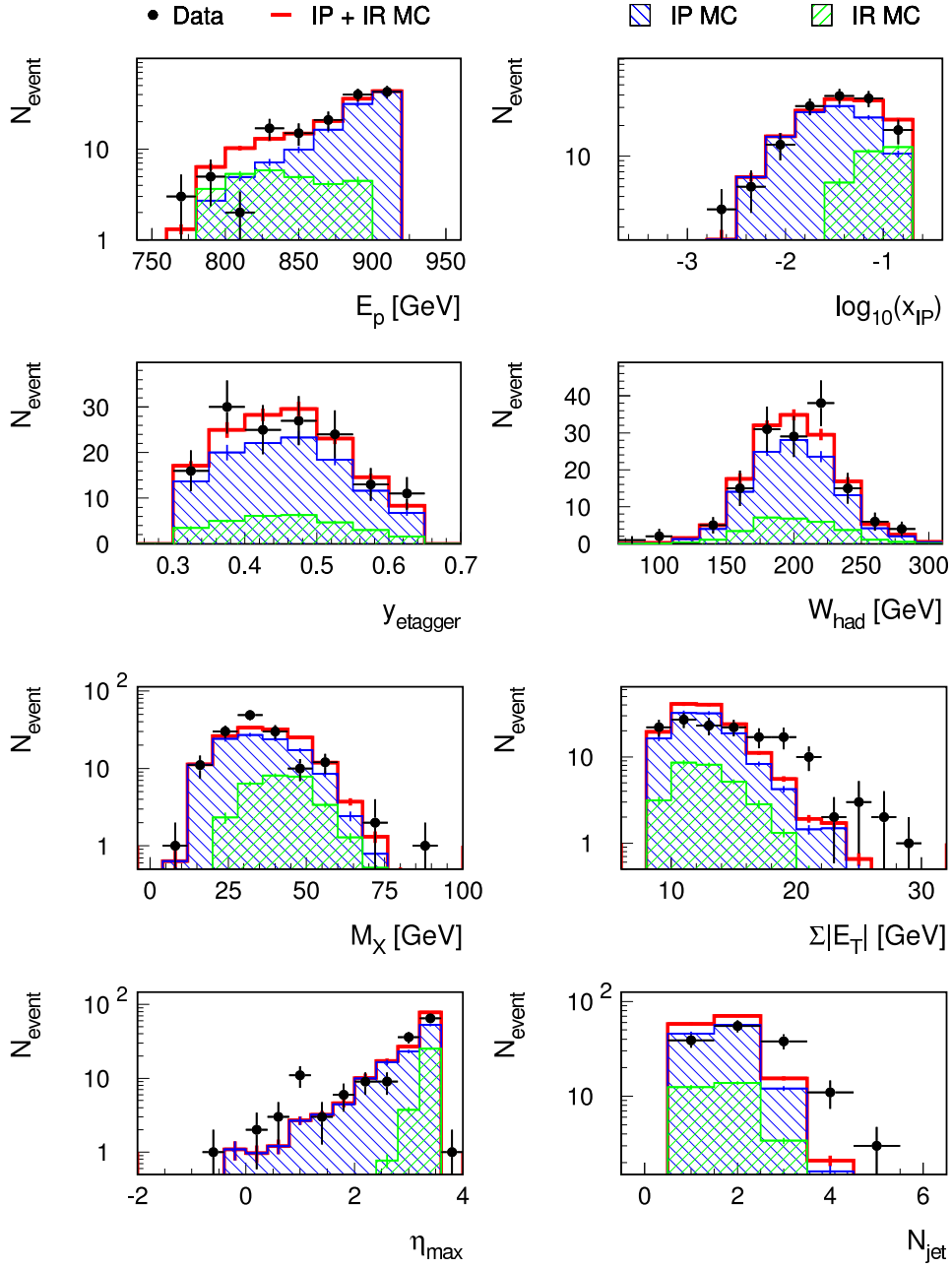
Figure 8.6: The description of the standard event variables in the photoproduction data by the Monte Carlo simulation. The histograms show the singlejet ($N_{jet} \geq 1$) event samples with $E_\perp^{total} > 8.0$ GeV.

Figure 8.7 presents the jet variables of the first jet in the singlejet ($N_{jet} \geq 1$) event samples. Both
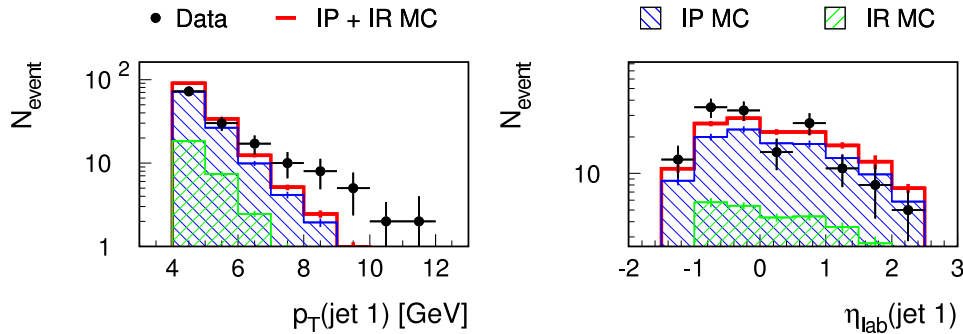
Figure 8.7: The jet variables of the first jet in the singlejet ($N_{jet} \geq 1$) γp event samples.

variables are not well described by the Monte Carlo simulation. The transverse momentum, $p_\perp^{jet\ 1}$, displays a large excess of high-$p_\perp$ events in the data compared to the Monte Carlo simulation. This is compatible with the significant excess of events with large $E_\perp^{total}$ in the data. As in deep-inelastic scattering (cf figure 4.16), a slight shift of the data distribution towards lower values is observed in $\eta_{lab}^{jet\ 1}$, although statistical uncertainties are rather large. Both discrepancies cannot be accounted for by varying the fractional Pomeron and Reggeon exchange contributions.

8.6.3 The Dijet Event Sample

Since the standard event variables display a very similar behaviour as in the case of the singlejet event sample, they are not displayed separately. Only the jet variables of the first and the second jet in the dijet events are presented in figure 8.8. Due to the large fraction of multijet events in the singlejet sample, the distributions of the leading jet exhibit the same effects as in the singlejet event sample. The second jet is generally better described than the first one. Only a slight excess of high-$p_\perp$ jets is observed, and no shift is displayed in the distribution of $\eta_{lab}^{jet\ 2}$. While $\left|\eta_{lab}^{jet\ 1} - \eta_{lab}^{jet\ 2}\right|$ is well described within the statistical uncertainties, the data distribution of $\left(\eta_{lab}^{jet\ 1} + \eta_{lab}^{jet\ 2}\right)$ is slightly shifted towards lower values compared to the Monte Carlo simulation.

According to the Monte Carlo simulation, photoproduction reactions are dominated by resolved photon interactions (cf figure 1.14, table 8.4). Due to the larger energy contribution from the photon side, direct photon processes are generally harder than resolved photon reactions (cf figure 1.14, $x_\gamma^{direct} = 1$, $x_\gamma^{resolved} < 1$). A variation of their relative contributions, ie a higher contribution of direct photon interactions, could thus ameliorate the description of the data by the Monte Carlo simulation, eg in $E_\perp^{total}$, or $p_\perp^{jets}$. This is investigated in more detail in the following section.

8.7 Direct and Resolved Photon Processes in Photoproduction

The description of the data by the Monte Carlo simulation is investigated in terms of resolved and direct photon contributions. Some of the less well described distributions are presented, separately showing the direct and resolved photon contributions to the Monte Carlo simulation. In contrast to most other sections, dark hatched histograms hence show resolved photon processes, direct photon processes are illustrated by light hatched distributions. The data is presented as black points, and the open histograms symbolise the complete Monte Carlo sample.
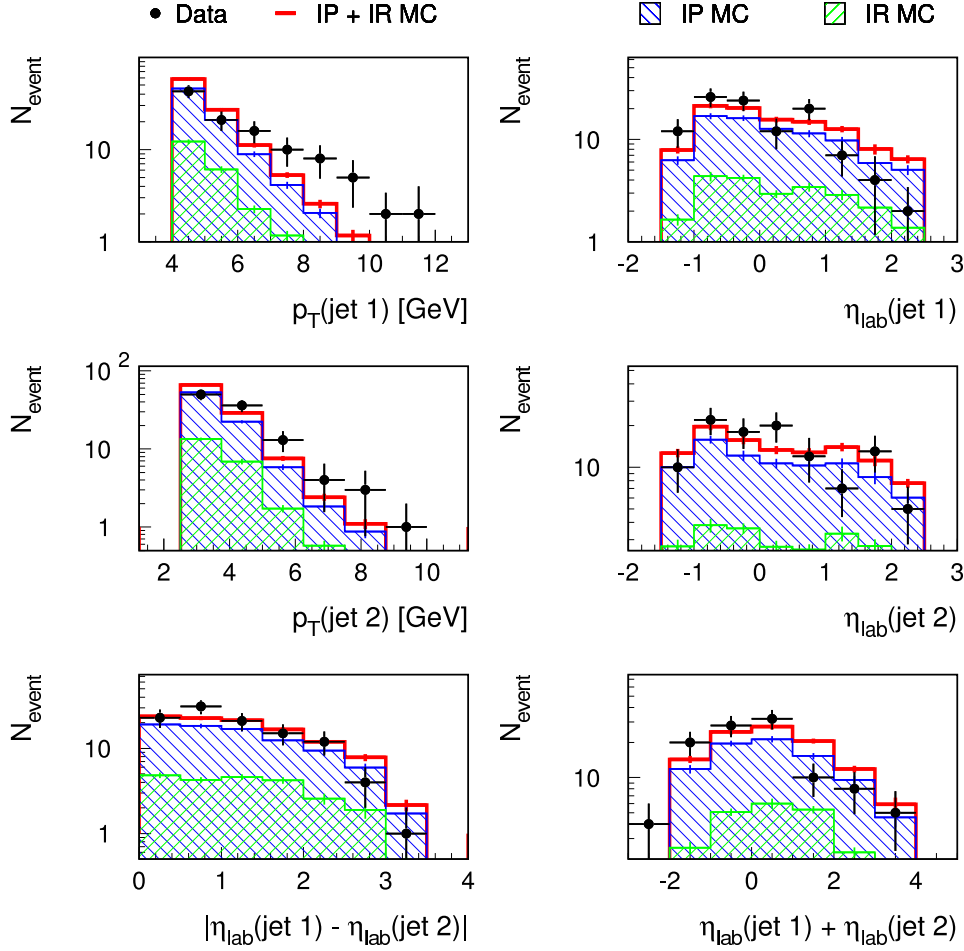
Figure 8.8: The jet variables of the first and the second jet in the dijet ($N_{jet} \geq 2$) γp event samples.

8.7.1 The Inclusive Photoproduction Event Sample

Figure 8.9 shows the resolved and the direct photon contributions to the inclusive Monte Carlo sample. It presents the distributions of η_{max} and $E_\perp^{total}$. The η_{max}-distribution of the resolved photon events exhibits a sharper forward peak at large values, and a faster decline towards low values, than the direct photon component. In the diagram of $E_\perp^{total}$, a sharper decline of the resolved photon contribution is observed towards large transverse energies. Direct photon processes are thus on average harder and less forward than resolved photon reactions. A better description of both data distributions could be achieved by considering a higher fraction of direct photon processes than predicted by the Monte Carlo simulation. The $E_\perp^{total}$-histograms also show that a huge increase of the direct contribution would be needed, and that this increase would nevertheless not be sufficient to obtain a good agreement between data and Monte Carlo simulation.

8.7.2 The Singlejet Photoproduction Event Sample

The direct and resolved photon contributions to the singlejet Monte Carlo sample are displayed in figure 8.10. Besides η_{max} and $E_\perp^{total}$, it also presents the jet distributions, ie $p_\perp^{jet\ 1}$ and $\eta_{lab}^{jet\ 1}$. The distributions of η_{max} and $E_\perp^{total}$ display a similar behaviour as for the inclusive event sample. $p_\perp^{jet\ 1}$ and $\eta_{lab}^{jet\ 1}$ show that direct photon jets are generally slightly harder, and especially more backward than jets in resolved photon events. This reinforces the fact that a better description of the data could
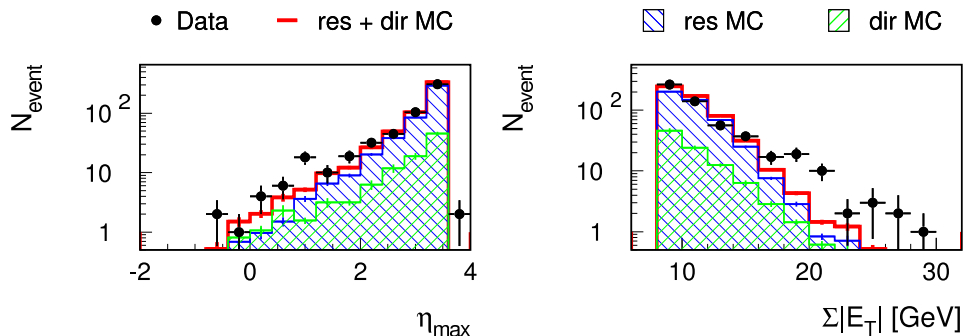
Figure 8.9: The direct and resolved photon contributions to the inclusive photoproduction sample. Both plots show the data, the complete Monte Carlo sample, the resolved (dark hatched), and the direct (light hatched) photon contributions.

be achieved by increasing the direct photon contribution to the Monte Carlo simulation. However, it remains obvious that a huge increase would be needed, and that significant discrepancies, eg in $E_\perp^{total}$ or $p_\perp^{jet\ 1}$ would still persist.

8.7.3 The Dijet Photoproduction Event Sample

Figure 8.11 shows the resolved and the direct photon contributions to the dijet Monte Carlo sample. In addition to η_{max} and $E_\perp^{total}$, it also presents the distributions of $p_\perp^{jet\ 1/2}$, $\left(\eta_{lab}^{jet\ 1} + \eta_{lab}^{jet\ 2}\right)$, and the fraction of the photon energy entering into the hard scattering process, x_γ. The first three variables exhibit a similar behaviour as in the case of the singlejet event sample. The transverse momentum of the second jet, $p_\perp^{jet\ 2}$ displays more clearly than the one of the first jet, that direct photon interactions are on average harder than resolved photon events. According to $\left(\eta_{lab}^{jet\ 1} + \eta_{lab}^{jet\ 2}\right)$, jets in direct photon events are more backward than those in resolved photon reactions. An excess of data events is observed at large values of x_γ, matched by a lack at low x_γ. Since resolved photon events are peaked towards low values of x_γ, a better description of the data could – in agreement with all other distributions – be achieved by an increase of the direct photon contribution to the Monte Carlo sample. However, the distribution of x_γ also shows that a huge increase by at least a factor of two would be needed to describe the data reasonably well. And despite such a huge increase, significant discrepancies would remain in the description of eg $E_\perp^{total}$ and $p_\perp^{jet\ 1}$. This suggests that the underestimation of the direct photon distribution to the data is not the only – and probably not the most important – reason for the observed discrepancies between data and Monte Carlo simulation.

8.8 Summary of the Photoproduction Analysis

In this chapter, a sample of photoproduction events with a scattered leading proton has been selected. The photoproduction selection (section 8.1) is based on selection criteria well-established within the H1 collaboration [11]. The FPS selection has been applied as described in chapters 3, 4. High-$p_\perp$ jets were defined in the hadronic final state (section 8.2.1). Due to the low event numbers (section 8.3), the inclusive event sample without any jets has also been considered. Cuts on the hadronic final state mass, and on the total transverse energy in the hadronic final state have been applied to reject soft physics, and to require a minumum hard interaction scale (section 8.2.2). Monte Carlo events were generated using a Monte Carlo generator based on a hard leading order resolved Pomeron model
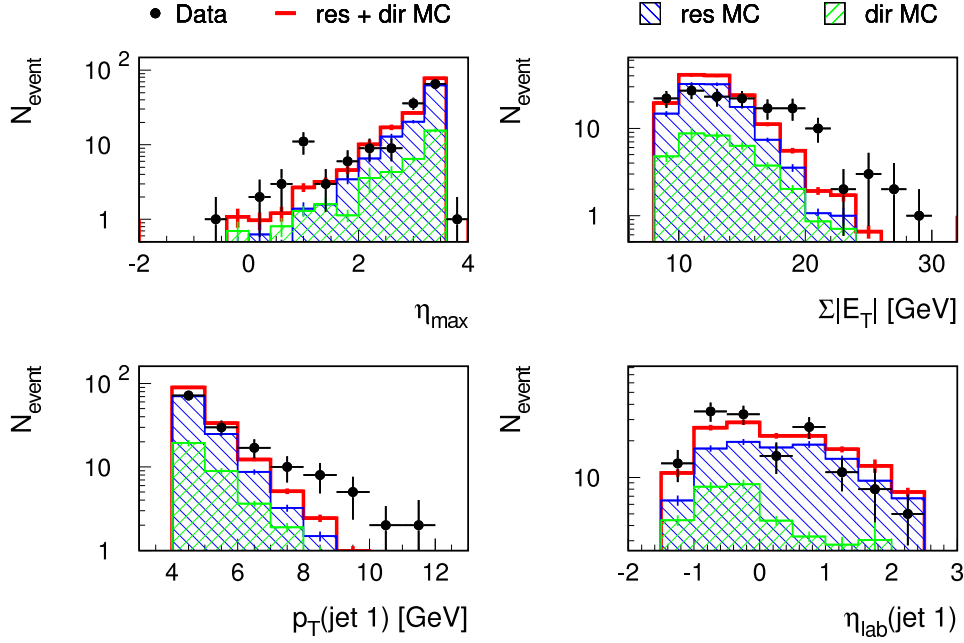
Figure 8.10: The direct and resolved photon contributions to the singlejet ($N_{jet} \geq 1$) photoproduction sample. All plots show the data, the complete Monte Carlo sample, the resolved (dark hatched), and the direct (light hatched) photon contributions.

(RAPGAP 2.08/18 [17], section 8.4). The following data event samples have been investigated:

$$
\begin{array}{lllllll}
\text{a) Inclusive sample} & & & : & N_{event} & = & 551 \\
\text{b) Singlejet sample} & N_{jet} & \geq \ 1 & : & N_{event} & = & 146 \\
\text{c) Dijet sample} & N_{jet} & \geq \ 2 & : & N_{event} & = & 107 \\
\end{array}
$$

The description of the photoproduction data by the Monte Carlo simulation is distinctly worse than in the case of the deep-inelastic scattering samples (cf section 4.7). The main discrepancy is a large excess of data events with high transverse energies, $E_\perp^{total}$, compared to the Monte Carlo simulation. In agreement with this observation, a large excess of multijet events is observed in the data, both for the inclusive and the jet samples. The measured jets in the data – especially the first (ie the hardest) one – are on average also much harder than in the Monte Carlo simulation. $\eta_{lab}^{jet\ 1}$ displays a similar backward shift in the data as is observed in the DIS samples, and the distribution of $(\eta_{lab}^{jet\ 1} + \eta_{lab}^{jet\ 2})$ is also shifted towards lower values. These discrepancies are correlated, and they have also been observed in hard rapidity gap selected diffractive dijet event samples with large event numbers [61]. They are thus no experimental problem of the FPS selection, but a deficit of the leading order Monte Carlo generator RAPGAP, which has been used in both cases.

The disagreement between the data and the Monte Carlo simulation cannot be explained by wrong fractional contributions of Pomeron and Reggeon exchange processes, since both exhibit very similar distributions in $E_\perp^{total}$, N_{jet}, and $p_\perp^{jet\ 1}$.

A better description of the data could be achieved by increasing the direct photon contribution to the Monte Carlo simulation, ie by down-weighting the resolved photon contribution. But a huge increase by at least a factor of two would be needed to describe the data reasonably well, and significant discrepancies, eg in $E_\perp^{total}$ and $p_\perp^{jet\ 1}$, would still remain. Furthermore, direct and resolved photon contributions are well described in the hard rapidity gap selected event samples [61]. This suggests that the underestimation of the direct photon contribution is not the only reason – and probably
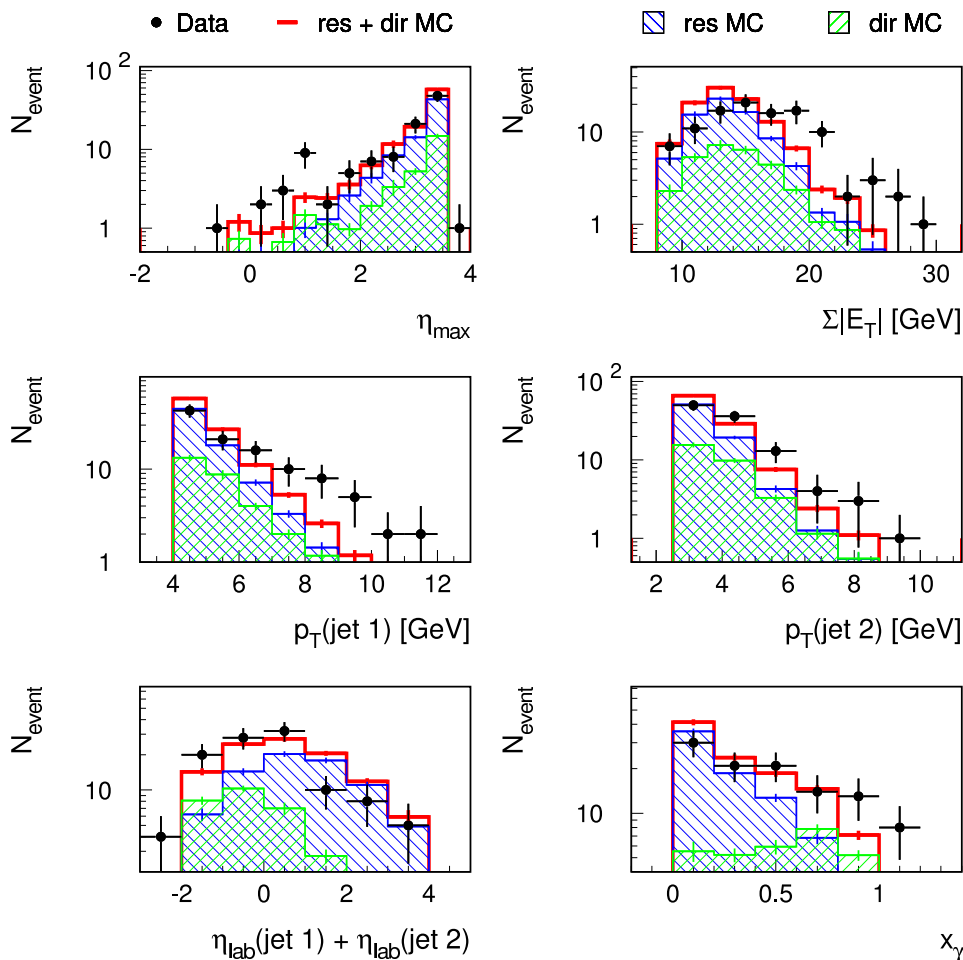
Figure 8.11: The direct and resolved photon contributions to the dijet ($N_{jet} \geq 2$) photoproduction sample. All plots show the data, the complete Monte Carlo sample, the resolved (dark hatched), and the direct (light hatched) photon contributions.

not the most important – for the observed disagreements. Since the measured discrepancies occur in inclusive and hard photoproduction event samples, but do not appear in DIS events (cf section 4.7), they are probably caused by deficiencies in the QCD description of the hard scattering process due to the missing hard scale Q^2. They would thus not be connected to the description of diffractive physics within the resolved Pomeron model – ie especially the forward energy flow caused by the Pomeron and Reggeon remnants. This is examined in more detail in the next chapter.

9 Energy Flow in Photoproduction

This chapter presents the energy flow in the main and forward detectors for the selected photoproduction event samples. The energy flow is investigated despite the observed kinematic discrepancies (cf section 8.8). Since these disagreements are probably not related to the diffractive description of the data, forward energy flow measurements allow the verification of the Pomeron and Reggeon remnant description within the resolved Pomeron model (cf chapter 6). The energy flow in the forward detectors is measured using the Plug calorimeter, the Forward Muon Detector, and the Forward Tagging System. General prerequisites were discussed in chapter 6. Since jets are identified in the laboratory system in the case of photoproduction (cf section 8.2.1), all plots in the following sections are shown in this reference frame.

9.1 The Inclusive Data Sample

Figures 9.1 and 9.2 show the complete set of energy flow plots for the inclusive event sample (ie without any jet requirements). Although most of them display a reasonable agreement between data
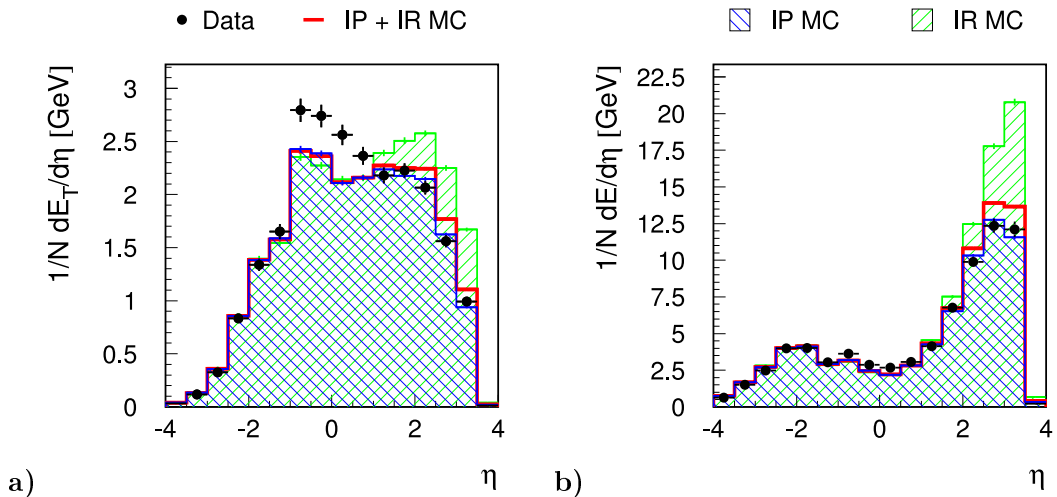
Figure 9.1: The central energy flow in inclusive data and Monte Carlo events. **a)** Transverse, and **b)** total energy flow in the main detector (LAr and SpaCal).

and simulated Monte Carlo distributions, the description is again worse than for the inclusive DIS sample. The transverse energy flow in the main detector (figure 9.1a) exhibits significant differences. A large energy excess is measured in the data around $\eta \sim 0$, and a slight lack of energy is observed in the forward region. The shape of the data distribution is not reproduced by the Monte Carlo sample. This is in accord with the observed excess of events with large total transverse energy, $E_\perp^{total}$, in the data (cf section 8.6). The total energy flow in the main detector (figure 9.1b) also shows a slight lack of forward energy flow in the data, but the overall shape is well reproduced by the Monte Carlo simulation.
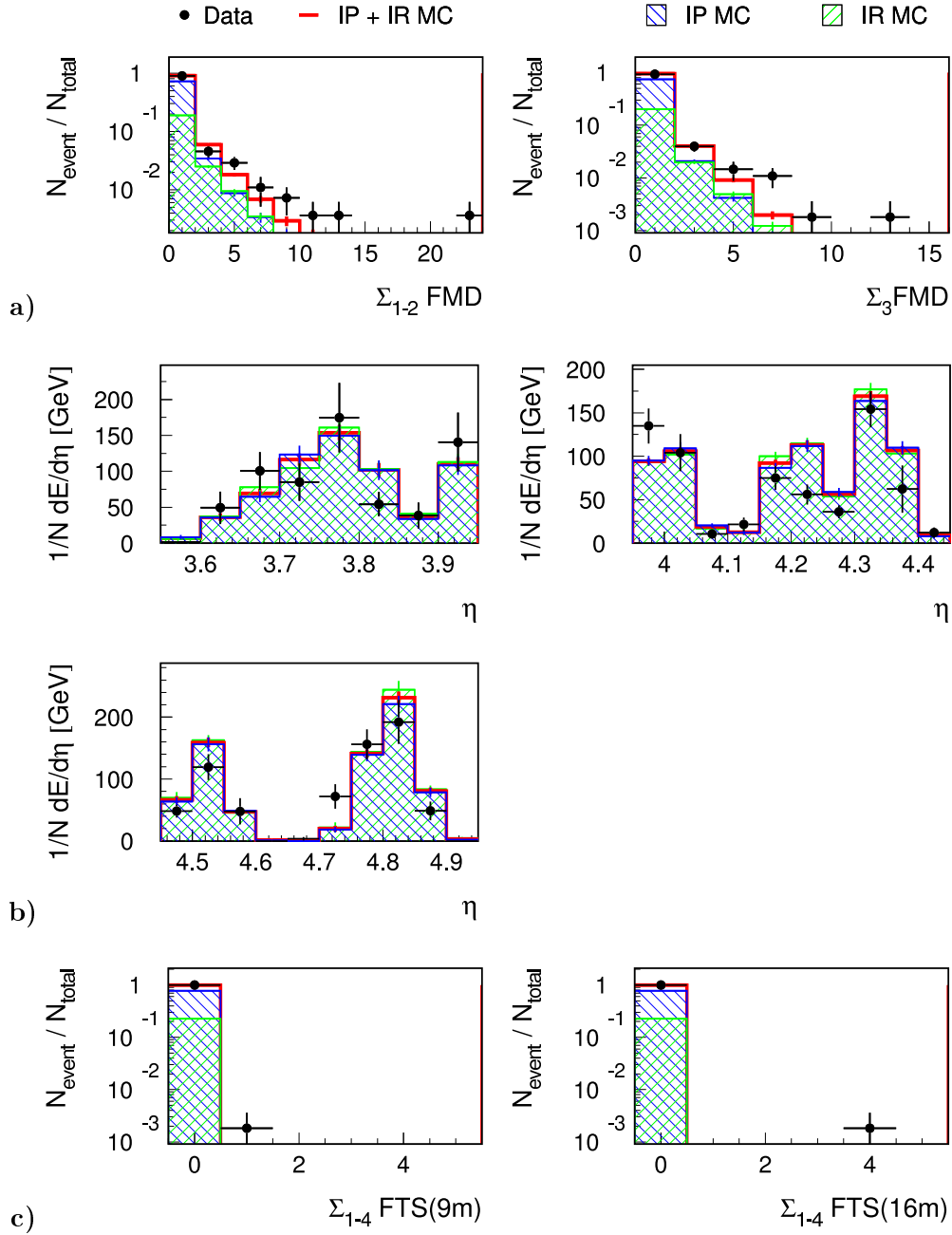
Figure 9.2: The forward energy flow in inclusive data and Monte Carlo events. **a)** Number of hit pairs per event in the FMD. **b)** Total energy flow in the three Plug calibration bins after the noise reduction cuts (cf section 5.1). **c)** Number of hits per event in the FTS.

Both distributions of the hit pairs in the FMD (figure 9.2a) are reasonably well described within the statistical uncertainties. The slight excess of data events with many hit pairs in the FMD might result from overlay events which are not removed by the cut on $\sum_f \left(E_f + p_{f_z} \right)$ (cf section 4.3.3).

Both FMD distributions also indicate that Pomeron and Reggeon exchange processes are needed to describe the data. They show that events with Reggeon mediated interactions are generally more forward than Pomeron exchange events, and that their fractional contributions are reasonably well described by the Monte Carlo simulation. A variation of the Pomeron and Reggeon contributions would again fail to provide a better description of the data (cf section 8.6.1). Within the large statistical uncertainties (cf sections 5.1, 6.1), the histograms of the energy flow in the Plug calorimeter (figure 9.2b) show a reasonable agreement between data and Monte Carlo distributions. Precision measurements are not possible, but the general shape and magnitude are well reproduced in the Monte Carlo simulation. As for the DIS event samples, the number of hits in the FTS allows no conclusion on the description of the data energy flow by the Monte Carlo simulation (cf section 6.1). It is thus not considered any further in this chapter.

9.2 The Singlejet Data Sample

The complete set of energy flow plots for the singlejet ($N_{jet} \geq 1$) event sample is shown in figures 9.3 and 9.4. They display a similar behaviour as for the inclusive event sample. A larger excess of
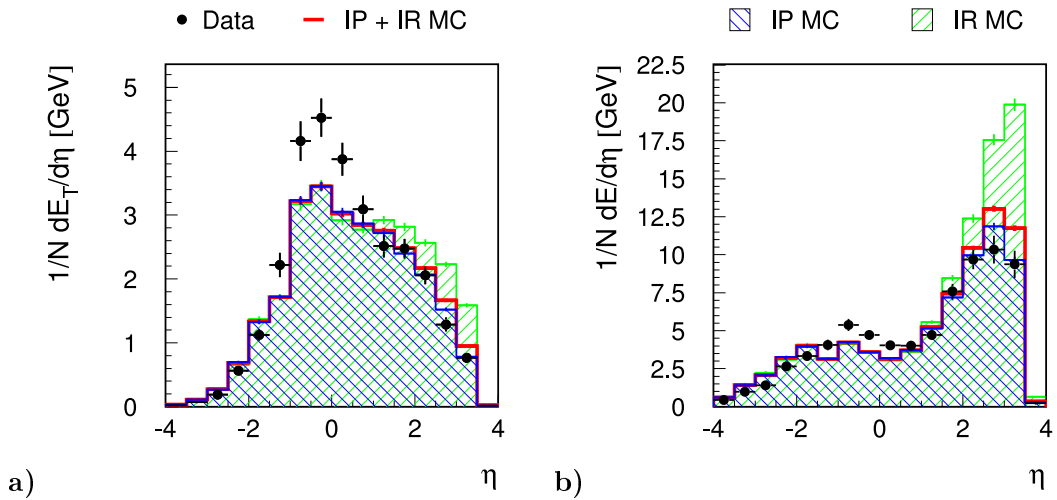
Figure 9.3: The central energy flow in the singlejet ($N_{jet} \geq 1$) data and Monte Carlo events. **a)** Transverse, and **b)** total energy flow in the main detector (LAr and SpaCal).

transverse energy (figure 9.3a) is observed in the data around $\eta \sim -0.5$. The shape of the total energy flow (figure 9.3b) is also less well described than for the inclusive event sample. Besides the lack of forward energy flow in the data, an energy excess is observed in the data around $\eta \sim -0.5$. Both effects – in transverse and total energy flow – are consistent, with the observed excess of transverse energy in the hadronic final state (cf section 8.6.2). A slight excess of transverse energy flow is also exhibited by the jet profiles which show that the jets are wider in the data than in the Monte Carlo simulation. Any differences in the jet profile with respect to $\Delta\phi$ might be caused by the different FPS acceptances in data and Monte Carlo simulation (cf section 6.2).
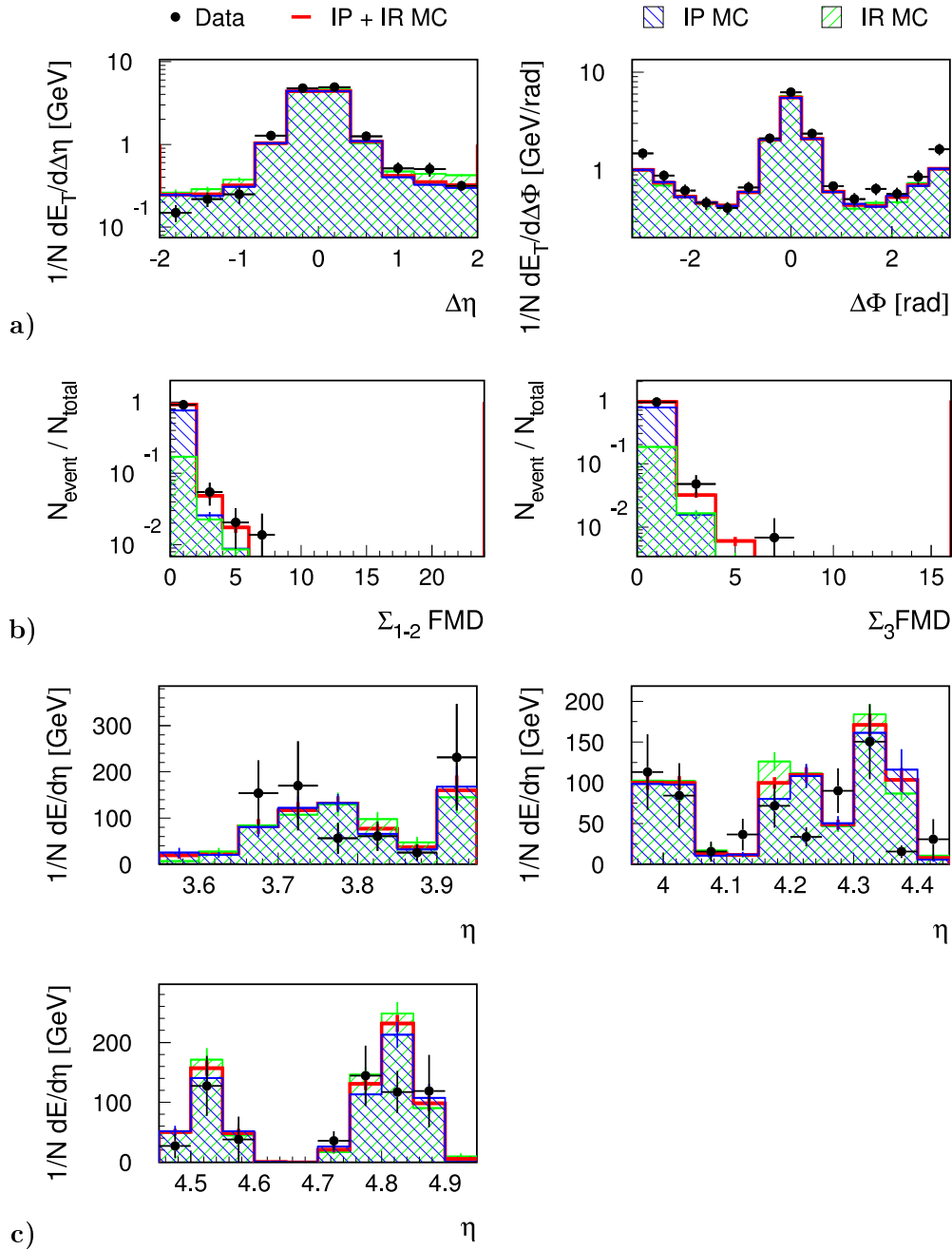
Figure 9.4: The jet and the forward energy flow in the singlejet ($N_{jet} \geq 1$) data and Monte Carlo events. **a)** Transverse energy flow relative to the leading jet (jet profile). **b)** Number of hit pairs per event in the FMD. **c)** Total energy flow in the three Plug calibration bins after the noise reduction cuts (cf section 5.1).

Both FMD distributions agree very well in the data and the Monte Carlo simulation. They show that Pomeron and Reggeon exchange processes are necessary to describe the data, and that their fractional contributions are well described by the Monte Carlo simulation. A variation of these contributions would fail to produce a better agreement between data and Monte Carlo simulation. Within the further increased statistical uncertainties, the energy flow distributions in the Plug calorimeter (figure 9.4c) are well reproduced by the Monte Carlo simulation.

9.3 The Dijet Data Sample

Figures 9.5 and 9.6 show the complete set of energy flow plots for the dijet ($N_{jet} \geq 2$) event sample. Due to the high fraction of dijet events in the singlejet event sample (cf section 8.3), no significant
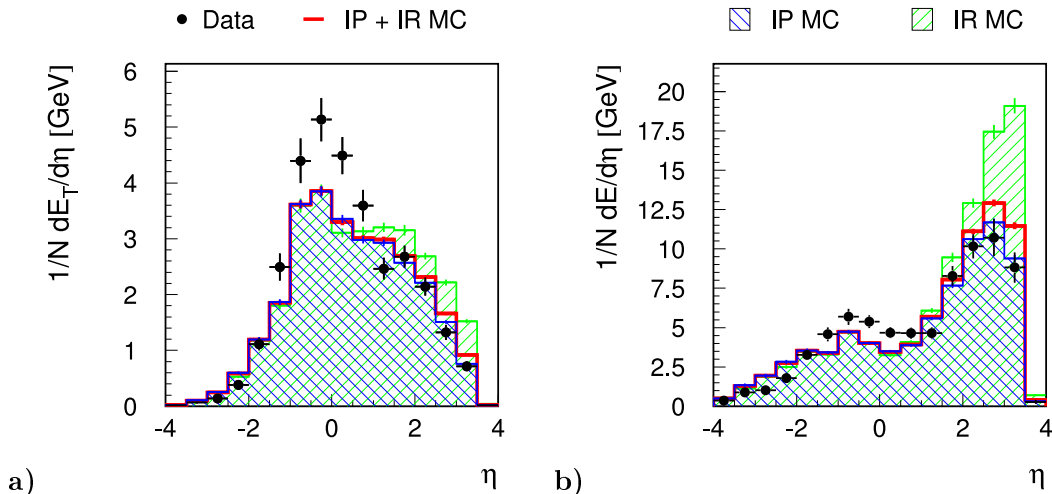
Figure 9.5: The central energy flow in the dijet ($N_{jet} \geq 2$) data and Monte Carlo events. **a)** Transverse, and **b)** total energy flow in the main detector (LAr and SpaCal).

changes are observed between the singlejet and the dijet energy flow distributions. Similar deviations in the transverse and total energy flow in the main detector, and in the jet profiles are visible.

As for the description of the event variables (cf section 8.8), a variation of the Pomeron and Reggeon contributions to the Monte Carlo simulation cannot resolve the observed discrepancies in the energy flow histograms (cf sections 9.1, 9.2). Direct and resolved photon contributions have distinctly different energy flow distributions – resolved photon events are generally more forward than direct photon processes (cf section 8.7). A variation of their relative contributions to the Monte Carlo samples might thus result in a better description of the data. This is investigated in the next section.
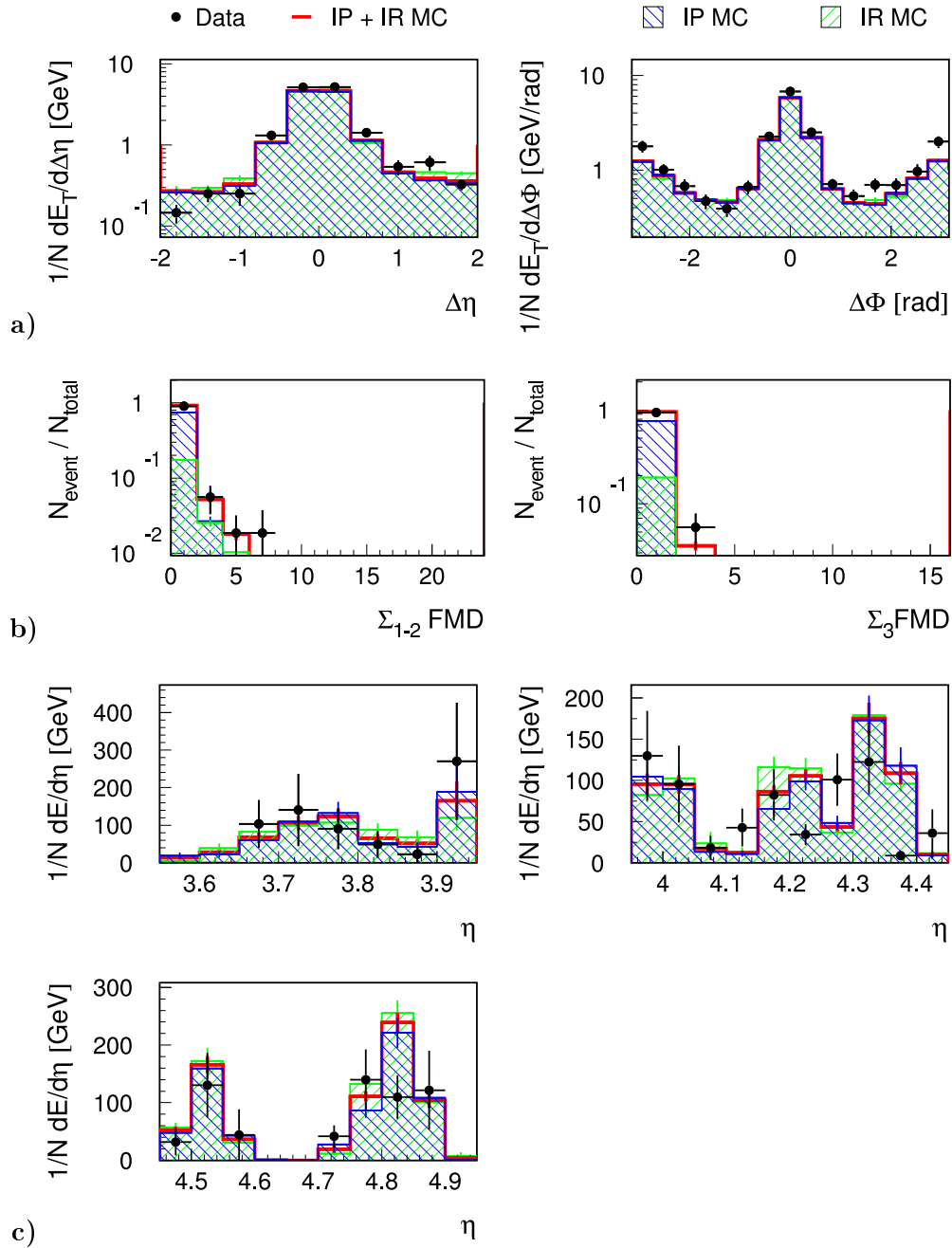
Figure 9.6: The jet and the forward energy flow in the dijet ($N_{jet} \geq 2$) data and Monte Carlo events.
a) Transverse energy flow relative to the leading jet (jet profile). **b)** Number of hit pairs per event in the FMD. **c)** Total energy flow in the three Plug calibration bins after the noise reduction cuts (cf section 5.1).

9.4 Energy Flow in Direct and Resolved Photon Processes

This section examines the energy flow in the main detector in terms of the contributions of direct and resolved photon processes. The dark hatched histograms represent resolved photon interactions, while the light hatched graphs symbolise direct photon reactions. Black points illustrate the energy flow in the data, and the open histogram shows the complete Monte Carlo distributions.

9.4.1 The Inclusive Event Sample

Figure 9.7 displays the energy flow in resolved and direct photon processes within the inclusive photoproduction event sample. Both plots show that direct photon processes are less forward than resolved
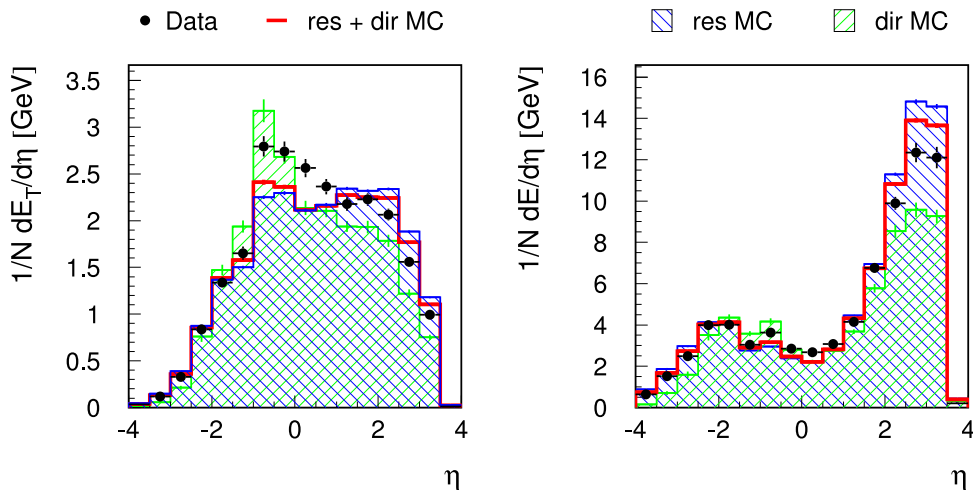
Figure 9.7: Energy flow in direct and resolved photon processes within the inclusive photoproduction event sample. Both plots show the data, the complete Monte Carlo sample, the resolved (dark hatched), and the direct (light hatched) photon contributions.

photon reactions, a conclusion which can also be drawn from the η_{max}-distribution (cf section 8.7.1). A better description of the data could be achieved by increasing the direct photon contribution to the Monte Carlo simulation. However, both diagrams also show that a huge increase of direct photon reactions – by at least a factor of two – would be needed to obtain a reasonable agreement between data and Monte Carlo distributions. And although this would ameliorate the description of many data distributions, significant discrepancies would remain in other variables, especially the total transverse energy, $E_{\perp}^{total}$ (cf section 8.7).

This suggests that underestimation of the direct photon contribution is not the only – and probably not the dominant – reason for the observed discrepancies between data and Monte Carlo distributions in the photoproduction event sample.

9.4.2 The Singlejet Event Sample

The direct and resolved photon contributions to the transverse and total energy flow in the main detector are presented in figure 9.8 for the singlejet ($N_{jet} \geq 1$) event sample. They show a similar behaviour as for the inclusive event sample. A better agreement between data and Monte Carlo distributions could be achieved by strongly increasing the direct photon contribution. However, some major discrepancies, eg in $E_{\perp}^{total}$, and the transverse momenta of the jets (cf section 8.7), would not be resolved by this procedure.
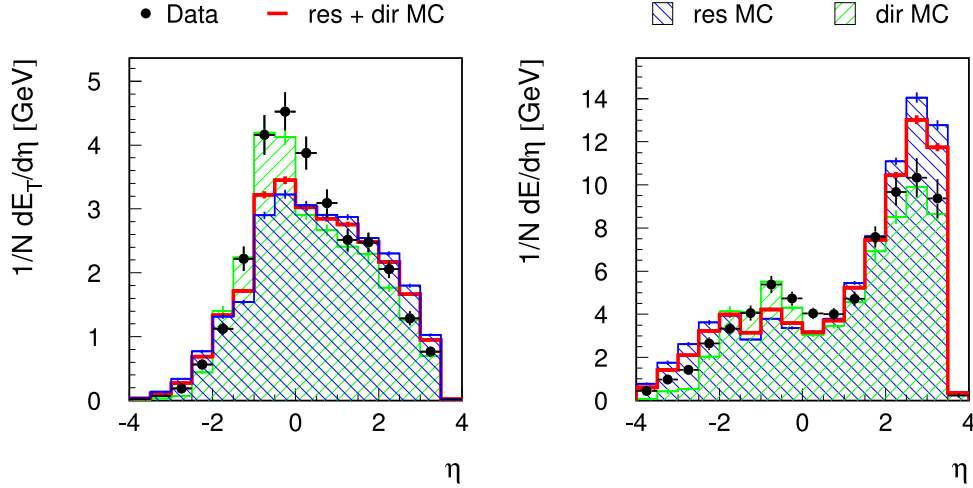
Figure 9.8: Energy flow in direct and resolved photon processes within the singlejet ($N_{jet} \geq 1$) photoproduction event sample. Both plots show the data, the complete Monte Carlo sample, the resolved (dark hatched), and the direct (light hatched) photon contributions.

9.4.3 The Dijet Event Sample

Figure 9.9 displays the central energy flow of the direct and resolved photon processes in the Monte Carlo simulation for the dijet ($N_{jet} \geq 2$) event sample. Apart from the slightly increased statistical
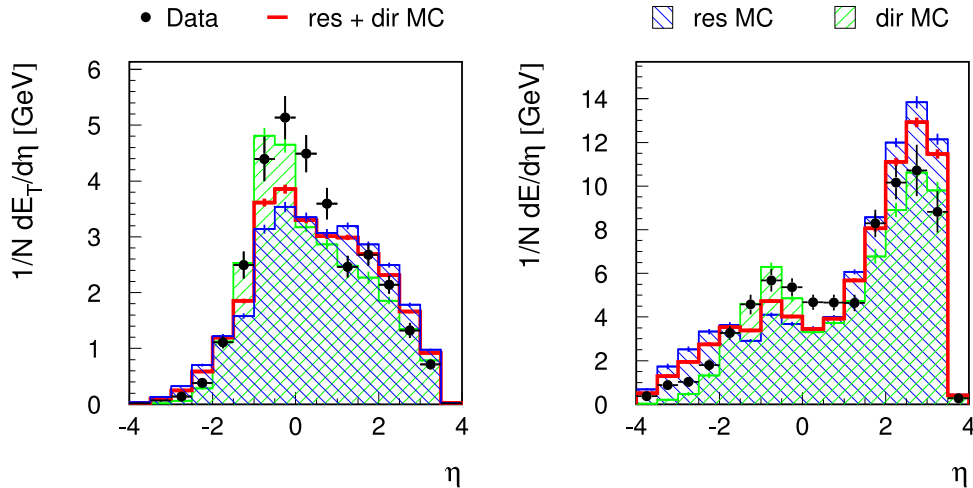
Figure 9.9: Energy flow in direct and resolved photon processes within the dijet ($N_{jet} \geq 2$) photoproduction event sample. All plots show the data, the complete Monte Carlo sample, the resolved (dark hatched), and the direct (light hatched) photon contributions.

uncertainties, they exhibit the same behaviour as in the case of the singlejet energy flow distributions.

9.5 Summary of the Energy Flow in Photoproduction Events with a Leading Proton

The description of the energy flow in photoproduction events with a leading proton is generally worse than in the case of deep-inelastic scattering (cf section 6.4). A significant excess of transverse energy in the data is observed in the central region of the main detector. The shapes of the transverse energy flow distributions in the data are not reproduced by the Monte Carlo simulation. In both jet samples, a significant excess of total data energy is observed in the central detector region, and the shapes of the total energy flow distributions differ significantly between data and Monte Carlo simulation. None of these effects can be explained by a variation of Pomeron and Reggeon contributions to the complete Monte Carlo sample. In contrast, a better description of the data could be achieved by increasing the direct photon contribution to the Monte Carlo simulation. A huge increase by at least a factor of two would be required to obtain a reasonable agreement for the energy flow distributions in the main detector. The measured discrepancies are thus consistent with the observed excess of transverse energy, $E_\perp^{total}$, in the data compared to the Monte Carlo event sample (cf section 8.8). They are probably caused by deficiencies in the QCD description of the hard scattering process, and thus not related to the description of diffractive physics within the resolved Pomeron model. This interpretation is reinforced by the fact that a reasonable description of all energy flow distributions is observed for a hard rapidity gap selected diffractive event sample, if the kinematic distributions of the Monte Carlo simulation are reweighted to agree with the measured data distributions [61].

Both, transverse and total energy flow exhibit a slight lack of data energy in the forward region of the main detector. This effect is most prominent in the inclusive event sample, and it is probably due to the general deficiencies in the description of forward energy flow by the RAPGAP generator (cf section 6.1, [56]).

All energy flow distributions in the forward detectors are reasonably well described within the statistical uncertainties. The FMD distributions show that Pomeron and Reggeon exchange processes are needed to describe the data, and that their relative contributions are reasonably well modelled by the Monte Carlo simulation. Due to the hard cut on the total transverse energy, $E_\perp^{total}$ (cf section 8.2.2), the Reggeon contribution is strongly suppressed already in the inclusive event sample.

Despite the observed differences in the central and forward regions of the main detector, the investigation of the (forward) energy flow hence shows – as for the DIS event samples (cf section 6.4) – that the data is reasonably well described by the concept of Pomeron and Reggeon remnants. This provides further support for the application of the resolved Pomeron model also in photoproduction reactions.

10 Rapidity Gap Selected Photoproduction Events

This chapter investigates the effects of the standard rapidity gap selection of diffractive events (cf section 7.1, [9]) on the description of the photoproduction data samples. The distributions of the rapidity gap variables are presented, and the description of the efficiency of the selection cuts, which is needed as correction factor in diffractive rapidity gap analyses (cf chapter 7), is examined. The description of the standard event variables in FPS (ie leading proton) and rapidity gap selected diffractive event samples is investigated, and energy flow measurements are discussed.

10.1 Rapidity Gap Selection of Diffractive Events

The rapidity gap selection has been discussed in section 7.1, and table 7.1 summarises the applied cuts. Figure 10.1 shows the relevant variables for the inclusive photoproduction event sample. All Monte Carlo distributions in this chapter are normalised using a universal normalisation factor which has been determined for the FPS event samples without rapidity gap selection (cf section 8.3). In this way, the losses of diffractive events by the rapidity gap cuts can be estimated separately for data and Monte Carlo samples (cf section 7.1.5). Each diagram in figure 10.1 is presented after the cut on the previously presented variable. The full FPS and photoproduction selections (cf tables 4.5, 8.1, 8.2) have been applied to all distributions. This allows separate investigations of each rapidity gap cut.

All data distributions are well described by the Monte Carlo simulation. η_{max} shows a slight excess of data events for $\eta > 2.0$, and a slight lack in the foremost bin. This results in a slight overestimation of the number of rejected events by the Monte Carlo simulation (cf table 10.1). A slight excess of data events with larger hit numbers is observed in the first two double layers of the FMD. The distribution of $x_{I\!P}$ also exhibits an excess of data events at large values. However, due to the rather large statistical uncertainties, none of the observed differences is statistically significant. The suppression of Reggeon exchange events by the rapidity gap selection – especially by the cut on η_{max} (cf section 8.6.1) – is visible. Three rapidity gap selected event samples are investigated in the following sections:

$$
\begin{array}{llllllllll}
\text{a) Inclusive sample} & & & & : & N_{event} & = & 220 & : & \frac{\Delta N}{N} & \sim & 6.7\ \% \\
\text{b) Singlejet sample} & N_{jet} & \geq & 1 & : & N_{event} & = & 72 & : & \frac{\Delta N}{N} & \sim & 11.8\ \% \\
\text{c) Dijet sample} & N_{jet} & \geq & 2 & : & N_{event} & = & 51 & : & \frac{\Delta N}{N} & \sim & 14.0\ \%
\end{array}
$$

All following plots in this chapter show the data and the Monte Carlo event samples after the full FPS and photoproduction selection (cf section 8.3), including the rapidity gap selection cuts. Applied jet cuts are specified for each plot individually.
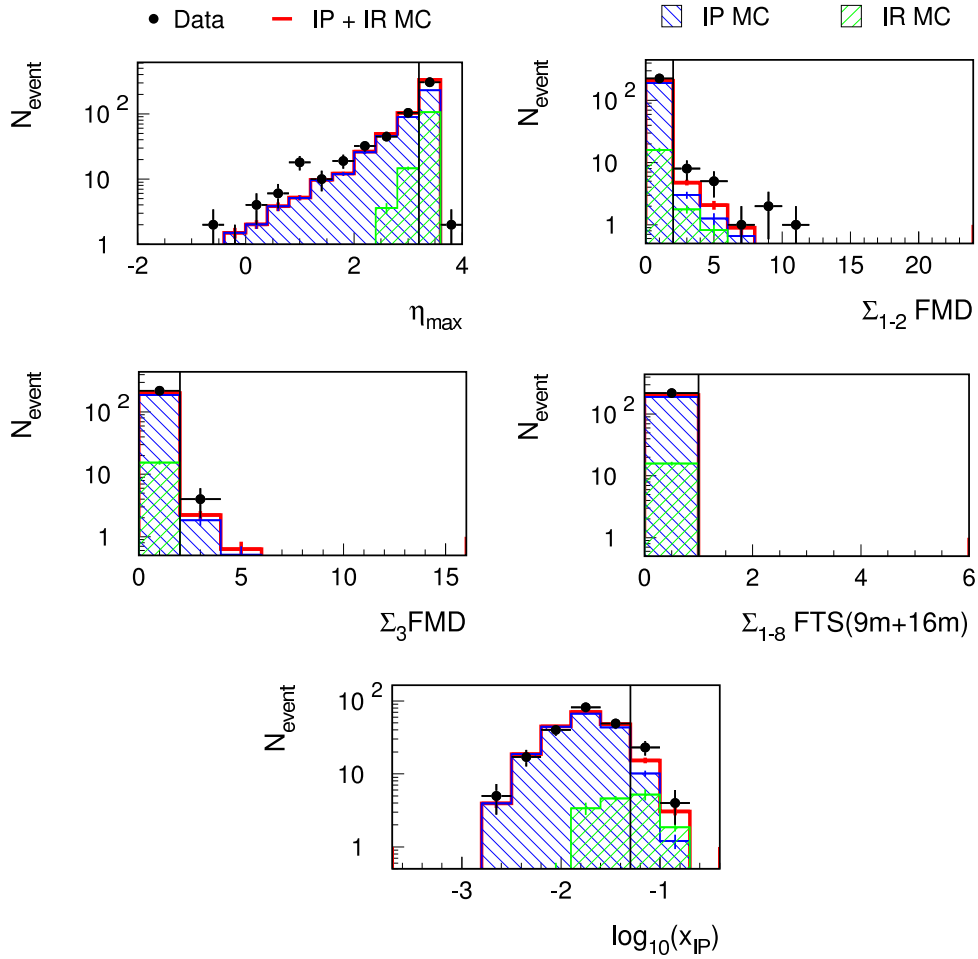
Figure 10.1: The description of the rapidity gap selection variables in the data by the Monte Carlo simulation. Each variable is displayed after the cut on the previously presented quantity. The full FPS and photoproduction selections (cf tables 4.5, 8.1, 8.2) have been applied to all displayed event samples. All Monte Carlo distributions have been normalised using the Monte Carlo normalisation factor of the FPS selected event samples without rapidity gap cuts (cf section 8.3). The rapidity gap cuts, and the cut on $x_{I\!P}$ which is not applied within this thesis, are indicated by the vertical lines.

10.2 Description of the Efficiency of the Rapidity Gap Cuts

This section examines the description of the efficiency of the rapidity gap selection. It is needed in diffractive cross section measurements to correct for the losses of diffractive events due to the rapidity gap selection. The prediction of the diffractive Monte Carlo simulation, which is used as correction factor in these analyses, is thus verified for the first time.

10.2.1 The Inclusive Photoproduction Event Sample

Table 10.1 presents the event numbers of the inclusive data and Monte Carlo event samples. It also displays the efficiency of the rapidity gap selection. A strong suppression of Reggeon mediated

Table 10.1: The efficiency of the rapidity gap selection for the inclusive photoproduction event sample. The table shows event numbers before and after the rapidity gap selection of diffractive events. It also displays the number of events after the cuts on the forward detector (FMD, FTS), but before the cut on η_{max}, $N_{event}^{forward}$, and the efficiency of the rapidity gap cuts, $\varepsilon = \frac{N_{after}}{N_{before}}$, including its statistical uncertainties.

	N_{event}^{before}	$N_{event}^{forward}$	N_{event}^{after}	ε [%]
Data	551	486	220	40 ± 3
MC	551	493	204	37 ± 3
$I\!P$	426	392	188	44 ± 4
$I\!R$	125	101	16	23 ± 6

interactions is visible, and a very slight and statistically not significant underestimation of the selection efficiency is observed for the Monte Carlo simulation.

A correction factor, f_ε, is calculated to correct the efficiency predicted by the Monte Carlo simulation to the one measured in the data. As for the DIS event samples (cf section 7.2.1), the main systematic uncertainty is due to the deficiencies in the description of the forward energy flow in the main detector within the RAPGAP generator. Since the energy flow in the forward detectors (FMD, FTS) is described well, this uncertainty is estimated by the full difference of the efficiency of the η_{max}-cut in the data and the Monte Carlo simulation, after the application of the cuts on the forward detectors:

$$f_\varepsilon = \frac{\varepsilon_{data}}{\varepsilon_{MC}} = 1.08 \pm 0.04_{syst} \pm 0.12_{stat} = 1.08 \pm 0.13$$

The predicted efficiency agrees well with the value measured for the data. The correction factor has been measured for the first time with an accuracy of 13 %.

10.2.2 The Singlejet Photoproduction Event Sample

The event numbers of the singlejet ($N_{jet} \geq 1$) data and Monte Carlo event samples are shown in table 10.2. It also presents the efficiency of the rapidity gap selection. As for the inclusive event sample, a strong suppression of Reggeon mediated interactions is visible. Due to the large statistical uncertainties, no significant differences are observed for the singlejet sample.

Estimating the systematic uncertainties as for the inclusive event sample, and adding them quadratically to the statistical uncertainties, the correction factor from Monte Carlo predicted to measured

Table 10.2: The efficiency of the rapidity gap selection for the singlejet ($N_{jet} \geq 1$) photoproduction event sample. The table shows event numbers before and after the rapidity gap selection of diffractive events. It also displays the number of events after the cuts on the forward detector (FMD, FTS), but before the cut on η_{max}, $N_{event}^{forward}$, and the efficiency of the rapidity gap cuts, $\varepsilon = \frac{N_{after}}{N_{before}}$, including its statistical uncertainties.

	N_{event}^{before}	$N_{event}^{forward}$	N_{event}^{after}	ε [%]
Data	146	128	72	49 ± 7
MC	146	133	65	44 ± 7
$I\!\!P$	116	109	61	53 ± 8
$I\!\!R$	30	24	4	23 ± 12

data efficiency, f_ε, is

$$f_\varepsilon = \frac{\varepsilon_{data}}{\varepsilon_{MC}} = 1.11 \pm 0.08_{syst} \pm 0.21_{stat} = 1.11 \pm 0.22.$$

This measurement is the first verification of the gap selection efficiency for a hard diffractive event sample, and it confirms the prediction of the Monte Carlo simulation with an accuracy of approximately 22 %. The above ratio is a crucial quantity for hard rapidity gap selected diffractive analyses, since the Monte Carlo prediction of the selection efficiency is used to correct for event losses in the data. Due to the virtually complete rejection of Reggeon exchange events, the measurement can be considered as a verification of the prediction of the gap selection efficiency for Pomeron exchange events.

10.3 Main Effects of the Rapidity Gap Selection

This section investigates the main effects of the rapidity gap selection on the description of the data by the Monte Carlo simulation. The distributions of $x_{I\!\!P}$, and the transverse energy flow in the main detector are directly compared before and after the rapidity gap selection (cf section 7.3). A more detailed discussion of the standard event variables after the rapidity gap selection of diffractive events will be presented in section 10.4.

10.3.1 The Inclusive Photoproduction Sample

Figure 10.2 presents the distributions of the data and the complete Monte Carlo event sample before (data: black points, Monte Carlo simulation: open histogram), and after (data: black triangles, Monte Carlo simulation: light hatched) the rapidity gap selection. The Pomeron and Reggeon contributions are shown in figure 10.3. They are also displayed before ($I\!\!P$: dark open histogram, $I\!\!R$: light open histogram), and after ($I\!\!P$: dark hatched, $I\!\!R$: light hatched) the rapidity gap selection. Both data distributions of $x_{I\!\!P}$ – before and after the rapidity gap cuts – are reasonably well described by the Monte Carlo simulation. Only a very slight and statistically not significant excess of data events is observed at large values after the gap cuts. Figure 10.3 displays a strong suppression of Reggeon mediated reactions by the rapidity gap cuts (cf table 10.1).

The energy flow exhibits the same excess in the data around $\eta \sim -0.5$ both, before and after the rapidity gap selection. But whereas the forward energy flow is overestimated by the Monte Carlo simulation before the rapidity gap cuts, it is reasonably well described afterwards.
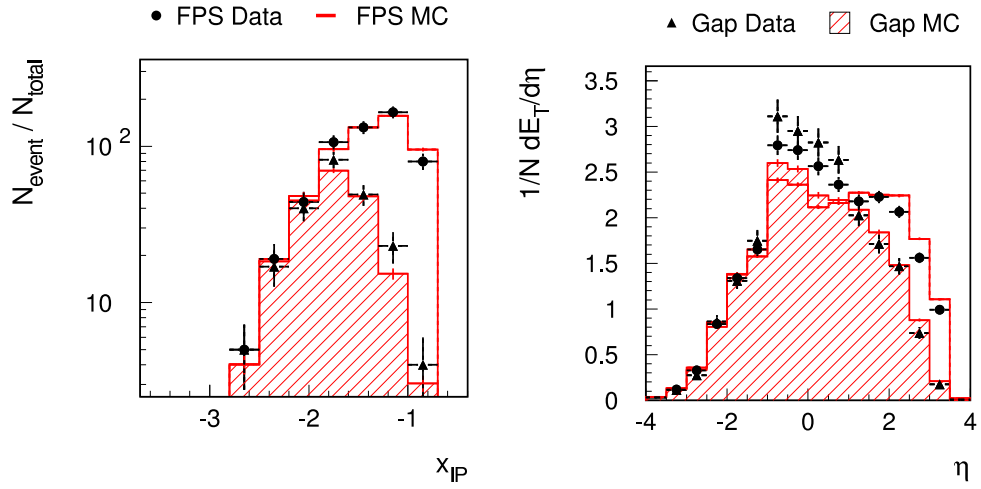
Figure 10.2: The main effects of the rapidity gap selection in the inclusive photoproduction event sample. Both plots show the data and the complete Monte Carlo samples before (data: black points, Monte Carlo simulation: open histogram), and after (data: black triangles, Monte Carlo simulation: hatched) the rapidity gap selection of diffractive events (cf table 7.1).
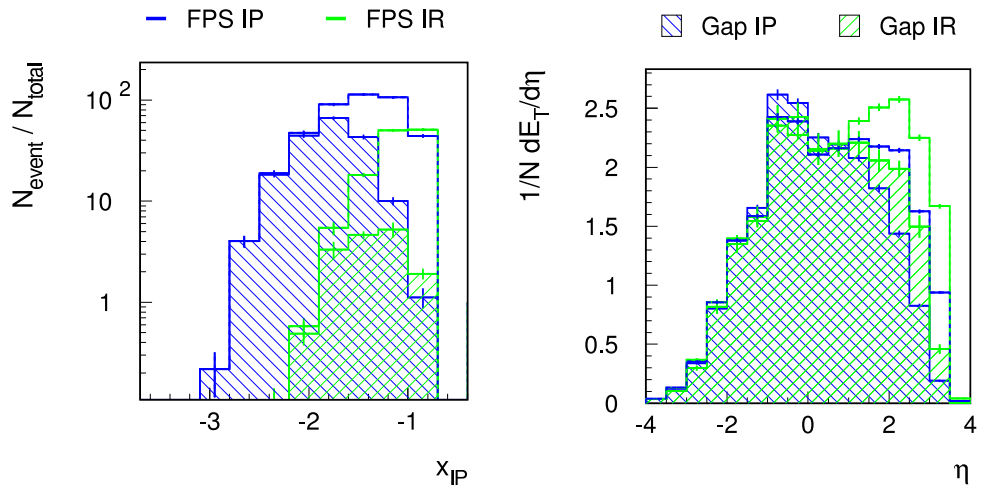
Figure 10.3: The main effects of the rapidity gap selection in the inclusive photoproduction event sample. Both plots show the Pomeron ($I\!P$) and the Reggeon ($I\!R$) contributions to the Monte Carlo sample before ($I\!P$: dark open histogram, $I\!R$: light open histogram), and after ($I\!P$: dark hatched, $I\!R$: light hatched) the rapidity gap selection of diffractive events (cf table 7.1).

10.3.2 The Singlejet Photoproduction Sample

The distributions of the data and the complete Monte Carlo simulation are shown before and after the rapidity gap selection in figure 10.4. Figure 10.5 presents the Pomeron and Reggeon contributions.
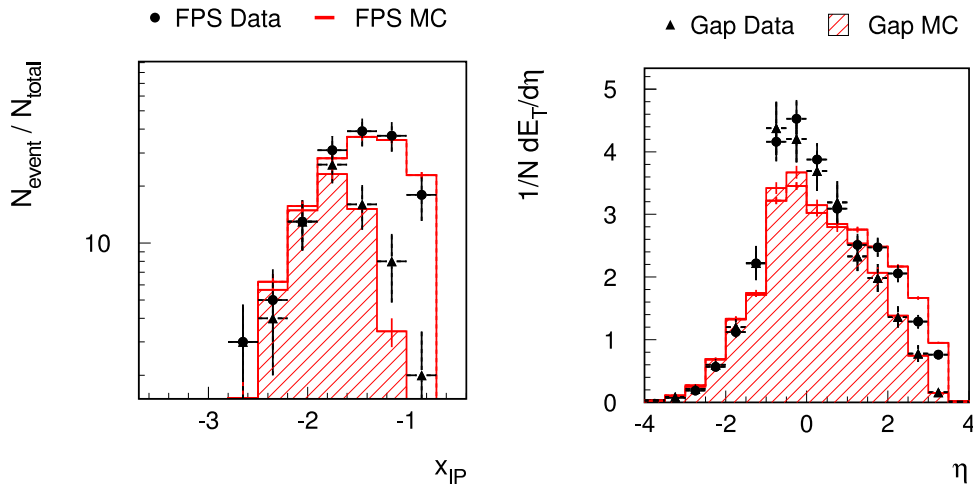
Figure 10.4: The main effects of the rapidity gap selection in the singlejet ($N_{jet} \geq 1$) photoproduction event sample. Both plots show the data and the complete Monte Carlo samples before (data: black points, Monte Carlo simulation: open histogram), and after (data: black triangles, Monte Carlo simulation: hatched) the rapidity gap selection of diffractive events (cf table 7.1).

Both, data and Monte Carlo simulated distributions display a similar behaviour as for the inclusive event sample. A slight excess of data events is still observed at large values of $x_{I\!P}$ after the rapidity gap selection (cf figure 10.4), but within the increased statistical uncertainties, the data is reasonably well described by the Monte Carlo simulation. Figure 10.5 illustrates the suppression of Reggeon mediated interactions by the rapidity gap cuts (cf table 10.2). The data energy flow exhibits a similar excess around $\eta \sim -0.5$ before and after the rapidity gap cuts, while the forward energy flow agrees well only after the rapidity gap selection (cf section 10.3.1). The dijet sample has also been investigated. All plots show a similar behaviour, and similar differences as observed for the singlejet event sample. They are thus not displayed separately.

10.4 Description of the Data by the Monte Carlo Simulation

This section investigates the description of the standard photoproduction event variables (cf section 8.6) in the data by the Monte Carlo simulation in more detail. The rapidity gap selection (cf table 7.1) has been applied to all considered event samples. In the rest of this chapter, as in section 8.6, the data is symbolised by black points, and the complete Monte Carlo sample by an open histogram. The Pomeron (dark hatched), and Reggeon (light hatched) distributions are also displayed.

10.4.1 The Inclusive Event Sample

Figure 10.6 shows the standard event variables for the inclusive event sample. The proton energy, $E_{p'}$, and the fractional longitudinal momentum transfer, $x_{I\!P}$, exhibit a slight, but not significant, excess of data events at large values of $x_{I\!P}$, ie at medium to small $E_{p'}$. All other variables exhibit discrepancies similar to the ones observed for the inclusive photoproduction sample with a leading
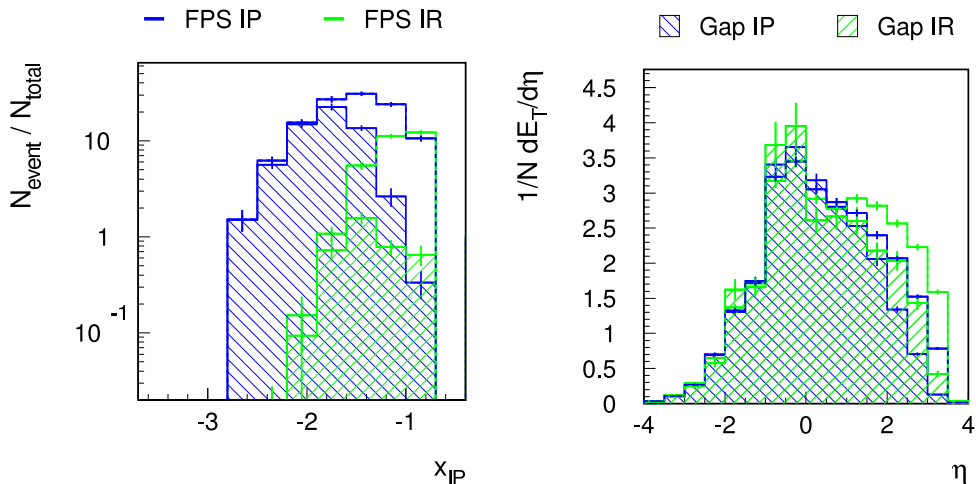
Figure 10.5: The main effects of the rapidity gap selection in the singlejet ($N_{jet} \geq 1$) photoproduction event sample. Both plots show the Pomeron ($I\!P$) and the Reggeon ($I\!R$) contributions to the Monte Carlo sample before ($I\!P$: dark open histogram, $I\!R$: light open histogram), and after ($I\!P$: dark hatched, $I\!R$: light hatched) the rapidity gap selection of diffractive events (cf table 7.1).

proton, but without rapidity gap requirements (cf section 8.6.1). The data distribution of $y_{etagger}$ is still shifted towards lower values, while the one of W_{had} displays an excess of data events at medium to large values. M_X is well described, but a significant excess of data events is observed at large $E_\perp^{total}$. This is consistent with the measured excess of multijet events in the data. η_{max} shows a slight excess of data events at lower values. As for the leading proton sample without rapidity gap cuts (cf section 8.6.1), the differences are probably caused by deficiencies in the QCD description of the scattering process, and are thus probably not related to the description of diffractive physics within the resolved Pomeron model (cf section 8.6.1).

10.4.2 The Singlejet Event Sample

The standard event variables are shown in figure 10.7 for the singlejet ($N_{jet} \geq 1$) event sample. They exhibit a similar behaviour as for the inclusive event sample. Due to the increased statistical uncertainties, $y_{etagger}$ is reasonably well described, but the discrepancies in W_{had}, η_{max}, and particularly in $E_\perp^{total}$ are still observed. In agreement with the photoproduction sample without rapidity gap cuts (cf section 8.6.2), a significant excess of multijet events compared to events with one or two jets is observed. This is consistent with the discrepancies measured for the jet variables of the leading jet which are presented in figure 10.8. The transverse momentum, $p_\perp^{jet\ 1}$, shows a considerable excess of data events with large values, and a slight backward shift of the data distribution is observed for $\eta_{lab}^{jet\ 1}$. All of these discrepancies show that the hard scattering process is not well described by the Monte Carlo simulation.

10.4.3 The Dijet Event Sample

As for the FPS selected event sample (cf section 8.6.3), only the jet variables for the first and the second jet are displayed in figure 10.9.
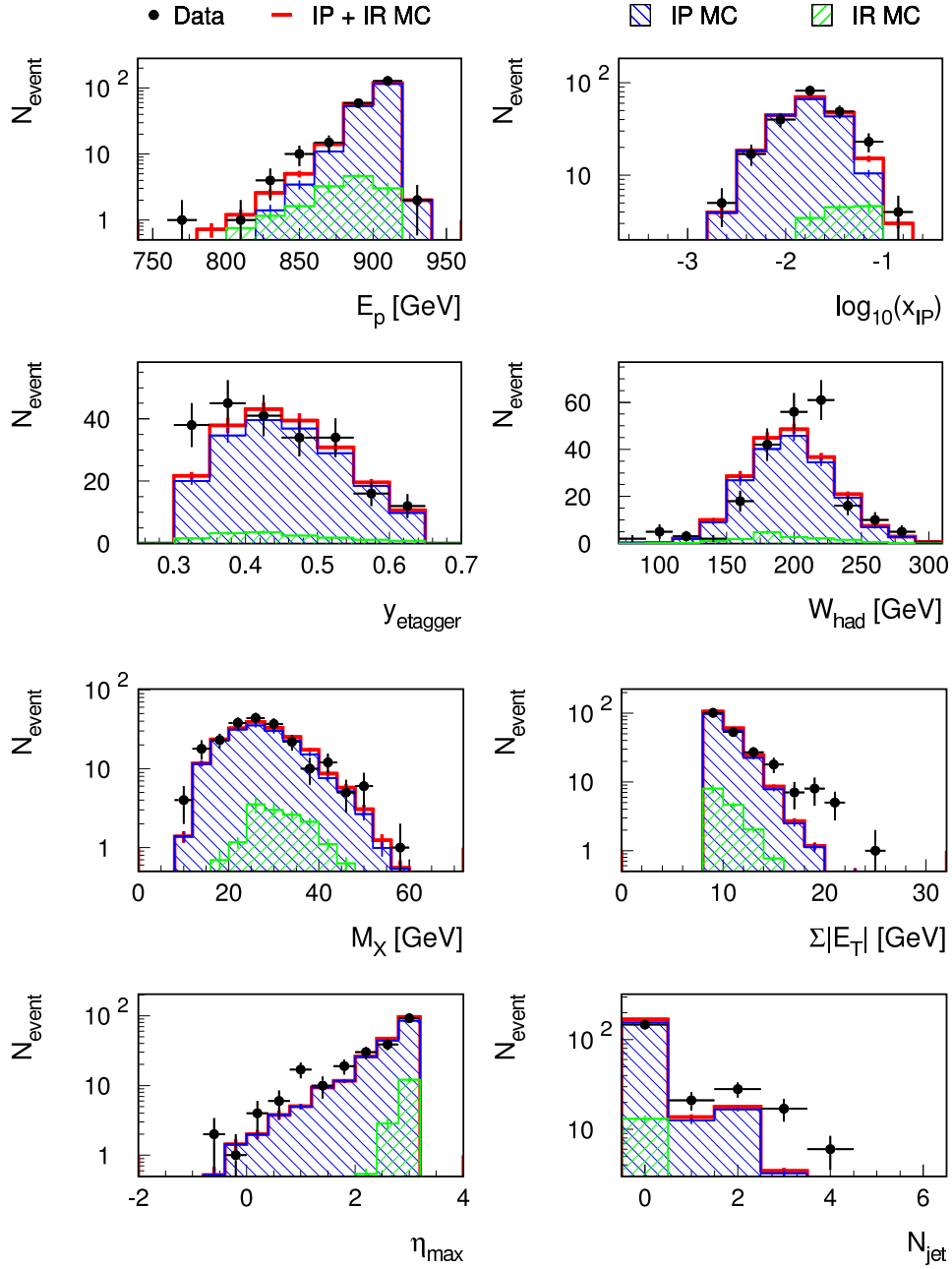
Figure 10.6: The description of the standard event variables in the photoproduction data by the Monte Carlo simulation. All histograms show the inclusive event samples.
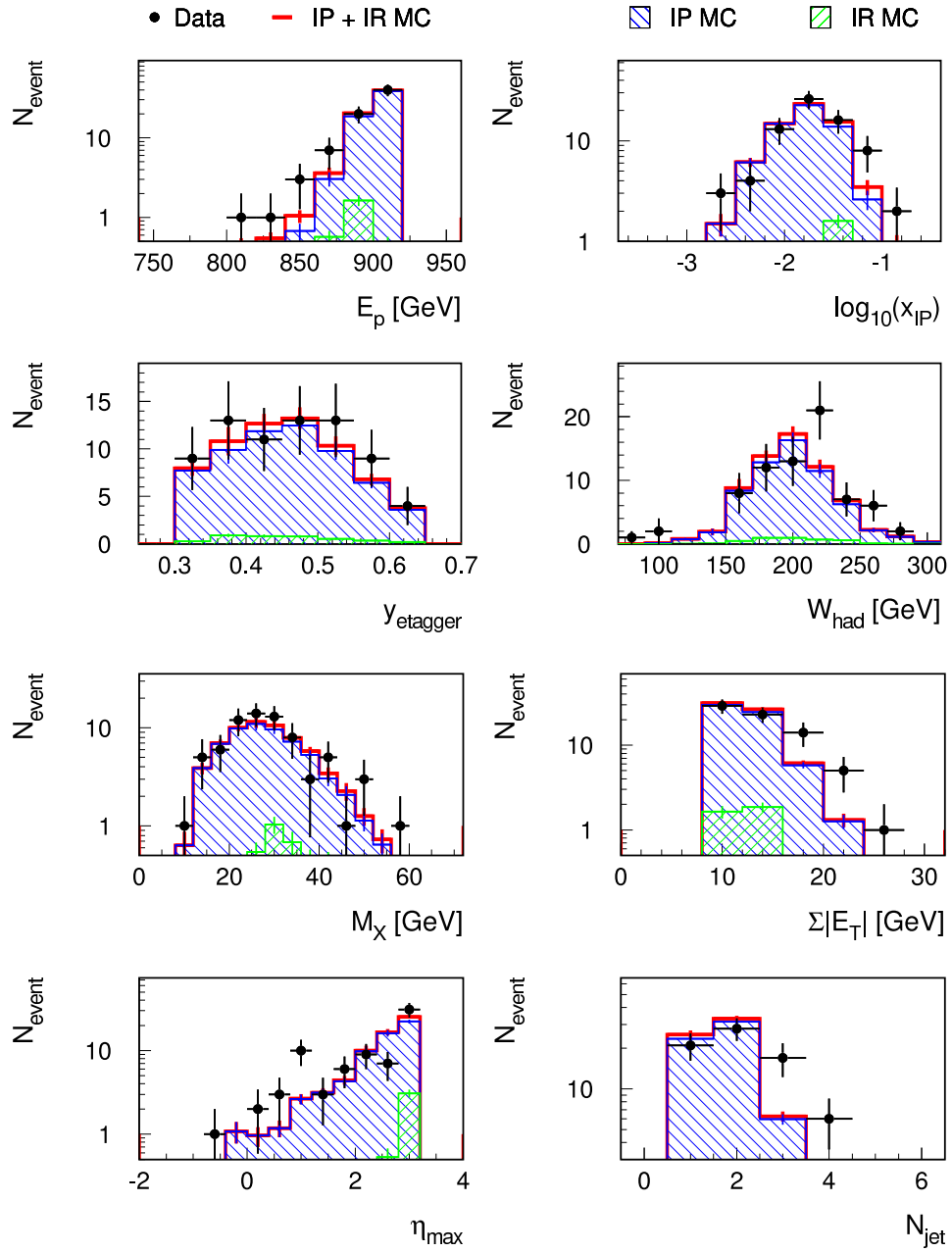
Figure 10.7: The description of the standard event variables in the photoproduction data by the Monte Carlo simulation. All histograms show the singlejet ($N_{jet} \geq 1$) event samples.
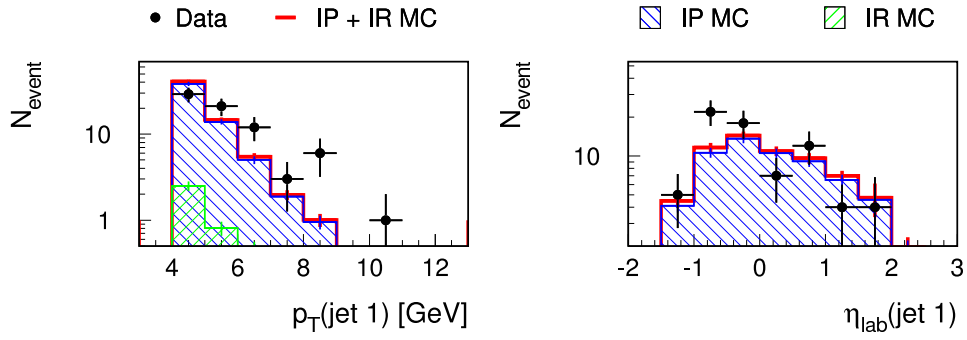
Figure 10.8: The jet variables for the first jet in the γp singlejet ($N_{jet} \geq 1$) event samples.
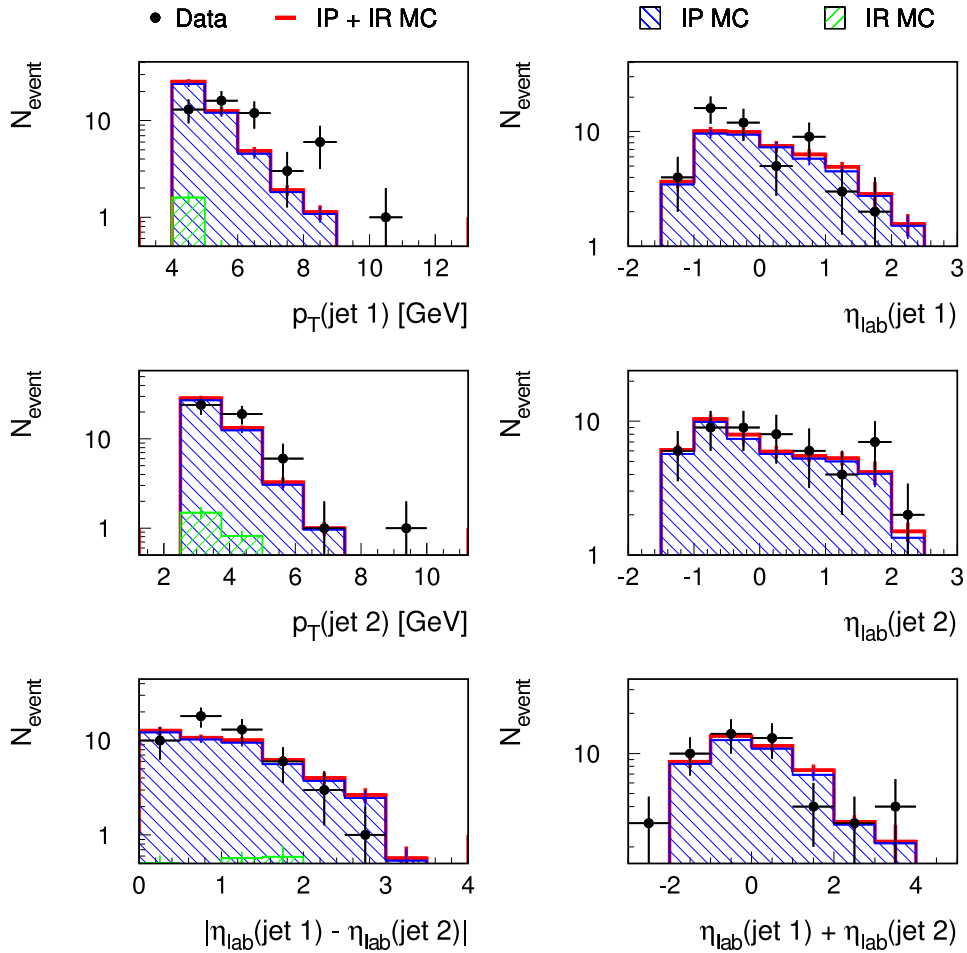
Figure 10.9: The jet variables for the first and the second jet in the dijet ($N_{jet} \geq 2$) γp event samples.

Due to the large fraction of multijet events in the singlejet sample, the distributions of the leading jet exhibit the same effects as in the singlejet event sample. The second jet is generally better described than the first one. Only a slight excess of high-$p_\perp$ jets is observed. Both $\left| \eta_{lab}^{jet\ 1} - \eta_{lab}^{jet\ 2} \right|$, and $\left(\eta_{lab}^{jet\ 1} + \eta_{lab}^{jet\ 2} \right)$ are described well within the large statistical uncertainties.

10.5 Energy Flow in Rapidity Gap Selected Diffractive Photoproduction Events

The energy flow is discussed after the standard rapidity gap selection of diffractive events. Since there is – per defintion – no energy flow in the forward detectors (FMD, FTS, and Plug calorimeter, cf section 10.1), only the energy flow in the main detector (LAr and SpaCal calorimeters) is presented. As for the event sample without rapidity gap cuts (cf section 9), all energy flows are measured in the laboratory system.

10.5.1 The Inclusive Data Sample

The transverse (a), and total (b) energy flow are shown in figure 10.10 for the inclusive event samples. They exhibit the same discrepancies as in the case of the photoproduction event sample without
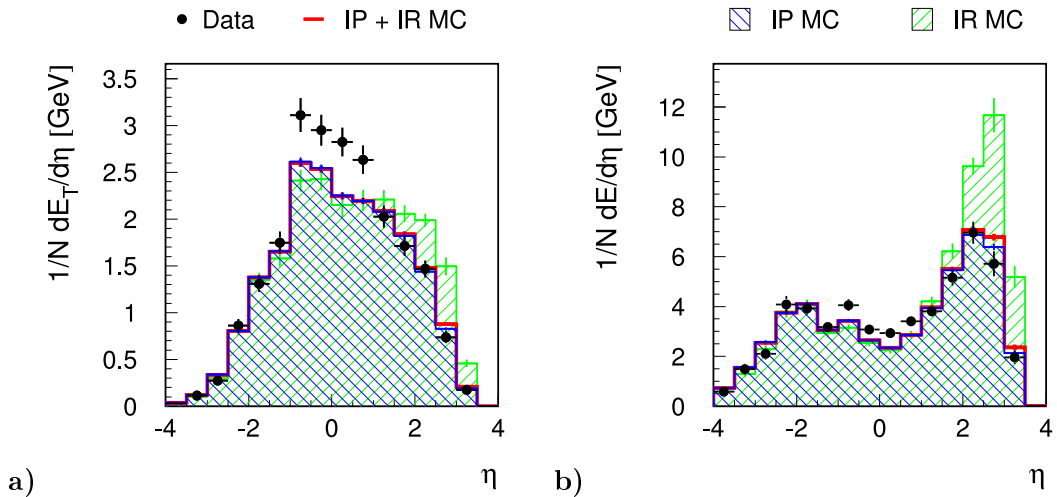
Figure 10.10: The energy flow in the inclusive photoproduction data and Monte Carlo events. **a)** Transverse, and **b)** total energy flow in the main detector (LAr and SpaCal).

rapidity gap cuts (cf section 9.1). A considerable excess of transverse data energy flow (a) is observed around $\eta \sim 0$. The total energy flow (b) also displays a slight excess in the data around $\eta \sim 0$. This is consistent with the measured excess of data events with high transverse energies, $E_\perp^{total}$ (cf figure 10.6). In contrast to the event sample without rapidity gap selection (cf figure 9.1), only a very slight lack of forward energy is observed in the main detector for both, the transverse (a), and the total (b) energy flow. Within the statistical uncertainties, the forward energy flow is described reasonably well.

10.5.2 The Singlejet Data Sample

Figure 10.11 displays the transverse (a) left), and total (a) right) energy flow, and the jet profiles of the leading jet (b) for the singlejet ($N_{jet} \geq 1$) event sample. Both, transverse and total energy flow
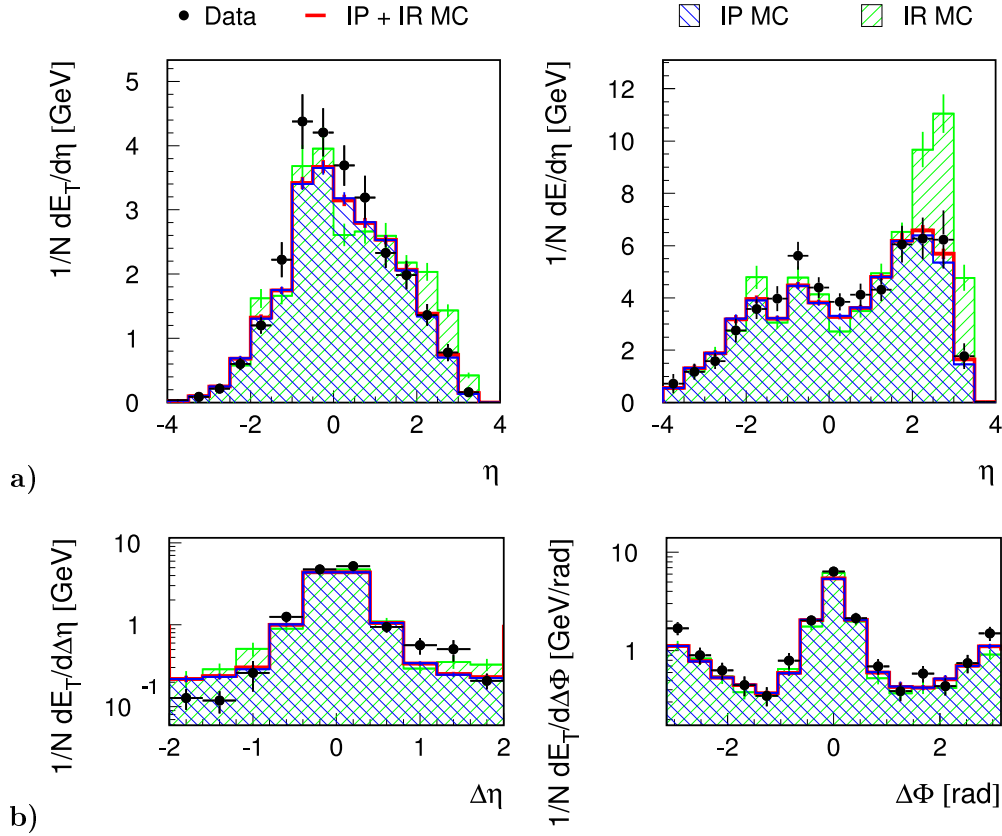
Figure 10.11: The energy flow in the singlejet ($N_{jet} \geq 1$) photoproduction data and Monte Carlo events. **a)** Transverse (left), and total (right) energy flow in the main detector (LAr and SpaCal). **b)** Transverse energy flow relative to the leading jet (jet profile).

exhibit similar differences between data and Monte Carlo simulation as the inclusive event sample, and as in the case of the singlejet event samples without rapidity gap cuts (cf section 9.2). An excess of transverse and total is observed in the data around $\eta \sim -0.5$. In contrast to the event samples without rapidity gap cuts, the forward energy flow in the main detector is well described by the Monte Carlo simulation. Any deviations in the jet profile with respect to $\Delta\phi$ might be caused by the different FPS acceptances in data and Monte Carlo simulation (cf section 6.2). The jet profiles show a slight excess of data energy before, and a slight lack behind the leading jet. Due to the increased statistical uncertainties, none of the observed deviations is statistically significant.

10.5.3 The Dijet Data Sample

The transverse (a) left), and the total (a) right) energy flow are presented in figure 10.12 for the dijet ($N_{jet} \geq 2$) event samples. It also shows the jet profiles of the leading jet (b). All plots display a very similar behaviour as in the case of the singlejet event sample, and as for the dijet event sample without rapidity gap cuts (cf section 9.3). The excess of total energy flow in the data around $\eta \sim -0.5$ has increased slightly compared to the singlejet event sample (cf figure 10.11). A slight lack of total data energy is observed in the backward region around $\eta \sim -2.5$. All other deviations remain basically unchanged.

In order to estimate the significance of the observed, statistically limited differences between data and Monte Carlo simulation, the energy flow measured in the above discussed rapidity gap selected diffractive events with a leading proton is compared to the energy flow measured in rapidity gap
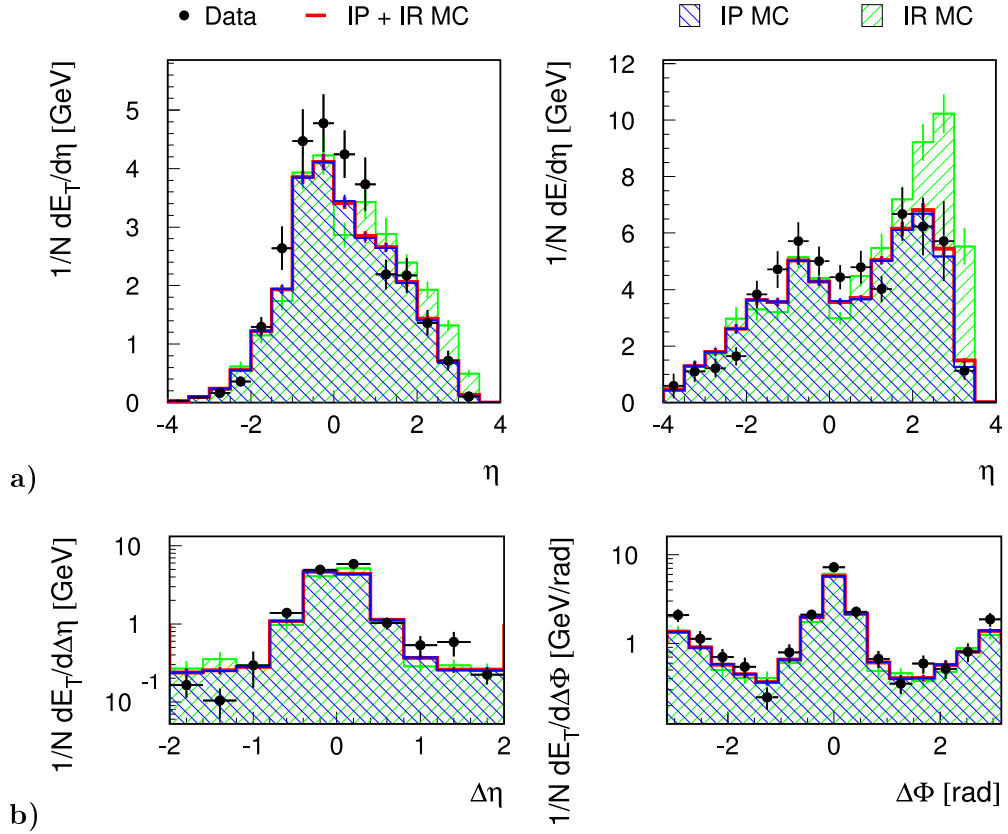
Figure 10.12: The energy flow in the dijet ($N_{jet} \geq 2$) photoproduction data and Monte Carlo events. **a)** Transverse (left), and total (right) energy flow in the main detector (LAr and SpaCal). **b)** Transverse energy flow relative to the leading jet (jet profile).

selected diffractive events without a leading proton. Due to the restricted acceptance of the horizontal FPS (cf section 3.2.2), the latter event sample contains much more events, leading to much smaller relative statistical uncertainties.

Rapidity Gap Selected Dijet Sample with Large Event Numbers

Figure 10.13 presents the absolute total energy flow, and the transverse energy flow with respect to the leading jet in a large ($N_{event} = 843$) diffractive dijet photoproduction sample. The plots have been provided by Sebastian Schätzel who investigates diffractive dijet photoproduction within the context of his PhD thesis [61]. The displayed data were recorded in 1997, and are subjected to the standard photoproduction and rapidity gap selections (cf tables 7.1, 8.1). No scattered leading proton is required. A cut on $x_{I\!P}$ is used to enhance Pomeron mediated exchange processes ($x_{I\!P} < 0.03$, cf section 7.1.4). Jets are selected with transverse momenta, $p_{\perp}^{jet\ 1} > 5.0$ GeV, $p_{\perp}^{jet\ 2} > 4.0$ GeV in the detector range $|\eta| < 1.0$ [61].

Taking into account the additional cut on $x_{I\!P}$ which further rejects events with high forward energy flow (cf section 8.6), and the different detector ranges for the measured jets ($|\eta| < 1.0$ compared to $-1.5 < \eta < 2.5$), a similar behaviour is observed as for the above discussed leading proton dijet event sample (cf figure 10.12). The data display an energy excess around $\eta \sim -0.5$, and a lack of energy flow in the forward and backward detector region. The much reduced forward energy flow compared to the above discussed sample with a leading proton is caused by the additional restrictions on $x_{I\!P}$, and η_{jet}. The jet profiles exhibit slightly harder jets in the data compared to the Monte Carlo simulation.
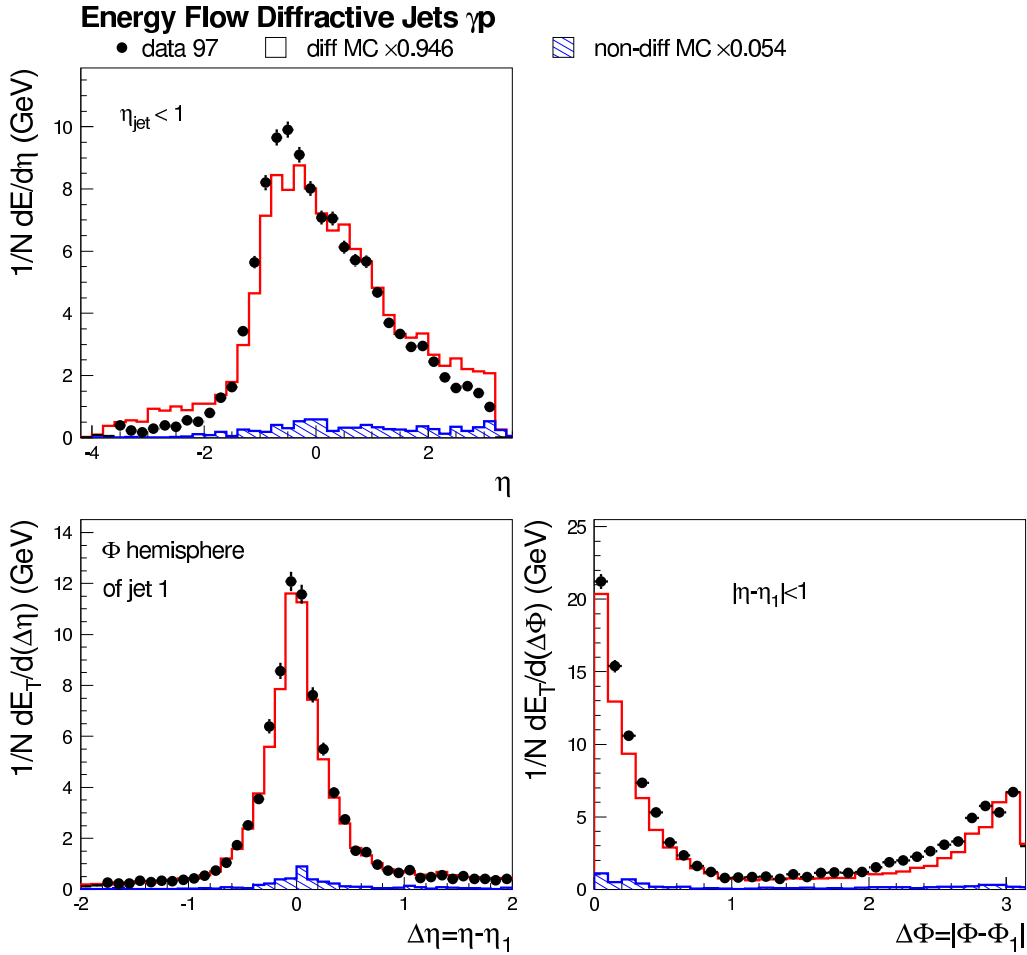
Figure 10.13: Energy flow in a rapidity gap selected diffractive dijet ($N_{jet} \geq 2$) event sample. The plots show the total energy flow (top), and the jet profiles of the leading jet with respect to $\Delta\eta$ (bottom left) and $\Delta\phi$ (bottom right). Black points represent the data, the complete Monte Carlo sample is displayed by the open histogram. The hatched histogram illustrates the non-diffractive background. (From [61].)

This comparison confirms that the observed deviations between data and Monte Carlo simulation in FPS selected events are not an artefact of the data selection, or a statistical fluctuation, but a genuine deficit of the RAPGAP generator.

10.6 Summary of the Effects of the Rapidity Gap Selection

In this chapter, a rapidity gap selection of diffractive events has been applied to the diffractive photoproduction event samples with a leading proton (cf chapters 3, 8, 9). The selection is based on the forward energy flow in the main and the forward detectors. It follows a standard procedure used to select diffractive interactions at the H1 detector (eg [9], cf [58]). The description of the following data event samples has been investigated after the rapidity gap selection cuts (cf tables 4.5,8.1, 8.2,

4.2):

a) Inclusive sample				:	N_{event}	=	220
b) Singlejet sample	N_{jet}	$\geq$	1	:	N_{event}	=	72
c) Dijet sample	N_{jet}	$\geq$	2	:	N_{event}	=	51

Despite the major differences in the transverse energy flow in the main detector (cf section 9.1), and in related variables, the quantities which are relevant for the rapidity gap selection are reasonably well described by the Monte Carlo simulation based on the resolved Pomeron model (cf section 10.1). As for the DIS event samples (cf section 7.2), the predicted efficiencies of the gap selection cuts have been compared to the ones measured in the data for the first time. They agree within an accuracy of 13 % for the inclusive, and 22 % for the hard jet event sample. The predicted efficiency in the hard jet sample is used within the standard rapidity gap analyses of hard diffractive scattering to correct for the diffractive event losses due to the selection cuts.

The differences observed for all FPS events also persist after the rapidity gap selection. Significant excesses in the data are observed at high transverse energies, $E_\perp^{total}$, at high transverse jet momenta, $p_\perp^{jet\ 1,2}$, and for the central energy flow in the main detector. A better description of the data could still be achieved by increasing the direct photon contribution to the Monte Carlo simulation (cf section 8.7).

The independence of the observed differences from the gap selection supports the interpretation of QCD deficiencies in the description of the hard scattering process as the reason for the observed disagreements. It is further supported by the observation that all energy flow distributions are well described for a hard rapidity gap selected diffractive event sample, if the kinematic Monte Carlo distributions are reweighted to describe the data. The differences are thus probably not related to the description of diffractive physics within the resolved Pomeron model. In consequence, it is noted that – despite the observed deviations in the central energy flow in the main detector – the simple leading order Monte Carlo simulation describes the efficiency and the effects of the rapidity gap selection well. This is a further support for the resolved Pomeron model, which is used within the RAPGAP Monte Carlo generator.

11 Discussion of the Results and Conclusions

11.1 Deep-Inelastic Scattering

Due to the limited acceptance of the Forward Proton Spectrometer, the number of events with a scattered leading proton is also limited. An inclusive event sample with moderate cuts has therefore been investigated in addition to the hard jet samples (singlejet, and dijet). All of these samples are well described in shape by a hard leading order Monte Carlo simulation which is based on the resolved Pomeron model, and which includes the diffractive parton density functions as determined from the H1 measurement of the diffractive structure function, F_2^D.

The Pomeron and Reggeon fractions have been estimated for the inclusive and singlejet DIS data samples. They show a good agreement with the prediction based on the inclusive measurement of F_2^D. No agreement is possible without a significant Reggeon contribution to the Monte Carlo simulation. The prediction of the F_2^D analysis for the ratio of the Reggeon to the Pomeron contribution has been verified by a direct measurement with an accuracy of 10 % for the inclusive event sample. The event kinematics are well described in shape by the Monte Carlo simulation for all three investigated event samples.

The measurement of the forward energy flow allows to test the predictions of the resolved Pomeron model – ie the description of the Pomeron remnant – in the forward detector region. This is only possible with FPS selected diffractive events with a scattered leading proton. The forward energy flow, and the hits in the forward detectors are all well described within the statistical uncertainties. Slight differences are observed in the Liquid Argon calorimeter. They are most likely caused by known effects of QCD dynamics which are also observed in non-diffractive deep-inelastic scattering, and they are probably not connected to the description of the diffractive physics within the resolved Pomeron model. The resolved Pomeron model thus works very well, and provides a good description of the observed forward energy flow.

For the first time, the efficiency of the rapidity gap selection of diffractive events has been measured using a data event sample. This gap selection efficiency is needed in hard diffractive analyses to correct for the event losses due to the gap cuts. The measurement shows that it is well described by a resolved Pomeron Monte Carlo simulation (RAPGAP), within an accuracy of 34 % for the hard jet sample. Due to the virtually complete rejection of the Reggeon contribution to the jet samples by the gap selection cuts, this measurement can be interpreted as a measurement of the efficiency of the rapidity gap selection for Pomeron mediated exchange processes.

11.2 Photoproduction

In contrast to deep-inelastic scattering, neither the inclusive, nor the samples with moderate jet requirements are well described by a hard leading order Monte Carlo simulation. Significant differences are observed in the total transverse energy, the transverse momentum of the leading jet, the number of multijet events, and the transverse energy flow in the central region of the main detector. All of these variables show that the data events are on average considerably harder than the Monte Carlo events. The measured discrepancies are all correlated, and they are also observed in a rapidity gap selected hard diffractive event sample with large event numbers. They are thus no experimental problem of

the FPS analysis, but a deficit in the RAPGAP generator, which is used for both analyses. Pomeron and Reggeon contributions are well described by the predictions of the inclusive F_2^D measurement. However, due to the low Reggeon contribution, no measurement of the Pomeron and Reggeon fractions is performed.

A better agreement between data and Monte Carlo simulation could be achieved by increasing the direct photon contribution to the Monte Carlo samples. A huge increase by at least a factor of two would however be needed, and significant differences would still remain. This is therefore not the solution to the observed deviations.

The discrepancies are hence probably caused by general deficiencies in the QCD description of the scattering process, which are possibly due to the missing hard scale Q^2. This is supported by the fact that the disagreement between data and Monte Carlo simulation remains untouched by the rapidity gap selection. Furthermore, a reasonable agreement has been observed for all energy flow distributions in a hard rapidity gap selected diffractive event sample, if the kinematic distributions of the Monte Carlo simulation are reweighted to describe the data. The observed differences are thus probably not connected to the description of the diffractive physics within the used resolved Pomeron model, ie to the description of the Pomeron and Reggeon remnants. Due to the statistical limitations, a thorough investigation of these discrepancies is beyond the possibilities of this analysis.

The energy flow in the forward region of the main detector, and in the forward detectors is well described by the Monte Carlo simulation, based on the resolved Pomeron model. Slight differences are observed in the forward part of the Liquid Argon calorimeter. They are probably due to similar QCD effects as in the case of deep-inelastic scattering, and thus not connected to the diffractive physics. The hits in the Forward Muon Detector, and the energy flow in the Plug calorimeter – both mainly caused by the Pomeron and Reggeon spectator – are well described. The resolved Pomeron model thus works well also in the case of photoproduction. No hints for changes in the forward energy flow compared to deep-inelastic scattering – eg due to remnant-remnant interactions in resolved photon processes, which could fill the rapidity gap (TeVatron effect) – have been observed.

As for the deep-inelastic scattering event samples, the efficiency of the rapidity gap selection of diffractive events has been measured for the first time using a data event sample. The efficiency predicted by a resolved Pomeron Monte Carlo simulation (RAPGAP) agrees with the data within an accuracy of 22 % for the hard jet sample, limited by the data statistics. Due to the hard cut on the total transverse energy, the Reggeon contribution is strongly reduced in all event samples, and the measurement can – in the case of hard jets – be interpreted as a measurement of the efficiency of the gap selection for Pomeron mediated exchange processes.

11.3 Conclusions

In conclusion, it is noted that the resolved Pomeron model works well, both in deep-inelastic scattering and photoproduction. Pomeron and Reggeon fractions are well described by the predictions from the inclusive F_2^D measurement. All forward energy flow distributions are reasonably well described by the concept of Pomeron and Reggeon remnants as implemented in the resolved Pomeron model. No changes in the forward energy flow – eg due to remnant-remnant interactions in resolved photon processes (Tevatron effect) – are observed in the photoproduction event samples. The efficiency and the effects of the standard rapidity gap selection of diffractive events agree reasonably well between the data and the resolved Pomeron Monte Carlo simulation.

Acknowledgements

Keine Rast

Seele, banger Vogel du,
Immer wieder mußt du fragen:
Wann nach so viel wilden Tagen
Kommt der Friede, kommt die Ruh?

O ich weiß: kaum haben wir
Unterm Boden stille Tage,
Wird vor neuer Sehnsucht dir
Jeder liebe Tag zur Plage.

Und du wirst, geborgen kaum,
Dich um neue Leiden mühen
Und voll Ungeduld den Raum
Als der jüngste Stern durchglühen.

Hermann Hesse

Acknowledgements

List of Figures

List of Figures

List of Tables

List of Tables

Bibliography

[1] K. Goulianos: *Diffractive Interactions of Hadrons at High Energies*, Physics Reports **101** (1983) 169.

[2] P.R. Newman: *A Study of the Dynamics of Diffractive Photoproduction at HERA*, Dissertation, University of Birmingham (1996), h1th-064.

[3] W. Demtröder: *Experimentalphysik 2: Elektrizität und Optik*, Springer Verlag (1995)

[4] K. Goulianos: *Diffractive Interactions of Hadrons at High Energies*, Physics Reports **101** (1983) 169.

[5] P.D.B. Collins: *An Introduction to Regge Theory and High Energy Physics*, Cambridge University Press (1977)

[6] J.R. Forshaw, D.A. Ross: *Quantum Chromodynamics and the Pomeron*, Cambridge University Press (1997)

[7] F.-P. Schilling: *Untersuchung von 2-Jet-Ereignissen in der diffraktiven tiefinelastischen Streuung mit dem H1-Detektor*, Diploma thesis, University of Heidelberg (1998)

[8] A. Donnachie, P.V. Landshoff: *Total Cross Sections*, Phys. Lett. **B 296** (1992) 227.

[9] F.-P. Schilling: *Diffractive Jet Production in Deep-Inelastic e^+p Collisions at HERA*, Dissertation, University of Heidelberg (2000), h1th-216.

[10] D.H. Perkins: *Introduction to High Energy Physics*, 4th edition, Cambridge University Press (2000)

[11] S. Schätzel: *Measurement of Dijet Cross Sections in Diffractive Photoproduction at HERA*, Diploma thesis, University of Heidelberg (2000), h1th-212.

[12] J. Stiewe: *HERA (and Non-HERA) Kinematics for Pedestrians* Private Communication (2003)

[13] M. Wüsthoff, A. Martin: *The QCD Description of Diffractive Processes*, J. Phys. **G 25** (1999) R309.

[14] J.C. Collins: *Proof of Factorization for Diffractive Hard Scattering*, Phys. Rev. **D 57** (1998) 3051.

[15] G. Ingelman, P. Schlein: *Jet Structure in High Mass Diffractive Scattering*, Phys. Lett. **B 152** (1985) 256.

[16] F.-P. Schilling: *Hard Diffraction at HERA*, APS-DPF Meeting, Williamsburg (2002) (see also http://www.desy.de/~fpschill)

[17] H. Jung: *Hard Diffractive Scattering in High-Energy ep Collisions and the Monte Carlo RAPGAP*, Madrid Workshop on Low x Physics (1997) (see also http://www-h1.desy.de/~jung/rapgap.html)

Bibliography

[18] A. Edin, G. Ingelman, P. Schlein: *Soft Colour Interactions as the Origin of Rapidity Gaps in DIS*, DESY-Report 95-077 (1995), hep-ph/9508386.

[19] F. Halzen, A.D. Martin: *Quarks and Leptons: An Introductory Course in Modern Particle Physics*, John Wiley & Sons Inc. (1984)

[20] W. Buchmüller, T. Gehrmann, A.Hebecker: *Inclusive and Diffractive Structure Functions at Small x*, Nucl. Phys. **B 537** (1999) 477.

[21] M. Wüsthoff, A. Martin: *The QCD Description of Diffractive Processes*, J. Phys. **G 25** (1999) R309.

[22] The H1 Collaboration: *Inclusive Measurement of Diffractive Deep-Inelastic $\vec{e}p$ Scattering*, Z. Phys. **C 76** (1997) 613.

[23] G. Altarelli, G. Parisi: Nucl. Phys. **B 126** (1977) 298.

[24] The H1 Collaboration: *Measurement and NLO DGLAP QCD Interpretation of Diffractive Deep-Inelastic Scattering at HERA* , Conference paper, DIS 2002, H1prelim-02-012.

[25] M. Glück, E. Reya, A. Vogt, Z. Phys. **C53** (1992) 651.

[26] The H1 Collaboration: *Measurement of Semi-Inclusive Diffractive Deep-Inelsatic Scattering with a Leading Proton at HERA*, 31st International Conference on High Energy Physics ICHEP02, Amsterdam 2002.

[27] M. Wobisch: *Measurement and QCD Analysis of Jet Cross Sections in Deep-Inelastic Positron-Proton Collisions at $\sqrt{s} = 300$ GeV*, Dissertation, University of Aachen (2000), DESY-THESIS-2000-049 (h1th-201)

[28] O. Kaufmann: *Messung des Zweijet-Wirkungsquerschnitts in Photon-Proton-Kollisionen und Bestimmung der Gluondichte im Photon*, Dissertation, University of Heidelberg (1998), h1th-185.

[29] The CDF Collaboration: *Diffractive Dijets with a Leading Antiproton in $p\bar{p}$ Collisions at $\sqrt{s} = 1800$ GeV*, Phys. Rev. Lett. **84**, 5043 (2000)

[30] H. Spiesberger, A. Kwiatkowski, H.-J. Moehring: *HERACLES – An Event Generator for ep Interactions at HERA Including Radiative Processes*, http://www.desy.de/~hspiesb/heracles.html (1996)

[31] B. Andersson et al., Phys. Rep. **97** (1983) 31.

[32] T. Sjöstrand: *PYTHIA 5.7 and JETSET 7.4*, CERN-TH-7112/93 (1993)

[33] C. Kleinwort: *CJC Status*, http://www-h1.desy.de/h1/iww/idet/itracker/icjc/cjc_status.html (2003)

[34] J.L. Augneres: *HERA – A Proposal for a Large Electron-Proton Colliding Beam Facility at DESY*, DESY HERA 81/10, (1981)

[35] The H1 Collaboration: *The H1 Detector at HERA*, Internal Report, DESY H1-96-01, (1996)

[36] S. Levonian: *H1 LUMI system components and tasks*, http://www-h1.desy.de/h1/www/h1det/lumi/ (1998)

[37] S. Levonian: *Help for the e-tagger related analyses*,
http://www-h1.desy.de/~levonian/QPETAC.html (2002)

[38] O. Karschnik: *Photoproduktion von ρ-Mesonen unter Nachweis des vorwärts gestreuten Protons*,
Dissertation, University of Hamburg (2001), h1th-290.

[39] Inter-University ULB-VUB, Brussels et al.: *Upgrade of the H1 Forward Proton Spectrometer*
(1995), H1 − 12/95 − 467.

[40] The H1 Collaboration: *Measurement of Dijet Cross-Sections at Low Q^2 and the Extraction of an Effective Parton Density for the Virtual Photon* (1998), DESY-98-205 (hep-ex/9812024)

[41] The H1 Collaboration, C. Adloff et al. , Z. Phys. **C 74** (1997) 221.

[42] G.A. Schuler, T. Sjöstrand: *Low- and High-Mass Components of the Photon Distribution Functions*, Z. Phys. C68, (1995) 607.

[43] S. Schätzel: *Private Communication*, University of Heidelberg (2003)

[44] W.R. Leo: *Techniques for Nuclear and Particle Physics Experiments: A How-to Approach*, Second Revised Edition, Springer Verlag (1994)

[45] V. Lendermann: *SpaCal: Analysis Issues*,
https://www-h1.desy.de/icalo/spacal/escale.html (2003)

[46] W. Hildesheim et al.: *The Plug Calorimeter Users Guide*, H1 Internal Note (1994), H1-IN-372.

[47] M. Krüger: *Kalibration des Plug-Kalorimeters und Verbesserung des Signal-Rauschverhältnisses*,
Diploma thesis, University of Hamburg (1996)

[48] E. Panaro: *Energy Measurements in e-p Collisions at HERA Using the Plug Calorimeter of the H1 Experiment*, Dissertation, University of Hamburg (1997)

[49] J. Dingfelder: *Private Communication*, University of Heidelberg (2003)

[50] M. Mozer: *Private Communication*, University of Heidelberg (2003)

[51] K. Sedlák: *Dijet Production at Low Q^2*, hep-ex/0207018v1 (2002)

[52] A.D. Martin, R.G. Roberts, W.J. Stirling, Durham preprints **DTP/95**/14 (1995)

[53] M. Mozer: *Private Communication*, University of Heidelberg (2003)

[54] D. Ozerov: *The Forward Tagger System of the H1 Experiment*,
http://www-h1.desy.de/h1/iww/idet/itracker/ifts/OLD/index.html (2000)

[55] M. Mozer: *Private Communication*, University of Heidelberg (2003)

[56] C. Werner: *Private Communication*, University of Heidelberg (2003)

[57] G.A. Schuler, H. Spiesberger: Proceedings of the Workshop on Physics at HERA, vol. 3, eds. W. Buchmüller, G. Ingelman, DESY (1992) 1419.

[58] F.-P. Schilling: *Diffractive Selection using forward detectors*,
https://www-h1.desy.de/iwork/idif/fwddet/main.html(2003)

[59] M. Mozer: *Private Communication*, University of Heidelberg (2003)

Bibliography

[60] M. Glück, E. Reya, A. Vogt, Phys. Rev. **D45** (1992) 3986; **D46** (1992) 1974.

[61] S. Schätzel: *Measurements of Dijet Cross Sections in Diffractive ep Collisions at HERA*, Dissertation, University of Heidelberg (2003)

Erklärung

Ich versichere, daß ich diese Arbeit selbständig verfaßt und keine anderen als die angegebenen Quellen und Hilfsmittel benutzt habe.

Heidelberg, den 20. November 2003   _____